Stephen Edkins

Visualising the Charge and Cooper-Pair Density Waves in Cuprates

Springer

Springer Theses

Recognizing Outstanding Ph.D. Research

Aims and Scope

The series "Springer Theses" brings together a selection of the very best Ph.D. theses from around the world and across the physical sciences. Nominated and endorsed by two recognized specialists, each published volume has been selected for its scientific excellence and the high impact of its contents for the pertinent field of research. For greater accessibility to non-specialists, the published versions include an extended introduction, as well as a foreword by the student's supervisor explaining the special relevance of the work for the field. As a whole, the series will provide a valuable resource both for newcomers to the research fields described, and for other scientists seeking detailed background information on special questions. Finally, it provides an accredited documentation of the valuable contributions made by today's younger generation of scientists.

Theses are accepted into the series by invited nomination only and must fulfill all of the following criteria

- They must be written in good English.
- The topic should fall within the confines of Chemistry, Physics, Earth Sciences, Engineering and related interdisciplinary fields such as Materials, Nanoscience, Chemical Engineering, Complex Systems and Biophysics.
- The work reported in the thesis must represent a significant scientific advance.
- If the thesis includes previously published material, permission to reproduce this must be gained from the respective copyright holder.
- They must have been examined and passed during the 12 months prior to nomination.
- Each thesis should include a foreword by the supervisor outlining the significance of its content.
- The theses should have a clearly defined structure including an introduction accessible to scientists not expert in that particular field.

More information about this series at http://www.springer.com/series/8790

Stephen Edkins

Visualising the Charge and Cooper-Pair Density Waves in Cuprates

Doctoral Thesis accepted by
the University of St Andrews, St Andrews, Scotland, UK

🐴 Springer

Author
Dr. Stephen Edkins
School of Physics and Astronomy
University of St Andrews
St Andrews
Scotland, UK

Supervisors
Prof. J.C. Davis
University of St Andrews
St Andrews
Scotland, UK

Prof. A.P. Mackenzie
University of St Andrews
St Andrews
Scotland, UK

In memory of my father, David John Edkins (1947–2007), who fostered my interest in science and technology.

Supervisor's Foreword

It was a great pleasure to co-supervise Stephen Edkins for his Ph.D. studies. We have collaborated for over a decade now and are always on the lookout for exceptionally talented graduate students. Our joint projects are very demanding both technically and because they require splitting the student's Ph.D. time between the UK and the USA. Stephen had an exemplary record as an undergraduate at the University of Cambridge, so when he applied to work on a joint project that we were offering to do spectroscopic imaging scanning tunneling microscopy (SI-STM) of cuprate and ruthenate superconductors, we were delighted to invite him to join the team. He first excelled on his graduate courses at the Scottish Centre for Doctoral Training in Condensed Matter Physics in St Andrews, and there he also performed useful finite element calculations that helped with the design of novel uniaxial pressure apparatus.

After that first year at St Andrews, Stephen moved to Cornell to begin working on the SI-STM projects. Atomically resolved visualization of electronic structure using standard single-electron tunneling allowed him to obtain important results on the symmetry of the famous density wave state that is the wide focus of studies in lightly doped cuprate superconductors. Stephen played a key role in establishing that this density wave has a d-symmetry form factor, a state that has never been observed in any other system or material. He showed that this exotic form factor exists not just at zero magnetic field but also in the density wave that can be induced within vortex cores. Not content with this, he also obtained excellent data from the superconductor Sr_2RuO_4 at dilution refrigerator temperatures.

In spite of the quality of the data obtained in all three of the above projects, in the end Stephen elected not to include the vortex core or Sr_2RuO_4 work in his thesis. This is because of a serendipitous development. During the project on the cuprates, he and his collaborator Mohammed Hamidian managed to pick up a nanoscale flake of high-temperature superconductor and have it terminate the standard tungsten STM tip. They recognized that this situation allowed them to form Josephson tunnel junctions with nanometer resolution so that, if such tips can be scanned stably, visualization of the superconducting condensate based on Cooper-pair tunneling would become possible for the first time. This discovery opened the way to an

entirely new class of instrument, a scanned Josephson tunneling microscope (SJTM). But this unanticipated project came with all the challenges associated with pursuing unprecedented research directions. With no literature comparisons to work from, the team had to understand what regime the Josephson junctions were operating in, and establish what classes of information the new SJTM could yield. Stephen's contributions to this were pivotal, and the comprehensive and didactic description that he has provided in this thesis will, we believe, underpin this new field as it moves forward.

As well as describing and developing the new instrument, Stephen's measurements revealed a periodically modulated superconducting condensate with a wavelength of a few nm in cuprates. Spatially modulated superconductivity was first postulated theoretically half a century ago, and also features prominently in coupled order parameter theories of high-temperature superconductivity; the data presented in Chap. 7 of this thesis are the first experimental observation of its existence.

We have both been privileged to supervise many outstanding graduate students, but few achieve something as novel and substantial as Stephen did on this project. This is one of the best PhD theses that we have supervised or read, and we are delighted to see it recognized in this way by Springer.

St Andrews, Scotland, UK   Prof. J.C. Davis
                                                         Prof. A.P. Mackenzie

Abstract

The study of cuprate high-temperature superconductors has undergone a recent resurgence due to the discovery of charge order in several families of cuprate materials. While its existence is now well established, little is known about its microscopic origins or its relationship to high-temperature superconductivity and the pseudogap. The aim of the research presented in this thesis is to address these questions.

In this thesis, I will report on the use of spectroscopic imaging scanning tunneling microscopy (SI-STM) to visualize the short-ranged charge density wave (CDW) in $Bi_2Sr_2CaCu_2O_{8+\delta}$ and $Na_xCa_{2-x}CuO_2Cl_2$. Building on previous measurements of the intra-unit-cell electronic structure of cuprates, I introduce sub-lattice segregated SI-STM to individually address the atomic sub-lattices in the CuO_2 plane with spatial phase sensitivity. Using this technique, I establish that the CDW in $Bi_2Sr_2CaCu_2O_{8+\delta}$ and $Na_xCa_{2-x}CuO_2Cl_2$ has a previously unobserved d-symmetry form factor, where a breaking of rotational symmetry within the unit cell is modulated periodically in space.

Toward identifying a mechanism of CDW formation, I establish that the amplitude of CDW modulations in the electronic structure is maximal at the pseudogap energy scale and that these modulations exhibit a spatial phase difference of π between filled and empty states. Together with the doping evolution of the CDW wave vector, this highlights the role of the low-energy electronic structure of the pseudogap regime in CDW formation.

To elucidate the relationship between the CDW and the superconducting condensate, I will introduce nanometer resolution scanned Josephson tunneling microscopy (SJTM). In this approach, the Cooper-pair (Josephson) tunneling current between a $Bi_2Sr_2CaCu_2O_{8+\delta}$ sample and a scannable $Bi_2Sr_2CaCu_2O_{8+\delta}$ nano-flake STM tip is used to directly visualize the superconducting condensate. I will report the observation of a periodic modulation in the Cooper-pair condensate at the same wave vector as the CDW, the first direct detection of a periodically modulating condensate in any superconductor.

Acknowledgements

I would first and foremost like to thank my supervisors Séamus Davis and Andy Mackenzie for their support and guidance, as well as teaching me a great deal. I have benefited greatly from the research environment in both of their groups, of which membership has been a privilege.

The research presented in Chap. 4 of this thesis was carried out in close collaboration with Mohammad Hamidian and Kazuhiro Fujita to whom I extend my gratitude for sharing their expertise in spectroscopic imaging STM. The research presented in Chaps. 5 and 7 was conducted in collaboration with Mohammad Hamidian and Andrey Kostin. I thank Mohammad for his tutelage in the operation of a cryogenic STM.

The idea of examining the difference between the oxygen sub-lattices of the CuO_2 plane in SI-STM spectroscopic maps to reveal a d-symmetry form factor CDW was originally suggested by Subir Sachdev. I would like to thank him for sharing this with us as well as for useful discussions. I would also like to thank Andrey Chubukov for his very useful comments in the preparation of Chap. 6.

Finally, I would like to thank all of my colleagues past and present for their help, advice, and friendship, as well as my family for their love and support.

Contents

Chapter 1
Introduction to Unconventional Superconductivity and Density Waves in Cuprates

Superconductors, known for their ability to conduct electricity without resistance, are fairly common in nature. This is a result of the fact that, despite the strong interactions between their electrons, most of the metals we know can be described by a liquid of electron-like quasi-particles. This liquid, known as a Fermi liquid, is intrinsically unstable to the formation of superconductivity. The vast majority of these superconductors only superconduct below a transition temperature which is within a few degrees of absolute zero, limiting their widespread commercial exploitation.

This thesis concerns a family of superconductors whose superconducting transition temperatures were unprecedentedly high upon their discovery by Bednorz and Muller in 1986 [1]. These materials, known as cuprates because their common constituents are copper and oxygen, won Bednorz and Muller the 1987 Nobel Prize for Physics for their discovery [2]. Although the cuprates lost their status as the highest temperature superconductors in the past couple of years to hydrides at ultra-high pressures, they retain the name "high temperature superconductors" and are still a system of unparalleled interest [3]. The high transition temperatures of the hydrides seems to be well understood in terms of extensions of traditional theory, but the mechanism of the more exotic superconductivity in cuprates is still the subject of active debate.

In addition to superconductivity, the cuprates also exhibit what is called a charge density wave (CDW). In a CDW the charge density in the material modulates with a periodicity that is different from that of the material's crystal structure. In this thesis I utilise recent developments in scanning tunnelling microscopy (STM), and develop nanometer-resolution scanned Josephson tunnelling microscopy (SJTM) with the aim of elucidating the role of CDW in the physics of these materials.

1.1 Superconductivity

1.1.1 What Is a Superconductor?

The concept of spontaneous symmetry breaking is a cornerstone of 20th century physics [4]. In condensed matter physics we have chosen to classify different phases of matter by the symmetries they break. If the state of a system is not invariant under an element of the symmetry group of the Hamiltonian to which it is a statistical solution, then it is said to break the corresponding symmetry.

As an example take a macroscopic number of particles in free space which interact with each other. The Hamiltonian which governs these particles is invariant under spatial translations. However, the particles could condense into a crystal. This is clearly a state which breaks translational symmetry as depicted in Fig. 1.1 in one dimension.

The crystal has broken translational symmetry by "choosing" where to fix the jth particle in space, the positions of the others following directly from the lattice constant a_0 in a perfect crystal. Any choice of position for this first particle would have resulted in a state with the same free energy. The crystal has spontaneously broken translational symmetry by its choice of a position for the jth particle from a degenerate manifold.

We can expand the density of particles in Fourier components,

$$\langle n(x) \rangle = n_0 + Re\{n_Q(x)e^{iQx}\} + \dots , \tag{1.1}$$

where $Q = 2\pi/a_0$. The complex field $n_Q(x) = |n_Q(x)|e^{i \arg\{n_Q(x)\}}$ is a sensible choice of order parameter for our crystalline phase. It will be zero above the melting temperature of the crystal and non-zero below. In this language, choosing a particular position for the jth particle corresponds to choosing a particular phase of $n_Q(x)$, $\phi(x) = \arg\{n_Q(x)\}$. This corresponds to spontaneously breaking a U(1) symmetry. The concept of spatial phase in a crystal will be a key theme in this thesis which I will return to in Chaps. 3 and 4, where the spatial phase sensitivity of spectroscopic-imaging STM (SI-STM) will be used to probe the intra unit cell electronic structure of cuprates.

Part of the utility of the classifying phases of matter by their broken symmetries is that the broken symmetry has an attendant generalised rigidity [4], i.e. a stiffness to
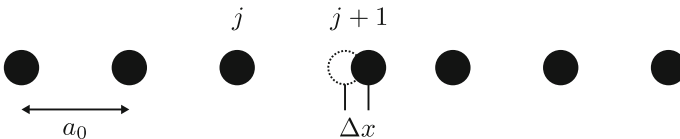
Fig. 1.1 Cartoon one-dimensional crystal with lattice constant a_0. The distance between the jth and $j + 1$th particle is stretched by a distance Δx

spatial gradients in the order parameter. For the crystal there is a very tangible rigidity to changing the separation between any two atoms, akin to stretching a spring. If we consider the order parameter description of this crystal then we can recast this as a phase rigidity. To change the distance between two particles, j and $j + 1$ by an amount Δx requires a phase gradient $\phi(x_{j+1}) - \phi(x_j) = Q\Delta x$, for which there is an energy cost.

If we make the constraint that the order parameter amplitude is spatially uniform so that $n_Q(x) = |n_0|e^{i\phi(x)}$ we can make the following expansion of the free energy

$$F[\phi(x)] = F_0 + \int dx\,K\,(\nabla\phi(x))^2 + \dots \tag{1.2}$$

where K is a positive constant and F_0 is the energy of the uniform crystal. Here there is a clear energy cost to gradients in $\phi(x)$; a phase rigidity. Viewed this way, that fact that crystals behave like rigid bodies is a natural consequence of their phase stiffness, which in turn is a direct consequence of breaking translational symmetry.

For a superconductor the relevant broken symmetry of the Hamiltonian is a global phase symmetry. This is the invariance of the Hamiltonian under a transformation of the quasi-particle operators of the form $\hat{\psi}^\dagger(\vec{r}) \rightarrow e^{i\theta}\hat{\psi}^\dagger(\vec{r})$, as must be the case if the number of particles is conserved. What are the consequences of breaking this symmetry?

An order parameter describing this phase would be a complex scalar field of the form $\Psi(\vec{r}) = |\Psi(\vec{r})|e^{i\phi(\vec{r})}$. If this order parameter is non-zero then everywhere this state breaks the U(1) phase symmetry of the Hamiltonian. We can construct a Ginzburg–Landau expansion of the Helmholtz free energy functional in this order parameter

$$F[\Psi(\vec{r})] = \int d^3\vec{r}\,\alpha(T - T_c)|\Psi(\vec{r})|^2 + \frac{\beta}{2}|\Psi(\vec{r})|^4 + \frac{1}{2m}|\left(-i\hbar\nabla - 2e\vec{A}\right)\Psi(\vec{r})|^2 + \frac{|\vec{B}|^2}{2\mu_0} + \dots \tag{1.3}$$

where $\vec{A}$ is the magnetic vector potential and $\vec{B} = \nabla \times \vec{A}$ [5]. This is the simplest expansion of an electrically charged complex scalar field that is gauge invariant. In anticipation of the microscopic description of a superconductor in terms of Cooper-pairs of electrons I have given the field a charge $2e$ where e is the electron charge. That the field is scalar implies that these Cooper-pairs are in a spin-singlet state. Below a critical temperature T_c the order parameter Ψ will become non-zero to minimise this free energy.

Now consider the case where the order parameter amplitude is everywhere constant so that $\Psi(\vec{r}) = |\Psi_0|e^{i\theta(\vec{r})}$. We can write the free energy functional as,

$$F[\theta(\vec{r})] = F_0 + \rho_s \int d^3\vec{r}\,\left(\nabla\theta(\vec{r}) + \frac{2e}{\hbar}\vec{A}\right)^2 + \dots\,, \tag{1.4}$$

with F_0 the free energy of the uniform superconducting state and ρ_s, the superfluid stiffness, given by

$$\rho_s = \frac{\hbar^2}{2m} |\Psi_0|^2 \ . \tag{1.5}$$

It is informative at this point to revisit the discussion of crystallisation and the analogies that can be drawn between that process and the formation of the superconducting condensate. The 1D crystal considered above breaks a global U(1) symmetry by choosing a lattice phase. This broken symmetry results in a generalised rigidity, a rigidity against deforming the inter-particle separation from its equilibrium value. This can be expressed as a phase stiffness. This phase stiffness essentially defines this 1D crystalline state of matter.

The same is true of the superconductor. It breaks a U(1) phase symmetry resulting in a stiffness, ρ_s, to gradients in the phase of the order parameter $\theta(\vec{r})$. Below I will show that the physical properties of a superconductor follow immediately from this broken phase symmetry and its resultant phase stiffness. This phase stiffness is the defining property of a superconductor.

Making a Legendre transformation, $g = f - \mu_0 \vec{H} \cdot \vec{B}$, of Eq. 1.4 to the Gibbs free energy and minimising with respect to variations $\delta \vec{A}$ yields a current

$$\vec{j}_s = -\frac{2e}{\hbar} \rho_s \left(\nabla \theta(\vec{r}) + \frac{2e}{\hbar} \vec{A} \right) \ . \tag{1.6}$$

This expression has profound consequences.

The first is that superconductors should expel magnetic flux from their bulk: the Meissner effect [6]. To see this we can take the curl of both sides resulting in the following differential equation for the magnetic field

$$\nabla^2 \vec{B} = \frac{\vec{B}}{\lambda^2} \ , \tag{1.7}$$

where $\lambda = \sqrt{\hbar^2 / 4\mu_0 e^2 \rho_s}$ is a phenomenological constant called the penetration depth. This implies that magnetic fields must exponentially decay into the bulk of a superconductor over a length scale λ. Thus superconductors expel magnetic fields from their bulk.

To act as perfect diamagnets and expel magnetic fields from their bulk, superconductors must produce screening currents that oppose an applied magnetic field. These must be equilibrium currents, implying that they experience zero resistance. These zero resistance equilibrium currents suggest the possibility of non-equilibrium currents with zero resistance which are a hallmark of superconductivity and give it its name.

A zero resistance transport current, the passing of current without any voltage dropped, was measured by Kamerlingh Onnes in mercury in 1911, heralding the discovery of superconductivity [7]. Clearly this property is remarkable and of great technological importance. However, it is not fundamental to superconductivity in the way that the equilibrium screening currents of the Meissner effect are.

1.1.2 BCS Theory of Superconductivity

Having considered what a superconductor is from a phenomenological point of view, I now turn to a microscopic description of such a state. Key insight into this came in 1957 with a paper from Bardeen, Cooper and Schrieffer, the exposition of what is now called the BCS theory of superconductivity [8].

Prior to this Cooper had shown that, in the presence of a Fermi surface and arbitrarily weak attractive interactions, two quasi-particles with opposite momenta are unstable to the formation of a bound state or Cooper pair. One way of demonstrating this instability of the Fermi liquid is to calculate the particle-particle (pairing) susceptibility within the random phase approximation (RPA),

$$\chi_{pp}(\vec{q}, \omega) = \frac{\chi_{pp}^0(\vec{q}, \omega)}{1 + g\chi_{pp}^0(\vec{q}, \omega)} \,, \tag{1.8}$$

which measures the response to a field that acts to pair particles [9]. Here g is an effective point-like interaction between Fermi liquid quasi-particles with spin σ of momentum $\vec{k}$ and energy $\epsilon_{\sigma,\vec{k}}$. χ_{pp}^0 is the bare (non-interacting) susceptibility,

$$\chi_{pp}^0(\vec{q} = 0, \omega) = \frac{1}{\Omega} \sum_{\vec{k}} \frac{f(\epsilon_{\sigma,\vec{k}}) - f(-\epsilon_{\sigma-\vec{k}})}{\hbar\omega - \epsilon_{\sigma,\vec{k}} - \epsilon_{-\sigma,-\vec{k}} + i0^+} \,, \tag{1.9}$$

where $f(\epsilon_{\sigma,\vec{k}})$ is the occupation factor of a quasi-particle state labelled by $\vec{k}$ and σ and Ω is the volume of the system.

In the limit where $\omega, \vec{q} \to 0$

$$\chi_{pp}^0(\vec{q} = 0, \omega = 0) \sim N(\epsilon = 0) \log(\Lambda/T) \,. \tag{1.10}$$

Here $N(\epsilon = 0)$ is the density of states of the Fermi energy and Λ is an ultra-violet cut-off [9]. Equation 1.10 shows that $\chi_{pp}^0(\vec{q} = 0, \omega = 0)$ is positive and logarithmically divergent with decreasing temperature. This results from the fact that, in the presence of time reversal symmetry, $\epsilon_{\sigma,\vec{k}} = \epsilon_{-\sigma,-\vec{k}}$. Examination of Eq. 1.8 then shows that for any arbitrarily small attractive interaction ($g < 0$) the particle-particle susceptibility will diverge at non-zero temperature. This signals an intrinsic instability of the metal towards forming Cooper pairs.

In the simplest case, the wave-function of the Cooper-pair can be written as a product of orbital and spin parts. Anti-symmetry under exchange then dictates that if the pair is in a spin-singlet state it must have an even parity orbital wave-function. If the pair is a spin-triplet state it must have an odd parity orbital wave-function. If we were to expand the orbital wave-function in spherical harmonics (which is valid in free space), spin-singlet pairs will have angular momentum quantum number $l = 0, 2, \dots$ which we call *s*- and *d*-wave respectively, by analogy with the orbitals

of the hydrogen atom. Likewise, spin-triplet superconductors will have $l = 1, 3, \ldots$ corresponding to p- and f-wave respectively.

With the insight that the Fermi liquid is unstable to the formation of Cooper-pairs in the presence of an attractive interaction, Bardeen, Cooper and Schrieffer considered the equivalent of the Hamiltonian,

$$\hat{H} = \sum_{\vec{k}\sigma} \epsilon_{\vec{k}} \hat{c}^{\dagger}_{\vec{k}\sigma} \hat{c}_{\vec{k}\sigma} + \sum_{\vec{k}\vec{q}} V_{\vec{k}\vec{q}} \hat{c}^{\dagger}_{\vec{k}\uparrow} \hat{c}^{\dagger}_{-\vec{k}\downarrow} \hat{c}_{-\vec{q}\downarrow} \hat{c}_{-\vec{q}\uparrow}, \tag{1.11}$$

where

$$V_{\vec{k}\vec{q}} = \begin{cases} -V & \text{if } |\epsilon_{\vec{k}}| \text{ and } |\epsilon_{\vec{q}}| \leq \hbar\omega_c \\ 0 & \text{otherwise} \end{cases} \tag{1.12}$$

so that there is an attractive interaction between quasi-particles up to a energy cut-off $\hbar\omega_c$ away from the Fermi energy. It is manifest in the form of the interaction chosen that any Cooper pairs formed will be of the spin-singlet type and thus must have an even parity orbital wave-function.

Anticipating the formation of a condensate of Cooper-pairs BCS introduced the variational wave-function,

$$|\Psi_{BCS}\rangle = \prod_{\vec{k}} \left(|u_{\vec{k}}| + |v_{\vec{k}}| e^{i\theta} \hat{c}^{\dagger}_{\vec{k}\uparrow} \hat{c}^{\dagger}_{-\vec{k}\downarrow} \right) |0\rangle , \tag{1.13}$$

where $|u_{\vec{k}}|^2 + |v_{\vec{k}}|^2 = 1$, θ is an arbitrary phase factor and $|0\rangle$ corresponds a sea of Fermi liquid quasi-particle states filled up to the Fermi wave-vector $\vec{k}_F$ [8]. This many-body wave-function takes the form of a superposition of a filled Fermi surface plus a Fermi surface with 0, 1, 2,…Cooper pairs. Making a connection with the previous section, this is a coherent state of Cooper pairs, with minimum uncertainty in the phase and indefinite particle number. It thus manifestly breaks phase symmetry and we can associate θ with the phase of the condensate.

BCS went on to find the parameters $u_{\vec{k}}$ and $v_{\vec{k}}$ of the ground state by the variational method. In Chap. 2 we will need to calculate the single-particle tunnelling current between a superconductor and either a normal metal or another superconductor. For this we will need to know the single-particle excitation spectrum of the superconductor. To calculate this one can follow Bogoliubov [10] who considered the following mean-field decoupling of Eq. 1.11

$$\hat{H} = \sum_{\vec{k}\sigma} \epsilon_{\vec{k}} \hat{c}^{\dagger}_{\vec{k}\sigma} \hat{c}_{\vec{k}\sigma} + \sum_{\vec{k}\sigma} \Delta_{\vec{k}} \hat{c}^{\dagger}_{\vec{k}\uparrow} \hat{c}^{\dagger}_{-\vec{k}\downarrow} + \Delta^*_{\vec{k}} \hat{c}_{-\vec{k}\downarrow} \hat{c}_{-\vec{k}\uparrow} , \tag{1.14}$$

with mean-field $\Delta_{\vec{k}}$ given by the self-consistency condition

$$\Delta_{\vec{k}} = \sum_{\vec{q}} V_{\vec{k}\vec{q}} \langle \hat{c}_{-\vec{q}\downarrow} \hat{c}_{\vec{q}\uparrow} \rangle . \tag{1.15}$$

The Hamiltonian in Eq. 1.14 can be diagonalised by a canonical transformation. First we introduce new quasi-particle operators which are mixtures of electron and hole creation operators,

$$\alpha_{\vec{k}} = u_{\vec{k}} \hat{c}_{\vec{k},\uparrow} - v_{\vec{k}} \hat{c}^{\dagger}_{-\vec{k},\downarrow} \tag{1.16}$$

$$\beta_{\vec{k}} = u_{\vec{k}} \hat{c}_{-\vec{k},\downarrow} + v_{\vec{k}} \hat{c}^{\dagger}_{\vec{k},\uparrow} \, , \tag{1.17}$$

where $|u_{\vec{k}}|^2 + |v_{\vec{k}}|^2 = 1$ to retain Fermionic anti-commutation relations. In terms of these operators the Hamiltonian can be written in the diagonal form,

$$\hat{H} = \sum_{k} E_k \left(\alpha^{\dagger}_{\vec{k}} \alpha_{\vec{k}} + \beta^{\dagger}_{\vec{k}} \beta_{\vec{k}} \right) \, , \tag{1.18}$$

where $E_{\vec{k}} = \sqrt{\epsilon_{\vec{k}}^2 + |\Delta_{\vec{k}}|^2}$ and the coefficients $u_{\vec{k}}$ and $v_{\vec{k}}$ that diagonalise the Hamiltonian are

$$|v_{\vec{k}}|^2 = 1 - |u_{\vec{k}}|^2 = \frac{1}{2} \left(1 - \frac{\epsilon_{\vec{k}}}{E_{\vec{k}}} \right) \, . \tag{1.19}$$

Equation 1.18 shows that there is a gap Δ_k to excitations of the superconductor as shown in Fig. 1.2. On exceeding the gap energy, the excitations are described by acting on the BCS ground state with a mixture of particle and hole creation operators. For example $\alpha^{\dagger}_{\vec{k}}$ creates a quasi-particle which for $E_{\vec{k}} = \Delta_{\vec{k}}$ is an equal admixture of electron and hole creation operators, but with increasing $E_{\vec{k}}$ the admixture of hole creation operator gradually diminishes. These quasi-particles, created by $\alpha^{\dagger}_{\vec{k}}$ and $\beta^{\dagger}_{\vec{k}}$ are often called Bogoliubov quasi-particles or Bogoliubons.
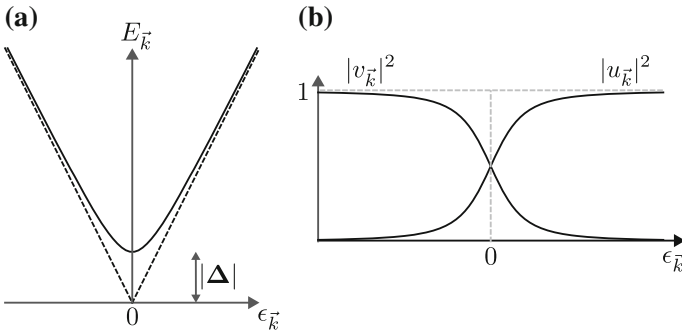
Fig. 1.2 a Excitation spectrum for BCS superconducting state with $\epsilon_{\vec{k}} = v_F(\vec{k} - \vec{k}_F)$ and s-wave superconducting gap $\Delta_k = \Delta$. *Dashed lines* are the bare band $|\epsilon_{\vec{k}}|$. **b** $|u_{\vec{k}}|^2$ and $|v_{\vec{k}}|^2$ for the excitation spectrum shown in **a**. At $E_{\vec{k}} = |\Delta|$ the Bogoliubov quasi-particle creation operators are an equal admixture of hole and electron creation operators but with increasing energy rapidly becomes the excitations of the bare band

What form does this gapping of the Fermi surface take? As I will discuss below, the conventional superconductors have an *s*-wave gap that has the same sign on all parts of the Fermi surface, leading to a fully gapped Fermi surface. Cuprate superconductors on the other hand have a gap that changes sign upon rotation by 90°, and thus necessarily has points where the gap goes through zero called nodes [11]. At these points there are gapless Bogoliubov quasi-particle excitations.

In the conventional superconductors considered by BCS, the effective attractive interaction is a result of the electron-phonon interaction. An electron moving through the lattice disturbs it, leaving a region of net positive charge in its wake. Another electron passing through will feel an attraction to this cloud of positive charge through the Coulomb interaction. Thus, there is an effective attractive interaction between the two electrons at the same point but at different times.

This retarded interaction is afforded by the mismatch is timescales over which electrons and phonons propagate in the material. That the electrons feel an attractive interaction at the same place leads the pair-wave function to be *s*-wave so that the probability of both electrons being in the same place is non-zero, maximising the potential energy gain. Key experiments confirming the predictions of BCS theory and the electron-phonon mechanism are reviewed in Ref. [12].

Having discussed the nature of and mechanism behind conventional superconducting states I will now go to discuss the cuprate high temperature superconductors whose superconductivity in unconventional in both its nature and mechanism.

1.2 High-Temperature Unconventional Superconductivity in Cuprates

The common constituent of all cuprate superconductors are the copper oxide planes shown in Fig. 1.3a. These copper oxide layers are incorporated between inert ionic layers which can act as a source of holes or electrons for the CuO_2 layers, thereby doping them.

Each CuO_2 plaquette contains one copper atom and two oxygen atoms. Much focus in this thesis will be given to a breaking of rotational symmetry within the unit cell via an inequivalence of these two oxygen sites, which I will term *x* and *y*-directed oxygens respectively.

Each copper contributes a singly occupied $3d_{x^2-y^2}$ orbital. *x* and *y* directed oxygens each contribute a doubly occupied $2p_x$ or $2p_y$ orbital respectively. The compact nature of the $3d_{x^2-y^2}$ orbital leads to a large energetic cost for double occupation arising from the Coulomb interaction. In cuprates the difference in energy between a singly and doubly occupied $3d_{x^2-y^2}$ orbital, U_d, is $\sim 7-10$ eV [13].

This onsite Coulomb repulsion, or Hubbard U_d, splits the spectral weight from the $3d_{x^2-y^2}$ orbitals into upper and lower Hubbard bands with a gap, U_d, for charge excitations between them as shown in Fig. 1.4. If this were the full story then this would lead to an insulator of the Mott-Hubbard type where hopping of electrons is
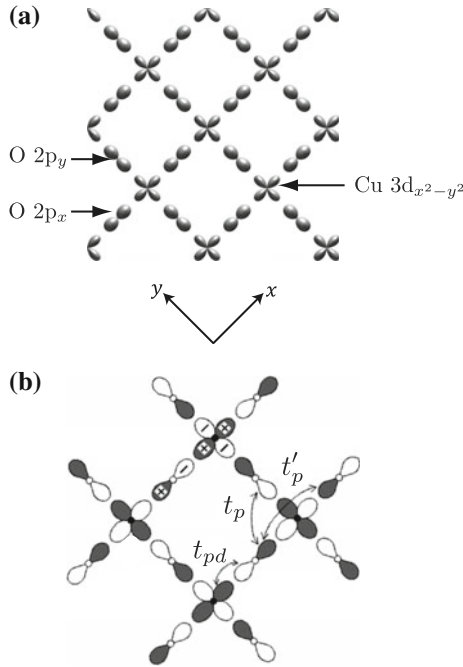
Fig. 1.3 **a** CuO$_2$ plaquettes consisting of copper $3d_{x^2-y^2}$ and oxygen $2p_{x,y}$ orbitals forming a square lattice plane. **b** *Arrows* indicate orbitals contributing the hopping integrals t_{pd}, t_p and t'_p. Reproduced from Ref. [13] with permission
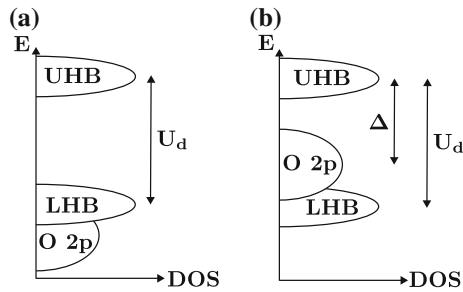
Fig. 1.4 **a** Schematic depiction of single-particle spectrum for a Mott-Hubbard insulator showing smallest optical gap, U_d, is between the lower and upper Hubbard bands (UHB and LHB) derived from the Cu $3d_{x^2-y^2}$ orbitals. **b** Depiction of a charge transfer insulator where the smallest optical gap, Δ, is between the O 2p derived band and the upper Hubbard band (UHB)

prohibited by the energetic cost of moving an electron from one Cu sites to doubly occupy another. Cuprates however fall into a related class of insulators, proposed by Zaanen, Sawatsky and Allen, known as charge-transfer insulators [14].

In a charge-transfer insulator the smallest gap for charge excitations is to take an electron from an oxygen 2p orbital and put it on the copper site. In cuprates, x-ray absorption spectroscopy has shown that this is the smallest charge excitation gap with value, $\Delta \sim 2-4\,\text{eV}$, which is smaller than U_d [15–17]. The consequence of this is that when holes are first doped into the CuO_2 plane, it is into the oxygen 2p orbitals.

1.2.1 Effective Models of the CuO₂ Plane

An effective model describing the essential physics of the CuO_2 plane is the three-band Hubbard model with Hamiltonian [18],

$$
\hat{H} = -t_{dp} \sum_{\langle i,j \rangle \sigma} \left(\hat{d}_{i\sigma}^{\dagger} \hat{p}_{j\sigma} + h.c \right) - t_p \sum_{\langle j,j' \rangle \sigma} \left(\hat{p}_{j\sigma}^{\dagger} \hat{p}_{j'\sigma} + h.c \right) + t_p' \sum_{\langle j,j'' \rangle \sigma} \left(\hat{p}_{j\sigma}^{\dagger} \hat{p}_{j''\sigma} + h.c \right)
$$
$$
+ \Delta \sum_{j\sigma} \hat{n}_{p,j\sigma} + U_d \sum_i \hat{n}_{d,i\uparrow}\hat{n}_{d,i\downarrow} + U_p \sum_i \hat{n}_{p,j\uparrow}\hat{n}_{p,j\downarrow} + V \sum_{\langle i,j \rangle} \hat{n}_{d,i}\hat{n}_{p,j} \,, \quad (1.20)
$$

where $\hat{d}_{i\sigma}$ annihilates a hole with spin σ on the Cu $3d_{x^2-y^2}$ orbital at site i, and $\hat{p}_{j\sigma}$ is that on the O 2p orbital at site j. The number operators are given by $\hat{n}_{d,i\sigma} = \hat{d}_{i\sigma}^{\dagger}\hat{d}_{i\sigma}$ and $\hat{n}_{p,j\sigma} = \hat{p}_{j\sigma}^{\dagger}\hat{p}_{j\sigma}$. The summation $\langle i, j \rangle$ represents that over nearest-neighbour Cu-O bonds while the sum over $\langle j, j' \rangle$ and $\langle j, j'' \rangle$ are for nearest and next-nearest-neighbour O-O bonds as shown in Fig. 1.3b. U_p is an onsite Coulomb repulsion for the oxygen 2p orbitals and V is an inter-site repulsion between electrons on nearest-neighbour Cu and O sites.

Typically however, the theoretical starting point for understanding of cuprate physics is that of the single band Hubbard or $t - J$ model. Zhang and Rice justified the potential applicability of these single-band models through the insight that a hole doped onto into the CuO_2 plane might delocalise over the 4 oxygens surrounding it and form a Kondo like singlet with the hole on the Cu site; known as a Zhang-Rice singlet [19]. This singlet state can then hop through the lattice as if it were a hole in a background of localised spins on Cu sites with an anti-ferromagnetic coupling. Thus a low-energy effective description of the three band Hubbard model is plausibly given by the $t - J$ Hamiltonian,

$$
\hat{H} = -t \sum_{\langle i,j \rangle \sigma} P_G \left(\hat{c}_{i\sigma}^{\dagger}\hat{c}_{j\sigma} + h.c \right) P_G + J \sum_{\langle i,j \rangle} \left(\hat{\vec{S}}_i \cdot \hat{\vec{S}}_i - \frac{1}{2}\hat{n}_i\hat{n}_j \right) \,, \quad (1.21)
$$

where $c_{i,\sigma}$ annhiliates a hole on site i with spin σ, $\hat{\vec{S}}_i$ is the spin operator and P_G is the Gutzwiller projection operator that projects out doubly occupancy of any site.

It is well known that this $t - J$ Hamiltonian can be obtained from the single band Hubbard Hamiltonian,

$$\hat{H} = -t \sum_{\langle i,j \rangle \sigma} \left(\hat{c}_{i\sigma}^{\dagger} \hat{c}_{j\sigma} + h.c \right) + U \sum_{i} \hat{n}_{i\uparrow} \hat{n}_{i\downarrow} \,, \tag{1.22}$$

by pertubatively intergrating out high energy degrees of freedom in the limit $U/t \gg 1$ [20], shrinking the relevant Hilbert space and leading to a more practically soluble model. Thus, the physics of the CuO_2 plane is often approached from one of these single-band models. However, as we will see in Chap. 4 this potentially misses some key aspects of cuprate phenomenology.

1.2.2 Phase Diagram

A schematic phase diagram of hole-doped cuprates is shown in Fig. 1.5. The most well-defined features of the phase diagram are an insulator that becomes anti-ferromagnetic for $T < T_N$ at small hole concentration, p, and a dome of high temperature superconductivity with highest transition temperature at p $\sim$ 17%. There is also a region of suppressed spectral weight at the Fermi energy known as the pseudogap regime and a region of anomalous normal state transport above the superconducting dome at optimal doping, often called the strange metal. These aspects of
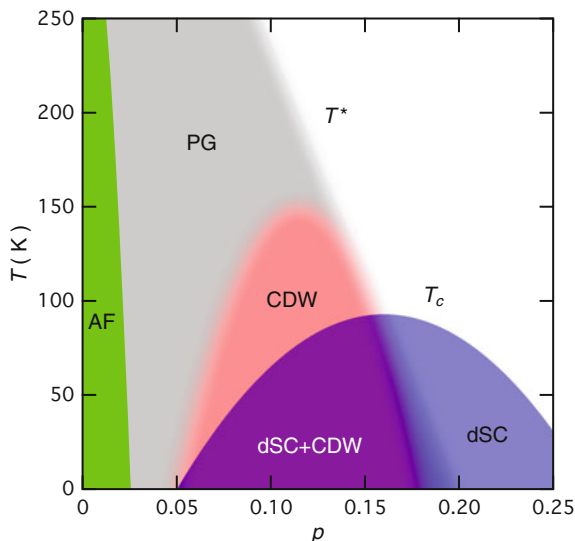
Fig. 1.5 Schematic hole-concentration - temperature phase diagram of cuprate superconductors. The *green* region labelled AF represents an anti-ferromagnetic insulating state. The *blue* region labelled dSC is a dome of high temperature *d*-wave superconductivity with critical temperature T_c. The *grey shaded region* denotes that pseudogap regime, with characteristic temperature T*, terminating at hole-doping, $p \sim 0.19$ holes per Cu. The *pink* area is a dome of charge density wave order

the phase diagram will be discussed further below. In Sect. 1.4 I will go on to discuss
the focus of this thesis: the density wave order which has recently been discovered
as ubiquitous in under-doped cuprates.

1.2.3   Anti-Ferromagnetism

The anti-ferromagnetism of the undoped cuprates arises from the Anderson super-
exchange mechanism, where virtual hopping of electrons between Cu $3d_{x^2-y^2}$
through the O 2p orbitals lowers the energy if the spins of the electrons localised
in $3d_{x^2-y^2}$ orbitals are anti-aligned [20]. This leads to Néel type anti-ferromagnetic
order with a critical temperature T_N. Doping of holes into the O 2p orbitals frustrates
this anti-ferromagnetic coupling and leads to a rapid suppression of T_N with hole
doping.

1.2.4   High-Temperature d-Wave Superconductivity

The superconductivity in cuprates in unconventional in several senses. The first and
most striking of these are superconducting critical temperatures as high as 165 K
[21]. To learn how such high transition temperatures arise and how we might extend
this towards room temperature is the aspiration behind research into cuprate super-
conductors.

Cuprate superconductivity is also unconventional in a more well defined sense:
its pairing symmetry. In the conventional superconductors discussed in Sect. 1.1.2
the pairing amplitude transforms like the trivial representation of the point group (s-
wave). In cuprates it is well established that the pairing amplitude is $d_{x^2-y^2}$ like [11]. It
changes sign under 90° rotations, leading to four line nodes in the gap function along
the (1,1) directions. In a tetragonal lattice, the pairing amplitude would transform
like the B_{1g} representation of the point group, breaking lattice rotation symmetry.

1.2.5   Strange Metal

Above the superconducting dome at optimal doping there is a region of strange
metallic behaviour characterised by T-linear resistivity persisting up to the highest
temperatures measured. Furthermore, the magnitude of the resistivity is such that
if one were to infer a mean free path for current carrying quasi-particles, it would
be less than their de-Broglie wavelength, seemingly invalidating the quasi-particle
picture.

This, and similar behaviour seen in other materials [22], thus far defies a coherent theoretical understanding and represents one of the greatest outstanding challenges in our understanding of the cuprates.

1.2.6 The Pseudogap

The hole doped cuprate phase diagram harbours a region which exhibits a pseudogap, i.e. a partial suppression of spectral weight at the Fermi energy for $T_c < T < T^*$. This region is indicated by the grey shaded region labelled PG in Fig. 1.5. The existence of such a suppression has been indicated by a large number of experimental techniques [23].

Angular Resolved Photoemission Spectroscopy (ARPES) has given particular insight into how the pseudogap forms in momentum space [24, 25]. For $T_c < T < T^*$ there are coherent quasi-particle peaks in a narrow region of momenta near the zone-diagonals (nodal regions). In contrast, the anti-nodal region of the Brillouin zone exhibits a suppression of low energy spectral weight over the pseudogap energy scale and an absence of any quasi-particle peaks. This is illustrated in Fig. 1.6. With increasing doping the coherent region grows and eventually forms a full Fermi surface of coherent quasi-particles.

STM of underdoped cuprates also exhibits a pseudogap in tunnelling spectroscopy measurements [26–28]. This is characterised by a suppression of tunnelling conductance near the chemical potential over a range of bias voltages Δ_0/e, the magnitude

Fig. 1.6 The form of the superconducting gap (Δ_{SC}) and pseudogap in momentum space. The $d_{x^2-y^2}$ like superconducting gap (*blue*) has nodes along the $(k_x, k_y) = (1, 1)$ directions whereas in the pseudogap regime ($T_c < T < T^8$) there are arcs of zero-energy excitations (shown in *red*). Reproduced from Ref. [23] with permission

$$\Delta_{SC}(k) = (\Delta_0/2) [\cos(k_x a) - \cos(k_y a)]$$
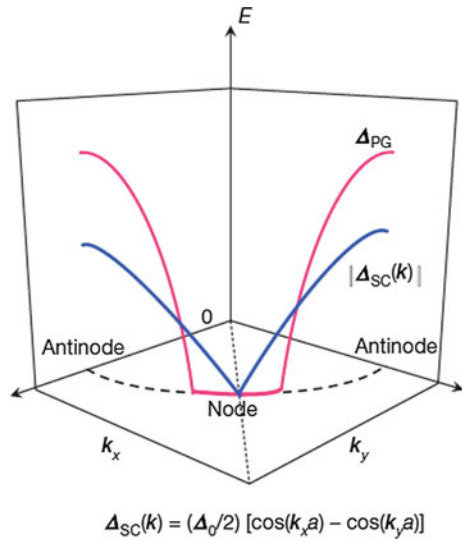
and doping dependence of Δ_0 being consistent with other measures of the pseudogap energy scale.

A lack of coherence in the anti-nodal regions of the Brillouin zone is also detected by STM quasi-particle interference measurements, albeit for $T < T_c$. In these measurements, modulations in the tunnelling conductance caused by scattering interference of Bogoliubov quasi-particles are not observed for states beyond the anti-ferromagnetic zone boundary in momentum space for $p < 0.19$. For $p > 0.19$, interference patters arising from Bogoliubov quasi-particles extending out to the full Brillouin zone boundary are observed [29, 30]. The precise relationship between this and the Fermi arcs observed by ARPES is not clear, because for $T < T_c$ ARPES indicates coherent quasi-particles in the anti-nodal region for all dopings within the superconducting dome [31].

Measurements indicating the existence of a plethora of broken symmetries in the pseudogap regime have been reported, including time-reversal, lattice-translational, point-group, spin-rotation and time-reversal symmetry-breaking [32–37]. Of central interest in this thesis are those that break lattice translational symmetry. I will now go on to discuss translational symmetry breaking as well as its discovery and phenomenology in cuprates.

1.3 Charge Density Waves

A charge density wave is a state of matter that breaks lattice translational symmetry whilst preserving time-reversal, spin rotation and phase symmetries. In such a state any density-like observable, i.e. one that is invariant under time-reversal, spin-rotation and phase-rotation operations, will be modulated with a periodicity different to that of the lattice. One such quantity is charge density, which gives its name to this state of matter [38].

For the square lattice of the CuO_2 plane we can expand the charge density wave in order parameters as follows:

$$\langle \hat{\psi}_\sigma^\dagger(\vec{r}_1)\hat{\psi}_\sigma(\vec{r}_2)\rangle =$$
$$F(\vec{r}_1 - \vec{r}_2)\left[\rho_{\vec{Q}_x}(\vec{R})e^{i\vec{Q}_x\cdot\vec{R}} + \rho_{-\vec{Q}_x}(\vec{R})e^{-i\vec{Q}_x\cdot\vec{R}} + \rho_{\vec{Q}_y}(\vec{R})e^{i\vec{Q}_y\cdot\vec{R}} + \rho_{-\vec{Q}_y}(\vec{R})e^{-i\vec{Q}_y\cdot\vec{R}}\right] + \dots,$$
$$(1.23)$$

where $\vec{R} = (\vec{r}_1 + \vec{r}_2)/2$ and $\rho_{\vec{Q}_x}$, $\rho_{-\vec{Q}_x}$, $\rho_{\vec{Q}_y}$ and $\rho_{-\vec{Q}_y}$ are charge density wave (CDW) order parameters. They are complex scalar fields that carry momenta $\vec{Q}_{\pm x}$ and $\vec{Q}_{\pm y}$ running along orthogonal directions $\vec{x}$ and $\vec{y}$. A constraint $\rho_{\vec{Q}_x} = \rho_{-\vec{Q}_x}^*$ ensures that the charge density is real. For $\vec{Q}_{x,y}$ that are incommensurate with the lattice, each order parameter spontaneously breaks a U(1) symmetry associated with the spatial phase of the density wave. If $\vec{Q}$ is commensurate with the lattice, the

Fig. 1.7 Bare particle-hole susceptibility, $\chi(q) = \chi_{ph}^0(|\vec{q}|, \omega = 0)$ for Fermi gas in d = 1, 2 and 3 at $T = 0$. The logarithmic divergence at q = $2k_F$ in d = 1 signifies a weak coupling instability to CDW order: the Peierls instability. In d > 1 the susceptibility is not divergent and there is no weak-coupling instability of the Fermi liquid to CDW
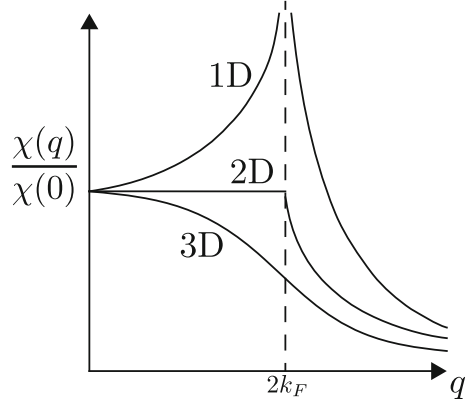
spontaneously broken symmetry becomes discrete. The function $F(\vec{r}_1 - \vec{r}_2)$ encodes the local rotational symmetry of the charge density wave or form factor.

In the above I discussed how superconductivity is a particle-particle instability or an instability to forming pairs. In the superconducting state there is a non-zero anomalous expectation $\langle \hat{c}_{\sigma,\vec{k}}^\dagger \hat{c}_{-\sigma,-\vec{k}}^\dagger \rangle$. The CDW however is a particle-hole instability with a non-zero value of $\langle \hat{c}_{\sigma,\vec{k}}^\dagger \hat{c}_{\sigma,\vec{k}+\vec{Q}} \rangle$. The best known example of such an instability is the Peierls transition [39].

Following the steps we took in Sect. 1.1.2, let us examine the RPA particle-hole susceptibility

$$\chi_{ph}(\vec{q}, \omega) = \frac{\chi_{ph}^0(\vec{q}, \omega)}{1 + g\chi_{ph}^0(\vec{q}, \omega)} \,, \tag{1.24}$$

where

$$\chi_{ph}^0(\vec{q}, \omega) = \frac{1}{\Omega} \sum_{\vec{k}} \frac{f(\epsilon_{\sigma,\vec{k}}) - f(-\epsilon_{\sigma,\vec{k}+\vec{Q}})}{\hbar\omega + \epsilon_{\sigma,\vec{k}} - \epsilon_{\sigma,\vec{k}+\vec{q}} + i0^+} \,. \tag{1.25}$$

The bare (non-interacting) susceptibility for $\chi_{ph}^0(\vec{q}, \omega)$ is shown in Fig. 1.7 for a free Fermi-gas is dimensions d = 1, 2 and 3 at $T = 0$. In d = 1 this function diverges at a wave-vector $\vec{q} = 2\vec{k}_F$ that connects points on opposite sides of the Fermi surface. This divergence arises because $\epsilon_{\sigma,\vec{k}} = \epsilon_{\sigma,\vec{k}+\vec{q}}$ over a finite domain in d = 1. From the denominator of Eq. 1.25 we can see that this will lead to a divergence in $\chi_{ph}^0(\vec{q}, \omega)$, signaling an instability towards CDW order. This property that $\epsilon_{\sigma,\vec{k}} = \epsilon_{\sigma,\vec{k}+\vec{Q}}$ over a finite domain is referred to as perfect nesting.

Peierls recognised that, due to this perfect nesting, a one-dimensional metal would always be unstable to distorting the lattice at wave-vector $\vec{Q} = 2\vec{k}_F$ [39]. The decrease in internal energy from opening a gap at the Fermi surface will always out-weigh

the increase due to the lattice distortion. This weak-coupling instability (it exists for arbitrarily small repulsive interactions) is known as the Peierls instability.

In d > 1 the story is quite different. The perfect nesting condition is not fulfilled except in finely tuned circumstances. Consequently there is no divergence of $\chi^0_{ph}(\vec{q}, \omega)$ (as show for the free Fermi gas in Fig. 1.7) and no weak-coupling instability to CDW order, except under finely tuned conditions. This is to be contrasted with the particle-particle susceptibility which always diverges because, in the presence of time-reversal symmetry, $\epsilon_{\sigma, \vec{k}} = \epsilon_{-\sigma, -\vec{k}}$. This can be viewed as another type of perfect nesting which persists to arbitrary dimension. Thus the BCS superconducting instability is, in general, the only weak-coupling instability of the Fermi liquid.

The cuprate superconductors are quasi two-dimensional. For realistic Fermi surfaces, any CDW order in these materials requires a critical effective interaction strength between quasi-particles. Consequently the ordering temperature will depend on the strength of the effective interactions and the wave-vector will be influenced by any momentum dependence of the interaction. Extending Eq. 1.24 to an interaction with momentum dependence, a rough criterion for forming density wave order at wave-vector $\vec{Q}$ is that $g(\vec{q})\chi^0_{ph}(\vec{q}, 0) = 1$. In considering a mechanism for the formation of CDW in cuprates, it is important to keep in mind the importance of both the the Fermi surface (if one exists) and the interaction between its quasi-particles.

1.4   Unconventional Density Waves in Cuprates

CDW order has now been detected in several hole-doped cuprate compounds and would thus appear to be ubiquitous in cuprates. This in turn suggests that it is an intrinsic and generic property of doping holes into the CuO_2 plane. However, its relationship to the high-temperature superconductivity and pseudogap remains unclear.

The first detection of CDW in cuprates was made in a family of cuprates based on the insulator La_2CuO_4. In $La_{2-x-y}Nd_ySr_xCuO_{4+\delta}$ and $La_{2-x}Ba_xCuO_{4+\delta}$, "stripe" order, where co-linear anti-ferromagnetic spin and charge modulations $\vec{Q}_s$ and $\vec{Q}_c$ exist with the relationship $\vec{Q}_c = 2\vec{Q}_s \approx (\frac{1}{4}, 0); (0, \frac{1}{4})$, was detected by neutron scattering [40]. The stripe order is strongest in the vicinity of hole-doping $p \approx 1/8$ where there is an anomalous suppression in the bulk superconducting T_c, known as the "1/8th anomaly" [41]. The resonant x-ray scattering study of Abbamonte et al. characterised this stripe order as the segregation of holes in the CuO_2 plane into regions of undoped antiferromagnetic insulator separated by domain walls of holes [42].

Short-ranged CDW order was first detected in $Bi_2Sr_2CaCu_2O_{8+\delta}$, $Bi_{2-y}Pb_ySr_{2-x}La_xCuO_{6+\delta}$ and $Na_xCa_{2-x}CuO_2Cl_2$ by scanning tunnelling microscopy [43–46]. Advances in resonant x-ray scattering then led to the detection of short-ranged CDW order in $YBa_2Cu_3O_{6+x}$, which was subsequently also detected by hard x-ray diffraction [47–49]. Resonant x-ray scattering also confirmed the presence of CDWs in the bulk of $Bi_2Sr_2CaCu_2O_{8+\delta}$ and $Bi_{2-y}Pb_ySr_{2-x}La_xCuO_{6+\delta}$ with the same wave-

vectors as those detected by STM studies, as well as detecting short-range CDW order in $HgBa_2CuO_{4+\delta}$ [50].

The first hint of CDW order in $YBa_2Cu_3O_{6+x}$ was given by the observation of quantum oscillations in $YBa_2Cu_3O_{6+x}$ whose frequencies correspond to small electron pockets [51]. Quantum oscillations, also implying the existence of small electron pockets, were subsequently detected in Hg-1012 [52]. A reconstruction of the Fermi surface by a CDW was proposed as an explanation of these observations [53].

Developments in high magnetic field x-ray diffraction techniques are providing exciting new information about the cuprate CDW [54–56]. Pulsed field measurements utilising a free electron laser have detected the onset of a CDW in $YBa_2Cu_3O_{6+x}$ in applied magnetic fields $\gtrsim 15\,T$, with a correlation volume of $\sim 10^5$ unit cells. This high-field CDW, which I will call CDW-II, appears distinct from the short-ranged charge order present at $B = 0$, in that it is coherent along the direction perpendicular to the CuO_2 planes with a periodicity of 1 unit cell. In contrast, the zero-field CDW shows very weak correlations along this direction, with a periodicity of ≈ 2 unit cells.

These high-field x-ray diffraction measurements also find that CDW-II is uni-directional, with modulations along only one of the Cu-O directions [55, 56]. This is in agreement with earlier high magnetic field NMR measurements showing a splitting of ^{63}Cu lines for $B > 28.5T$, consistent with a uni-directional modulation of charge density along a Cu-O direction [57].

Details of the experimental evidence for CDW order in cuprates is given in the appropriate chapters throughout this thesis. A recent review can also be found in Ref. [58].

1.5 The Significance of CDW in Cuprates

Although they differ slightly in detail, the CDWs observed in the cuprates have several generic features. The wave-vector(s) are axial, meaning that they are along the Cu-O directions $\vec{Q}_x = (Q, 0)$ and $\vec{Q}_y = (0, Q)$. At zero magnetic field the CDW order is short-ranged with correlation length no longer than 2 wavelengths, except in the case of $La_{2-x}Ba_2CuO_{4+\delta}$ [58].

The CDW onset temperature forms a dome centered on $p = 0.12$ as shown in Fig. 1.5. At this doping there is an anomaly in $T_c(p)$ so that it either forms a local minimum or a point of inflection, with T_c in some materials being suppressed to very low temperatures [59]. In others the effect is weaker at zero field, but the application of a magnetic field suppresses T_c to zero at this doping, splitting the superconducting dome in two [60]. This already suggests an intimate relationship between the CDW and superconductivity.

In 2002 Hoffman et al., using SI-STM, discovered halos of periodic conductance modulations surrounding superconducting vortex cores in $Bi_2Sr_2CaCu_2O_{8+\delta}$ [45]. These modulations, shown in Fig. 1.8a, are indicative of CDW order enhanced by the suppression of superconductivity.
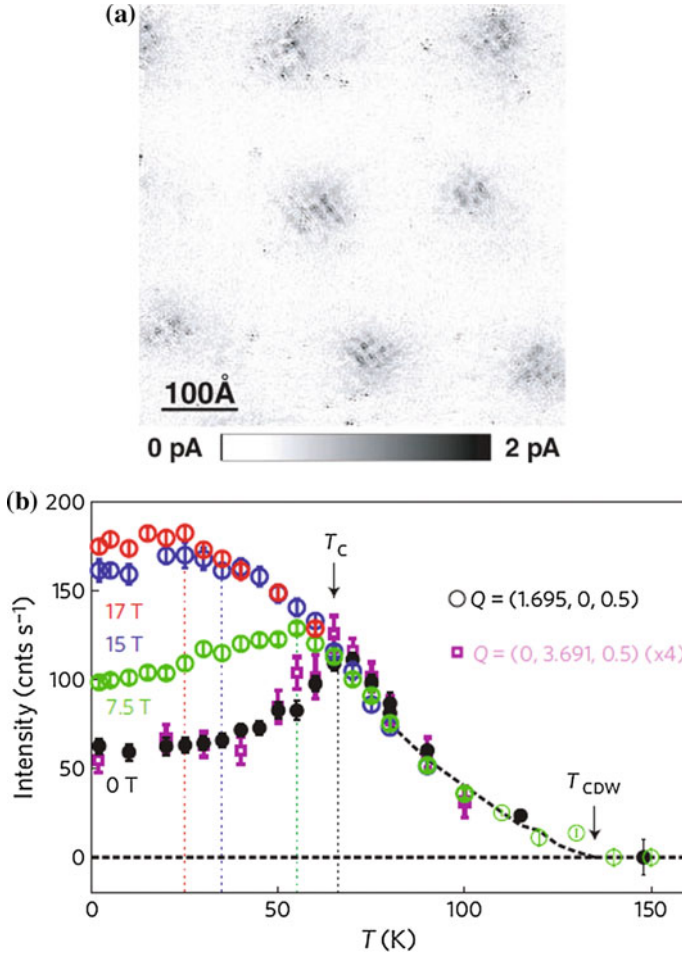
Fig. 1.8 a Approximately $4a_0$ periodic tunnelling conductance modulations surrounding super-conducting vortex cores in $Bi_2Sr_2CaCu_2O_{8+\delta}$, measured using SI-STM. These suggest halos of enhanced CDW order forming due to the suppression of superconductivity. Reproduced from Ref. [45] with permission. **b** Temperature and magnetic field dependence of x-ray diffraction intensity at CDW wave-vectors in $YBa_2Cu_3O_{6+x}$. With decreasing temperature, the scattering intensity onsets gradually at a temperature $T_{CDW} > T_c$ and rises to a maximum at T_c for B = 0T and then decreases again. As a magnetic field is applied this decrease in scattering intensity is lessened and for the B = 15 and 17 T data continues to rise through T_c and saturate. Reproduced from Ref. [49] with permission

Further evidence of a strong relationship between superconductivity and CDW order is seen by x-ray scattering studies in a magnetic field. Figure 1.8b shows data from Chang et al. on $YBa_2Cu_3O_{6+x}$ [49]. At zero magnetic field the scattering intensity at the CDW wave-vector increases gradually with decreasing temperature, reach-

ing a maximum at T_c and then decreasing again. The application of a magnetic field has no effect on the scattering intensity above T_c but the intensity rapidly increases with magnetic field below T_c. This is suggestive of a strong competition between CDW formation and superconductivity.

The most basic but fundamental question that needs to be addressed is what set of symmetries does the cuprate CDW break? To answer this question is to establish what phase of matter it is. It is clear that translational symmetry is broken but what of the point group symmetry? This would be broken in a stripe-like state with CDW along $\bar{Q}_x$ or $\bar{Q}_y$ but not both.

It is possible that experimental observations of CDW result from a state which breaks both translational and phase symmetry. This would be a superconductor that breaks translational symmetry, akin to that first proposed by Fulde, Ferrel, Larkin and Ovchinnikov but in the absence of an applied magnetic field [61–63]. Certain forms of this "pair density wave" (PDW) order would also result in a CDW. This is because the density of Cooper-pairs, which are charged, is modulated. A PDW would offer a natural explanation of why the superconductivity and CDW are so strongly coupled to each other in cuprates.

The PDW is a state of matter which has never been directly detected. Establishing its existence in cuprate superconductors would be profound, not just within condensed matter physics but also in high-energy physics and astronomy where PDW states have been predicted to exist in dense quark matter [64].

There is still great interest and uncertainty in the nature of the cuprate pseudogap. It is natural to question the relationship between the charge order and the pseudogap. For instance, is the pseudogap caused by the CDW; either as a static or fluctuating entity? If not, then by what mechanism does the CDW form out of the pseudogap liquid? Key insights into this can be gained from examining the spectral function in the CDW and pseudogap regimes of the cuprate phase diagram.

Ultimately, given such a strong coupling between CDW and superconductivity, it is important to establish the relationship between them. Is CDW order a necessary ingredient or consequence of a minimal model that describes high temperature superconductivity in cuprates? The goal of the research described in this thesis was to investigate issues such as this.

1.6 Organisation of This Thesis

Chapter 2 describes spectroscopic imaging STM (SI-STM), the experimental technique used throughout the research reported in this thesis. It also details the materials studied. Chapter 3 details the extension of SI-STM to image states of matter with non-trivial structure within the unit cell of a material.

In Chap. 4 I describe utilising the techniques detailed in Chaps. 2 and 3 to characterise the CDW in $Bi_2Sr_2CaCu_2O_{8+\delta}$ and $Na_xCa_{2-x}CuO_2Cl_2$. I will show that the CDW in these materials modulates a broken rotational symmetry within each unit cell. I will also present evidence that the CDW in cuprates has a tendency to

break rotational symmetry globally as well as locally. The effects of the CDW on the electronic structure will also be discussed.

In Chap. 5 I will outline the theoretical basis and development of nanometer resolution scanned Josephson tunnelling microscopy (SJTM) in cuprates. In Chap. 6 I will describe inhomogeneous superconducting states of matter known as "pair density waves", as well as evidence and theoretical proposals for their existence in cuprates. In Chap. 7 I will detail the use of SJTM to detect periodically modulated superconductivity in $Bi_2Sr_2CaCu_2O_{8+\delta}$, the first direct detection of such a state in any superconductor. Combining this with knowledge of the CDW from Chap. 4 and other reported measurements, I will discuss the consequences of this for the cuprate phase diagram.

In Chap. 8 I will summarise the main results and conclusions of this thesis. I will also propose future experiments that may address any remaining open questions and discuss future directions for SJTM.

References

1. J. Bednorz, K. Muller, Possible high Tc superconductivity in the Ba - La - Cu - O system. Zeitschrift für Phys. B Condens. Matter **64**, 189–193 (1986)
2. J.G. Bednorz, K.A. Müller, Perovskite-type oxides - the new approach to high-tc superconductivity. Nobel Lect. Phys. **1981–1990**, 424–457 (1993)
3. A.P. Drozdov et al., Conventional superconductivity at 203 kelvin at high pressures in the sulfur hydride system. Nature **525**(7567), 73–76 (2015)
4. P.W. Anderson, *Basic Notions in Condensed Matter Physics* (The Benjamin/Cummings Publishing Company, Menlo Park, 1984)
5. L.D. Landau, *Collected Papers of L.D. Landau* (Gordon and Breach, New York, 1965)
6. W. Meissner, R. Ochsenfeld, Ein neuer Effekt bei Eintritt der Supraleitfhigkeit. Die Naturwissenschaften **21**(44), 787–788 (1933)
7. D.V. Delft, P. Kes, The discovery of superconductivity. Phys. Today **63**(9), 38–42 (2010)
8. J. Bardeen, L.N. Cooper, J.R. Schrieffer, Theory of superconductivity. Phys. Rev. **108**(5), 1175–1204 (1957)
9. T. Giamarchi, *Quantum Physics in One Dimension*, vol. 6. 38 (Oxford University Press, Oxford, 2003), pp. 1–28
10. N.N. Bogoliubov, On a new method in the theory of superconductivity. Il Nuovo Cimento **7**(6), 794–805 (1958)
11. C. Tsuei, J. Kirtley, Pairing symmetry in cuprate superconductors. Rev. Mod. Phys. **72**(4), 969–1016 (2000)
12. M. Tinkham, Tunneling generation, relaxation, and tunneling detection of holeelectron imbalance in superconductors. Phys. Rev. B **6**(5), 1747–1756 (1972)
13. M. Ogata, H. Fukuyama, The t - J model for the oxide high-Tc superconductors. Rep. Prog. Phys. **71**(3), 36501 (2008)
14. J. Zaanen, G.A. Sawatzky, J.W. Allen, Band gaps and electronic structure of transition-metal compounds. Phys. Rev. Lett. **55**(4), 418–421 (1985)
15. A. Fujimori et al., Spectroscopic evidence for strongly correlated electronic states in La-Sr-Cu and Y-Ba-Cu oxides. Phys. Rev. B **35**(16), 8814–8817 (1987)
16. T. Takahashi et al., Synchrotron-radiation photoemission study of the high-Tc Superconductor $YBa_2Cu_3O_7 - \delta$. Phys. Rev. B **36**(10), 5686–5689 (1987)
17. A. Bianconi et al., Localization of Cu 3d levels in the high Tc superconductor YBa2Cu3O7by Cu 2p X-ray photoelectron spectroscopy. Solid State Commun. **63**(12), 1135–1139 (1987)

18. V.J. Emery, Theory of high-Tc superconductivity in oxides. Phys. Rev. Lett. **58**(26), 2794–2797 (1987)
19. F.C. Zhang, T.M. Rice, Effective hamiltonian for the superconducting Cu oxides. Phys. Rev. B **37**(7), 3759–3761 (1988)
20. P. Fazekas, *Lecture Notes on Electron Correlation and Magnetism* (World Scientific, Singapore, 1999)
21. L. Gao et al., Superconductivity up to 164 K in $HgBa_2Cam - 1Cu_mO2m + 2 + \delta$ (m = 1, 2, and 3) under quasihydrostatic pressures. Phys. Rev. B **50**(6), 4260–4263 (1994)
22. J.N. Bruin et al., Similarity of scattering rates in metals showing t-linear resistivity. Science **339**(6121), 804–807 (2013)
23. B. Keimer et al., From quantum matter to high-temperature superconductivity in copper oxides. Nature **518**(7538), 179–86 (2015)
24. A. Damascelli, Z. Hussain, Z.-X. Shen, Angle-resolved photoemission studies of the cuprate superconductors. Rev. Mod. Phys. **75**(2), 473–541 (2003)
25. A.A. Kordyuk, Pseudogap from ARPES experiment: three gaps in cuprates and topological superconductivity. Low Temp. Phys. **41**(5), 319–341 (2015)
26. Fischer et al., Scanning tunneling spectroscopy of high-temperature superconductors. Rev. Mod. Phys. **79**(1), 353–419 (2007)
27. K. Fujita et al., Spectroscopic Imaging scanning tunneling microscopy studies of electronic structure in the superconducting and pseudogap phases of cuprate high-tc superconductors. J. Phys. Soc. Jpn. **81**(1), 011005 (2012)
28. A. Yazdani, E.H. da Silva Neto, P. Aynajian., Spectroscopic imaging of strongly correlated electronic states. Annu. Rev. Condens. Matter Phys. **7**(1), 11–33 (2016)
29. K. Fujita et al., Simultaneous transitions in cuprate momentum-space topology and electronic symmetry breaking. Science **344**(6184), 612–616 (2014)
30. Y. He et al., Fermi surface and pseudogap evolution in a cuprate superconductor. Science **344**(6184), 608–11 (2014)
31. I.M. Vishik et al., A momentum-dependent perspective on quasiparticle interference in $Bi_2Sr_2CaCu_2O_8 + \delta$. Nat. Phys. **5**(10), 718–721 (2009)
32. M.J. Lawler et al., Intra-unit-cell electronic nematicity of the high-Tc copperoxide pseudogap states. Nature **466**(7304), 347–51 (2010)
33. Y. Li et al., Hidden magnetic excitation in the pseudogap phase of a high-Tc superconductor. Nature **468**(7321), 283–285 (2010)
34. P. Hosur et al., Kerr effect as evidence of gyrotropic order in the cuprates. Phys. Rev. B **87**(11), 1–8 (2013)
35. J. Xia et al., Polar kerr-effect measurements of the high-temperature YBa2Cu3O6+x superconductor: evidence for broken symmetry near the pseudogap temperature. Phys. Rev. Lett. **100**(12), 3–6 (2008)
36. H. Karapetyan et al., Magneto-optical measurements of a cascade of transitions in superconducting La1:875Ba0:125CuO4 single crystals. Phys. Rev. Lett. **109**(14), 1–5 (2012)
37. P. Hosur et al., Erratum: Kerr effect as evidence of gyrotropic order in the cuprates. Phys. Rev. B **87**, 115116 (2013): Phys. Rev. B **91.3**, 039908 (2015)
38. G. Gruner, *Density Waves in Solids* (Perseus, Cambridge, 1994)
39. R. Peierls, *Quantum Theory of Solids* (Oxford University Press, Oxford, 1955)
40. J.M. Tranquada et al., Evidence for stripe correlations of spins and holes in copper oxide superconductors. Nature **375**(6532), 561–563 (1995)
41. A.R. Moodenbaugh et al., Superconducting properties of La2.xBaxCuO4. Phys. Rev. B **38**(7), 4596–4600 (1988)
42. P. Abbamonte et al., Spatially modulated 'Mottness' in La2.xBaxCuO4. Nat. Phys. **1**(3), 155–158 (2005)
43. C. Howald et al., Periodic density-of-states modulations in superconducting $Bi_2Sr_2CaCu_2O_8 + \delta$. Phys. Rev. B **67**(1), 014533 (2003)
44. W.D. Wise et al., Charge density wave origin of cuprate checkerboard visualized by scanning tunneling microscopy. Nat. Phys. **4**, 696 (2008)

45. J.E. Hoffman et al., A four unit cell periodic pattern of quasi-particle states surrounding vortex cores in $Bi_2Sr_2CaCu_2O_8 + \delta$. Science **295**(5554), 466–469 (2002)
46. T. Hanaguri et al., A 'checkerboard' electronic crystal state in lightly hole-doped Ca2-xNaxCuO2Cl2. Nature **430**, 1001–1005 (2004)
47. G. Ghiringhelli et al., Long-range incommensurate charge fluctuations in (Y, Nd)Ba2Cu3O6+x. Science **337**(6096), 821–825 (2012)
48. E. Blackburn et al., X-Ray diffraction observations of a charge-density-wave order in superconducting ortho-II YBa2Cu3O6:54. Phys. Rev. Lett. **110**(13), 137004 (2013)
49. J. Chang et al., Direct observation of competition between superconductivity and charge density wave order in YBa2Cu3O6:67. Nat. Phys. **8**(12), 871–876 (2012)
50. W. Tabis et al., Charge order and its connection with Fermi-liquid charge transport in a pristine high-Tc cuprate. Nat. Commun. **5**, 5875 (2014)
51. N. Doiron-Leyraud et al., Quantum oscillations and the Fermi surface in an underdoped high-Tc superconductor. Nature **447**(7144), p. 565 (2007)
52. N. Barišić et al., Universal quantum oscillations in the underdoped cuprate superconductors. Nat. Phys. **9**(12), 761–764 (2013)
53. S.E. Sebastian, N. Harrison, G.G. Lonzarich, Towards resolution of the Fermi surface in underdoped high-tc superconductors. Rep. Prog. Phys. **75**(10), 102501 (2012)
54. S. Gerber et al., Three-dimensional charge density wave order in $YBa_2Cu_3O_6$.67 at high magnetic fields. Science **350**(6263), 949–952 (2015)
55. J. Chang et al., Magnetic field controlled charge density wave coupling in underdoped YBa2Cu3O6+x. Nat. Commun. **7**, 11494 (2016)
56. H. Jang et al., Ideal charge density wave order in the high-field state of superconducting YBCO (2016). arXiv:1607.05359
57. T. Wu et al., Magnetic-field-induced charge-stripe order in the high-temperature superconductor YBa2Cu3Oy. Nature **477**(7363), 191–4 (2011)
58. R. Comin, A. Damascelli, Resonant x-ray scattering studies of charge order in cuprates 1–26 (2015)
59. M. Vojta, Lattice symmetry breaking in cuprate superconductors: stripes, nematics, and superconductivity. Adv. Phys. **58**(6), 699–820 (2009)
60. B.J. Ramshaw et al., Quasiparticle mass enhancement approaching optimal doping in a high-tc superconductor. Science 1–9 (2015)
61. A.I. Larkin, Y.N. Ovchinnikov, Inhomogeneous state of superconductors. Sov. Phys. JETP **20**, 762–769 (1964)
62. P. Fulde, R.A. Ferrell, Superconductivity in a strong spin-exchange field. Phys. Rev. **135**(3A), A550–A563 (1964)
63. E. Berg, E. Fradkin, S.A. Kivelson, Theory of the striped superconductor. Phys. Rev. B **79**(6), 1–15 (2009)
64. R. Anglani et al., Crystalline color superconductors. Rev. Mod. Phys. **86**(2), 509–561 (2014)

Chapter 2
Spectroscopic-Imaging STM (SI-STM)

In this chapter I detail the main experimental technique used in this thesis: Spectroscopic-Imaging Scanning Tunnelling Microscopy (SI-STM). I outline the theoretical basis for its use as a tunnelling spectroscopy of superconductors as well as data analysis techniques specific to cuprate superconductors. I also give details of the cuprate samples studied.

Scanning tunnelling microscopy (STM) is a technique which uses the tunnelling current of electrons between a sharp metal tip and a sample to image its surface [1]. An exponential dependence of the tunnelling current on the distance between tip and sample makes the STM very sensitive to small changes in surface topography, allowing atomic resolution imaging. STM can also act as a spectroscopic tool by using the tunnel junction between tip and sample to carry out tunnelling conductance spectroscopy, revealing information about the electronic states contributing to the tunnelling current. The advantage of performing spectroscopy with an STM is that it can be done with atomic resolution. The theoretical basis for the topographic and spectroscopic capabilities of STM are outlined in this chapter.

STM came to take a prominent role in the study of quantum matter with the advent of spectroscopic imaging STM (SI-STM) [2, 3]. In SI-STM the topographic and spectroscopic abilities of the STM are systematically combined. The sample's surface topography and spectroscopic information are obtained simultaneously across a two-dimensional grid of points, or pixels. In doing so, one is essentially visualising the energy-resolved density of states of electrons in the material. In this chapter I will detail the techniques needed to obtain both real and momentum space information about the wave-functions in cuprate superconductors.

The rapid and fairly specialised development of the field means that for completeness I must touch on a fairly large number of sub-topics, some of which are fairly technical; one way to use this chapter might be to back-reference to it from the main results chapters of the thesis rather than try to take in every detail on first reading.

2.1 Quantum Tunnelling as a Spectroscopy

The experiments presented in this thesis rely on measuring the tunnelling current of electrons between a sample and a metal electrode across an insulating barrier [4, 5]. The tunnelling process consists of transferring an electron from a many-body state that is localised in the left electrode to another many-body state localised in the right electrode. Of course, by symmetry we expect the reverse process to have an equal rate, resulting in zero net current. However, under external application of a bias such as a current or voltage this symmetry is broken resulting in a net a current.

The variation of the current with the applied bias can yield information about the many-body states involved. Calculating the rates of these tunnelling processes from first principles is not generally possible. In the following section I will describe the tunnelling Hamiltonian formalism that can be used to extract spectroscopic information from the tunnelling current, without exactly solving the tunnelling problem [6, 7].

2.1.1 Tunnelling Hamiltonian Formalism

Within the tunnelling Hamiltonian formalism, the total Hamiltonian is given by

$$\hat{H} = \hat{H}_L + \hat{H}_R + \hat{H}_T \,, \tag{2.1}$$

where $\hat{H}_L$ and $\hat{H}_R$ describe the many-body states in the left and right electrodes separately, in the absence of each other [7]. $\hat{H}_T$ contains all additional terms that arise from coupling the electrodes to each other through the tunnel junction.

An exact treatment of this problem for two interacting many-body states in the right and left electrodes is not generally analytically tractable. Instead, we can treat $\hat{H}_T$ perturbatively. Typically we use a tunnelling Hamiltonian of the form,

$$\hat{H}_T = \sum_{i,j} \left(M_{i,j} \hat{c}_{L,i}^\dagger \hat{c}_{R,j} + M_{j,i}^* \hat{c}_{R,j}^\dagger \hat{c}_{L,i} \right) \,, \tag{2.2}$$

where $\hat{c}_{L,i}^\dagger$ creates an electron in state i on the left electrode and $\hat{c}_{R,j}^\dagger$ creates an electron in state j on the right electrode [7]. I will now examine the consequences of this Hamiltonian for various choices of the Hamiltonians $\hat{H}_L$ and $\hat{H}_R$ corresponding to Normal-Insulator-Normal (NIN), Superconductor-Insulator-Normal (SIN) and Superconductor-Insulator-Superconductor (SIS) tunnel junctions.

2.1.2 Normal-Insulator-Normal (NIN) Tunnelling

In the case of two normal metal electrodes the Hamiltonians are given by

$$\hat{H}_L = \sum_{\vec{k}} \epsilon_{\vec{k}} \hat{c}^{\dagger}_{L,\vec{k}} \hat{c}_{L,\vec{k}} \tag{2.3}$$

$$\hat{H}_R = \sum_{\vec{q}} \epsilon_{\vec{q}} \hat{c}^{\dagger}_{R,\vec{q}} \hat{c}_{R,\vec{q}} \tag{2.4}$$

$$\hat{H}_T = \sum_{\vec{k},\vec{q}} \left(M_{\vec{k},\vec{q}} \hat{c}^{\dagger}_{L,\vec{k}} \hat{c}_{R,\vec{q}} + M^*_{\vec{q},\vec{k}} \hat{c}^{\dagger}_{R,\vec{q}} \hat{c}_{L,\vec{k}} \right) \tag{2.5}$$

where $\hat{c}^{\dagger}_{L,\vec{k}}$ creates an electron of crystal momentum $\vec{k}$ in the left electrode with energy ϵ_k measured relative to the Fermi energy. Here, spin indices have been suppressed under the assumption that no spin-flip processes take place in tunnelling.

We can then perturbatively calculate the current of electrons from the left to the right electrode using Fermi's golden rule as

$$I_{L \to R} = \frac{2\pi e}{\hbar} \sum_{\vec{k},\vec{q}} |M_{\vec{k},\vec{q}}|^2 f_{\vec{k}} [1 - f_{\vec{q}}] \delta(\epsilon_{\vec{k}} - \epsilon_{\vec{q}}) , \tag{2.6}$$

where $f_{\vec{k}}$ is the occupation number of the state $\vec{k}$. Similarly, the reverse current is given by

$$I_{R \to L} = \frac{2\pi e}{\hbar} \sum_{\vec{k},\vec{q}} |M_{\vec{k},\vec{q}}|^2 f_{\vec{q}} [1 - f_{\vec{k}}] \delta(\epsilon_{\vec{q}} - \epsilon_{\vec{k}}) , \tag{2.7}$$

with the net current from left to right given by $I = I_{L \to R} - I_{R \to L}$.

Under the simplifying assumption that $T = 0$ and the matrix elements, $|M_{\vec{k},\vec{q}}| = |M|$, are a constant for states within eV of the chemical potential then this reduces to the form

$$I = \frac{2\pi e}{\hbar} |M|^2 \int_0^{eV} n_L(\epsilon + eV) n_R(\epsilon) d\epsilon , \tag{2.8}$$

where $n(\epsilon)$ is the momentum integrated density of states at energy ϵ [7].

Under a further assumption that we choose a right hand electrode with a constant density of states $n_R(E) = n_R(0)$, then Eq. 2.8 becomes

$$I = \frac{2\pi e}{\hbar} |M|^2 n_R(0) \int_0^{eV} n_L(\epsilon + eV) d\epsilon \tag{2.9}$$
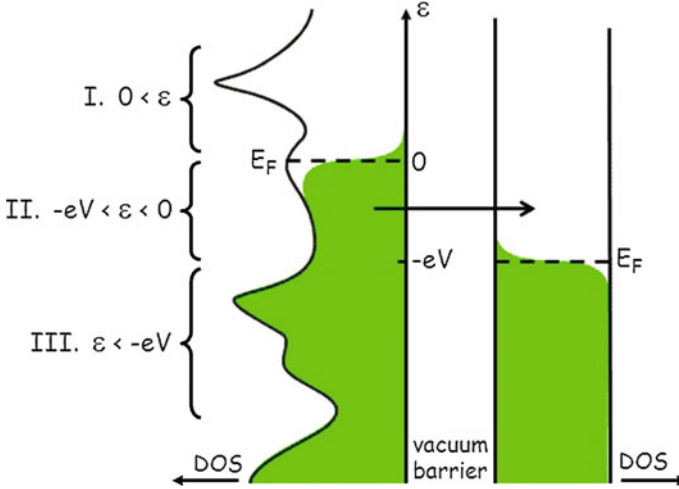
Fig. 2.1 Schematic of tunnelling from *left hand* electrode with negative bias applied, to *right hand* electrode. *Green shading* indicates filled states. Only energy ranges where left-hand states are filled and right-hand states are empty (i.e. region II) contribute to the net tunnelling current. The *right hand* density of states (DOS) is drawn flat as is required if useful spectroscopic information is to be obtained without deconvolution. Figure adapted from Ref. [8]

and $n_L(E)$ can be measured directly through the differential tunnelling conductance

$$\frac{dI}{dV} = \frac{2\pi e^2}{\hbar} |M|^2 n_R(0) n_L(eV) . \tag{2.10}$$

The physical tunnelling processes resulting in these equations are depicted in Fig. 2.1. Tunnelling may only occur from filled states to empty states. Hence by applying a positive bias we are probing the empty states of the left electrode (or sample) and with a negative bias its filled states.

The assumption of an energy independent matrix element, $|M_{\vec{k},\vec{q}}| = |M|$, is not in any sense innocuous. For metals described by the independent-particle pictures used in Eqs. 2.3 and 2.4, Harrison calculated the matrix elements $M_{\vec{k},\vec{q}}$ within the WKB approximation [9]. The conclusion was that the energy dependence of the matrix elements exactly cancels that of the density of states. This results in featureless, ohmic tunnelling $I(V)$ curves.

On the face of it, this would indicate the we cannot use tunnelling as a spectroscopy on metals. However, if the sample we wish to measure is not a single-band metal, well described by a Fermi liquid, then the cancellation between the density of states and the matrix element does not hold and spectroscopy becomes possible [6, 7, 9]. Specifically, Eqs. 2.9 and 2.10 which we derived for metals of independent electrons, are actually also valid for tunnelling between a superconductor and a normal metal electrode. In the next section I will outline why this is the case.

2.1.3 Superconductor-Insulator-Normal (SIN) Tunnelling

Now I will discuss tunnelling between a normal metal and a superconductor. This is the configuration of electrodes used in the STM studies of cuprate superconductors in Chap. 4, where a tungsten tip is used to perform spectroscopy on cuprate superconductor samples. In this case the normal and superconducting electrode Hamiltonians, $\hat{H}_N$ and $\hat{H}_S$, are given by

$$\hat{H}_N = \sum_{\vec{q}} \epsilon_{\vec{q}} \hat{c}^\dagger_{L,\vec{q}} \hat{c}_{L,\vec{q}} \tag{2.11}$$

$$\hat{H}_S = \sum_{\vec{k}} E_{\vec{k}} (\hat{\alpha}^\dagger_{\vec{k}} \hat{\alpha}_{\vec{k}} + \hat{\beta}_{\vec{k}} \hat{\beta}^\dagger_{\vec{k}}) \tag{2.12}$$

where

$$\alpha_{\vec{k}} = u_{\vec{k}} \hat{c}_{R,\vec{k},\uparrow} - v_{\vec{k}} \hat{c}^\dagger_{R,-\vec{k},\downarrow} \tag{2.13}$$

$$\beta_{\vec{k}} = u_{\vec{k}} \hat{c}_{R,-\vec{k},\downarrow} + v_{\vec{k}} \hat{c}^\dagger_{R,\vec{k},\uparrow} \tag{2.14}$$

and $u_{\vec{k}}$ and $v_{\vec{k}}$ are the BCS coherence factors [7, 10].

As presented in Chap. 1, the ground state of condensed pairs in the superconducting electrode is described by the BCS wave-function [10]. Its Bogoliubov quasiparticle excitations are a superposition of holes and electrons and are annihilated by the α_q and β_q operators. Their energy spectrum is given by

$$E_{\vec{k}} = \sqrt{\epsilon_{\vec{k}}^2 + |\Delta|^2} \tag{2.15}$$

where $\epsilon_{\vec{k}}$ are the single-particle energies of the normal state band from which the superconducting instability arises and Δ is the superconducting gap.

In order to consider the current between the electrodes arising from the tunnelling Hamiltonian it is convenient to define new operators which definitely create either an electron or hole in the superconductor, rather than a superposition of the two [11, 12]. These four operators are

$$\hat{\alpha}^\dagger_{e,\vec{k}} = u^*_{\vec{k}} \hat{c}^\dagger_{\vec{k}\uparrow} - v^*_{\vec{k}} \hat{S}^\dagger \hat{c}_{-\vec{k}\downarrow} \tag{2.16}$$

$$\hat{\alpha}^\dagger_{h,\vec{k}} = u^*_{\vec{k}} \hat{S} \hat{c}^\dagger_{\vec{k}\uparrow} - v^*_{\vec{k}} \hat{c}_{-\vec{k}\downarrow} \tag{2.17}$$

$$\hat{\beta}^\dagger_{e,\vec{k}} = u^*_{\vec{k}} \hat{c}^\dagger_{-\vec{k}\downarrow} + v^*_{v} \hat{S}^\dagger \hat{c}_{\vec{k}\uparrow} \tag{2.18}$$

$$\hat{\beta}^\dagger_{h,\vec{k}} = u^*_{\vec{k}} \hat{S} \hat{c}^\dagger_{-\vec{k}\downarrow} + v^*_{\vec{k}} \hat{c}_{\vec{k}\uparrow} \tag{2.19}$$

where $\hat{\alpha}^{\dagger}_{e,\vec{k}}$ creates an electron with wave-vector $\vec{k}$ and $\hat{S}^{\dagger}$ adds a Cooper-pair to the condensate. We can invert these definitions to express the electron creation operator in terms of the new operators, yielding

$$\hat{c}^{\dagger}_{k\uparrow} = u_{\vec{k}}\hat{\alpha}^{\dagger}_{e,\vec{k}} + v^{*}_{\vec{k}}\hat{\beta}_{h,\vec{k}} . \tag{2.20}$$

Now consider a term in the tunnelling Hamiltonian $M_{\vec{k},\vec{q}}\hat{c}^{\dagger}_{L,q}\hat{c}_{R,k}$. Using Eq. 2.20 this will contribute a term in the current proportional to $|u_{\vec{k}}|^2|M_{\vec{k},\vec{q}}|^2$ because the second term in Eq. 2.20 annihilates the BCS ground state. The physical interpretation of the coefficient $|u_{\vec{k}}|^2$ is that it is the probability that a state $\vec{k}$ is not occupied in the BCS wave-function and hence is able to accept an incoming electron.

   The coherence factors $u_{\vec{k}}$ and $v_{\vec{k}}$, which encode details of the superconducting wave-function, actually drop out of the full expression for the tunnelling current to leave a remarkably simple result. There is another state $\vec{k}'$ with $E_{\vec{k}'} = E_{\vec{k}}$ but with $\epsilon_{\vec{k}'} = -\epsilon_{\vec{k}}$. This will contribute to the current a term $|u_{\vec{k}'}|^2|M_{\vec{k}',\vec{q}}|^2 = |v_{\vec{k}}|^2|M_{\vec{k}',\vec{q}}|^2$ because $|u(-\epsilon)| = |v(\epsilon)|$. If $|M_{\vec{k}',\vec{q}}| \approx |M_{\vec{k},\vec{q}}|$, since $\vec{k}$ and $\vec{k}'$ are near the same point on the Fermi surface then the total contribution from these two terms will be proportional to $(|u_{\vec{k}}|^2 + |v_{\vec{k}}|^2)|M_{\vec{k}\vec{q}}|^2 = |M_{\vec{k},\vec{q}}|^2$ because $|u_{\vec{k}}|^2 + |v_{\vec{k}}|^2 = 1$ as a result of fermionic particle statistics.

   At $T = 0$ this independence of the coherence factors results in an SIN current

$$I_{SIN} = \frac{2\pi e}{\hbar} \sum_{\vec{k},\vec{q}} |M_{\vec{k},\vec{q}}|^2 \delta(E_{\vec{k}} - |\epsilon_{\vec{q}}|) . \tag{2.21}$$

From this it is evident that we can treat the tunnelling from a normal metal into a superconductor as if the superconductor were described by independent particles in a semiconductor with density of states

$$\frac{n_s(E)}{n_{s0}} = \begin{cases} \frac{E}{\sqrt{E^2 - |\Delta|^2}} & E > |\Delta| \\ 0 & E < |\Delta| . \end{cases} \tag{2.22}$$

Here $n_S(E)$ is the Bogoliubon density of states and n_{s0} the density of states of the underlying normal band, assumed to be constant. Here I show the result for an s-wave superconducting gap. For a d-wave gap $n_S(E)$ can simply be replaced by the d-wave Bogoliubon density of states.

   Under the assumption that $|M_{\vec{k},\vec{q}}| = |M|$, we arrive at

$$I_{SIN} = \frac{2\pi e}{\hbar} |M|^2 \int_0^{eV} n_s(\epsilon + eV)n_n(\epsilon)d\epsilon , \tag{2.23}$$

which is the same form for the tunnelling current derived for a metal of non-interacting quasi-particles derived in Sect. 2.1.2. If we choose a normal metal

electrode with a constant density of states n_0 (such as a tungsten STM tip) then the differential tunnelling conductance

$$\frac{dI}{dV} = \frac{2\pi e^2}{\hbar}|M|^2 n_0 n_s(eV) \tag{2.24}$$

measures $n_s(E)$ directly [6, 7, 9, 12].

2.1.4   Superconductor-Insulator-Superconductor (SIS) Tunnelling

If we only consider the tunnelling of single electrons between two superconducting electrodes then the semiconductor model presented in the previous section still holds due to a similar simplification of the coherence factors [13]. This results in a superconductor-insulator-superconductor tunnelling current

$$I_{SIS} = \frac{2\pi e}{\hbar}|M|^2 \int_0^{eV} n_{S1}(E - eV)n_{S2}(E)dE \ . \tag{2.25}$$

$n_{S1}(E)$ and $n_{S2}(E)$ would be given by Eq. 2.22 with superconducting gaps Δ_1 and Δ_2 respectively. Neither of the electrodes has a constant density of states near the Fermi energy, resulting in a more complicated expression for the differential tunnelling current [13]:

$$\frac{dI}{dV} = \frac{2\pi e^2}{\hbar}|M|^2 \left[n_{S1}(E)n_{S2}(E + eV) + \int_0^{eV} n_{S1}(E)\frac{d}{d(eV)}n_{S2}(E + eV)dE \right] \ . \tag{2.26}$$

This will be used in Chap. 5 for the scanned Josephson tunnelling microscope, which uses a superconducting STM tip to measure a superconducting sample.

In addition to the single electron tunnelling processes between superconductors considered here, there is also the possibility of the tunnelling of Cooper-pairs between the electrodes [11]. This is known as the Josephson effect and it will be discussed in Chap. 5, where I will demonstrate the use of Cooper-pair tunnelling to directly visualise the Cooper-pair condensate in $Bi_2Sr_2CaCu_2O_{8+\delta}$.

Having outlined the theoretical basis for vacuum tunnelling and its use as a spectroscopy I will now go on to describe how it is used in an STM.

2.2   STM - Principles

The STM consists of a sharp conducting tip that can be rastered across a conducting sample surface. This is typically achieved by attaching the tip to a piezoelectric
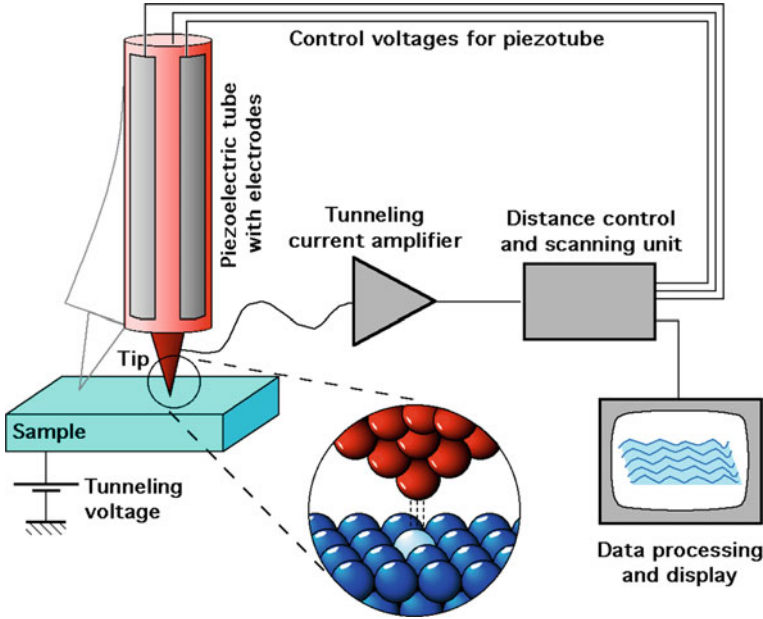
Fig. 2.2 Schematic of STM operation. This figure illustrates tunnelling between a voltage-biased sample and an atomically sharp tip. In constant current operation the piezoelectric tube is used to scan the tip in the x and y directions. As this is done the tunnelling current is measured. A feedback system (PID) is used to adjust z using the piezo-tube so as to keep the current constant. Reproduced from Ref. [14]

scanner tube as shown schematically in Fig. 2.2 [1]. A bias voltage, V, is applied between the two and the vacuum tunnelling current measured. We shall see below that its utility as an extremely sensitive topographic probe derives from the exponential dependence of the tunnelling current on the tip-sample distance. The principles of tunnelling spectroscopy detailed in the previous section can also be applied to STM to give access to the atomically resolved local density of states (LDOS).

Focussing on the case of SIN tunnelling between a normal metal STM tip and a superconducting sample pertinent to Chap. 4, the elastic tunnelling current between tip and sample under applied bias voltage V at $T = 0$ is

$$I_{SIN}(\vec{r}, z, E = eV) = \frac{2\pi e}{\hbar} n_T(0)|M(\vec{r}, z)|^2 \int_0^{eV} n_S(\vec{r}, \epsilon)d\epsilon \, . \qquad (2.27)$$

$n_s(\vec{r}, E)$ is the superconducting LDOS of the sample at position $\vec{r} = (x, y)$, z is the tip-sample separation and energy $E = eV$. The density of states of the STM tip, n_T, has been taken to be constant here. In the measurements presented in this thesis this was achieved using tungsten STM tips which have a flat density of states

near the Fermi energy. Thus, we see that at a given position, $I_{SIN}(\vec{r}, z, V)$ is directly proportional to the energy-integrated density of states.

The spatially resolved differential tunnelling conductance is given by

$$g(\vec{r}, z, E = eV) = \frac{2\pi e^2}{\hbar}|M(\vec{r}, z)|^2 n_0 n_S(\vec{r}, E = eV) . \tag{2.28}$$

Thus at a given position, $g(\vec{r}, V)$ is directly proportional to the local density of states $n_S(\vec{r}, E)$.

To see why STM is such an effective atomic scale probe we now need to examine the dependence of the matrix elements $|M(\vec{r}, z)|$ on the tip sample distance z. Bardeen has shown [6] that if the many-body tip and sample states are known then in principle the matrix elements $|M_{\mu\nu}|$ can be calculated via

$$M_{\mu\nu} = \frac{\hbar^2}{2m} \int d\vec{S} \cdot (\psi_\mu^* \nabla \psi_{nu} - \psi_\nu \nabla \psi_{mu}^*) , \tag{2.29}$$

where the integral is over any surface lying entirely within the vacuum region. These wave-functions are typically not known but an analytical model that provides much insight was provided by Tersoff and Hamann [15]. They showed that

$$|M_{\mu\nu}|^2 \propto \exp(-2\kappa z) , \tag{2.30}$$

where $\kappa = \sqrt{\frac{2m\phi}{\hbar^2}}$ with ϕ being the work functions of the tip and sample (which are assumed to be the same), z the tip-sample distance and m the electron mass. κ^{-1} represents the maximum decay length of sample wave-functions into the vacuum.

This exponential decay with z is what we might have expected from considering a simple 1D square barrier of height ϕ within the WKB approximation. It gives STM an extreme sensitivity to changes in the topographic height of the sample. Below I will discuss how Eqs. 2.27, 2.28 and 2.30 are utilised in the topographic and spectroscopic imaging modalities of STM.

2.3 STM - Modes of Operation

2.3.1 Topography

To record a topograph a set-point bias V_s is applied between tip and sample. A feedback loop is then used to keep $I(\vec{r}, Z, eV_s)$ constant at a set-point value I_s, by varying z, as the tip rasters across a sample [16]. In this way one is able to resolve sub-Angström changes in sample topography. An STM topograph, $T(\vec{r})$, consists of an image in which each pixel at position $\vec{r}$ records the value of z required to attain the set-point current.
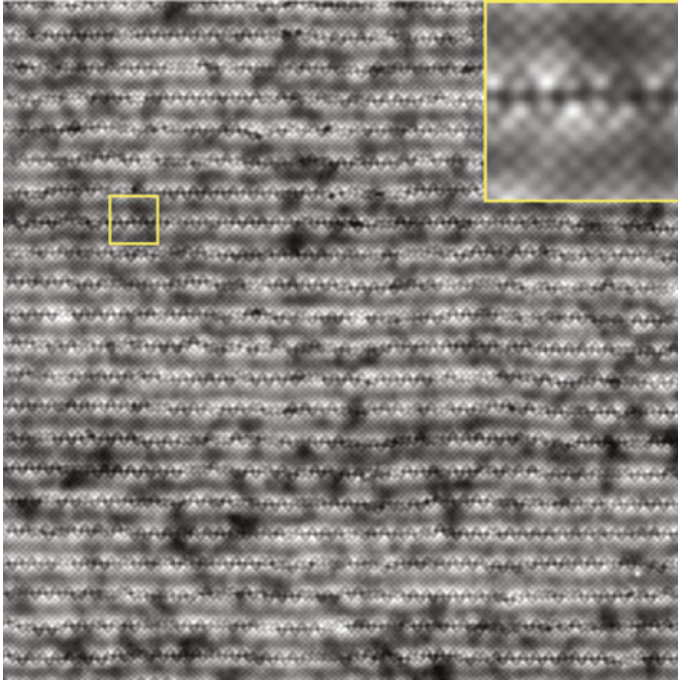
Fig. 2.3 Atomically resolved topograph, $T(\vec{r})$, of a $Bi_2Sr_2CaCu_2O_{8+\delta}$ sample in a 65×65 nm field of view. *Inset* is magnified image of the section outlined in *yellow*

Let us term $\int_0^{eV_s} n_S(\epsilon, \vec{r})d\epsilon$ the integrated LDOS. If this and the matrix element are uniform across the sample then the STM "topograph" will be a good approximation to the true topography of the surface.

Figure 2.3 shows an atomically resolved topograph of the BiO surface of Bi_2Sr_2 $CaCu_2O_{8+\delta}$. Here the atomic contrast is known to result from the Bi atoms on the insulating surface layer. This layer does not contribute to the low energy LDOS and hence the atomic contrast in Fig. 2.3 must arise through atomic scale variations in the tunnelling matrix elements.

2.3.2 Spectroscopy

As shown above in Eq. 2.28, the differential conductance $g(\vec{r}, V) = dI(\vec{r}, z, V)/dV$ at bias voltage V is proportional to $n_S(\vec{r}, eV)$. Thus by holding the tip at constant z, sweeping the bias voltage and recording $g(\vec{r}, V)$ one can measure $n_S(\vec{r}, eV)$ [16]. While it is possible to measure $I(\vec{r}, z, V)$ and then take a numerical derivative to give $g(\vec{r}, V)$, a considerably better signal to noise ratio can be obtained by using a small AC modulation of V from a lock-in amplifier to measure this quantity directly. Let $V(t) = V_0 + V_m \cos(\omega t + \phi)$ then,

Fig. 2.4 Typical differential conductance spectrum, $g(V)$, for a $Bi_2Sr_2CaCu_2O_{8+\delta}$ sample with $p = 6\%$
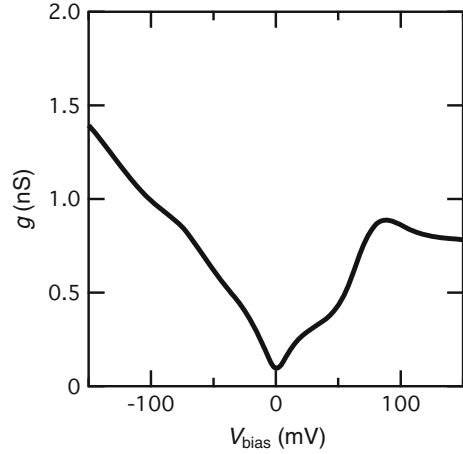
$$I(\vec{r}, z, V(t)) = I(\vec{r}, z, V_0) + \left.\frac{dI(\vec{r}, z, V)}{dV}\right|_{V_0} V_m \cos(\omega t + \phi) + \left.\frac{d^2 I(\vec{r}, z, V))}{dV^2}\right|_{V_0} V_m^2 \cos^2(\omega t + \phi) + \dots ,$$

(2.31)

and hence measurement of the amplitude of the first harmonic gives $g(\vec{r}, z, V)$.

Taking a measurement of this type at a single point on the sample, $\vec{r}$, for a range of DC bias voltages results in a conductance spectrum, proportional to the LDOS, such as that shown in Fig. 2.4. I will now go on the discuss the systematic collection of these conductance spectra on a fine array of points on the sample to allow an energy resolved visualisation of the electronic structure. This is known as spectroscopic imaging STM (SI-STM).

2.4 SI-STM

In spectroscopic imaging STM (SI-STM) current and conductance spectra, $I(\vec{r}, z, E = eV)$ and $g(\vec{r}, z, E = eV)$, are collected on a fine 2D array of points on the sample to provide energy resolved maps of the local density of states and its integral [2, 3]. Simultaneously, a topographic image is also collected so that the spectroscopic maps can be registered to the lattice.

The procedure for collecting data of this type is as follows:

1. Define an regular array of points $\vec{r}_1, \vec{r}_2...\vec{r}_N$ on the surface of the sample where measurements will be made. Each of these points will form a pixel in the resulting spectroscopic maps and simultaneous topograph.
2. Specify a set-point voltage and current, V_s and I_s, which will be used at all pixels to establish a tunnel junction. With the feedback loop turned on and a bias voltage V_s applied, the tip is moved to the first point in the measurement array and allowed to attain the set-point current I_s by varying z.

3. The feedback loop is then turned off and the value of z recorded as $T(\vec{r}_1)$.
4. An AC voltage modulation is then added to the DC bias. The DC bias V_0 is sequentially moved through a series of values $V_1, V_2, ..., V_i, ..., V_M$, pausing at each to average and record the values of current and differential conductance as $I(\vec{r}_1, E_i = eV_i)$ and $g(\vec{r}_1, E_i = eV_i)$. These are the spectra that make up the first pixel of the spectroscopic maps $I(\vec{r}, E)$ and $g(\vec{r}, E)$.
5. Ramp voltage back to V_S, turn on feedback loop and move to next pixel in array. Repeat steps 3–5 until a measurement has been made at every pixel.

The results of this procedure are spectroscopic maps $I(\vec{r}, E)$ and $g(\vec{r}, E)$ measured for $\vec{r} = \vec{r}_1, \vec{r}_2...\vec{r}_N$ and $E = eV_1, V_2, \ldots, V_i, \ldots, V_M$, as well as the simultaneous topograph $T(\vec{r})$. The SI-STM data collection modality and resultant data are depicted in Fig. 2.5.
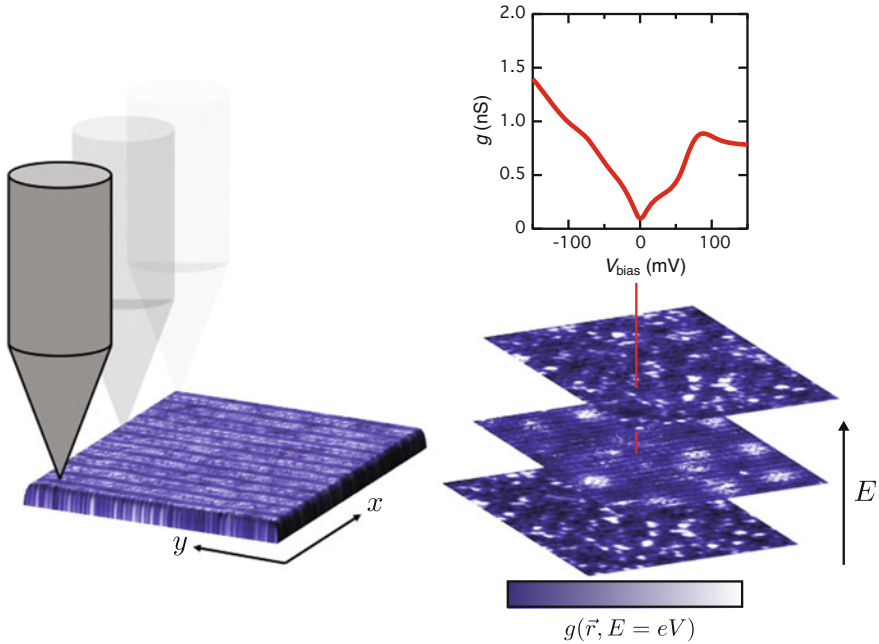
Fig. 2.5 Schematic illustration of SI-STM. The STM tip sequentially establishes a junction at an array of points on the surface of the sample and records current and conductance spectrum at each. This results in spectroscopic maps $I(\vec{r}, E)$ and $g(\vec{r}, E)$ as well a simultaneous topograph $T(\vec{r})$. $g(\vec{r}, E)$ is shown on the *left hand side* in three dimensions (x, y, E). The *colour* scale in each slice corresponds to $g(\vec{r}, E)$ at a fixed energy. The *red line* parallel to the energy axis shows the path through this 3D space which results in the conductance spectrum (also shown in *red*) at a fixed point on the sample

2.4.1 The Setup Effect

SI-STM provides energy resolved electronic structure images that can be used to identify the presence of LDOS modulations. However the protocol described above, by which a tunnelling junction is established in SI-STM, can imprint conductance modulations from one set of energies onto another. This systematic error, which results in a misidentification of the energy of states undergoing spatial modulations, is called the setup effect. Therefore, determining the physically real modulations and especially their correct energies can present a grave challenge. Ignoring the setup effect, as is often the case, leads to incorrect characterisation of the electronic structure of materials.

The basic observable in STM experiments is the tunnelling current, $I(\vec{r}, z, E = eV)$, which depends on the bias between the tip and the sample, V, the tip sample separation, z, and the position on the sample surface, $r = (x, y)$, according to

$$I(\vec{r}, z, V) = f(\vec{r}, z) \int_0^{eV} n(\vec{r}, \epsilon) d\epsilon . \qquad (2.32)$$

The function $f(\vec{r}, z)$ captures spatial variations due to surface corrugation, work function, matrix elements and proximity z of the tip to the surface. The integral of the LDOS, $\int_0^{eV} n(\vec{r}, \epsilon) d\epsilon$, includes spatial variation of the electronic structure.

SI-STM entails establishing a stable tunnel junction at every $\vec{r}$ by using the same set-point current and bias voltage I_S and V_S. These set-point values then constrain the pre-factor of the integral in Eq. 2.32 via

$$I(\vec{r}, z, V_S) = I_S = f(\vec{r}, z) \int_0^{eV_S} n(\vec{r}, \epsilon) d\epsilon \qquad (2.33)$$

$$\Rightarrow f(\vec{r}, z) = \frac{I_S}{\int_0^{eV_S} n(\vec{r}, \epsilon) d\epsilon} \qquad (2.34)$$

and thus the expressions for $I(\vec{r}, E = eV)$ and $g(\vec{r}, E = eV)$ are given by

$$I(\vec{r}, E = eV) = I_S \frac{\int_0^{eV} n(\vec{r}, \epsilon) d\epsilon}{\int_0^{eV_S} n(\vec{r}, \epsilon) d\epsilon} \qquad (2.35)$$

$$g(\vec{r}, E = eV) = I_S \frac{n(\vec{r}, eV)}{\int_0^{eV_S} n(\vec{r}, \epsilon) d\epsilon} . \qquad (2.36)$$

The term in the denominator is responsible for the setup effect since it imprints the integral of the LDOS over the range of energies 0 to eV_s onto every energy in $I(\vec{r}, E = eV)$ or $g(\vec{r}, E = eV)$.

Figure 2.6 demonstrates how the choice of setup bias to establish the tunnelling junction strongly influences the acquired data. While both the left and right panels are spatial images of $g(\vec{r}, E = eV)$ taken at $V = 50\,\text{mV}$ in the same field of view,

$$g(\vec{r}, 50\text{meV})$$
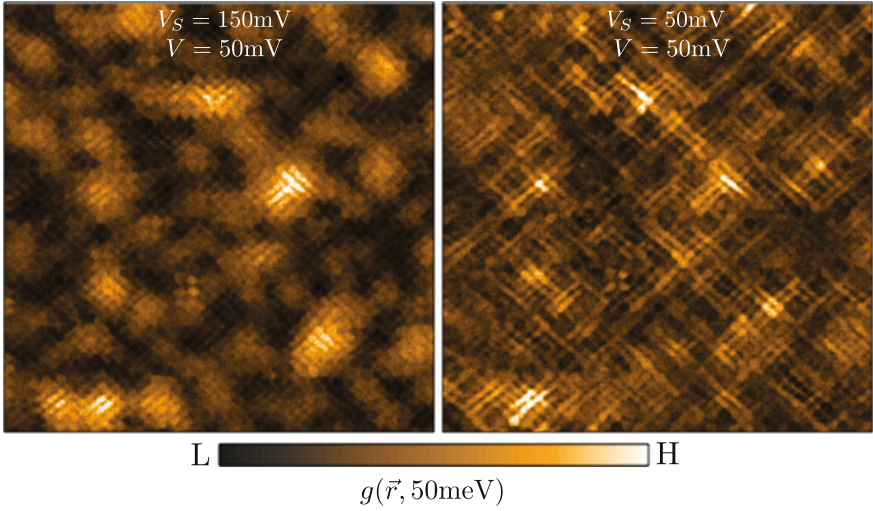
Fig. 2.6 The two panels show the spatial differential conductance of an under-doped Bi$_2$Sr$_2$CaCu$_2$O$_{8+\delta}$ sample at $E = 50$ meV acquired in the same field of view. The *left panel* was acquired with a setpoint bias of $V_S = 150$ mV while the *right* with one of $V_S = 150$ mV

the left was measured with $V_S = 150$ mV setup bias while the right with $V_S = 50$ mV. It is clear that the spatial patterns of the same set of states in the material are imaged differently based on the setup bias parameter.

In order to faithfully resolve which modulations in $g(\vec{r}, E)$ arise from which energies in the LDOS, one must find a setup bias, V_S, for which $\int_0^{eV_S} n(\vec{r}, \epsilon)d\epsilon$ does not exhibit any modulations at the wave-vector of interest. In general, this is difficult because if $n(\vec{r}, E)$, for $E < eV_S$, has modulations at wave-vector $\vec{Q}$ then it is likely that $\int_0^{eV_S} n(\vec{r}, \epsilon)d\epsilon$ also will, unless there is an evolution of the modulation phase with energy.

In cases where no suitable set-point can be found, we can use ratios of $g(\vec{r}, E = eV)$ at different voltages, typically of equal magnitude but opposite polarity. Such combinations have the effect of cancelling the setup effect described here and will be discussed in the following section.

2.4.2   Spectroscopic Functions $g(\vec{r}, E)$, $I(\vec{r}, E)$, $Z(\vec{r}, E)$, and $R(\vec{r}, E)$

I will now consider how, by defining new spectroscopic functions, one can remove the setup effect described in Sect. 2.4.1. Equations 2.35 and 2.36 show us that at a given location, $\vec{r}$, and setup bias, V_S, the conductance and current values at all bias voltages contain the same constant factor $I_S / \int_0^{eV_S} n(\epsilon, \vec{r})d\epsilon$. Thus, by defining a

function that is a ratio of two conductances or currents at the same location, one obtains a function that is independent of V_S and hence setup effect free. In doing so, however, one must combine conductance or current values from different bias voltages and convolve LDOS modulations from different energies.

In this thesis the two setup free functions analysed are

$$Z(\vec{r}, |E|) = \frac{g(\vec{r}, +|E|)}{g(\vec{r}, -|E|)} = \frac{n(\vec{r}, +|E|)}{n(\vec{r}, -|E|)} \ , \tag{2.37}$$

and

$$R(\vec{r}, |E|) = \frac{I(\vec{r}, +|E|)}{I(\vec{r}, -|E|)} = \frac{\int_0^{|E|} n(\vec{r}, \epsilon) d\epsilon}{\int_0^{|E|} n(\vec{r}, -\epsilon) d\epsilon} \ . \tag{2.38}$$

These functions remove the setup effect by sacrificing the distinction between filled and empty states (negative and positive bias voltages respectively). $Z(\vec{r}, |E|)$ is the ratio of tunnelling probabilities for states at opposite polarity bias and similarly $R(\vec{r}, |E|)$ is the ratio of integrated tunnelling probabilities. As such they are often called tunnelling asymmetries.

One effect of these functions is that they naturally enhance any modulations present in the tunnelling conductance that have a π phase shift between states above and below the Fermi energy. As we will see in Chap. 4, this is the case for the predominantly d-symmetry form factor CDW present in $Bi_2Sr_2CaCu_2O_{8+\delta}$ and $Na_xCa_{2-x}CuO_2Cl_2$. The use of $Z(\vec{r}, |E|)$ and $R(\vec{r}, |E|)$ naturally enhances the signals arising from these phenomena.

While $Z(\vec{r}, |E|)$ measures the tunnelling asymmetry between states at energies eV above and below the Fermi energy, $R(\vec{r}, |E|)$ measures the tunnelling asymmetry of all states up to an energy eV above and below the Fermi energy. $R(\vec{r}, |E|)$ then naturally gains a greater weight from modulations that are non-dispersive in energy, such as those from a charge density wave.

The final benefit of $Z(\vec{r}, |E|)$ and $R(\vec{r}, |E|)$ is that they correct for digitisation errors in the junction setup process. This is not a fundamental problem (as with the setup effect) but a purely technical malady. The high voltages applied to the piezo scanner tube are produced by a 16-bit digital to analogue converter (DAC) whose output is passed through a high voltage amplifier. The bin size of the DAC then determines a precision with which the set-point current can be attained by z-axis motion of the STM tip. This means that all pixels in an STM are taken at very slightly different values of I_S. Under the low mechanical and electrical noise conditions used for data acquisition in this thesis, this can be the dominant source of noise in the Fourier transform of $g(\vec{r}, V)$. Luckily, Eqs. 2.35–2.38 imply that this effect is cancelled exactly in $Z(\vec{r}, |E|)$ and $R(\vec{r}, |E|)$.

2.5   Experimental Apparatus

I will now describe briefly the specific experimental implementation of cryogenic SI-STM used to collect the data presented in this thesis.

2.5.1   STM Head

The STMs used in these studies all follow a construction similar to that shown in Fig. 2.7. Their design and construction is detailed in Ref. [17].

The STM tip is held atop a split electrode piezoelectric tube. By applying voltages to the electrodes, the x, y and z position of the tip can be controlled with sub-Angström precision over a total range of ~1 μm. This tube is held inside a sapphire prism. This can be actuated up and down by the slip-stick motion of shear piezo stacks, giving coarse positioning in the z-direction. This assembly is housed inside a rigid Macor body, designed to give its vibrational modes as high a frequency as possible.

Sample are inserted into the top of the STM head on brass sample holders which mate with the head assembly and are held tightly in place by a BeCu spring plate. This plate also applies the bias voltage to the sample, with the tip being held at ground.

Unless otherwise stated all measurements reported in this thesis were made using a chemically etched tungsten STM tip.
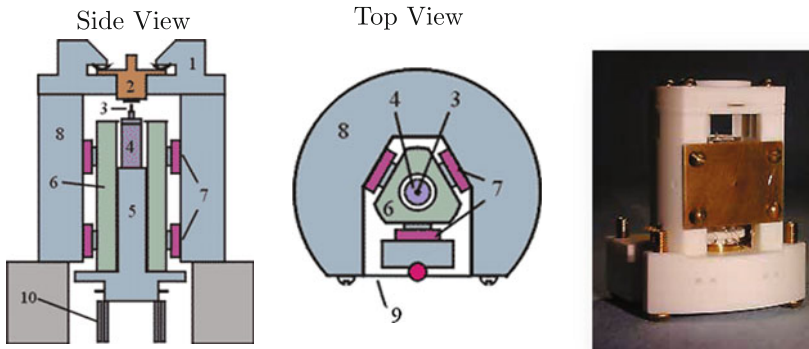
Fig. 2.7 Schematic drawing and photograph of STM head. Parts labelled 1–10 are: (*1*) Sample Receptacle (*2*) Sample Holder (*3*) Tip (*4*) Piezo-tube Scanner (*5*) Scanner Holder (*6*) Sapphire Prism (*7*) Shear Piezo Stacks (*8*) Macor Body (*9*) BeCu Spring Plate (*10*) Capacitive Position Sensor

2.5.2 Cryogenics

The data presented in this thesis were taken at temperatures between 45 K and 45 mK. All instruments were mounted in vacuum cans immersed in liquid ^{4}He resulting in a cryogenic ultra-high vacuum where the STM head is housed. The measurements presented in Chaps. 5 and 7 utilise a dilution refrigerator.

   All samples were inserted from room temperature into the vacuum using an insertion rod and cleaved at ∼4 K. From here they were then inserted directly into the STM head.

2.5.3 Vibration and RF Isolation

Mechanical vibrations introduce noise into STM measurements primarily by varying the tip-sample distance. To maximise the signal to noise ratio of our measurement we utilise passive vibration isolation. This method relies on successive stages having very different resonant frequencies. A concrete block (∼10 tonnes, f_{res}∼1 Hz) is separated from the foundations of the building and supported on air springs. The cryostat is then suspended from a vibrational isolation table (∼1 tonne, f_{res}∼10 Hz), again using air springs.
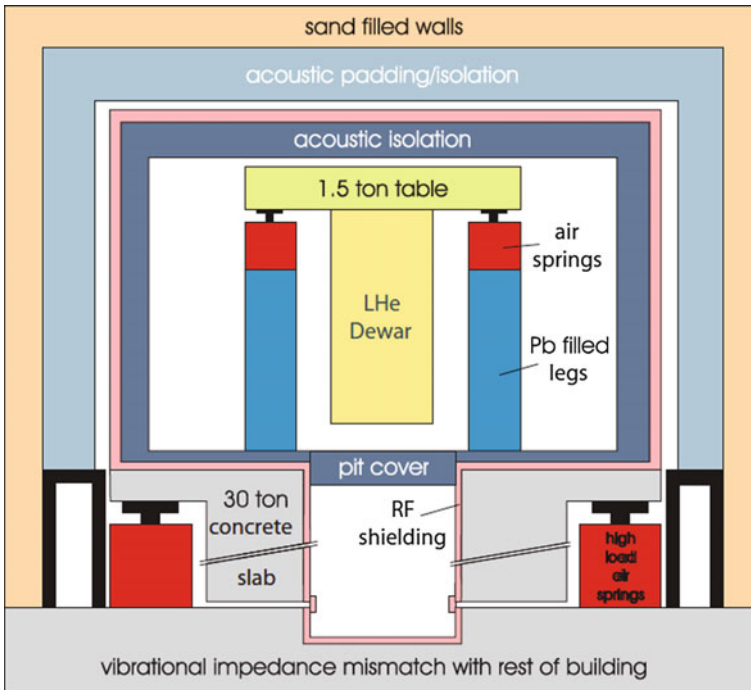
Fig. 2.8 Passive vibration isolation utilised in SI-STM experiments. Reproduced from Ref. [18]

Acoustic isolation is achieved by constructing a room around the cryostat on the floating block, incorporating sound absorbing material. This is then housed inside another room whose walls are filled with sand and the interior lined with sound absorbing material. This is shown in Fig. 2.8.

For the scanned Josephson experiments reported in Chaps. 5 and 7 the floating experimental room is RF shielded.

2.5.4 Instrumentation

The instrumentation used in our SI-STM measurements is shown in Fig. 2.9. Tip-sample current measurements are made with a low-noise current to voltage pre-
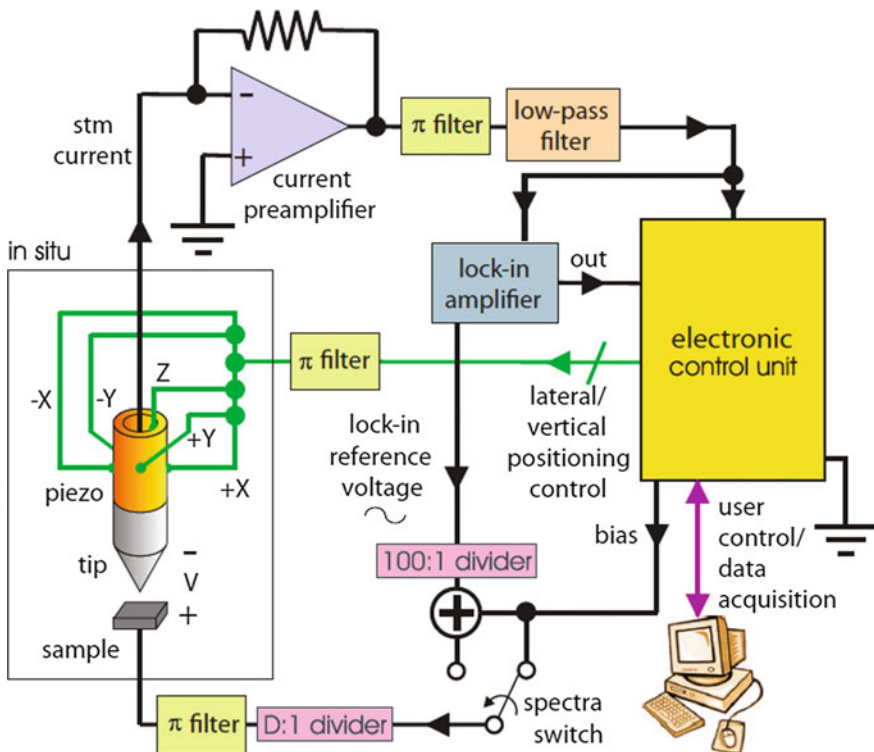
Fig. 2.9 A bias applied to the sample is sourced from the electronic control unit (ECU), a Topometrix SPM controller. The resulting tunnelling current is measured using a low noise current-voltage pre-amplifier situated at the cryostat head in the floating experimental room. The position of the tip is controlled by a piezoelectric scanner tube. The control voltages for this are supplied by the ECU. In topographic mode the z piezo-tube voltage is controlled by a PID feedback loop in the ECU to keep the tunnelling current constant. In spectroscopic mode, this feedback loop is turned of and a constant z piezo voltage used. An AC bias modulation from a lock-in amplifier is added to the sample bias. This lock-in amplifier measures the differential conductance through the resulting AC modulation in the tunnelling current. Reproduced from Ref. [20]

amplifier situated inside the floating experimental room. Differential conductance measurements are made using a lock-in amplifier. The DC bias voltage, feedback loop and high voltage signal to control the piezoelectrics are provided by a Topometrix SPM controller, interfaced to a computer running custom designed control software [19].

2.6 Cuprate Materials

In this thesis, SI-STM and SJTM are applied to cuprate superconductors to visualise charge density wave (CDW) modulations as well as those in the Cooper-pair condensate. Here I will briefly describe the cuprate samples studied.

The common feature of all cuprate superconductors are the CuO_2 planes. The variety in this family of materials arises from how these planes are incorporated into a crystal. In this thesis measurements of two cuprate materials, $Bi_2Sr_2CaCu_2O_{8+\delta}$ and $Na_xCa_{2-x}CuO_2Cl_2$, are presented. These materials were chosen for their compatibility with SI-STM because they both cleave easily and reproducibly to yield atomically flat surfaces that are not reconstructed. Below I will briefly describe the crystallography and properties of these two cuprate superconductors, as well as the fabrication of the samples measured in our studies.

2.6.1 $Bi_2Sr_2CaCu_2O_{8+\delta}$

In $Bi_2Sr_2CaCu_2O_{8+\delta}$ the CuO_2 planes are sandwiched between BiO, SrO and Ca layers, as shown in Fig. 2.10. There are two CuO_2 layers per BiO layer, leading to the description of $Bi_2Sr_2CaCu_3O_{10+\delta}$ as a bi-layer compound, with $Bi_2Sr_2CuO_{6+\delta}$ and $Bi_2Sr_2Ca_2Cu_2O_{8+\delta}$ being its single and triple layer relatives respectively. $Bi_2Sr_2CaCu_2O_{8+\delta}$ has the I_4/mmm space group with 4 CuO_2 planes per unit cell, with an offset of $(1/2, 0, 0)$ between the two bilayers. The mirror plane between adjacent BiO layers leads to BiO being the natural cleave plane of the material. Note that bismuth atoms always lie directly above copper atoms, allowing one to determine the copper positions from the surface topography. The nearest neighbour distance between copper atoms forming approximately square lattice planes is 3.82Å.

The CuO_2 plaquettes are not exactly square in $Bi_2Sr_2CaCu_2O_{8+\delta}$ due to the presence of a bulk incommensurate structural super-modulation [21, 22]. This buckling of the whole crystal, at 45° to the Cu-O directions (along the b-axis in Fig. 2.10) results from a lattice mismatch between the BiO and other layers of the crystal. Importantly, this modulation leaves intact a mirror symmetry between the two Cu-O directions in the CuO_2 plane. Thus, any breaking of this symmetry is spontaneous.
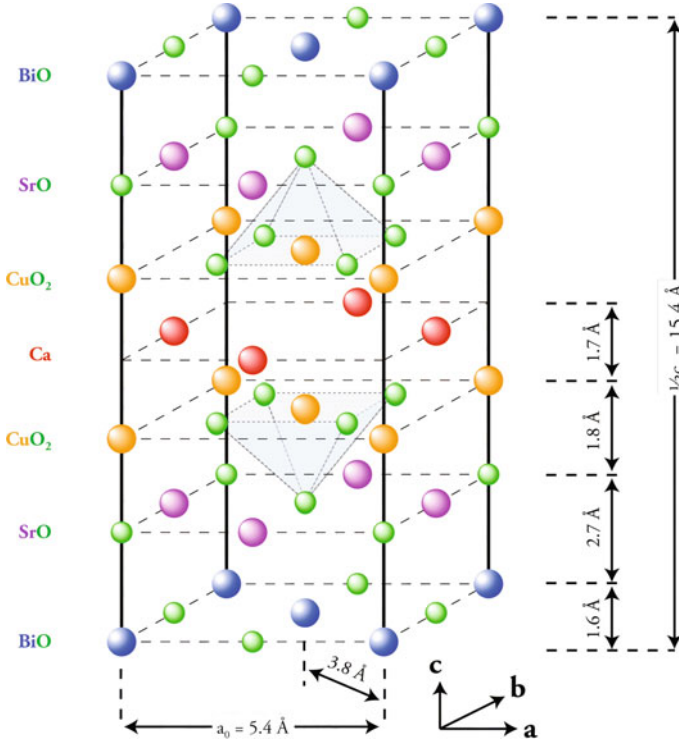
Fig. 2.10 Cartoon unit cell of the bi-layer cuprate $Bi_2Sr_2CaCu_2O_{8+\delta}$. CuO_2 planes are incorporated between Ca, SrO and BiO layers. Only half of the unit cell is shown along the c-axis. The second half of the unit cell is a repeat of that shown but offset by (1/2, 0, 0). The natural cleavage plane is the BiO layer. Bi atoms are directly above the Cu atoms in the crystal structure allowing the Cu positions to be identified from surface topography. Reproduced from Ref. [23]

The $Bi_2Sr_2CaCu_2O_{8+\delta}$ samples used for the measurements presented here were grown by K. Fujita in the group of S. Uchida at the University of Tokyo. For hole dopings $p \leq 0.08$ $Bi_{2.2}Sr_{1.8}Ca_{0.8}Dy_{0.2}Cu_2O_{8+\delta}$ samples were used whereas for $p > 0.08$ the composition $Bi_{2.1}Sr_{1.9}CaCu_2O_{8+\delta}$ was employed.

High-quality single crystals were grown using the travelling solvent floating zone method. The samples were synthesised from dried powders of Bi_2O_3, $SrCO_3$, $CaCO_3$ and CuO. The crystal growth was carried out in air and at growth speeds of 0.15-0.2 mm/h for all samples. Annealing was used to vary the hole doping of each sample. Oxidation annealing is performed in air or under oxygen gas flow, and deoxidation annealing is done in vacuum or under nitrogen gas flow. Inductively coupled plasma spectroscopy was used for the composition analysis and a vibrating sample magnetometer was used for measurement of T_c. Each sample was inserted into the cryogenic ultra-high vacuum of the SI-STM system and cleaved at $T \approx 4K$ to reveal an atomically flat BiO surface.

Fig. 2.11 Cartoon unit cell of $Na_xCa_{2-x}CuO_2Cl_2$. CuO_2 planes are incorporated between CaCl layers. Hole doping is achieved by substituting Ca^{2+} ions for Na^+ ions, introducing holes into the CuO_2 planes. Reproduced from Ref. [25]
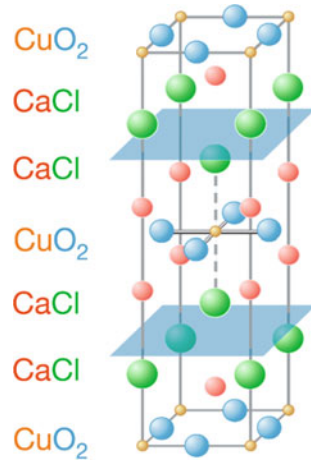
2.6.2 $Na_xCa_{2-x}CuO_2Cl_2$

The other material for which measurements are reported in this thesis is $Na_xCa_{2-x}CuO_2Cl_2$. In this material the CuO_2 planes are incorporated between CaCl layers, as shown in Fig. 2.11. The material is tetragonal, with the I_4/mmm space group and does not have any incommensurate structural super-modulation. Hole doping is achieved by substituting Ca^{2+} ions for Na^+ ions, introducing holes into the CuO_2 planes. In this thesis I present data from $Na_xCa_{2-x}CuO_2Cl_2$ samples with $p = 12\%$.

The $Na_xCa_{2-x}CuO_2Cl_2$ samples were grown by Y. Kohsaka at the University of Tokyo [24]. A flux method was used for growth, with high pressures used to increase the solubility of Na. The samples were synthesised from powders of $Ca_2CuO_2Cl_2$, $NaClO_4$ and NaCl in a high pressure anvil cell at pressures of 2–5.5 GPa.

2.7 Quasi-Particle Interference in Cuprates

Quasi-particle interference (QPI) is a technique used to extract the energy-momentum dispersion of quasi-particles in a material using SI-STM [2, 3, 26]. It uses the characteristic wave-lengths present in the density of states modulations formed by quasi-particles scattering from impurities, often called Friedel oscillations. With a suitable model, one can use the bias voltage dependence of these characteristic wave-lengths to determine the quasi-particle dispersion.

This technique is applicable to both normal Landau quasi-particles as well as Bogoliubov quasi-particles in a superconductor. In Chap. 4 I will use Bogoliubov quasi-particle interference in $Bi_2Sr_2CaCu_2O_{8+\delta}$ to determine geometric details of the Fermi surface. In the following I will outline how this technique works and its specific application to cuprates.

2.7.1 QPI - A Qualitative Understanding

For a clean metal where the quasi-particle states are described by Bloch functions, $\Psi_{\vec{k}} = e^{i\vec{k}\cdot\vec{r}}u_{\vec{k}}(\vec{r})$, the spatial dependence of the LDOS, $n(\vec{r}, E = eVs) = \sum_{\vec{k}}|\Psi_{\vec{k}}|^2\delta(E - \epsilon_{\vec{k}})$, only contains modulations with the periodicity of the atomic lattice, encoded in $u_{\vec{k}}$.

The introduction of impurities into the lattice leads to elastic scattering between Bloch states, which are no longer the true eigenstates. The new eigenstates will be linear superpositions of Bloch states that lie on the same constant energy contour in $\vec{k}$-space. This mixing of $\vec{k}$-states leads to oscillations in $n(\vec{r}, E)$ with wave-vectors $\{\vec{q}\}$ linking points on the contour of constant energy E. This can be illustrated as follows:

$$|\Psi(\vec{r})|^2 = |a_1 u_{\vec{k}_1}(\vec{r})e^{i\vec{k}_1\cdot\vec{r}} + a_2 u_{\vec{k}_2}(\vec{r})e^{i\vec{k}_2\cdot\vec{r}}|^2 \tag{2.39}$$

$$= |a_1 u_{\vec{k}_1}(\vec{r})|^2 + |a_2 u_{\vec{k}_2}(\vec{r})|^2 + (a_1 u_{\vec{k}_1}(\vec{r})a_2^* u_{\vec{k}_2}^*(\vec{r})e^{i\vec{q}\cdot\vec{r}} + c.c) \tag{2.40}$$

where $\vec{q} = \vec{k}_1 - \vec{k}_2$. This will be observed as modulations of the local density of states, $n(\vec{r}, E)$ with wavelength $\lambda = \frac{2\pi}{|\vec{q}|}$.

As discussed above in Sect. 2.4, SI-STM yields spectroscopic maps $I(\vec{r}, E)$ and $g(\vec{r}, E)$. Further, $g(\vec{r}, E)$ is proportional to the local density of states $n(\vec{r}, E)$. For a fixed energy, $g(\vec{r}, E)$ is a two-dimensional image and will contain quasi-particle interference modulations from scattering between the contours of constant energy E. By taking a two-dimensional Fourier transform to yield $\tilde{g}(\vec{q}, E)$ we can extract the LDOS modulation wave-vectors and hence infer geometric information about the constant energy contours (CCEs) in the quasi-particle dispersion. By tracking the wave-vectors present in these Fourier transforms systematically with energy we can potentially extract the quasi-particle dispersion in a material.

To illustrate this consider a quasi-2D material with a cylindrical Fermi surface with Fermi wavevector $|\vec{k}_F|$ in the presence of a point impurity (whose scattering form factor will be momentum independent). The power spectrum of a conductance map taken at zero bias will show a strong cusp at a circle of radius $|\vec{q}| = 2|\vec{k}_F|$ because this is where the joint density of states for scattering is largest.

In this example it is easy to work backwards from the power spectrum to deduce the Fermi-surface and by varying the bias we can determine the dispersion relation. However, in cases where the scattering potential is not isotropic or the constant energy contours are complicated this process becomes non-trivial and is one of the major challenges of analysing this type of experiment. Luckily in cuprates, we have a well established model of Bogoliubov quasi-particle interference called the "octet model", which I will now introduce.

2.7.2 The Octet Model

It is well established that cuprate superconductors exhibit a *d*-wave superconducting gap of the form,

$$\Delta_{\vec{k}} = \frac{\Delta_0}{2} \left(\cos(k_x a_0) - \cos(k_y a_0) \right) , \qquad (2.41)$$

with four nodes along the zone diagonals. This leads to a Bogoliubov quasi-particle dispersion

$$E_{\vec{k}} = \sqrt{\epsilon_{\vec{k}}^2 + \Delta_{\vec{k}}^2} , \qquad (2.42)$$

where $\epsilon_{\vec{k}}$ is the dispersion of the underlying normal band. In the cuprates $\partial_{k_\perp} \Delta_{\vec{k}} \ll \partial_{k_\parallel} \epsilon_{\vec{k}}$ ($\partial_{k_\parallel} \epsilon_{\vec{k}} / \partial_{k_\perp} \Delta_{\vec{k}} \approx 20$ at the gap nodes [27]), where $k_\perp$ and $k_\parallel$ are perpendicular and parallel to the Fermi wave-vector respectively. This results in banana-like constant energy contours (CECs) in the Bogoliubon dispersion as shown in the Fig. 2.12.

As discussed in the previous section, the strongest modulations are usually seen at wave-vectors for which the joint density of states for scattering between points on the CECs are maximal. One way this can arise is through nesting, where large sections of a Fermi surface are parallel to each other in $\vec{k}$-space.

In cuprates the situation is different. The points with the largest density of states

$$n(\vec{k}, E) \propto \frac{1}{|\nabla_{\vec{k}}(E)|} \qquad (2.43)$$
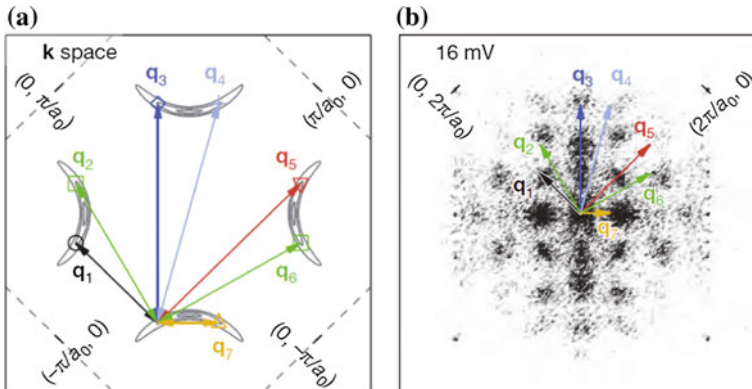
Fig. 2.12 a Banana shaped constant energy contours (CECs) of the *d*-wave Bogoliubov quasi-particle dispersion in $\vec{k}$-space. In the octet model, quasi-particle interference modulations in the LDOS primarily arise from scattering between the eight tips of these bananas. This results in 7 scattering vectors $\vec{q}_1, \ldots, \vec{q}_7$. **b** Measured fourier transform $Z(\vec{q}, |E|)$ from underdoped Bi$_2$Sr$_2$CaCu$_2$O$_{8+\delta}$ shown LDOS modulations at the wave-vectors $\vec{q}_1, \ldots, \vec{q}_7$. Reproduced from Ref. [2]

are those at the eight tips of the banana like CECs. In the absence of nesting, the largest joint density of states for scattering will also be between these eight points [8, 27]. Thus QPI LDOS modulations will arise from the set of $8 \times 7 = 56$ pairings that connect these.

These 56 pairings are not all distinct because the same scattering vector connects multiple points. Taking this into account there are 16 independent $\vec{q}$ vector measurements that we can make at each bias voltage. But again, some of these are related by the crystal symmetry, allowing us to make multiple independent measurements of the 7 scattering vectors,

$$\vec{q}_1(E) = (2k_x, 0) \tag{2.44}$$
$$\vec{q}_2(E) = (k_x + k_y, k_y - k_x) \tag{2.45}$$
$$\vec{q}_3(E) = (k_x + k_y, k_x + k_y) \tag{2.46}$$
$$\vec{q}_4(E) = (2k_x, 2k_y) \tag{2.47}$$
$$\vec{q}_5(E) = (0, 2k_y) \tag{2.48}$$
$$\vec{q}_6(E) = (k_x - k_y, k_x + k_y) \tag{2.49}$$
$$\vec{q}_7(E) = (k_x - k_y, k_y - k_x) , \tag{2.50}$$

where $\vec{k} = (k_x, k_y)$ corresponds to the momentum space coordinates of the banana tips at a given energy.

Ultimately, we wish to determine an energy momentum-dispersion relation $\vec{k}(E)$. To do this we can invert Eqs. 2.44–2.50 to yield,

$$2k_x(E) = |\vec{q}_1|, q_{2x} - q_{2y}, q_{6y} - q_{6x}, |\vec{q}_3 - \vec{q}_7|/\sqrt{2}, |\vec{q}_5| - \sqrt{2}|\vec{q}_7|, q_{4x} \tag{2.51}$$
$$2k_y(E) = |\vec{q}_5|, q_{2x} + q_{2y}, q_{6y} + q_{6x}, |\vec{q}_3 + \vec{q}_7|/\sqrt{2}, \sqrt{2}|\vec{q}_7| - |\vec{q}_1|, q_{4y} . \tag{2.52}$$

These expressions show that this octet model is geometrically over-constrained. At each energy, E, we are able to make 6 independent estimates of $\vec{k}(E)$. Although I have given some justification for this octet model above, its strength lies in its geometrical over-determination. That the 6 independent estimates of $\vec{k}(E)$ agree demonstrates that the octet model is an internally consistent model of QPI in cuprates.

Having measured $\vec{k}(E)$, how should we interpret this information? Due to the condition $\partial_{\vec{k}} \Delta_{\vec{k}} \ll \partial_{\vec{k}} \epsilon_{\vec{k}}$ being realised in cuprates, and Eq. 2.41, $E \approx \Delta_{\vec{k}}$. For every measurement energy, the superconducting gap takes this value at the position $\vec{k}(E)$ in momentum space. Thus we can directly determine the momentum space gap function as shown in Fig. 2.13.

As can be seen in Fig. 2.12, the tips of the banana shaped CECs lie very close to the position of the underlying Fermi surface in momentum space. Thus, by plotting all of the points $\vec{k}(E)$, one can trace out the position of the Fermi surface in momentum space as shown in Fig. 2.13.
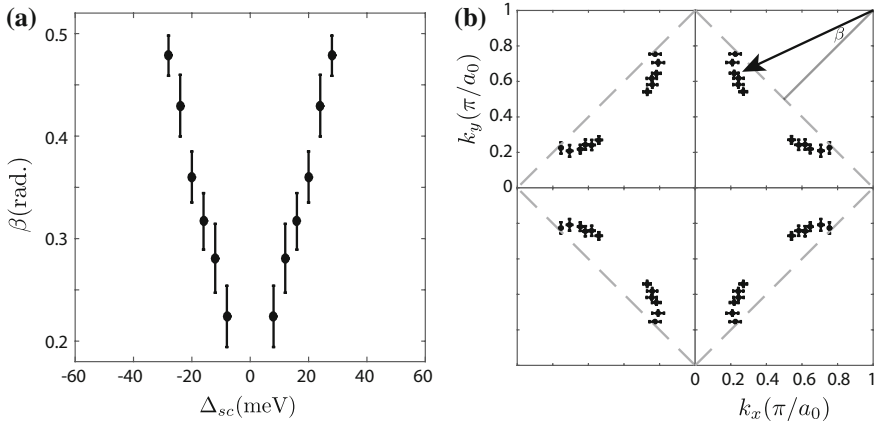
Fig. 2.13   a d-wave superconducting gap function measured for $Bi_2Sr_2CaCu_2O_{8+\delta}$ with $p = 17\%$ using quasi-particle interference. Gap values are plotted against β, the angle from the nodal (π, π) directions. **(b)** (k_x, k_y) values of all points shown in **a**. They trace out the underlying Fermi surface. In $Bi_2Sr_2CaCu_2O_{8+\delta}$ with $p < 19\%$ no quasi-particle interference is observed from quasi-particles beyond the anti-ferromagnetic Brillouin zone (*dashed lines*). Plotted points represent the mean of 6 independent k_x and k_y estimates made from measured wave-vectors $\vec{q}_1, \ldots, \vec{q}_7$ using Eqs. 2.51 and 2.52. Error bars represent the standard deviation of these 6 independent estimates

This technique will be used in Chap. 4 to extract the Fermi surface geometry of $Bi_2Sr_2CaCu_2O_{8+\delta}$ for a range of dopings. Here, instead of using the full octet of scattering vectors, $\vec{q}_4$ alone is used. The set of relations Eqs. 2.51 and 2.52 show that this is sufficient.

2.8   Mapping Spatial Variations in the Amplitude and Phase of LDOS Modulations

SI-STM spectroscopic maps contain a vast amount of information, with modulations occurring on multiple length scales and in multiple directions. Often we are only interested in the amplitude and phase of a small sub-set of these modulations. These quantities can be extracted from our data sets by filtering their complex Fourier transforms so that only wave-vectors proximal to those of interest remain. For instance, if we are interested in modulations of the spectroscopic map $M(\vec{r}, E)$ at wave-vector $\vec{Q}$ we would filter its Fourier transform $\tilde{M}(\vec{q}, E)$ to yield

$$M_{\tilde{Q}}(\vec{q}, E) = \tilde{M}(\vec{q}, E)e^{-\frac{(\vec{q}-\vec{Q})^2}{2\Lambda^2}} , \qquad (2.53)$$

where Λ^{-1} is the characteristic length scale below which variations in the amplitude or phase of modulations at $\vec{Q}$ will not be resolved in this process. I will refer to this process as Fourier filtration.

Using an inverse Fourier transform one can then proceed to create the complex real-space map,

$$M_{\vec{Q}}(\vec{r}, E) = \frac{2}{(2\pi)^2} \int d\vec{q}\, e^{i\vec{q}\cdot\vec{r}} \tilde{M}_{\vec{Q}}(\vec{q}, E)\,, \tag{2.54}$$

that only contains modulations at wave-vectors proximal to $\vec{Q}$.

To make a real-space map of modulations at wave-vector $\vec{Q}$ one simply takes the amplitude of $M_{\vec{Q}}(\vec{r})$,

$$A_{\vec{Q}}(\vec{r}, E) = \sqrt{(ReM_{\vec{Q}}(\vec{r}, E))^2 + (ImM_{\vec{Q}}(\vec{r}, E))^2}\,. \tag{2.55}$$

Similarly the phase of these modulations, $\phi(\vec{r})$, is given by

$$\phi(\vec{r}) = \arctan \frac{ImM_{\vec{Q}}(\vec{r}, E)}{ReM_{\vec{Q}}(\vec{r}, E)}\,. \tag{2.56}$$

In other cases we are interested in removing a specific Fourier component from an image because it is visually dominating and we wish to examine a smaller modulation at another wave-vector. In this case we can remove those modulations at wave-vectors $\pm\vec{Q}'$ to create the real-space map

$$M'_{\pm\vec{Q}'}(\vec{r}, E) = \frac{2}{(2\pi)^2} \int d\vec{q}\, e^{i\vec{q}\cdot\vec{r}} \left[\tilde{M}(\vec{q}, E) - \tilde{M}'_{\pm\vec{Q}'}(\vec{q}, E) \right]\,, \tag{2.57}$$

where

$$M'_{\pm\vec{Q}}(\vec{q}, E) = \tilde{M}(\vec{q}, E) \times \left[e^{-\frac{(\vec{q}-\vec{Q}')^2}{2\Lambda^2}} + e^{-\frac{(\vec{q}+\vec{Q}')^2}{2\Lambda^2}} \right]\,. \tag{2.58}$$

References

1. G. Binnig, H. Rohrer, Scanning tunneling microscopy. Surf. Sci. **126**(126), 236–244 (1982)
2. K. Fujita et al., Spectroscopic imaging scanning tunneling microscopy studies of electronic structure in the superconducting and pseudogap phases of cuprate high-tc superconductors. J. Phys. Soc. Jpn. **81**(1), 011005 (2012)
3. A. Yazdani, E.H. da Silva Neto, P. Aynajian, Spectroscopic imaging of strongly correlated electronic states. Ann. Rev. Condensed Matter Phys. **7**(1), 11–33 (2016)
4. L. Esaki, New phenomenon in narrow germanium p-n junctions. Phys. Rev. **109**(2), 603–604 (1958)
5. I. Giaever, Energy gap in superconductors measured by electron tunneling. Phys. Rev. Lett. **5**(4), 147–148 (1960)
6. J. Bardeen, Tunnelling from a many-particle point of view. Phys. Rev. Lett. **6**(2), 6–8 (1961)
7. M.H. Cohen, L.M. Falicov, J.C. Phillips, Superconductive tunneling. Phys. Rev. Lett. **8**(8), 316–318 (1962)
8. J. Hoffman, Search for alternative electronic order in the by scanning tunneling high temperature superconductor $Bi_2Sr_2CaCu_2O_8+\delta$ by scanning tunneling microscopy. Ph.D. thesis. University of California, Berkeley (2003)

9. W.A. Harrison, Tunneling from an independent-particle point of view. Phys. Rev. **123**(1), 85–89 (1961)
10. J. Bardeen, L.N. Cooper, J.R. Schrieffer, Theory of superconductivity. Phys. Rev. **108**(5), 1175–1204 (1957)
11. B. Josephson, Possible new effects in superconductive tunnelling. Phys. Lett. **1**(7), 251–253 (1962)
12. J. Bardeen, Tunneling into superconductors. Phys. Rev. Lett. **9**(4), 147–149 (1962)
13. M. Tinkham, *Introduction to Superconductivity* (McGraw-Hill Book Co., New York, 1975)
14. *Adapted from IAP/TU Wien STM Gallery under Creative Commons Attribution ShareAlike 2.0 Austria License*
15. J. Tersoff, D.R. Hamann, Theory of the scanning tunneling microscope. Phys. Rev. B **31**(2), 805–813 (1985)
16. C.J. Chen, *Introduction to Scanning Tunneling Microscopy* (Oxford University Press, Oxford, 2007), pp. 1–40
17. S.H. Pan, E.W. Hudson, J.C. Davis, 3He refrigerator based very low temperature scanning tunneling microscope. Rev. Sci. Instrum. **70**(2), 1459 (1999)
18. M.H. Hamidian, Imaging the Realm of the Strongly Correlated: Visualising Heavy Fermion Formation and The Impact of Kondo Holes in URu2Si2. Ph.D. thesis. Cornell University (2011)
19. E.W. Hudson, Investigating High-Tc Superconductivity on the Atomic Scale by Scanning Tunneling Microscopy (1994)
20. C.B. Taylor, Coexistence of Bogoliubov Quasiparticles and Electronic Cluster Domains in Lightly Hole-Doped Cuprate Superconductors. Ph.D. thesis. Cornell University (2008), p. 211
21. M. Zhiqiang et al., Relation of the superstructure modulation and extra-oxygen local-structural distortion in Bi. Phys. Rev. B **55**(14), 9130–9135 (1997)
22. X.B. Kan, S.C. Moss, Fourdimensional crystallographic analysis of the incommensurate modulation in a Bi2Sr2CaCu2O8 single crystal. Acta Crystallogr. Sect. B **48**(2), 122–134 (1992)
23. J.A. Slezak, Atomic-Scale Impact of Unit Cell Dimensions on Pairing in a High-Temperature Superconductor. Ph.D. thesis. Cornell University (2007)
24. Y. Kohsaka et al., Growth of Na-doped Ca2CuO2Cl2 single crystals under high pressures of several GPa. J. Am. Chem. Soc. **124**(41), 12275–12278 (2002)
25. T. Hanaguri et al. A 'checkerboard' electronic crystal state in lightly hole-doped Ca_2-$xNa_xCuO_2Cl_2$. Nature **430**, 1001–1005 (2004)
26. M.F. Crommie, C.P. Lutz, D.M. Eigler, Imaging standing waves in a two-dimensional electron gas. Nature **363**, 524 (1993)
27. Q.-H. Wang, D.-H. Lee, Quasiparticle scattering interference in hightemperature superconductors. Phys. Rev. B **67**(2), 020511 (2003)

Chapter 3
Sub-lattice Segregated SI-STM in Cuprates

In this chapter I will detail novel methods, developed by myself and others in our group over the past 6 years, extending spectroscopic-imaging STM (SI-STM) to imaging states which have significant intra-unit-cell structure. I will a introduce a method of finding and segregating different atomic sites or sub-lattices. I will also outline the technical steps required to use the complex Fourier transform of SI-STM spectroscopic maps to probe intra-unit-cell symmetry breaking. Focussing on cuprate superconductors, these methods will be used in Chap. 4 to determine the intricate intra-unit-cell structure of the charge density wave in cuprates.

SI-STM is a real-space probe and therefore in principle retains all phase information about spatial modulations, in contrast to scattering probes. One has access to the full complex Fourier transform of conductance maps, $\tilde{g}(\vec{q}, E)$, as opposed to just the power spectrum $|\tilde{g}(\vec{q}, E)|^2$.

This turns out to be incredibly useful for studying the structure of electronic states within the unit cell. Consider the CuO_2 plane with one copper and two oxygens per unit cell. In a perfectly periodic lattice, these sets of different atoms or sub-lattices will contribute to its Fourier transform with different phases. For instance, in cuprates if we measure the function $Re\tilde{Z}((\frac{2\pi}{a_0}, 0), E) - Re\tilde{Z}((0, \frac{2\pi}{a_0}), E)$, we are directly measuring only differences in electronic structure between the two oxygen sites in the unit cell [1]. The utility of phase-resolved SI-STM lies in this sub-lattice specificity.

In order to enact such a scheme one must remove artifacts introduced in the measurement process that distort the lattice in SI-STM spectroscopic maps away from perfect periodicity. A procedure for correcting these distortions to give a perfect lattice with the origin of co-ordinates lying on a specific atomic site, first introduced by Lawler et al. in Ref. [1], will be described below.

Another advantage of mapping SI-STM data to a perfectly periodic lattice is that it enables you to easily find the positions of atoms belonging to different sub-lattices. Spectroscopic maps can then be segregated into several maps, each containing only the sites of a single sub-lattice.

All of these techniques will be heavily employed in Chap. 4 where they are used to make a direct detection of a d-symmetry form factor charge density wave in cuprates, a state where a breaking of the symmetry between the oxygen sub-lattices within the unit cell is periodically modulated in space.

As with the previous chapter, the rapid and fairly specialised development of the field means that for completeness I must touch on a fairly large number of sub-topics, some of which are fairly technical; one way to use this chapter might be to back-reference to it from the main results chapters of the thesis rather than try to take in every detail on first reading.

3.1 Data Acquisition Parameters

In order to implement sub-lattice segregated, phase-resolved SI-STM one requires a large number of pixels within every unit cell. To effectively discriminate between different sub-lattices we need at least three physical measurements along each Cu-O-Cu bond; a minimum of 9 pixels per CuO_2 plaquette. Measurements presented in this thesis typically have between 9 and 25 pixels per unit cell. For $Bi_2Sr_2CaCu_2O_{8+\delta}$ this gives a pixel density 0.62–1.71Å^{-2} corresponding to between $\approx 400 \times 400$ and 650×650 measurement pixels in a typical 50 nm $\times$ 50 nm field of view.

3.2 Atomic Phase Correction Algorithm

I will now describe an algorithm for correcting picometer distortions in STM images caused by the non-ideality of the scanner. Such an algorithm is required to sensibly obtain intra-unit-cell information using the phase of spectroscopic map Fourier transforms and is employed throughout this thesis. This algorithm was first designed and implemented by Lawler et al. in Ref. [1].

Consider an atomically resolved STM topograph, $T(\vec{r})$, of a square lattice where two orthogonal wave-vectors generate the atomic corrugations. These are the reciprocal lattice vectors $\vec{Q}_a = (\vec{Q}_{ax}, \vec{Q}_{ay})$ and $\vec{Q}_b = (\vec{Q}_{bx}, \vec{Q}_{by})$ with $|\vec{Q}_a| = |\vec{Q}_b| = 2\pi/a_0$. The ideal topographic image of this perfect square lattice can be written as

$$T_{\text{ideal}}(\vec{r}) = T_0 \left[\cos(\vec{Q}_a \cdot \vec{r}) + \cos(\vec{Q}_b \cdot \vec{r}) \right] . \tag{3.1}$$

In SI-STM, $T(\vec{r})$ and its simultaneously measured spectroscopic current map, $I(\vec{r}, V)$, and differential conductance map, $g(\vec{r}, V)$, are measured on a square array of pixels with coordinates labeled $\vec{r} = (x, y)$. The Fourier transform of $T(\vec{r})$, $\tilde{T}(\vec{q}) = Re\tilde{T}(\vec{q}) + i\tilde{T}(\vec{q})$, then exhibits two distinct peaks at $\vec{q} = \vec{Q}_a$ and $\vec{Q}_b$.

In an actual experiment, $T(\vec{r})$ suffers picometer scale distortions from the ideal representation in Eq. 3.1 because of the time-dependent response of the piezo-tube over the period of data acquisition ($\sim$1 week). This has the effect of applying a slowly varying displacement field, $\vec{u}(\vec{r})$, to the atoms in the experimental topograph $T_{\text{exp}}(\vec{r})$. Identical distortions are also found in the spectroscopic data. Thus, a topographic image, including distortions, is schematically written as

$$T_{\text{exp}}(\vec{r}) = T_0 \left[\cos(\vec{Q}_a \cdot (\vec{r} + \vec{u}(\vec{r}))) + \cos(\vec{Q}_b \cdot (\vec{r} + \vec{u}(\vec{r}))) \right] . \qquad (3.2)$$

Then, to remove the effects of $\vec{u}(\vec{r})$ requires a local transformation $\vec{r} + \vec{u}(\vec{r}) \mapsto \vec{r}\,'$ so that the corrected topograph $T_{\text{corr}}(\vec{r}) = T_{\text{exp}}(\vec{r}\,')$. If $\vec{u}(\vec{r})$ is known exactly this results in a perfect square lattice in $T_{\text{corr}}(\vec{r})$. Thus we must establish a method to reliably estimate $\vec{u}(\vec{r})$.

It helps to recast this problem in terms of the phase of the fundamental component of atomic modulations at a given point $\vec{r}$

$$\phi(\vec{r}) = \vec{Q}_a \cdot \vec{r} + \theta_a(\vec{r}) \qquad (3.3)$$

$$\phi(\vec{r}) = \vec{Q}_a \cdot \vec{r} + \theta_a(\vec{r}) , \qquad (3.4)$$

where $\theta_i(\vec{r}) = \vec{Q}_i \cdot \vec{u}(\vec{r})$ is an additional slowly varying phase generated by the displacement field. If there were no distortions and the $T_{\text{exp}}(\vec{r})$ image were perfectly periodic then $\theta_i(\vec{r})$ would be constant. In turn this recasts Eq. 3.2 as

$$T_{\text{exp}}(\vec{r}) = T_0 \left[\cos(\phi_a(\vec{r})) + \cos(\phi_b(\vec{r})) \right] . \qquad (3.5)$$

From this perspective, the two-dimensional lattice in Eq. 3.5 is a function of phase alone. For example, the apex of every atom in the topographic image has the same phase (modulo 2π) regardless of where it is in the image. When viewed in the $\vec{r}$ coordinates, the distance between such points of equal phase in the "perfect" lattice and distorted lattice is not the same. The problem of correcting $T_{\text{exp}}(\vec{r})$ then reduces to finding a transformation to map points of equal phase in $T_{\text{exp}}(\vec{r})$ and $T_{\text{ideal}}(\vec{r})$ onto each other. This is equivalent to finding a local transformation which makes $\theta_a(\vec{r})$ and $\theta_b(\vec{r})$ constants over all space; call them $\bar{\theta}_a$ and $\bar{\theta}_b$ respectively.

$\theta_a(\vec{r})$ and $\theta_b(\vec{r})$ are determined by a "computational lock-in" method first used by Slezak et al. [2]. $T_{\text{exp}}(\vec{r})$ is first Fourier filtered, with filter width λ, separately for the wave-vectors $\vec{Q}_a$ and $\vec{Q}_b$ to create two images $T_a^\lambda(\vec{r})$ and $T_b^\lambda(\vec{r})$. These are then multiplied by reference sine and cosine functions with periodicity set by $\vec{Q}_a$ and $\vec{Q}_b$ to yield four images

$$X_a(\vec{r}) = T_a^\lambda(\vec{r}) \times \cos(\vec{Q}_a \cdot \vec{r}) , \ Y_a(\vec{r}) = T_a^\lambda(\vec{r}) \times \sin(\vec{Q}_a \cdot \vec{r}) \qquad (3.6)$$

$$X_b(\vec{r}) = T_b^\lambda(\vec{r}) \times \cos(\vec{Q}_b \cdot \vec{r}) , \ Y_b(\vec{r}) = T_b^\lambda(\vec{r}) \times \sin(\vec{Q}_b \cdot \vec{r}) . \qquad (3.7)$$

The phases $\theta_a(\vec{r})$ and $\theta_b(\vec{r})$ are then given by

$$\theta_a(\vec{r}) = \arctan\frac{Y_a(\vec{r})}{X_a(\vec{r})} \,, \theta_b(\vec{r}) = \arctan\frac{Y_b(\vec{r})}{X_b(\vec{r})} \,. \tag{3.8}$$

It is then fairly simple to construct the transformation that needs to be applied to $T_{\exp}(\vec{r})$. Let $\vec{r}$ be a point on the unprocessed $T_{\exp}(\vec{r})$ and let $\vec{r}\,'$ be the point of equal phase on the perfect lattice periodic image, which needs to be determined. This produces a set of relations

$$\vec{Q}.\vec{r} + \theta_a(\vec{r}) = \vec{Q}_a \cdot \vec{r}\,' + \bar{\theta}_a \tag{3.9}$$

$$\vec{Q}.\vec{r} + \theta_b(\vec{r}) = \vec{Q}_b \cdot \vec{r}\,' + \bar{\theta}_b \,. \tag{3.10}$$

To solve for $u(\vec{r})$ rewrite Eqs. 3.9 and 3.10 in matrix form

$$\mathbf{Q}\begin{pmatrix}x'\\y'\end{pmatrix} = \mathbf{Q}\begin{pmatrix}x\\y\end{pmatrix} - \mathbf{Q}\begin{pmatrix}\bar{\theta}_a - \theta_a(\vec{r})\\\bar{\theta}_b - \theta_b(\vec{r})\end{pmatrix} \tag{3.11}$$

where

$$\mathbf{Q} = \begin{pmatrix}Q_{ax} & Q_{ay}\\Q_{bx} & Q_{by}\end{pmatrix} \,. \tag{3.12}$$

Because $\vec{Q}_a$ and $\vec{Q}_b$ are orthogonal, $\mathbf{Q}$ is invertible allowing one to solve for the displacement field $\vec{u}(\vec{r})$ which maps $\vec{r}$ to $\vec{r}'$:

$$\vec{u}(\vec{r}) = \mathbf{Q}^{-1}\begin{pmatrix}\bar{\theta}_a - \theta_a(\vec{r})\\\bar{\theta}_b - \theta_b(\vec{r})\end{pmatrix} \,. \tag{3.13}$$

In practice, we use the convention $\theta_i = 0$ which generates a "perfect" lattice with an atomic peak centered at the origin. This is equivalent to setting to zero the imaginary component of the Bragg peaks in the Fourier transform.

To construct to corrected topograph, $T_{corr}(\vec{r})$, one simply makes the assignment $T_{corr}(\vec{r}) = T_{exp}(\vec{r} + u(\vec{r}))$.

3.3 Finding Atomic Positions

In order to examine tunnelling spectra of the individual atomic sub-lattices in a material one must first find the locations of the different species of atom in the field of view. Using the atomic phase correction procedure detailed in Sect. 3.2 this is fairly simple in cuprates. Having mapped the topograph to a near perfect square lattice and having set the origin of co-ordinates on an atomic site, we know that apices of the atoms in the topograph appear at points where $\vec{Q}_a \cdot \vec{r} = 0 \mod 2\pi$ and $\vec{Q}_b \cdot \vec{r} = 0 \mod 2\pi$.

In $Bi_2Sr_2CaCu_2O_{8+\delta}$ the cleavage plane is a BiO surface and the atomic contrast originates from Bi atoms. It has been shown that the copper sites in the CuO_2 plane are registered to the Bi atoms to within a phase accuracy of 2% of 2π [3]. Thus in spectroscopic maps we identify the positions of copper (Cu), x-directed oxygen (O_x) and y-directed oxygen (O_y) using the criteria

$$\vec{r} \in \begin{cases} \vec{r}_{Cu} & \theta_a = 0 \mod 2\pi \text{ and } \theta_b = 0 \mod 2\pi \\ \vec{r}_{O_x} & \theta_a = \pi \mod 2\pi \text{ and } \theta_b = 0 \mod 2\pi \\ \vec{r}_{O_y} & \theta_a = 0 \mod 2\pi \text{ and } \theta_b = \pi \mod 2\pi . \end{cases} \quad (3.14)$$

In $Na_xCa_{2-x}CuO_2Cl_2$ the atoms primarily giving rise to atomic contrast in topography are chlorine which, again, are positioned above the copper atoms in the CuO_2 plane. As such the criteria listed in Eq. 3.14 are also used for $Na_xCa_{2-x}CuO_2Cl_2$.

3.4 Sub-lattice Segregation

Once lists of the positions of atoms lying in different sub-lattices have been constructed as detailed in Sect. 3.3, we can segregate maps according to sub-lattice specific maps. From the three lists of atomic co-ordinates $\{\vec{r}_{Cu}\}$, $\{\vec{r}_{O_x}\}$ and $\{\vec{r}_{O_y}\}$, three masking images, $S_{Cu}(\vec{r})$, $S_{O_x}(\vec{r})$ and $S_{O_y}(\vec{r})$ are created. These are discrete, having the same number of pixels as the map we wish to segregate into sub-lattices, $M(\vec{r})$.

For each of the elements in $\{\vec{r}_{Cu}\}$, the closest pixel in $S_{Cu}(\vec{r})$ is assigned the value 1 and all other pixels the value zero. The same process is carried out for $\{\vec{r}_{O_x}\}$ and S_{O_x}; $\{\vec{r}_{O_y}\}$ and S_{O_y}. To minimise the mismatch between the true atomic positions and the pixel positions, the maps can be interpolated to higher pixel density.

If we wish to select more than 1 pixel around each atom, the isolated non-zero values in $S_{Cu}(\vec{r})$, $S_{O_x}(\vec{r})$ and $S_{O_y}(\vec{r})$ can be replaced with appropriately sized square blocks of ones. Typically between 1 and 9 pixels are used per atom.

The sub-lattice segregated functions $Cu(\vec{r})$, $O_x(\vec{r})$ and $O_y(\vec{r})$ are then given by

$$Cu(\vec{r}) = S_{Cu}(\vec{r})M(\vec{r}) \quad (3.15)$$
$$O_x(\vec{r}) = S_{O_x}(\vec{r})M(\vec{r}) \quad (3.16)$$
$$O_y(\vec{r}) = S_{O_y}(\vec{r})M(\vec{r}) . \quad (3.17)$$

Figure 3.1a shows $Z(\vec{r}, |E| = 150\,\text{mV})$ for an $Na_xCa_{2-x}CuO_2Cl_2$ sample with $p \sim 12 \pm 1\%$. In Fig. 3.1b–d I show sub-lattice segregated images $Cu(\vec{r})$, $O_x(\vec{r})$ and $O_y(\vec{r})$ derived from (a).
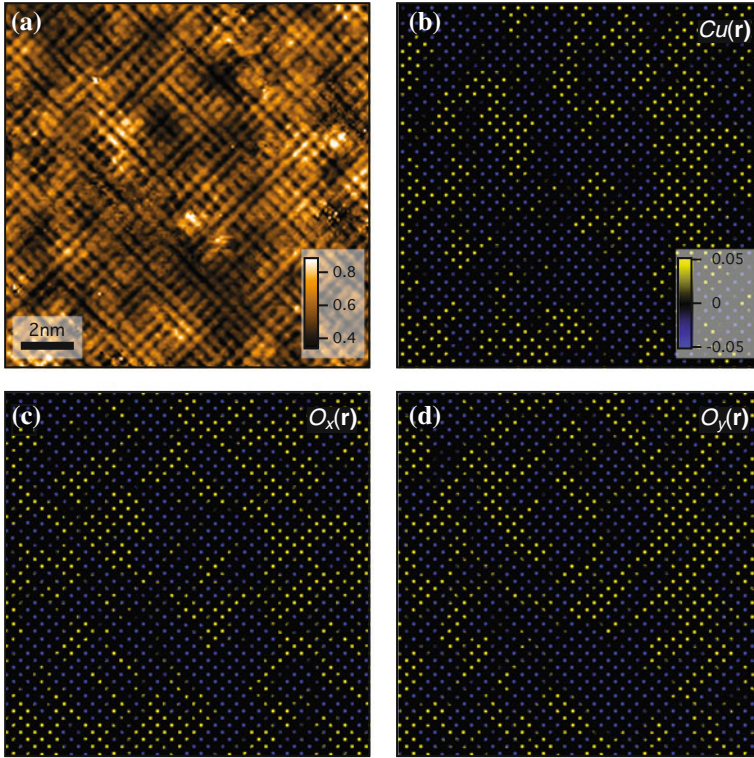
Fig. 3.1 **a** Measured $Z(\vec{r}, |E| = 150\,\text{mV})$ for an $Na_x Ca_{2-x} CuO_2 Cl_2$ sample with $p \sim 12 \pm 1\%$. **b** Copper sub-lattice segregated image, $Cu(\vec{r})$, with copper sites selected from **a**. **c** x-direction oxygen sub-lattice segregated image, $O_x(\vec{r})$, with x-oxygen sites selected from **a**. **d** y-directed oxygen sub-lattice segregated image, $O_y(\vec{r})$, with y-oxygen sites selected from **a**. The spatial mean has been subtracted from **b**–**d**

3.5   Intra-Unit-Cell Spatial Registration of Measurements

Sometimes one would like to examine how the intra-unit-cell electronic structure changes as a function of a tuning parameter, such as setup bias or magnetic field. To do this we must register data sets, measured in the same field-of-view under identical conditions apart from the change in tuning parameter, and register them to each other with picometer accuracy. Unfortunately this is not possible to implement directly in the measurement because of time-dependent variations in the response of the piezo-tube to applied voltages. However, this can be implemented at the data analysis stage.

For the two data sets to be registered, we will use their topographs, $T_1(\vec{r})$ and $T_2(\vec{r})$, to align identical atoms in one data set with those in the other. The algorithm is as follows:

Fig. 3.2 Spatially registered topographs of $Bi_2Sr_2CaCu_2O_{8+\delta}$ taken at **a** B = 8.25T and **b** B = 0T. The images show a 65 nm × 65 nm region of the sample and are registered to within 10 pm. *Insets* show magnified images of the region indicated by the *yellow squares*
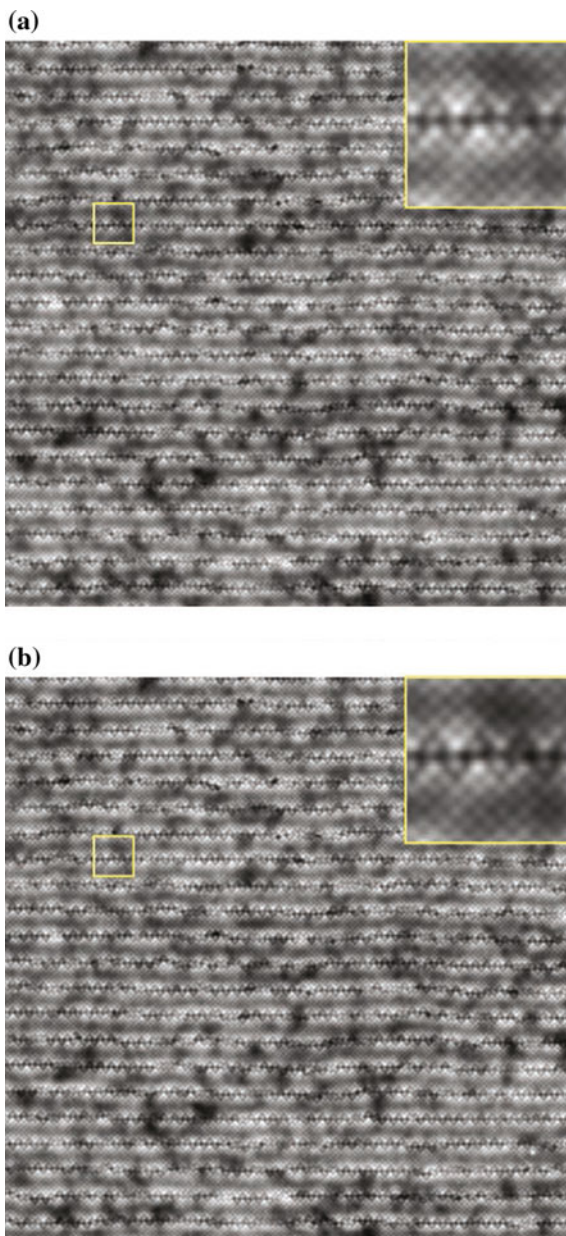
1. Apply the phase-correction algorithm detailed in Sect. 3.2 to both $T_1(\vec{r})$ and $T_2(\vec{r})$ to remove picometer distortions of the image introduced by non-ideality of the piezo-tube.
2. $T_1(\vec{r})$ and $T_2(\vec{r})$ are then roughly aligned. This corrects for any small difference in field-of-view between the measurements. It is implemented through an optimisation process where rigid spatial translations are applied to $T_2(\vec{r})$ to yield $T_2'(\vec{r})$. The parameter that is optimised is the cross-correlation of $T_2'(\vec{r})$ and $T_1(\vec{r})$.
3. For both $T_2'(\vec{r})$ and $T_1(\vec{r})$ the positions of the Cu, O_x and O_y atoms are determined. The positions of atoms 1 ... i in $T_1(\vec{r})$ form a set $\{\vec{r}_i^{\,1}\}$. The identical set of atoms in $T_2'(\vec{r})$ have positions $\{\vec{r}_i^{\,2}\}$. The positions $\{\vec{r}_i^{\,2}\}$ are used to form a mesh by Delaunay triangulation. Then, an affine transformation within each triangle of the mesh is applied to move the points $\{\vec{r}_i^{\,2}\}$ to positions $\{\vec{r}_i^{\,1}\}$, creating a topograph $T_2''(\vec{r})$.
4. After this process, the atoms in topographs $T_1(\vec{r})$ and $T_2''(\vec{r})$ are registered with an accuracy determined by the the filter size λ used in step 1, typically picometers (see Sect. 3.2).
5. All transformations applied to $T_2(\vec{r})$ and $T_2'(\vec{r})$ are then applied to the simultaneously acquired spectroscopic maps.

Two registered topographs of a $Bi_2Sr_2CaCu_2O_{8+\delta}$ surface taken with B $= 8.25$T and B $= 0$T respectively, registered with picometer accuracy, are shown in Fig. 3.2.

References

1. M.J. Lawler et al., Intra-unit-cell electronic nematicity of the high-Tc copperoxide pseudogap states. Nature **466**(7304), 347–51 (2010)
2. J.A. Slezak et al., Imaging the impact on cuprate superconductivity of varying the interatomic distances within individual crystal unit cells. Proc. Natl. Acad. Sci. U.S.A. **105**(9), 3203–8 (2008)
3. M.H. Hamidian et al., Picometer registration of zinc impurity states in Bi2Sr2 CaCu$_2$O$_8 + \delta$ for phase determination in intra-unit-cell Fourier transform STM. New J. Phys. **14**(5), 053017 (2012)

Chapter 4
Atomic-Scale Electronic Structure of the Cuprate d-Symmetry Form Factor Charge Density Wave

The results of this chapter are reported in "Direct Phase-Sensitive Identification of a d-Form Factor Density Wave in Underdoped Cuprates", *Proceedings of the National Academy of Sciences*, **111**, E3026 (2014) and "Atomic-Scale Electronic Structure of the Cuprate d-Symmetry Form Factor Density Wave State", *Nature Physics*, **12**, 150 (2016).

This chapter details the use of sub-lattice segregated spectroscopic-imaging STM to reveal the intra unit cell electronic structure of the charge density wave in the cuprate superconductors $Bi_2Sr_2CaCu_2O_{8+\delta}$ and $Na_xCa_{2-x}CuO_2Cl_2$.

In Chap. 1 I reviewed recent experimental evidence demonstrating that unconventional density wave order is a generic feature of cuprate superconductors. Many authors have predicted that the charge density wave (CDW) in cuprates should exhibit a d-symmetry form factor, characterised by the modulation of a breaking of intra unit cell rotational symmetry [1–17]. In this chapter I will demonstrate that the short-ranged CDW order in $Bi_2Sr_2CaCu_2O_{8+\delta}$ and $Na_xCa_{2-x}CuO_2Cl_2$ has a predominantly d-symmetry form factor, hitherto unobserved in nature.

While CDW order appears to be ubiquitous amongst cuprate materials, the mechanism of its formation, which lattice symmetries it breaks, and its relationship to the pseudogap and high-temperature superconductivity are unknown. Furthermore, little is understood about how the CDW is derived from or imparts itself upon the electronic structure of the CuO_2 plane. In this chapter I will utilise the development of sub-lattice segregated spectroscopic-imaging STM (SI-STM), detailed in Chap. 3, to address these questions.

4.1 Form Factor Decomposition of Modulations in the CuO_2 Plane

In this chapter I will report on the detection of a predominantly d-symmetry form factor CDW in cuprates. Such a CDW consists of an intra-unit-cell breaking of rotational symmetry that is modulated periodically in space. In cuprates, the CuO_2
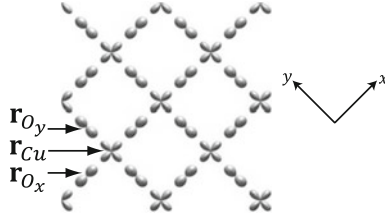
Fig. 4.1 Cu, O$_x$ and O$_y$ orbitals, on the three sub-lattices in the CuO$_2$ plane; $\vec{r}_{Cu}$ sub-lattice contains only the Cu sites, $\vec{r}_{O_x}$ sub-lattice contains only the O$_x$ sites, and $\vec{r}_{O_y}$ sub-lattice contains only the O$_y$ sites

plane has three sub-lattices (Fig. 4.1): copper sites at positions $\{\vec{r}_{Cu}\}$, x-directed oxygen sites at positions $\{\vec{r}_{O_x}\}$ and y-directed oxygen sites at positions $\{\vec{r}_{O_y}\}$.

Density waves consisting of modulations on the x-directed oxygen sites (O$_x$) that are distinct from those on the y-directed oxygen sites (O$_y$) can be challenging to conceptualise. Among the many ways of organising density waves in the CuO$_2$ plane, one is to think of them as a modulation on the copper sites (Cu), a modulation on the O$_x$ sites, and a modulation on the O$_y$ sites. The results presented in this chapter, however, present a compelling case that another organisation captures the density wave observed in a remarkably simple way. This way organises them by form factors that I will call *s*, *s'* and *d*.

The wave-vector of a CDW itself breaks rotational symmetry. This means that the form factor of a CDW does not alone determine its rotational symmetries. Consequently there is a freedom in the choice of form factor definition. Here I adopt the convention introduced by Sachdev and La Placa in Ref. [10] which is detailed in Appendix B. In the discussion below I will refer to spatial modulations of a density $\rho(\vec{r})$. This density could be any density-like observable (i.e., invariant under time-reversal and spin rotations), such as charge or local density of states.

We can think of the form factor organisation as a modulation of intra-unit-cell ($\vec{q} = 0$) electronic configurations whose point group symmetry is well defined, as shown in Fig. 4.2. The $\vec{q} = 0$ *s*-symmetry form factor has a density,

$$\rho(\vec{r}_{Cu}) = A_s, \rho(\vec{r}_{O_x}) = 0, \rho(\vec{r}_{O_y}) = 0 , \qquad (4.1)$$

the $\vec{q} = 0$ *s'*-symmetry form factor has density,

$$\rho(\vec{r}_{Cu}) = 0, \rho(\vec{r}_{O_x}) = A_{s'}, \rho(\vec{r}_{O_y}) = A_{s'} , \qquad (4.2)$$

and the $\vec{q} = 0$ *d*-symmetry form factor has density,

$$\rho(\vec{r}_{Cu}) = 0, \rho(\vec{r}_{O_x}) = A_D, \rho(\vec{r}_{O_y}) = -A_D . \qquad (4.3)$$

As these three intra-unit-cell configurations preserve lattice translational symmetry, they correspond to specific representations of the point group symmetry of the
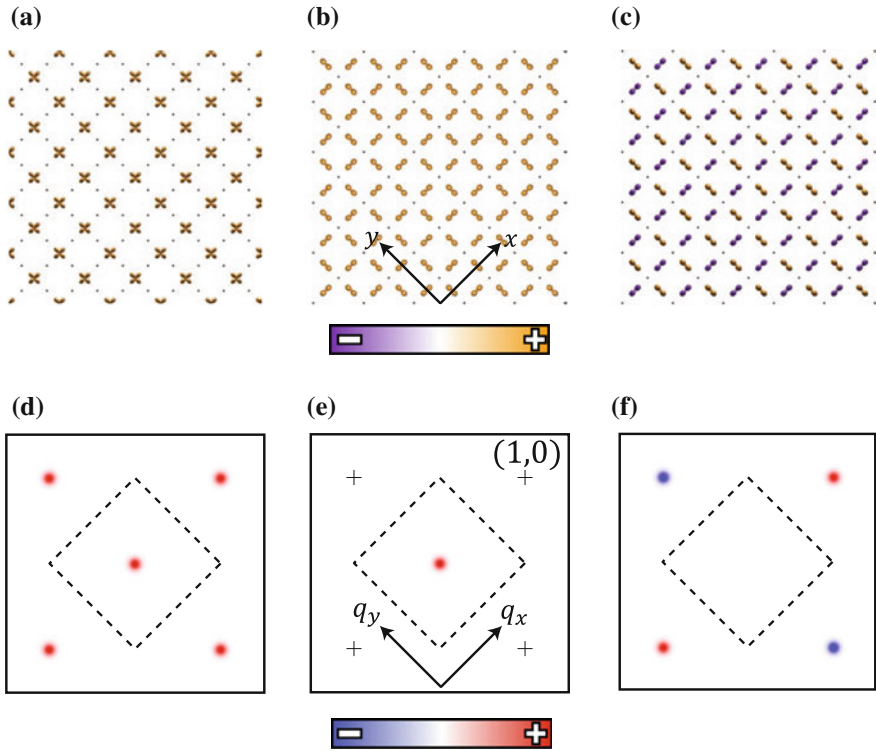
Fig. 4.2 **a** Schematic of uniform density on the Cu atoms (*s*-symmetry). The inactive O sites are now indicated by *black dots*. **b** Schematic of uniform density on the O atoms (also an *s*-symmetry referred to here as extended-*s* or *s'*-symmetry). The inactive Cu sites are indicated by *black dots*. **c** Schematic pattern with opposite-sign density on O$_x$ and O$_y$ (*d*-symmetry). The inactive Cu sites are indicated by *black dots*. **d** Real component of Fourier transform of the *s*-symmetry intra-unit-cell patterns derived only from Cu sub-lattice in **a** and with no CDW modulation. The Bragg peaks have the same sign, indicating the intra-unit-cell states have *s*-symmetry. **e** Real component of Fourier transform of the *s'*-symmetry intra-unit-cell patterns derived only from O$_x$ and O$_y$ sub-lattices in **b** and with no CDW. The only Bragg peaks within the CuO$_2$ reciprocal unit cell is at (0,0). **f** Real component of Fourier transform of the *d*-symmetry intra-unit-cell patterns derived only from O$_x$ and O$_y$ sub-lattices as shown in **c** and with no CDW modulation. The Bragg peaks now have the opposite sign, indicating the intra-unit-cell states have *d*-symmetry

lattice.[1] Phase-resolved Fourier transforms of each arrangement could reveal their point group symmetry from the relative signs of the Bragg amplitudes. The *s*- and *s'*-symmetry form factors both share 90° rotational symmetry in their Bragg-peak amplitudes, whereas the Bragg-peak amplitudes for a *d*-symmetry form factor change sign under 90° rotations as shown in Fig. 4.2. Thus, by studying the magnitude and sign of the Bragg amplitudes in phase-resolved sub-lattice segregated SI-STM images, one

---

[1]Note that *s*- and *s'*-symmetry form factors both transform as the trivial representation of the point group and thus, even at $\vec{q} = 0$, are not symmetry distinct.

can extract the degree to which any translationally invariant intra-unit-cell arrangement has an *s*, an *s'*, or a *d*-symmetry form factor.

The intra-unit-cell ($\vec{q} = 0$) nematic previously reported by phase-resolved STM measurements in underdoped cuprates, in this description, consists of an admixture of all three of these form factors [18–20]. The presence of a non-zero *d*-symmetry component is that which indicates a breaking of the point group symmetry.

Modulating these form factors at $\vec{Q} \neq 0$, we then obtain,

$$\rho_s(\vec{r}) = \begin{cases} A_s \cos(\vec{Q} \cdot \vec{r} + \phi_s), & \vec{r} = \vec{r}_{Cu} \\ 0, & \vec{r} = \vec{r}_{O_x} \\ 0, & \vec{r} = \vec{r}_{O_y} \end{cases} \tag{4.4}$$

$$\rho_{s'}(\vec{r}) = \begin{cases} 0, & \vec{r} = \vec{r}_{Cu} \\ A_{s'} \cos(\vec{Q} \cdot \vec{r} + \phi_{s'}), & \vec{r} = \vec{r}_{O_x} \\ A_{s'} \cos(\vec{Q} \cdot \vec{r} + \phi_{s'}), & \vec{r} = \vec{r}_{O_y} \end{cases} \tag{4.5}$$

$$\rho_D(\vec{r}) = \begin{cases} 0, & \vec{r} = \vec{r}_{Cu} \\ A_D \cos(\vec{Q} \cdot \vec{r} + \phi_D), & \vec{r} = \vec{r}_{O_x} \\ -A_D \cos(\vec{Q} \cdot \vec{r} + \phi_D), & \vec{r} = \vec{r}_{O_y} , \end{cases} \tag{4.6}$$

where $\phi_{S,S',D}$ are the phases of each of the CDW form factor components. If, for simplicity, we choose $\phi_S = \phi_{S'} = \phi_D = \phi(\vec{r})$ and allow for spatial disorder of the phase of the CDW we arrive at

$$\rho(\vec{r}) = \left[S(\vec{r}) + S'(\vec{r}) + D(\vec{r}) \right] \cos(\vec{Q} \cdot \vec{r} + \phi(\vec{r})) , \tag{4.7}$$

with $S(\vec{r}) = A_S$ if $\vec{r} \in \vec{r}_{Cu}$ and otherwise zero; $S'(\vec{r}) = A_{S'}$ if $\vec{r} \in \vec{r}_{O_x}$ or $\vec{r}_{O_y}$ and otherwise zero; $D(\vec{r}) = A_D$ if $\vec{r} \in \vec{r}_{O_x}$, $-A_D$ if $\vec{r} \in \vec{r}_{O_y}$ and otherwise zero.

Switching back to the individual sub-lattice picture we can see that an *s*-symmetry form factor CDW consists of a modulation of the Cu sites alone. An *s'*-symmetry form factor CDW will modulate the O_x and O_y sites with equal amplitude and in-phase. In the case of a *d*-symmetry form factor CDW, the O_x and O_y sites are modulated with equal amplitude but in anti-phase. This π phase shift between the oxygen sub-lattices is the essence of the *d*-symmetry form factor and encodes the local breaking of rotation symmetry. Cartoons of these different form factor modulations are shown Fig. 4.3a–c.

A generic CDW can actually have *S*, *S'*, and *D* all nonzero because the directionality of the modulation wave-vector $\vec{Q}$ breaks rotational symmetry itself. Therefore, to measure the form factor components of a CDW, one should consider the structure of its Fourier transform. Figure 4.3d–f show the Fourier transforms for *s*-, *s'* and *d*-symmetry form factor CDWs respectively.

For an *s*-symmetry form factor CDW with wave-vector $\vec{Q}_x$, the Fourier transform (Fig. 4.3d) will exhibit peaks at the primary wave-vectors $\pm \vec{Q}_x$, as well as Bragg-satellites $\vec{Q}' = (1, 0) \pm \vec{Q}_x$ and $\vec{Q}'' = (0, 1) \pm \vec{Q}_x$. In the absence of disorder all
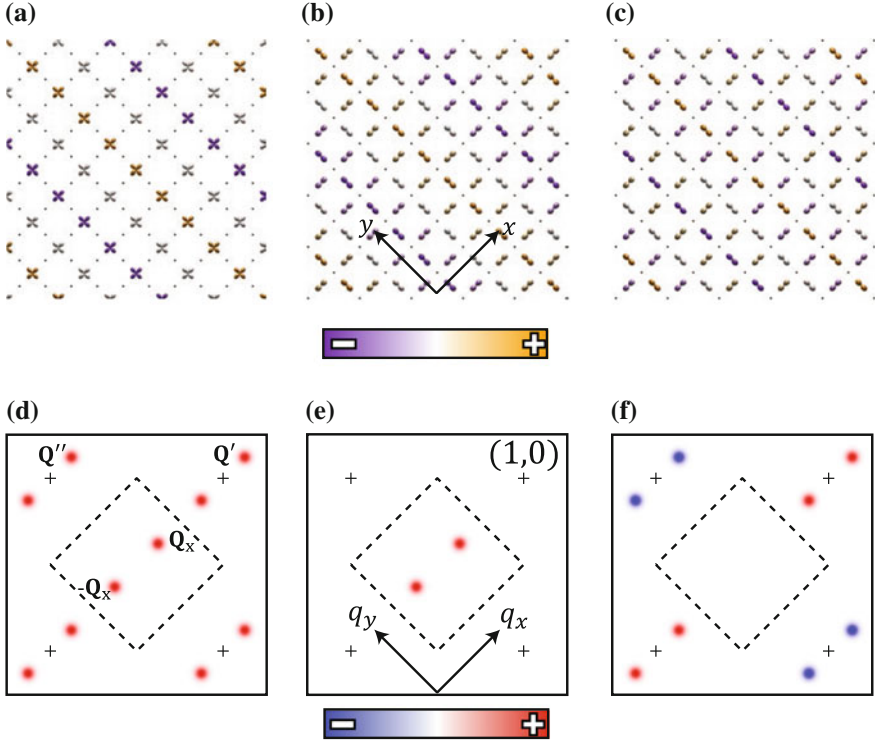
Fig. 4.3 **a** Spatial modulation with wave-vector $\vec{Q} = (Q, 0)$ of the s-symmetry intra-unit-cell patterns in Fig. 4.2a is described by $\rho_S(\vec{r}) = S(\vec{r}) \cos(\vec{Q} \cdot \vec{r})$; only Cu sites are active. The inactive O sites are indicated by *black dots*. **b** Spatial modulation with wave-vector $\vec{Q}$ of the patterns in Fig. 4.2b described by $\rho'_S(\vec{r}) = S'(\vec{r}) \cos(\vec{Q} \cdot \vec{r})$; only O$_x$ and O$_y$ sites are active but they are always equivalent within each unit cell. The inactive Cu sites are indicated by *black dots*. **c** Spatial modulation with wave-vector $\vec{Q}$ of the patterns in Fig. 4.2c described by $\rho_D(\vec{r}) = D(\vec{r}) \cos(\vec{Q} \cdot \vec{r})$; only O$_x$ and O$_y$ sites are relevant but now they are always inequivalent and indeed π out of phase. **d** $Re\tilde{\rho}_S(\vec{q})$, the real component of Fourier transform of the pattern in **a**. For this s-form factor CDW, the CDW satellites of Bragg peaks $\vec{Q}'$ and $\vec{Q}''$ exhibit the same sign. **e** $Re\tilde{\rho}_{S'}(\vec{q})$, the real component of Fourier transform of the pattern in **b**. For this s'-form factor CDW, the peaks at $\vec{Q}$ are clear but there are no Bragg-satellites at $\vec{Q}'$ and $\vec{Q}''$. **f** $Re\tilde{\rho}_D(\vec{q})$, the real component of Fourier transform of the pattern in **c**. For this d-symmetry form factor CDW, the CDW Bragg-satellite peaks at $\vec{Q}'$ and $\vec{Q}''$ exhibit opposite sign. More profoundly, because they are out of phase by π the contributions of O$_x$ and O$_y$ sites in each unit cell cancel, resulting in the disappearance of the CDW modulation peaks $\vec{Q}$ within the Brillouin zone (*dashed box*)

peaks will have the same sign. An s'-symmetry form factor CDW will also have peaks the primary wave-vector $\pm\vec{Q}_x$, but not at the Bragg-satellites (Fig. 4.3e).

A d-symmetry form factor has modulations on both oxygen sub-lattices but with a π phase shift between them. This leads to a cancellation of the peaks at the primary wave-vectors $\pm\vec{Q}_x$ within the first Brillouin zone (dashed box Fig. 4.3f). However,

there will be peaks at the Bragg satellites $\vec{Q}' = (1, 0) \pm \vec{Q}_x$ and $\vec{Q}'' = (0, 1) \pm \vec{Q}_x$ but with a sign change between them. An equivalent effect is seen for the $\vec{q} = 0$ case in Fig. 4.2f.

These distinct patterns of peaks in the Fourier transforms allow us to measure the relative proportion of each form factor component in a CDW. A strategy for doing so using sub-lattice segregated SI-STM will be discussed in Sect. 4.3, with specific emphasis on the experimental signatures of a predominantly d-symmetry form factor CDW. The next section will discuss theoretical proposals for why a cuprate CDW might possess this quality.

4.2 Proposals for a d-Symmetry Form Factor CDW in Cuprates

Many recent theories of a cuprate CDW predict that it should exhibit a predominantly d-symmetry form factor [1–17]. These theories can be assigned to one of three broad categories with regard to their physical reason for the predominance of the d-symmetry form factor.

One class of models used to consider a cuprate CDW are the spin-fermion "hot-spot" models [5–8, 12, 14, 15]. In these models a complete hole-like Fermi surface arising from an effective one-band model of the CuO_2 plane is coupled to anti-ferromagnetic spin fluctuations. The effective interaction between fermions can lead to both particle-particle and particle-hole instabilities. The former is an instability to $d_{x^2-y^2}$ superconductivity and the latter an instability towards a CDW with a predominantly d-symmetry form factor [5]. In both cases the d-wave character of the order arises from the momentum dependence of the effective interaction. The effective interaction is maximal and repulsive on-site, but attractive on nearest neighbour sites [21]. This naturally leads to d-wave like ordering.

Another potential physical reason for a predominantly d-symmetry form factor CDW in cuprates is coupling to a phonon with $d_{x^2-y^2}$ character [3, 4]. Such a scenario is supported by "kinks" in the band dispersion, as determined by ARPES, associated with coupling to a B_{1g} phonon [22] as well as the softening of phonon modes at the CDW wave-vector in $YBa_2Cu_3O_{6+x}$ [23].

The third scenario is that the predominantly d-symmetry form factor of the CDW arises as a result of the Coulomb interaction within the unit cell [9, 13, 16, 17]. The large on-site Coulomb repulsion (Hubbard U) for the Cu 3d orbitals acts to suppress charge modulations on this site, naturally favouring a modulation in the occupation of oxygen $2p_{x,y}$ orbitals instead (an s' or d-symmetry form factor). The Coulomb interaction between the x and y directed oxygen sites will then favour a predominantly d-symmetry from factor CDW. Additionally this would also minimise the net charge accumulation within the unit cell and hence reduce the long range coulomb interaction between unit cells [24].

4.3 SI-STM Signatures of a *d*-Symmetry Form Factor CDW

With the recent development of STM techniques to image intra-unit-cell electronic structure detailed in Chap. 3 [18–20, 25], it was suggested by Subir Sachdev that a practical approach to determining the form factor of underdoped cuprate CDWs would be to partition each such image of the CuO_2 electronic structure into three separate images. The first image contains only the measured values at Cu sites, $Cu(\vec{r})$, and the other two images $O_x(\vec{r})$ and $O_y(\vec{r})$ contain only the measurements at the x/y-directed oxygen sites. Once the original electronic structure image is thus separated, the phase-resolved Fourier transform of $Cu(\vec{r})$, $O_x(\vec{r})$ and $O_y(\vec{r})$ ($\tilde{Cu}(\vec{q})$, $\tilde{O}_x(\vec{q})$, $\tilde{O}_y(\vec{q})$) may, in principle, be used to reveal the form factor of a CDW.

Figure 4.4a shows a $\vec{q} = 0$ state with a *d*-symmetry form factor, a state known as an intra-unit-cell nematic. Its phase-resolved Fourier transform (Fig. 4.4b) has a sign change between Bragg peaks that are related by 90° rotations. In Fig. 4.4c this $\vec{q} = 0$ state is modulated at the wave-vector $\vec{Q} = \vec{Q}_x$ to give a *d*-symmetry form factor CDW. By considering the two trajectories parallel to $\vec{Q}_x$ marked O_x and O_y, we see that the amplitude of the wave on O_x is exactly π out of phase with that along the adjacent trajectory on O_y. For this reason, when its Fourier transform is determined in Fig. 4.4d, no peaks occur at the primary wave-vectors $\pm\vec{Q}_x$, inside the first Brillouin zone (dashed box). The second distinctive feature of the Fourier transform is that the Bragg satellite peaks at $\vec{Q}' = (1, 0) \pm \vec{Q}_x$ and $\vec{Q}'' = (0, 1) \pm \vec{Q}_x$ have opposite sign.

A *d*-symmetry form factor CDW with modulations along both x and y axes at $\vec{Q} = (Q, 0); (0, Q)$ should then exhibit two key characteristics exemplified by Fig. 4.4e whose equivalent experimental information is contained in $Re\,\tilde{O}_x(\vec{q}) + Re\,\tilde{O}_y(\vec{q})$. The first is that modulation peaks at $\pm\vec{Q}$ should disappear in $Re\,\tilde{O}_x(\vec{q}) + Re\,\tilde{O}_y(\vec{q})$ whereas the Bragg-satellite peaks at $\vec{Q}' = (1, 0) \pm \vec{Q}$ and $\vec{Q}'' = (0, 1) \pm \vec{Q}_x$ should exist with opposite sign as shown in Fig. 4.4e (the same being true for $Im\,\tilde{O}_x(\vec{q}) + Im\,\tilde{O}_y(\vec{q})$).

The second predicted characteristic is that the primary CDW peaks at $\pm\vec{Q}$ should exist clearly in $Re\,\tilde{O}_x(\vec{q}) - Re\,\tilde{O}_y(\vec{q})$ whereas their Bragg-satellite peaks at $\vec{Q}' = (1, 0) \pm \vec{Q}$ and $\vec{Q}'' = (0, 1) \pm \vec{Q}_x$ should disappear (the same being true for $Im\,\tilde{O}_x(\vec{q}) - Im\,\tilde{O}_y(\vec{q})$). This is required because, if all O_y sites are multiplied by -1, as when we take the difference $Re\,\tilde{O}_x(\vec{q}) - Re\,\tilde{O}_y(\vec{q})$, a *d*-symmetry form factor CDW is converted to an *s'*-form factor CDW. For this reason, the signature of a *d*-symmetry form factor CDW in $Re\,\tilde{O}_x(\vec{q}) - Re\,\tilde{O}_y(\vec{q})$ is that it should exhibit the characteristics of Fig. 4.4f. A calculation demonstrating that these signatures are robust, in the presence of arbitrary disorder of the CDW amplitude and phase is presented in Appendix C.
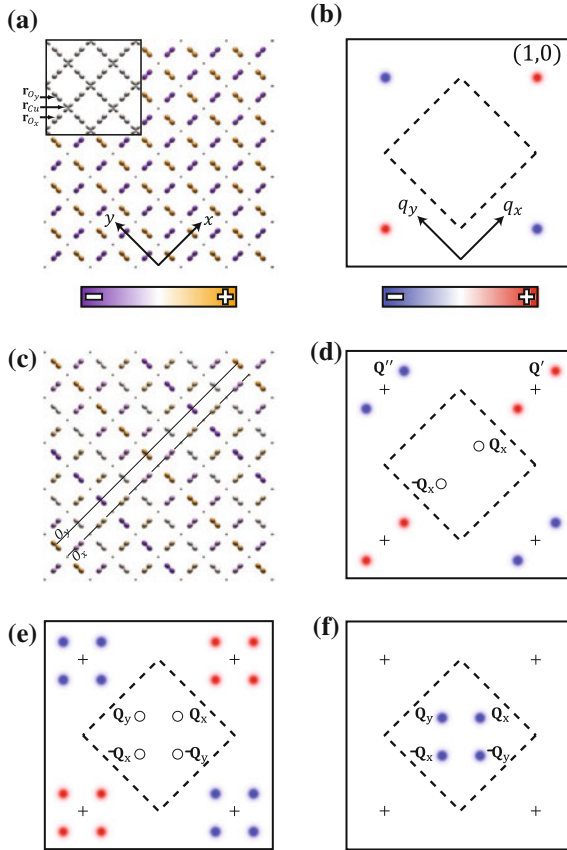
Fig. 4.4 a Schematic of translationally invariant electronic structure pattern with opposite-sign density on O_x and O_y (d symmetry). The inactive Cu sites are indicated by *gray circles*. *Inset* shows elementary Cu, O_x, and O_y orbitals, on the three sub-lattices in the CuO_2 plane. **b** Fourier transform of the $\vec{q} = 0$ C_4-breaking pattern of opposite-sign density on O_x and O_y in **a**. The Bragg peaks have the opposite sign, as a result of the intra-unit-cell states having d-symmetry. **c** Schematic of a d-symmetry form factor CDW $\rho_D(\vec{r}) = D(\vec{r}) \cos(\vec{Q}_x \cdot \vec{r})$ with the origin chosen at a Cu site and modulating only along the x-axis. The *colors* represent the density $\rho_D(\vec{r})$ at every oxygen site. *Two thin lines* are shown; one labeled O_x traverses parallel to $\vec{Q}_x$ and passes only through oxygen sites oriented along the x axis, and the second one labeled O_y again traverses parallel to $\vec{Q}_x$ but passes only through oxygen sites oriented along the y axis. The *colour scale* demonstrates how the amplitude of the CDW is exactly π out of phase along these two trajectories. **d** The real component of the Fourier transform of the pattern in **c**. For this d-symmetry form factor CDW, the Bragg-satellite peaks at $\vec{Q}'$ and $\vec{Q}''$ exhibit opposite sign. More profoundly, because they are out of phase by π, the modulations of O_x and O_y sites cancel, resulting in the disappearance of the CDW modulation peaks at $\pm\vec{Q}$ within the first Brillouin zone (*dashed box*). **e** The Fourier transform $Re\,\tilde{O}_x(\vec{q}) + Re\,\tilde{O}_y(\vec{q})$ of a $d$symmetry form factor CDW having modulations at $\vec{Q} = (Q, 0)$; $(0, Q)$; the CDW satellites at $\vec{Q}'$ and $\vec{Q}''$ exhibit opposite sign, and the primary CDW modulation peaks at $\pm\vec{Q}$ have disappeared from within the first Brillouin zone, as indicated by *open circles*. **f** The Fourier transform $Re\,\tilde{O}_x(\vec{q}) - Re\,\tilde{O}_y(\vec{q})$ of a $d$symmetry form factor CDW having modulations at $\vec{Q} = (Q, 0)$; $(0, Q)$; the CDW satellites of inequivalent Bragg peaks at $\vec{Q}'$ and $\vec{Q}''$ now cancel whereas the primary CDW modulation peaks at $\pm\vec{Q}$ are robust within the first Brillouin zone

4.4   Detection of a *d*-Symmetry Form Factor CDW in Cuprates

In this section I will present sub-lattice segregated, phase-resolved SI-STM data on the short-ranged incommensurate CDW in $Bi_2Sr_2CaCu_2O_{8+\delta}$ and $Na_xCa_{2-x}CuO_2Cl_2$ [25–27]. These data provide a direct determination of the CDW form factor, allowing the hypothesis that these CDWs exhibit a predominantly *d*-symmetry form factor to be tested.

Throughout this section I will refer to the non-dispersing modulations at wave-vectors $\vec{Q}_x \approx (0.25, 0)2\pi/a_0$ and $\vec{Q}_y \approx (0, 0.25)2\pi/a_0$ observed in SI-STM spectroscopic maps as a CDW. This is justified because, despite STM not directly measuring local charge density, the quantities measured by STM are scalar, phase invariant and time-reversal invariant quantities. This does not in itself mean that the state is not best described microscopically by another order such as a spin density wave or pair density wave but, as described in Sect. 6.3, these orders will generally induce attendant CDW components. The only modulations that may manifest in the local density of states are those of the symmetry allowed CDW components. In this sense, the assignment of non-dispersive modulations in SI-STM spectroscopic maps to CDW modulations is rigorously justified.

I will begin by analysing the energy integrated function $R(\vec{r}, E) = I(\vec{r}, +|E|)/I(\vec{r}, -|E|)$ which, as detailed in Sect. 2.4.2, naturally includes greater contributions from the non-dispersing modulations expected of a CDW. It also removes the setup-effect artifact discussed in Chap. 2. In Sect. 4.5 I will go on to discuss how the CDW imparts itself on the energy-resolved tunnelling spectra using the functions $g(\vec{r}, E)$ and $Z(\vec{r}, E) = g(\vec{r}, +|E|)/g(\vec{r}, -|E|)$.

4.4.1   Form Factor Measurement Using Sub-Lattice Segregated SI-STM

As detailed in Chap. 2, to study non-trivial intra-unit-cell structure it is highly advantageous to collect data with many pixels within each unit cell, whilst maintaining a large field-of-view (FOV). This allows for effective discrimination of distinct atomic sites in the lattice. Data acquired under these circumstances are displayed in Fig. 4.5a which shows the measured $R(\vec{r}, |E| = 150\,\text{meV})$ for a $Bi_2Sr_2CaCu_2O_{8+\delta}$ sample with hole concentration $p \sim 8 \pm 1\%$. This field-of-view (FOV) contains $\sim$15,000 each of individually resolved Cu, O_x, and O_y sites. Figure 4.5b shows a magnified part of this $R(\vec{r})$ with Cu sites indicated by blue dots.

Figure 4.5c is the simultaneous topographic image from which the positions of the Cu, O_x, and O_y atoms are determined. The atomic contrast in this topograph comes primarily from the Bi atoms of the BiO surface layer. These atoms sit directly above the Cu sites in the CuO plane and indicate their positions [20]. Oxygen sites are assumed to lie equidistant between Cu sites. The detailed algorithm for determining atomic positions is discussed in Chap. 3.

Fig. 4.5 **a** Measured $R(\vec{r})$ with ~16 pixels within each CuO_2 unit cell and ~45 nm square FOV for a $Bi_2Sr_2CaCu_2O_{8+\delta}$ sample with $p = 8 \pm 1\%$. This $R(\vec{r})$ electronic structure image reveals extensive local intra-unit-cell C_4 symmetry breaking [18, 28, 29]. **b** Smaller section of $R(\vec{r})$ in FOV of **a**, now showing the location of the Cu lattice as *blue dots*. The well-known breaking of C_4 rotational symmetry within virtually every CuO_2 unit cell and the modulations thereof are obvious. **c** Topographic image of FOV in **b** showing Cu lattice sites as identified from the Bi atom locations as *blue dots*. By using the Lawler–Fujita algorithm [18, 20] spatial-phase accuracy for the CuO_2 plane of ~0.01π is achieved throughout. **d** In the same FOV as **b**, we measure the value of R at every O_x site and show the resulting function $O_x(\vec{r})$. **e** In the same FOV as **b**, we measure the value of R at every O_y site and show the resulting function $O_y(\vec{r})$
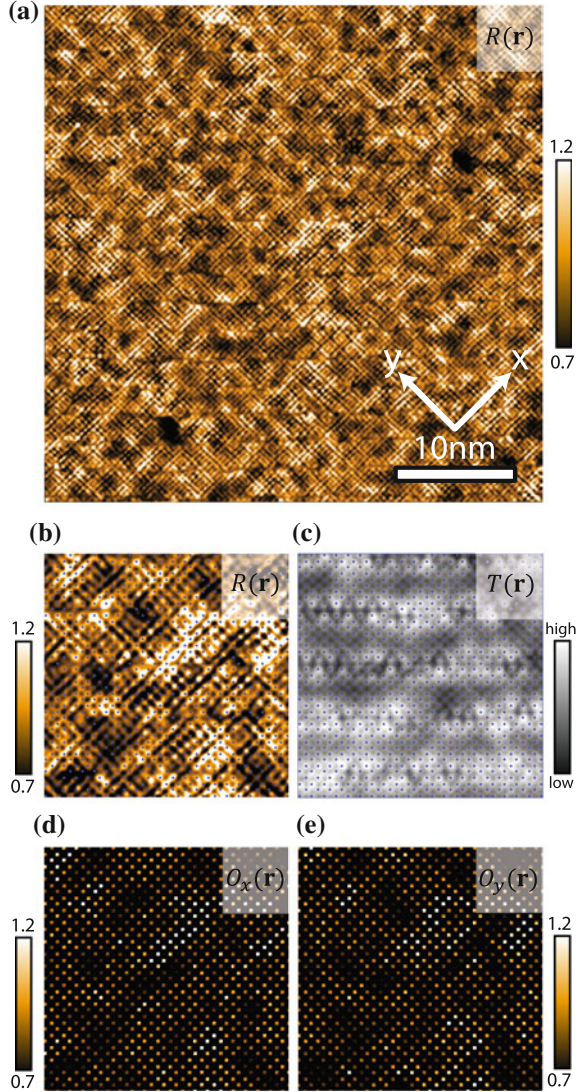
Figure 4.5d, e show the segregation of measured $R(\vec{r})$ into two oxygen sub-lattice images $O_x(\vec{r})$ and $O_y(\vec{r})$ determined from Fig. 4.5b. Larger FOV Cu, O_x and O_y sub-lattice segregated images, derived from Fig. 4.5a, are shown in Fig. 4.6.

Now consider the complex Fourier transforms of $O_x(\vec{r})$ and $O_y(\vec{r})$, $\tilde{O}_x(\vec{q})$ and $\tilde{O}_y(\vec{q})$, as shown in Fig. 4.7a, b. I show only the real part here but both real and imaginary parts are shown in Appendix D. Each of these exhibit broad peaks at wave-vectors $\vec{Q}_{x,y}$ within the first Brillouin zone. They also exhibit Bragg-satellite peaks at wave-vectors $\vec{Q}' = (1,0)2\pi/a_0 \pm \vec{Q}_{x,y}$ and $\vec{Q}'' = (0,1)2\pi/a_0 \pm \vec{Q}_{x,y}$. In
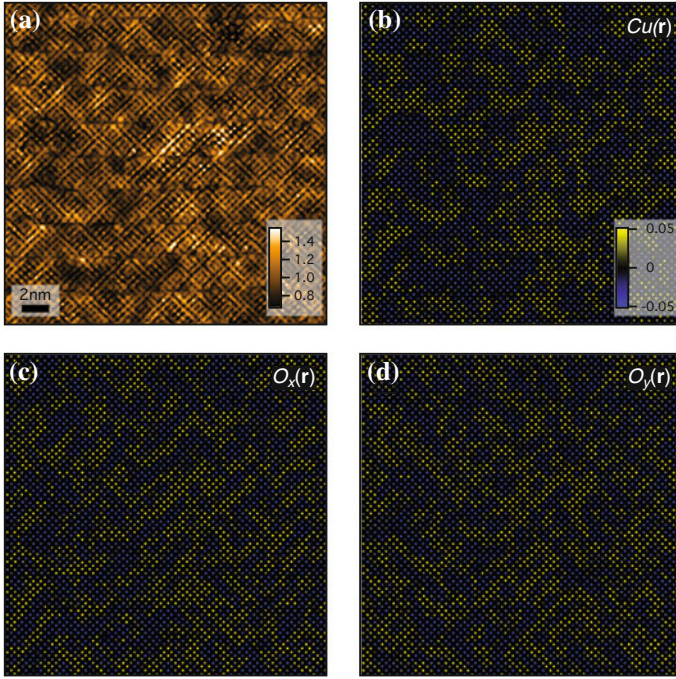
Fig. 4.6 **a** Measured $R(\vec{r})$ for $Bi_2Sr_2CaCu_2O_{8+\delta}$ sample with $p \sim 8 \pm 1\%$. These data are a subset of Fig. 4.5a. **b** Copper site segregated image, $Cu(\vec{r})$, with copper sites selected from **a**. **c** x-directed oxygen sub-lattice segregated image, $O_x(\vec{r})$, with x-oxygen sites selected from **a**. **d** y-directed oxygen-site segregated image, $O_y(\vec{r})$, with y-oxygen sites selected from **a**. The spatial mean has been subtracted from **b**–**d**

Sect. 4.3 we concluded that to search for a CDW with a predominantly *d*-symmetry form factor we should look at the combinations of these sub-lattice Fourier transforms $\tilde{O}_x(\vec{q}) \pm \tilde{O}_y(\vec{q})$. Upon calculating the sum $Re\,\tilde{O}_x(\vec{q}) + Re\,\tilde{O}_y(\vec{q})$ as shown in Fig. 4.7c, we find no CDW modulation peaks in the vicinity of $\vec{Q}_{x,y}$. This is exactly as expected for a CDW with a *d*-symmetry form factor and results from the π phase shift between the modulation on x and y directed oxygen sub-lattices.

The peaks at $\vec{Q}_{x,y}$ inside the first Brillouin zone that are weak in Fig. 4.7a, b and absent in Fig. 4.7c are clearly visible in $Re\,\tilde{O}_x(\vec{q}) - Re\,\tilde{O}_y(\vec{q})$ as shown in Fig. 4.7d. Hence the absence of this feature in $Re\,\tilde{O}_x(\vec{q}) + Re\,\tilde{O}_y(\vec{q})$ cannot be ascribed to broadness of the features surrounding $\vec{q} = 0$; rather, it is due to a high-fidelity phase cancellation between the modulations on O_x and O_y occurring with $\vec{q} \sim \vec{Q}_{x,y}$.

Finally, the Bragg-satellite peaks at $\vec{Q}'$ and $\vec{Q}''$ that were clear in $Re\,\tilde{O}_x(\vec{q}) + Re\,\tilde{O}_y(\vec{q})$ are absent in $Re\,\tilde{O}_x(\vec{q}) - Re\,\tilde{O}_y(\vec{q})$. Comparison of these observations with predictions for a *d*-symmetry form factor CDW in Fig. 4.4 demonstrates that the modulations at $\vec{Q}_{x,y}$ maintain a phase difference of approximately π between O_x and O_y within each unit cell and therefore constitute a CDW with a predominantly *d*-symmetry form factor.
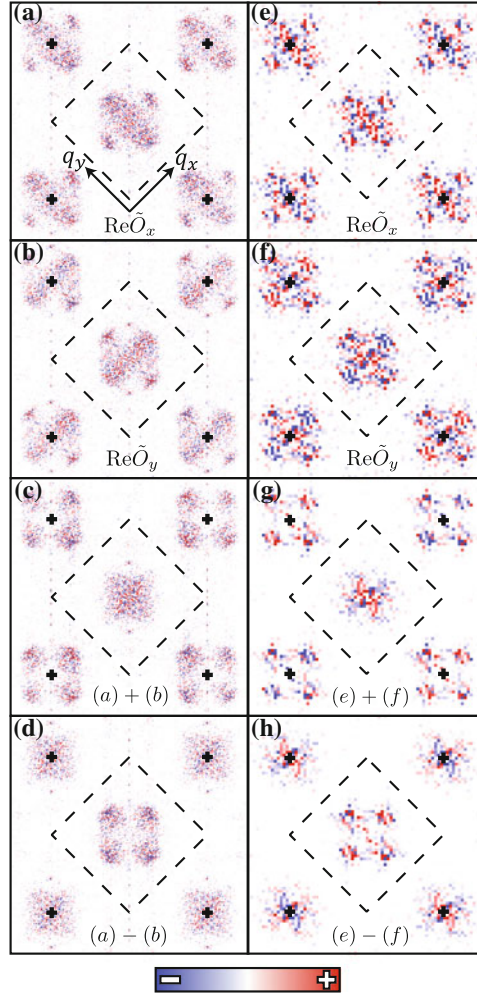
Fig. 4.7 **a** Measured $Re\tilde{O}_x$ from $R(\vec{r})$ in Fig. 4.5a. It shows four CDW peaks at $\vec{Q}_{x,y}$ and 16 CDW Bragg-satellite peaks. **b** $Re\tilde{O}_x$ from $R(\vec{r})$ in Fig. 4.5a. Again, it shows four CDW peaks at $\vec{Q}_{x,y}$ and 16 CDW Bragg-satellite peaks. **c** Measured $Re\tilde{O}_x(\vec{q}) + Re\tilde{O}_y(\vec{q})$ from **a** and **b**. The four CDW peaks at $\vec{Q}_{x,y}$ are not detectable whereas the CDW Bragg-satellite peaks are enhanced and well resolved. Compared to Fig. 4.4, these are the expected phenomena of a d-symmetry form factor CDW. **d** Measured $Re\tilde{O}_x(\vec{q}) - Re\tilde{O}_y(\vec{q})$ from **a** and **b**. The primary CDW peaks at $\vec{Q}_{x,y}$ are strongly enhanced whereas the CDW Bragg-satellite peaks have disappeared. Compared to Fig. 4.4, these are once again the expected phenomena of a d-symmetry form factor. **e** Measured $Re\tilde{O}_x$ for an $Na_xCa_{2-x}CuO_2Cl_2$ sample with $p \sim 12 \pm 1\%$. It shows four CDW peaks at $\vec{Q}_{x,y}$ and 16 CDW Bragg-satellite peaks. **f** Measured $Re\tilde{O}_x$ for $Na_xCa_{2-x}CuO_2Cl_2$. It also shows four CDW peaks at $\vec{Q}_{x,y}$ and 16 CDW Bragg-satellite peaks. **g** Measured $Re\tilde{O}_x(\vec{q}) + Re\tilde{O}_y(\vec{q})$ from **e** and **f**. The four CDW peaks at $Q_{x,y}$ are no longer detectable whereas the CDW Bragg-satellite peaks are enhanced and well resolved. Compared to Fig. 4.4, these are the expected phenomena of a d-symmetry form factor CDW. **(h)** Measured $Re\tilde{O}_x(\vec{q}) - Re\tilde{O}_y(\vec{q})$ from **e** and **f**. The four CDW peaks at $\vec{Q}_{x,y}$ are enhanced whereas the CDW Bragg-satellite peaks have disappeared. Compared to Fig. 4.4, these confirm the conclusion that the CDW has a predominantly d-symmetry form factor

To demonstrate that these phenomena are not a specific property of a given crystal symmetry, surface termination layer, or cuprate material family, we carry out the identical analysis on data from $Na_x Ca_{2-x} CuO_2 Cl_2$ samples with $p \sim 12 \pm 1\%$. For this compound, Fig. 4.7e, f show the measured $Re \tilde{O}_x(\vec{q})$ and $Re \tilde{O}_y(\vec{q})$. Again, the absence of CDW peaks at $\vec{Q}_{x,y}$ in Fig. 4.7g, which shows $Re \tilde{O}_x(\vec{q}) + Re \tilde{O}_y(\vec{q})$, is due to cancellation between O_x and O_y contributions, as these peaks are visible in $Re \tilde{O}_x(\vec{q}) - Re \tilde{O}_y(\vec{q})$.

$Re \tilde{O}_x(\vec{q}) - Re \tilde{O}_y(\vec{q})$ reveals again that the peaks at $\vec{Q}_{x,y}$ inside the first Brillouin zone that are invisible in Fig. 4.7g become vivid in Fig. 4.7h, whereas the Bragg-satellites disappear. One can see directly that these results are comprehensively consistent with observations in Fig. 4.7a–d, meaning that the CDW of $Na_x Ca_{2-x} CuO_2 Cl_2$ also exhibits a robust *d*-symmetry form factor. This observation rules out materials systematics as the source of the signal and therefore signifies that these *d*-symmetry form factor charge correlations are an intrinsic property of the underdoped CuO_2 plane, at least in $Bi_2 Sr_2 CaCu_2 O_{8+\delta}$ and $Na_x Ca_{2-x} CuO_2 Cl_2$.

One can quantify the magnitude of the *s*-, *s'*-, and *d*-symmetry form factor components of the observed CDW near $\vec{Q}_{x,y}$. As form factor specific measures of CDW amplitude I introduce the complex Fourier transforms

$$S(\vec{q}) = \tilde{C} u(\vec{q}) \tag{4.8}$$

$$S'(\vec{q}) = \frac{1}{2} \left[\tilde{O}_x(\vec{q}) - \tilde{O}_y(\vec{q}) \right] \tag{4.9}$$

$$D(\vec{q}) = \frac{1}{2} \left[\tilde{O}_x(\vec{q}) - \tilde{O}_y(\vec{q}) \right] , \tag{4.10}$$

where the factors of two arise because there are twice as many atomic sites included in $S'(\vec{r})$ and $D(\vec{r})$ as in $S(\vec{r})$. In Fig. 4.8a–c I show the power spectral densities $|S(\vec{q})|^2$, $|S'(\vec{q})|^2$ and $|D(\vec{q})|^2$. Note that (b) and (c) show the same pattern of peaks as Fig. 4.7c, d, indicating that the conclusions drawn from the real part of the Fourier transform hold for the full complex Fourier transform. In Fig. 4.8d, line-cuts along the dashed lines through $\vec{Q}_{x,y}$ in Fig. 4.8 show that the *d*-form factor component is by far the predominant component. No peak above the background is evident at $\vec{Q}_{x,y}$ in $|S(\vec{q})|^2$ and $|S'(\vec{q})|^2$.

This information can now be used to understand the real-space patterns observed by intra-unit-cell resolution STM [18, 28, 29]. In Fig. 4.9a I show one typical wavelength of the CDW in underdoped $Bi_2 Sr_2 CaCu_2 O_{8+\delta}$ and $Na_x Ca_{2-x} CuO_2 Cl_2$. Here the CDW modulations are almost entirely along the *x*-direction and the electronic structure retains lattice translational symmetry along *y*. I will term this a unidirectional domain.

In Fig. 4.9b I plot a simulation of one $4a_0$ wavelength of a unidirectional *d*-symmetry form factor CDW. Comparison with Fig. 4.9a is a compelling real-space confirmation that the CDW in $Bi_2 Sr_2 CaCu_2 O_{8+\delta}$ and $Na_x Ca_{2-x} CuO_2 Cl_2$ is an $\approx 4a_0$ period modulation with a predominately *d*-symmetry form factor.
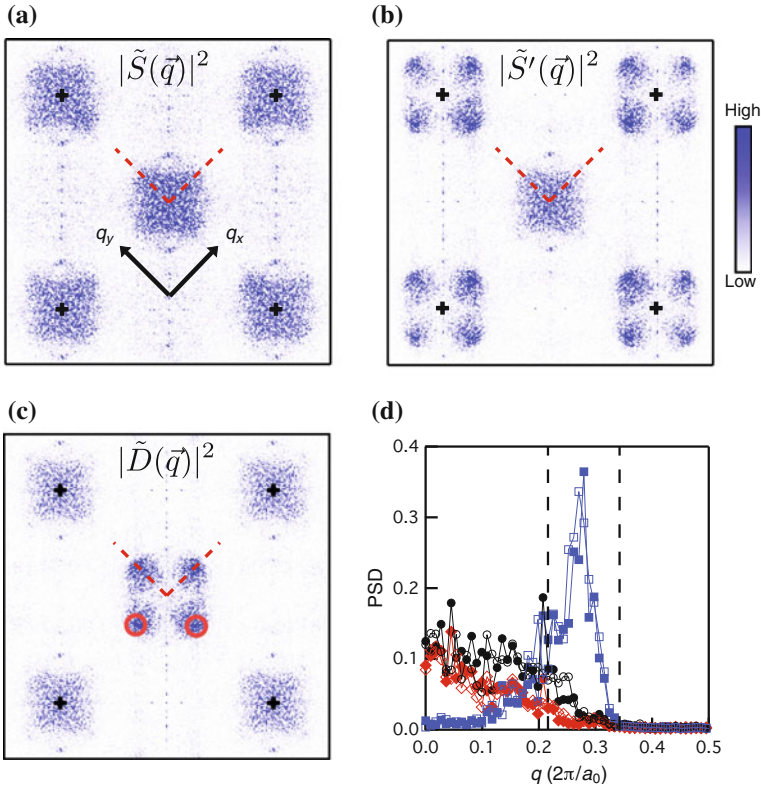
Fig. 4.8 Power spectral-density (PSD) Fourier transforms **a** $|S(\vec{q})|^2$, **b** $|S'(\vec{q})|^2$ and **c** $|D(\vec{q})|^2$. The spectral weight proximal to $\vec{Q}_{x,y}$ in these images provides a measure of the relative weight of the s-, s'-, and d-symmetry form factor contributions to the CDW respectively. **d** $|S(\vec{q})|^2$ (*black*), $|S'(\vec{q})|^2$ (*red*) and $|D(\vec{q})|^2$ (*blue*) plotted along the *dashed line* through $\vec{Q}_{x,y}$ shown in **a**–**c**. The d-symmetry form factor is clearly predominant

Recent advances in resonant x-ray scattering methods have allowed access to similar information in the bulk [26]. A special geometry where the sample is rotated by an angle α about an axis parallel to the CDW ordering wave-vector $\vec{Q}$ is used. Through analysis of the scattering intensity for scans in momentum space through $\vec{Q}$ as a function of α and of incident photon polarisation these studies concluded that the charge order in $YBa_2Cu_3O_{6+x}$ has a predominantly d-symmetry form factor [30].

Resonant x-ray scattering is primarily sensitive to modulations in the valence electronic states [26]. In contrast, conventional (non-resonant) x-ray diffraction experiments are sensitive to modulations in the total electronic charge, typically dominated by the concomitant displacement of atomic positions and core electrons. By studying the CDW hard x-ray diffraction peaks in many Brillouin zones for $YBa_2Cu_3O_{6+x}$, Forgan *et al.* found the three-dimensional pattern of atomic displacements associated with the CDW. These results are consistent with a predominantly d-symmetry form factor [31].
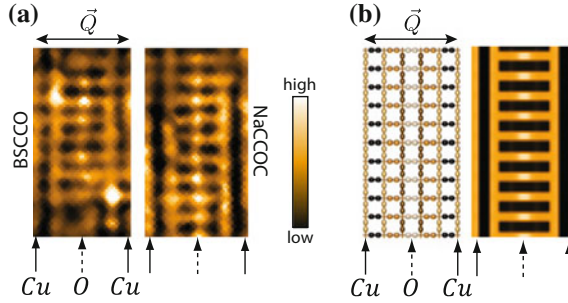
Fig. 4.9 **a** Measured $R(\vec{r})$ images of local unidirectional CDW patterns that commonly occur in $Bi_2Sr_2CaCu_2O_{8+\delta}$ and $Na_xCa_{2-x}CuO_2Cl_2$ [18, 28, 29]. The Cu and O_x sites (labeled by *solid* and *dashed arrows*, respectively) were determined independently and directly from topographic images. **b** (*Left*) *d*-symmetry form factor CDW model with $\vec{Q} = (0.25, 0)2\pi/a_0$ and amplitude maximum on the central O_x site (*dashed arrow*). (*Right*) The calculated density-wave pattern from this model. Therefore, a *d*-symmetry form factor CDW model with this particular spatial phase provides an excellent explanation for the patterns observed in **a** and reported previously in [18, 28, 29]

As a counterpoint this, resonant x-ray scattering studies of $La_{2-x}Ba_xCuO_{4+\delta}$ have revealed that the charge order has a predominantly *s'*-symmetry form factor [32]. This is just one of the many differences between charge order in La_2CuO_4 based cuprates and the other cuprate materials explored in this chapter.

It is perhaps not surprising that the predominance of one specific form factor of the CDW is not universal across cuprate materials. After all, these form factors do not uniquely determine the point group symmetry of the CDW. Hence, long-range ordered versions of the CDW present in different materials would not constitute different states of matter (based on the set of symmetries they break). However, differences in predominant form factor between materials may give some insight into the microscopic mechanism of charge ordering in these materials.

The high-temperature superconductivity and the CDW form factor share a $d_{x^2-y^2}$ symmetry in $Bi_2Sr_2CaCu_2O_{8+\delta}$, $Na_xCa_{2-x}CuO_2Cl_2$ and $YBa_2Cu_3O_{6+x}$. Does this observation have any significance? For a certain class of cuprate CDW theories; yes. In spin-fermion "hot-spot" models, CDW and *d*-wave superconductivity are formed by the exchange of (π, π) spin-fluctuations between the eight "hot-spots" where the Fermi surface intersects the anti-ferromagnetic zone boundary [33]. In this situation, there is a deep connection between the symmetry of the superconductivity and the form factor of the CDW because they arise from the same fermions and the same interactions. However, the applicability of these models to real cuprate materials has been questioned [24].

In a less model specific way, *d*-wave superconductivity and short-ranged *d*-symmetry form factor CDW are, in a sense, natural partners. The form factor for scattering of Bogoliubov quasi-particles from a puddle of *d*-symmetry form factor CDW is vanishing at the *d*-wave nodes, thus protecting the coherence of nodal

quasi-particles in what have been termed "cold-spots" [34]. It is tempting to draw a connection between the s'-symmetry form factor (for which no such protection exists) and the extremely small T_c in the stripe phase of in $La_{2-x}Ba_xCuO_{4+\delta}$.

Combining these x-ray studies with our STM results we can conclude that the charge order in $Bi_2Sr_2CaCu_2O_{8+\delta}$, $Na_xCa_{2-x}CuO_2Cl_2$ and $YBa_2Cu_3O_{6+x}$ all have a predominantly d-symmetry form factor. This discovery is in accord with many theoretical treatments of charge order in the CuO_2 plane [1–17]. However, this does not in itself allow us to discriminate between different mechanism of CDW formation. For this we will require additional information. To this end, the following sections will investigate the temperature dependence of the CDW, whether it is unidirectional (stripe-like) or bi-directional (chequerboard-like) and how the CDW manifests itself in the energy resolved tunnelling spectrum.

4.4.2 Temperature Dependence of the CDW Phenomena

So far all data shown were taken deep in the superconducting state ($T \ll T_c$). However, x-ray scattering studies show that the CDW correlations onset at a temperature $T_{CDW} > T_c$ [26]. I will now compare and contrast sub-lattice segregated SI-STM data taken with $T < T_{CDW}$ but for $T < T_c$ and $T > T_c$. Figure 4.10a shows a typical $Z(\vec{r}, 150\,meV)$ image of $Bi_2Sr_2CaCu_2O_{8+x}$ with $p = 8\%$ for $T < T_c$ in the superconducting phase. Figure 4.10b shows the equivalent $Z(\vec{r}, 150\,meV)$ for $T > T_c$ in the cuprate pseudogap phase for a sample of the same doping. Both visually in real-space and through their Fourier transforms $|\tilde{D}(\vec{q})|^2$, no pronounced differences in phenomenology are observed between the two.

The clear peaks at $\vec{Q}_{x,y}$ in $|\tilde{D}(\vec{q})|^2$ (Fig. 4.10c, d) with approximately the same line-width indicate a predominantly d-symmetry form factor CDW with approximately the same correlation length above and below T_c. Figure 4.10 shows some evidence for an enhanced s' component of the CDW above T_c, but this has not been systematically studied.

These observations show that the CDW detected in $Bi_2Sr_2CaCu_2O_{8+\delta}$ for $T \ll T_c$ persists to temperatures above T_c (but below T_{CDW}) with little change in phenomenology. That these conductance modulations (specifically those at $|E| \approx \Delta_1$) are essentially unchanged between $T < T_c$ and $T > T_c$ is significant for their interpretation. It implies that these modulations are not the spectroscopic signature of a modulation in charge caused by the co-existence of the d-wave superconductivity with a pair density wave with wave-vector $\vec{Q}_{x,y}$. As will be explained in detail in Sect. 6.6, this scenario would entail a disappearance of the conductance modulations above T_c which is clearly not observed in experiment.
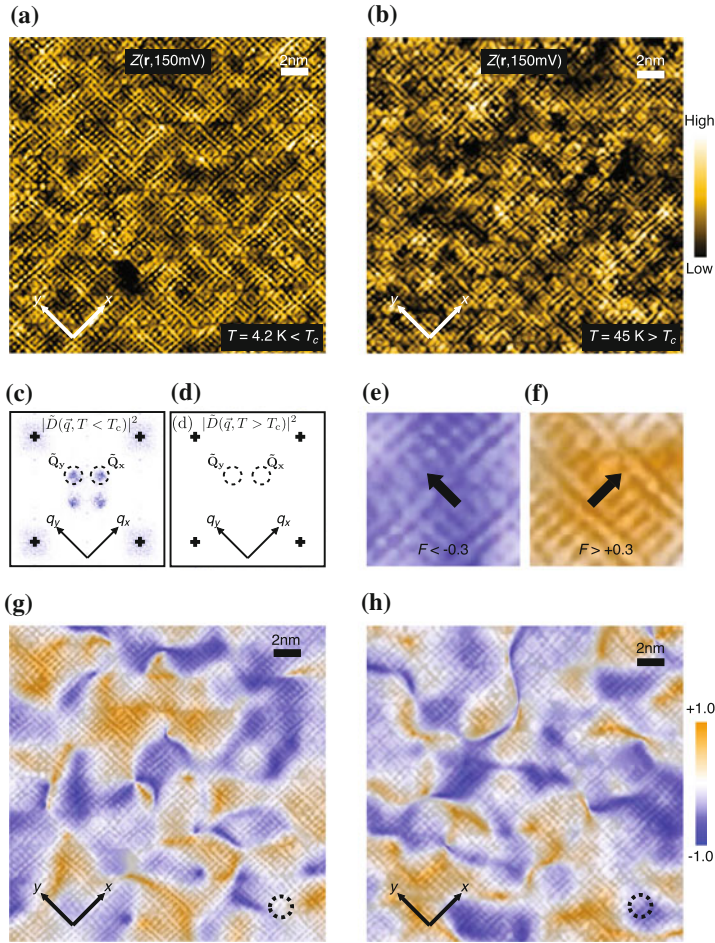
Fig. 4.10 a Measured $Z(\vec{r}, 150\,\text{meV})$ at $T < T_c$ in the superconducting phase of $p \sim 8\%$ hole-doped $Bi_2Sr_2CaCu_2O_{8+\delta}$ ($T = 4.2\,\text{K}$). **b** Measured $Z(\vec{r}, 150\,\text{meV})$ at $T > T_c$ in the pseudogap phase of $p \sim 8\%$ hole-doped $Bi_2Sr_2CaCu_2O_{8+\delta}$ ($T \sim 45\,\text{K}$). The CDW phenomena are essentially indistinguishable from observations at $T < T_c$. **c** The *d*-symmetry form factor power spectral density $|D^Z(\vec{q}, |E|)|^2 = |(\tilde{O}_x^Z(\vec{q}, |E|) - \tilde{O}_y^Z(\vec{q}, |E|))/2|^2$ determined from sub-lattice segregated analysis of data in **a**. **d** $|D^Z(\vec{q}, |E|)|^2$ determined from sub-lattice segregated analysis of data in **b**. The $\vec{q}$-space structure of the CDW phenomenology is identical in the pseudogap phase and in the superconducting phase (apart from a slightly larger *s'*-symmetry form factor component). **e, f** Using only the regions within the *dashed circles* in **c** and **d** the $\vec{r}$-space amplitudes of the CDW in **a** and **b** are calculated for modulations along $\vec{Q}_x$ and $\vec{Q}_y$. Then using $F(\vec{r}) = (|D_x(\vec{r})| - |D_y(\vec{r})|)/(|D_x(\vec{r})| + |D_y(\vec{r})|)$ regions primarily modulating along y-axis with $-1.0 < F(\vec{r}) < -0.3$ are *shaded blue*. Regions primarily modulating along x-axis with $+0.3 < F(\vec{r}) < +1.0$ are *shaded orange*. **g** Configuration of unidirectional *d*-symmerty form factor CDW modulations contained in **a** at $T < T_c$. The unidirectionality *colour scale* for $F(\vec{r})$ demonstrated in **e** and **f** is overlaid on the data in **a**. The *dashed circle* shows the $\vec{r}$-space radius equivalent to the $\vec{q}$-space filter used to generate the $D_{x,y}(\vec{r})$ images by Fourier filtering. **h** Domain configuration of unidirectional *d*-symmetry form factor CDW modulations contained in figure at $T > T_c$. The unidirectionality *colour scale* for $F(\vec{r})$ demonstrated in **e** and **f** is overlaid on the data in **b**. The dashed circle has same definition as in **g**

4.4.3 Short-Range Unidirectional CDW Domains

I will now go on to discuss how the objects shown in Fig. 4.9a are tiled in space to
fill a large field of view. Although elements indistinguishable from Fig. 4.9a can be
seen in Fig. 4.10a, b, no long-range order is obvious. In Fourier space this manifests
itself as the broad peaks in Fig. 4.10c, d. These correspond to a spatial correlation
length of $\approx 24\text{Å}(6.3a_0$ or ~ 1.6 CDW wavelengths).

To explore the spatial arrangements of the CDW I introduce the complex functions
$D_x(\vec{r})$ and $D_y(\vec{r})$, which are a spatially-resolved measure of the d-symmetry form
factor amplitude. $D(\vec{q})$ is Fourier filtered around the wave-vectors $\vec{Q}_{x,y}$ to determine
the complex-valued $D_{x,y}(\vec{r})$, as detailed in Sect. 2.8. Summarising, we take the full
complex Fourier transform $D(\vec{q})$ and Fourier filter to create two complex real-space
maps of d-symmetry Form Factor CDW amplitude at wave-vectors $\vec{Q}_{x,y}$,

$$D_x(\vec{r}) = \frac{2}{(2\pi)^2} \int d\vec{q}\, e^{i\vec{q}\cdot\vec{r}} \tilde{D}(\vec{q}) e^{-\frac{(\vec{q}-\vec{Q}_x)^2}{2\Lambda^2}} \tag{4.11}$$

$$D_y(\vec{r}) = \frac{2}{(2\pi)^2} \int d\vec{q}\, e^{i\vec{q}\cdot\vec{r}} \tilde{D}(\vec{q}) e^{-\frac{(\vec{q}-\vec{Q}_y)^2}{2\Lambda^2}} \,, \tag{4.12}$$

where Λ^{-1} is the characteristic length scale over which variations in $D_{x,y}(\vec{r})$ can
be resolved and is set by the filter width in Fourier space. The magnitudes of these
functions,

$$|D_x(\vec{r})| = \sqrt{(Re D_x(\vec{r}))^2 + Im D_x(\vec{r}))^2} \tag{4.13}$$

$$|D_y(\vec{r})| = \sqrt{(Re D_y(\vec{r}))^2 + Im D_y(\vec{r}))^2} \,, \tag{4.14}$$

represent the local amplitude of d-symmetry form factor CDW modulations along
$\vec{Q}_x$ and $\vec{Q}_y$ respectively. As such, we may visualise the local directionality of CDW
domains through

$$F(\vec{r}) = \frac{|D_x(\vec{r})| - |D_y(\vec{r})|}{|D_x(\vec{r})| + |D_y(\vec{r})|} \,. \tag{4.15}$$

Through its sign, this function will identify regions where the CDW modulation is
primarily along the x or y axis.

Figure 4.10e, f shows how regions of $-1.0 < F(\vec{r}) < -0.3$ (shaded blue) are
primarily modulating along y-axis whereas regions $+0.3 < F(\vec{r}) < +1.0$ (shaded
orange) are primarily modulating along x-axis (those with $-0.3 < F(\vec{r}) < +0.3$
shaded white appear at boundaries). Figure 4.10g, h reveal the results of this analysis
for the data in Fig. 4.10a, b respectively.

Overall, the system is configured into spatial regions within which the CDW along
only one direction is dominant. By overlaying the colour scale for $F(\vec{r})$ on the data in
Fig. 4.10a, b to create Fig. 4.10g, h, one can see directly these unidirectional domains
of short-ranged CDW.

That the CDW in $Bi_2Sr_2CaCu_2O_{8+\delta}$ is short-ranged (short correlation length) is quantitatively consistent with x-ray scattering studies [35]. Similarly short correlation lengths ($\lesssim 80\,Å$) are observed in $Bi_{2-y}Pb_ySr_{2-x}La_xCuO_{6+\delta}$, $HgBa_2CuO_{4+\delta}$ and $YBa_2Cu_3O_{6+x}$ [26, 36–38]. That the CDW is not long-ranged in these materials is not surprising. A Ginzburg–Landau analysis shows that an incommensurate CDW cannot be truly long ranged ordered in a system with quenched charge disorder, which is present in all of these materials [39]. But is disorder the factor limiting correlation lengths or are the short correlation lengths a more intrinsic property of the CuO_2 plane?

The question of whether disorder is limiting the zero magnetic field CDW correlation length in $YBa_2Cu_3O_{6+x}$ was addressed by Achkar et al. [40]. They used resonant x-ray scattering to measure oxygen-ordered $YBa_2Cu_3O_{6+x}$ samples before and after disordering the oxygens in the chain layer by heating and quench-cooling. They concluded that while the additional disorder did reduce the scattering intensity in the CDW peaks, it did not significantly alter the wave-vector or correlation length. This suggests that disorder is not the factor limiting the CDW correlation length in $YBa_2Cu_3O_{6+x}$.

That the in-plane correlation length is seen to peak and then decrease again below T_c with decreasing temperature in $YBa_2Cu_3O_{6+x}$ suggests the role of superconductivity in limiting the correlation length [41, 42]. Further weight is added to this by the observation in $YBa_2Cu_3O_{6+x}$, at B = 30 T, of a magnetic field induced CDW with a resolution limited in-plane correlation length $\xi \geq 230\,Å$ [43].

In our STM studies of both $Bi_2Sr_2CaCu_2O_{8+\delta}$ and $Na_xCa_{2-x}CuO_2Cl_2$ we find that the short-range ordered CDW takes the form of small locally unidirectional domains. These observations of coexisting nanoscale unidirectional regions are in reasonable agreement with deductions from x-ray studies of $YBa_2Cu_3O_{6+x}$ [44]. Again, the question of whether this unidirectionality is property of the quenched disorder or instead something intrinsic to the CuO_2 plane arises [45].

Interestingly the high field CDW observed in $YBa_2Cu_3O_{6+x}$ appears to be completely unidirectional [43, 46]. However, the orthorhombicity of $YBa_2Cu_3O_{6+x}$ means that this is not a true breaking of rotational symmetry because the Cu-O directions were not equivalent to begin with. One could argue, though, that the symmetry breaking field provided by the orthorhombicity is sufficiently weak that the observed unidirectionality reflects an intrinsic property of the CuO_2 plane. This is supported by theoretical work finding that unidirectional (striped) states have a lower energy than bi-directional (chequerboard) states [6, 47].

One way to determine whether this unidirectionality is truly an intrinsic property of the CuO_2 plane would be to search for a inequivalence of the magnetic field induced CDW at wave-vectors $\vec{Q}_x$ and $\vec{Q}_y$ in a material whose crystal structure has symmetry equivalent Cu-O directions. The observation of any inequivalence in the field enhanced CDW amplitude between the two Cu-O directions would be a positive identification of an intrinsic tendency toward unidirectional CDW order in the CuO_2 planes.

4.5 Characteristics of CDW Modulations in the Spectral Function

Figure 4.11 shows how a typical tunnelling conductance spectrum representative of strongly underdoped cuprates exhibits two characteristic energies. The lower energy scale Δ_0 represents the maximum energy at which Bogoliubov quasi-particle interference (QPI) modulations are observed [19, 28] while the higher energy scale Δ_1 (dashed blue line) is the cuprate pseudogap energy scale, as determined from its comparison with the doping dependence of the pseudogap in photoemission [25].

These two energy scales, Δ_0 and Δ_1, are also manifest in the set of spatial modulations observed in $Z(\vec{r}, |E|)$. For $|E| < \Delta_0$ a set of dispersive wave-vectors $\vec{q}_1$, $\vec{q}_2, \ldots \vec{q}_7$ arising from Bogoliubov QPI is observed in $Z(\vec{q}, |E|)$ [25]. For energies $|E| > \Delta_0$ these dispersive wave-vectors give way to ultra-slowly dispersing CDW modulations at $\vec{q}_1^* \approx \vec{q}_1(\Delta_0)$ and $\vec{q}_5^* \approx \vec{q}_5(\Delta_0)$, as shown in Fig. 4.12. Importantly, $\vec{q}_5^* = 2\pi/a_0 - \vec{q}_5^*$, signifying that these two wave-vectors correspond to two different form factor components of the same CDW modulation. Those at $\vec{q}_1^*$ correspond to CDW modulations with s-/s'- symmetry form factor whereas those at $\vec{q}_5^*$ have d-symmetry form factor. With increasing energy the s-/s' form factor CDW modulations quickly die off and those with d-symmetry form factor grow to a maximum at the pseudogap energy scale $|E| = \Delta_1$ [19, 28].

In the previous section I showed, through the use of $R(\vec{r})$, that CDW modulations in the tunnelling current, arising from the integrated contributions of states up to an energy $|E|$=150 meV away from the chemical potential, exhibit a predominantly d-symmetry form factor. In the following I will use the energy resolved functions $g(\vec{r}, E)$ and $Z(\vec{r}, E) = g(\vec{r}, +|E|)/g(\vec{r}, -|E|)$ to investigate which electronic states, labelled by energy and momentum, are primarily responsible for these modulations.

Fig. 4.11 The tunnelling differential conductance spectrum $g(E = eV) = dI/dV$ for a $Bi_2Sr_2CaCu_2O_{8+\delta}$ sample with $p \sim 6\%$, typical of underdoped cuprates. The energy Δ_0 beyond which Bogoliubov QPI is not observed [19, 28] and the pseudogap energy Δ_1 are indicated by *dashed red* and *blue lines* respectively
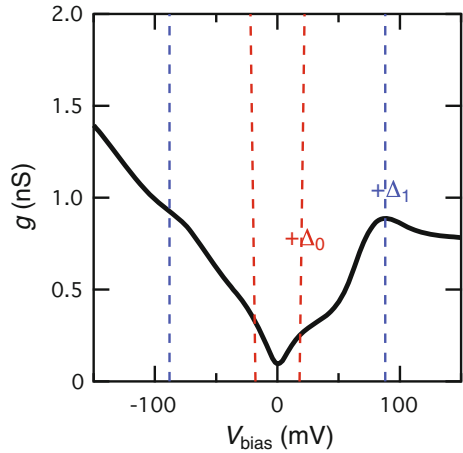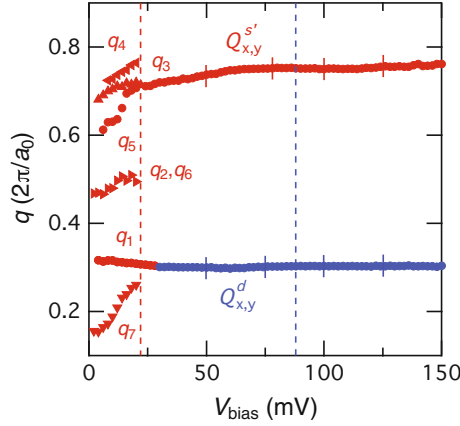
Fig. 4.12 The energy dispersion of seven dispersive modulations characteristic of Bogoliubov QPI in cuprate superconductors ($\vec{q}_1 \ldots \vec{q}_7$) are shown as *red triangles*, except for $\vec{q}_1$ and $\vec{q}_5$ which are plotted as *red circles*. These Bogoliubov QPI modulations are all simultaneously observable only below the energy Δ_0, as indicated by *dashed red line*. Here we demonstrate that they exhibit a predominantly s'-symmetry form factor, indicated by the *red colour*. At energies above Δ_0, $Z(\vec{r}, E)$ evolves quickly to consist of only non-dispersive $\vec{Q}_x$ and $\vec{Q}_y$ wave-vectors of the d-symmetry form factor CDW. We plot the dispersion of these modulations by showing the energy dependence of the maxima in $|\tilde{D}^Z(\vec{q}, E)|$ as *blue squares*, with the *blue bars* representing the full width at half maximum (FWHM) of each such peak. The same physical modulations when analysed using $|S'^Z(\vec{q}, |E|)|$ appear as the non-dispersive wave-vectors shifted by one reciprocal lattice vector shown as *red circles*, with the *red bars* representing the FHWM of each such peak

To this end I introduce the energy-resolved counterparts to Eq. 4.8 derived from $Z(\vec{r}, |E|)$,

$$S^Z(\vec{q}, |E|) = \tilde{C}u^Z(\vec{q}, |E|) \tag{4.16}$$

$$S'^Z(\vec{q}, |E|) = \frac{1}{2} \left[\tilde{O}_x^Z(\vec{q}, |E|) - \tilde{O}_y^Z(\vec{q}, |E|) \right] \tag{4.17}$$

$$D^Z(\vec{q}, |E|) = \frac{1}{2} \left[\tilde{O}_x^Z(\vec{q}, |E|) - \tilde{O}_y^Z(\vec{q}, |E|) \right] . \tag{4.18}$$

Examples of these form factor specific Fourier transforms are shown in Fig. 4.13. Peaks proximal to the wave-vectors $\vec{Q}_x$ and $\vec{Q}_y$ (circled by broken lines) signify CDW modulations with s-, s'- and d-symmetry form factors respectively. Note that d-symmetry form factor modulations appear in $S'(\vec{r}, |E|)$ and visa versa but shifted by a reciprocal lattice vector as show in Fig. 4.14.

The amplitude of each form factor component at a given energy can be quantified by summing the spectral weight inside the the red circles proximal to $\vec{Q}_{x,y}$ to yield energy-resolved form factor amplitudes $S(|E|)$, $S'(|E|)$ and $D(|E|)$. As shown in Fig. 4.15, for $|E| < \Delta_0$, where dispersive Bogoliubov QPI modulations are observed, the s- and s'-symmetry form factors are dominant ($S(|E|), S'(|E|) > D(|E|)$). For

(a)   **(b)**   **(c)**
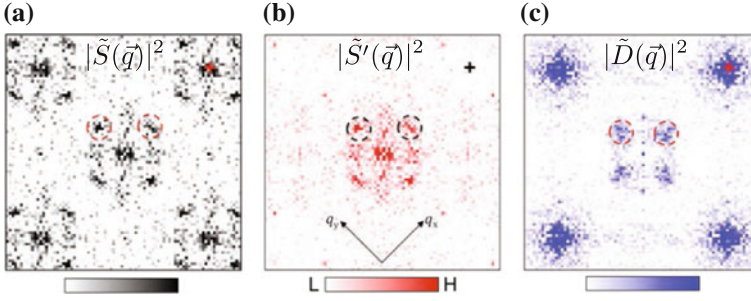
Fig. 4.13 Power spectral densities **a** $|S^Z(\vec{q}, 18\,\text{meV})|^2$, **b** $|S'^Z(\vec{q}, 18\,\text{meV})|^2$, and **c** $|D^Z(\vec{q}, 88\,\text{meV})|^2$. The amplitude of the *s*-, *s'*- and *d*-symmetry form factor components in a modulation at $\vec{Q}_{x,y}$ are calculated by integrating the weight inside the *dashed circles* for each of **a–c** respectively. The energies shown are chosen to be near where each of the form factor amplitudes are maximal. Bragg peak locations are marked by +
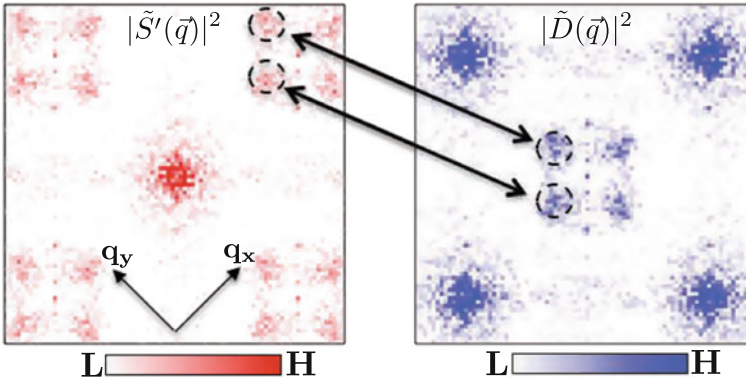
Fig. 4.14 $|S'^Z(\vec{q}, 88\,\text{meV})|$ (*left*) and $|D^Z(\vec{q}, 88\,\text{meV})|$ (*right*). The *black arrows* demonstrate that the *d*-symmetry form factor modulations at wave-vector $\vec{Q}_{x,y}$ present $|E| = \Delta_1$ in underdoped $Bi_2Sr_2CaCu_2O_{8+\delta}$ manifest themselves in both $|S'^Z(\vec{q}, 88\,\text{meV})|$ and $|D^Z(\vec{q}, 88\,\text{meV})|$ but shifted by a reciprocal lattice vector

$|E| > \Delta_0$, $S(|E|)$ and $S'(|E|)$ diminish rapidly. In contrast $D(|E|)$ grows rapidly for $|E| > \Delta_0$ to a maximum at the pseudogap energy scale $|E| = \Delta_1$. This demonstrates that the non-dispersive CDW modulations have a predominantly *d*-symmetry form factor, in accord with the analysis of the energy integrated function $R(\vec{r})$. Further, it demonstrates that the CDW results in modulations in the electronic structure which are maximal in amplitude for states with $|E| \approx \Delta_1$.

Fig. 4.15 Measured energy dependence of form factor amplitudes $S(E)$ (*black*), $S'(E)$ (*red*) and $D(E)$ (*blue*). To calculate these, $\vec{q}$ is integrated over the region inside the *solid red circles* in Fig. 4.13. These data reveal that the *d*-symmetry form factor amplitude is concentrated at energies surrounding 90 meV, which, at this hole density, is the independently measured pseudogap energy scale Δ_1
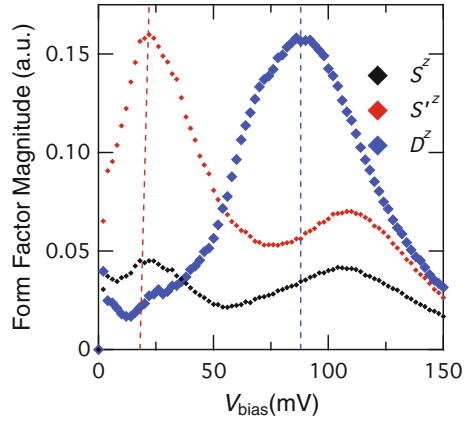
4.6 Phase Relationship Between the Modulation of Filled and Empty States

Key information on the microscopic cause of the CDW is also contained in the relationship between modulations of states above and below the Fermi energy. To explore this issue in $Bi_2Sr_2CaCu_2O_{8+x}$, I show in Fig. 4.16a, b the measured $g(\vec{r}, +94\,\text{meV})$ from filled states and $g(\vec{r}, -94\,\text{meV})$ from empty states respectively, each at the pseudogap energy scale Δ_1 for this doping ($p \sim 6\%$).

For these two images the sub-lattice Fourier transform, $\tilde{D}^g(\vec{q}, E)$, is calculated and reveals a predominantly *d*-symmetry form factor modulation with wave-vectors near $\vec{Q}_x$ and $\vec{Q}_y$. Next, we use $\tilde{D}^g(\vec{q}, E)$ to determine the complex-valued functions $D_x^g(\vec{r})$ and $D_y^g(\vec{r})$. These encode the amplitude and spatial phase of the CDW modulation along Q_x and Q_y. $D^g(\vec{q}, E)$ is Fourier filtered around the wave-vectors $\vec{Q}_{x,y}$ to determine the complex-valued $D_{x,y}^g(\vec{r})$, as detailed in Sect. 2.8. Summarising, we take the full complex Fourier transform $D^g(\vec{q})$ and Fourier filter to create two complex real-space maps of *d*-symmetry form factor CDW amplitude at wave-vectors $\vec{Q}_{x,y}$,

$$D_x(\vec{r}) = \frac{2}{(2\pi)^2} \int d\vec{q}\, e^{i\vec{q}\cdot\vec{r}} \tilde{D}(\vec{q}) e^{-\frac{(\vec{q}-\vec{Q}_x)^2}{2\Lambda^2}} \tag{4.19}$$

$$D_y(\vec{r}) = \frac{2}{(2\pi)^2} \int d\vec{q}\, e^{i\vec{q}\cdot\vec{r}} \tilde{D}(\vec{q}) e^{-\frac{(\vec{q}-\vec{Q}_y)^2}{2\Lambda^2}} \,, \tag{4.20}$$

where Λ^{-1} is the characteristic length scale over which variations in $D_{x,y}(\vec{r})$ can be resolved, and is set by the filter width in Fourier space. The phase of the CDW modulation along $\vec{Q}_y$, say, is then given by

$$\phi_y(\vec{r}, E) = \arctan(Im D_y^g(\vec{r}, E)/Re D_y^g(\vec{r}, E)) \,. \tag{4.21}$$

(a)   **(c)**   **(e)**

(b)   **(d)**   **(f)**
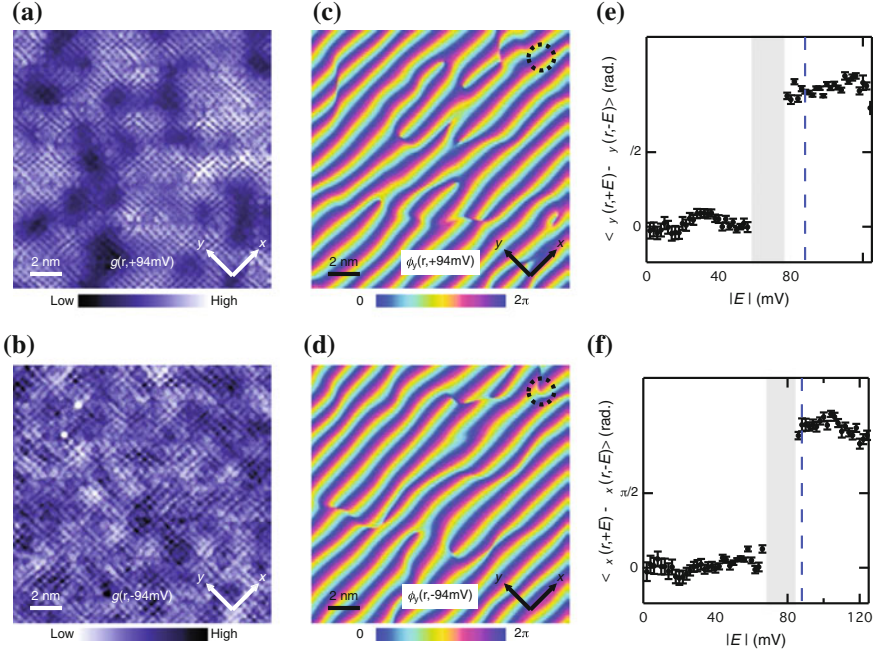
Fig. 4.16 a Differential tunnelling conductance image $g(\vec{r}, +94\,\text{meV})$. **b** Differential tunnelling conductance image $g(\vec{r}, -94\,\text{meV})$. The *colour scale* is reversed compared to **a**. **c** The spatial phase of the *d*-symmetry form factor CDW modulating along the y-direction, $\phi_y(\vec{r})$ is calculated using Eq. 4.21 from $g(\vec{r}, +94\,\text{meV})$ shown in **a**. The *dashed circle* shows the $\vec{r}$-space radius equivalent to the $\vec{q}$-space filter used to generate the $\phi_{x,y}(\vec{r}, E)$ images by Fourier filtering (see Sect. 2.8). **d** The spatial phase of the *d*-symmetry form factor CDW modulating along the y-direction $\phi_y(\vec{r})$ is calculated using Eq. 4.21 from $g(\vec{r}, -94\,\text{meV})$ shown in **b**. **e** From the field of view of **a** and **b**, we show the energy dependence of the relative phase of $g(\vec{r}, +E)$ and $g(\vec{r}, -E)$ modulations along the y-axis: $\phi_y(\vec{r}, +E) - \phi_y(\vec{r}, -E)$ when summed over every pair of identical pixel locations $\vec{r}$. **f** Similarly we show the relative phase of $g(\vec{r}, +E)$ and $g(\vec{r}, -E)$ for modulations along the x-axis: $\phi_x(\vec{r}, +E) - \phi_x(\vec{r}, -E)$. The low-energy modulations at $+E$ and $-E$ are in phase spatially and so have a relative phase difference of 0. As the pseudogap energy, Δ_1 ($\approx 90\,\text{meV}$ at this doping), is approached the relative spatial phase of empty state and filled state CDW modulations varies wildly in the narrow energy grange *shaded grey*, and then quickly develops a robust phase shift of π

This is shown for $E = +94\,\text{meV}$ in Fig. 4.16c and for $E = -94\,\text{meV}$ in Fig. 4.16d. Visual comparison reveals that these two $\phi_y(\vec{r}, \pm E)$ images are out of phase with each other by π. Indeed, the spatial-average value of $\phi_y(\vec{r}, +E) - \phi_y(\vec{r}, -E)$ as a function of E (over the whole field of view of Fig. 4.16a, b) is shown in Fig. 4.16e. It reveals that the relevant $\vec{Q}_y$ components of $g(\vec{r}, +E)$ and $g(\vec{r}, -E)$ are in phase with each other at low energy but rapidly evolve at $|E| > 70\,\text{meV}$ and become π out of phase at $|E| \sim \Delta_1$ (Fig. 4.16a, b). The shaded region indicates evolution through a situation where some areas exhibit $\phi \sim 0$ and some $\phi \sim \pi$, but this is quickly resolved on reaching the pseudogap energy Δ_1. In Appendix F I demonstrate that this cannot be an effect of the "setup-effect" artifact described in Chap. 2.

Similar analysis of the phases $\phi_x(\vec{r}, \pm E)$ of $\vec{Q}_x$ modulations yields a virtually identical result (Fig. 4.16f). These phenomena occur throughout the underdoped region of the $Bi_2Sr_2CaCu_2O_{8+\delta}$ phase diagram (see Appendix G). This demonstrates that a π phase shift between CDW modulations in the density of states above and below the chemical potential at the energy scale Δ_1 is a generic feature of the CDW in these materials.

4.7 Doping-Dependence of the CDW Wave-Vector

Figure 4.12 shows the dispersion of the scattering vectors, $\vec{q}_2, \ldots \vec{q}_7$, arising from Bogoliubov QPI for $|E| < \Delta_0$ (extracted from $|S'^Z(\vec{q}, |E|)|$) as red points. As detailed in Sect. 2.7, these scattering vectors originate from scattering between the tips of "bananas" formed by equal energy contours of the Bogoliubon dispersion. These banana tips trace out the $\vec{k}$-space path of the ungapped Fermi surface [25, 48]. As such, the octet of scattering vectors can be inverted to infer position of the underlying Fermi surface in $\vec{k}$-space.

It is known that for $Bi_2Sr_2CaCu_2O_{8+\delta}$ with $p \lesssim 0.19$ the tips of these bananas do not trace out a complete Fermi surface [19]. Rather, the QPI modulations, which extinguish at $|E| \approx \Delta_0$, trace out incomplete "Fermi-arcs". These arcs are shown for a series of hole concentrations in Fig. 4.17a.

For energies $|E| > \Delta_0$ the wave-vectors of d-symmetry form factor CDW modulations, $|\vec{Q}_{x,y}|$, (extracted from $|D^Z(\vec{q}, |E|)|$) are shown as blue points. As stated above and as expected for a CDW, the modulations are non-dispersive over a wide range of energies. Adopting the common convention in x-ray studies [35–37] for estimating the CDW wave-vector magnitude $|\vec{Q}|$, we measure $|\tilde{D}^Z(\vec{q}, |E|)|$ along lines in the high symmetry directions (1,0) and (0,1) that pass through the CDW peak and fit these data to a background plus Gaussian. The peak positions of the two Gaussians are then assigned to be the values of $\vec{Q}_x$ and $\vec{Q}_y$.

It is important to appreciate that a wide range of $\vec{Q}$ values can actually be detected under each peak in $|\tilde{D}^Z(\vec{q}, |E|)|$ and in x-ray scattering intensities. It remains to be determined whether these broad peaks with incommensurate maxima are due to domains of continuously incommensurate CDW or domains of commensurate CDW separated by discommensurations [49]. Indeed recent work in our group concludes that the latter is true [50].

In Fig. 4.17b, the doping dependence of the CDW wave-vector is shown using blue symbols. It is a decreasing function of hole concentration in agreement with x-ray studies of $Bi_2Sr_2CaCu_2O_{8+\delta}$, $Bi_{2-y}Pb_ySr_{2-x}La_xCuO_{6+\delta}$, $YBa_2Cu_3O_{6+x}$ and $HgBa_2CuO_{4+\delta}$ [26]. On the same axes I also plot the magnitude of the shortest vector joining the tips of the arcs shown in Fig. 4.17a for the same series of hole concentrations. There is reasonable quantitative agreement between these two evolutions. This trend is also reported in combined ARPES and x-ray studies linking the CDW wave-vector the vector linking the tips of the Fermi-arcs observed in the pseudo-
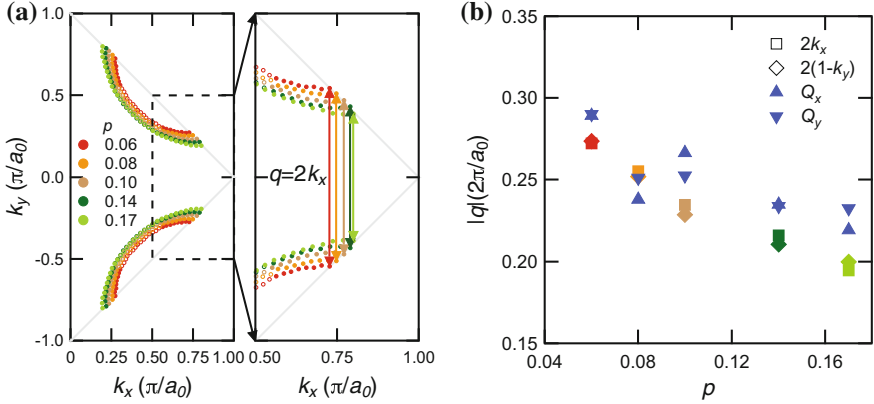
Fig. 4.17 a Measured doping dependence of $\vec{k}$-space arcs traced out by Bogoliubov QPI vector $\vec{q}_4$ indicating the position of arc like sections of the Fermi surface. The Bogoliubov QPI is observed to terminate at the anti-ferromagnetic Brillouin zone boundary (*grey line*) for $p < 0.19$ in $Bi_2Sr_2CaCu_2O_{8+\delta}$. *Coloured double headed arrows* indicate the doping dependence of the $\vec{q}$-vector linking tips of these arcs. **b** Doping dependence of the CDW $\tilde{Q}_x$ and $\tilde{Q}_y$ in underdoped $Bi_2Sr_2CaCu_2O_{8+\delta}$ as measured from the position of the peak maxima in $|\tilde{D}^Z(\vec{q}, \Delta_1)|$ is shown using *blue* symbols. The measured doping dependence of the $\vec{q}$-vector linking tips of arcs beyond which the signature of Bogoliubov QPI disappears (Fig. 4.12 and references [19, 28]) is shown by all other colours

gap regime ($T > T_c$) of $Bi_{2-y}Pb_ySr_{2-x}La_xCuO_{6+\delta}$ [37]. In contrast, in La_2CuO_4 derived cuprates the wave-vector increases with increasing hole doping, consistent with segregation into hole-rich conducting regions separated by insulating regions.

These results are curious because they are in clear agreement with many of the predictions of Fermi-surface driven CDW instability whilst being in similarly clear disagreement with others. Specifically, for a CDW of wave-vector $\vec{Q}$ formed by nesting of two sections of Fermi surface for which $\vec{k}_1 - \vec{k}_2 = \vec{Q}$ over some finite domain, a gap should open at the Fermi energy in the nested regions. The resulting wave-functions would then form bonding/anti-bonding states below/above the Fermi level which are proportional to $e^{i\vec{k}_1 \cdot \vec{r}} \pm e^{i\vec{k}_2 \cdot \vec{r}}$. The local density of states would then exhibit spatial modulations given by $|e^{i\vec{k}_1 \cdot \vec{r}} \pm e^{i\vec{k}_2 \cdot \vec{r}}|^2 = 2(1 \pm \cos(\vec{Q} \cdot \vec{r}))$. Here modulations above and below the chemical potential are π out of phase as is observed in our measurements.

However, it has been established that the doping evolution of the CDW wave-vector does not match that connecting the anti-nodal sections of the Fermi surface but rather the vector joining the tips of Fermi arcs [37]. If it were strong coupling between these eight points, or "hot-spots", that leads to CDW formation the CDW gap formed should be maximal at these points. Clearly what is observed is that this is exactly the point where the pseudogap closes [25, 51].

Nevertheless, that the CDW wave-vector in $Bi_2Sr_2CaCu_2O_{8+\delta}$, $Bi_{2-y}Pb_ySr_{2-x}La_x$ $CuO_{6+\delta}$, $YBa_2Cu_3O_{6+x}$ and $HgBa_2CuO_{4+\delta}$ evolves in the same way as a vector linking sections of the Fermi surface suggests that the Fermi surface plays some role in determining it.

4.8   Conclusions and Proposed Future Experiments

In this chapter I have shown that the short-ranged CDW present in $Bi_2Sr_2CaCu_2O_{8+\delta}$ and $Na_xCa_{2-x}CuO_2Cl_2$ has a predominantly d-symmetry form factor. While predicted for some time, this is the first CDW with a d-symmetry form factor to be observed in nature. Similar observations have also been made in $YBa_2Cu_3O_{6+x}$ by x-ray scattering, which is in contrast to the predominantly s'-symmetry form factor observed in $La_{2-x}Ba_xCuO_{4+\delta}$ [30–32].

A d-symmetry form factor arises naturally in spin-fermion "hot-spot" models of the cuprates, where it has a deep connection with the d-wave superconductivity because they arise out of the same fermions and the same effective interaction [5–8, 12, 14, 15]. A d-symmetry form factor is also a natural partner to d-wave superconductivity in the sense that it acts to protect the coherence of nodal quasi-particles against scattering from the disordered CDW in so called "cold-spots" [34].

Another possible explanation for the observed d-symmetry form factor is the Coulomb repulsion between holes on the oxygen sites of the CuO_2 plane, which acts to favour their unequal occupation within the unit cell, i.e. a d-symmetry form factor [9, 13, 16, 17]. The observation of a short ranged CDW in the electron doped cuprate $Nd_{2-x}Ce_xCuO_4$, where carriers are first doped into bands derived from the Cu $3d_{x^2-y^2}$ orbitals, provides a way to falsify this hypothesis [52]. If measurements sensitive to the CDW form factor reveal that it is predominantly d-symmetry in electron doped cuprates the hypothesis cannot be true.

I also showed in this chapter that the magnitude of the incommensurate CDW wave-vector in $Bi_2Sr_2CaCu_2O_{8+\delta}$ decreases with increasing hole concentration, as also observed by x-ray studies of $Bi_2Sr_2CaCu_2O_{8+\delta}$, $Bi_{2-y}Pb_ySr_{2-x}La_xCuO_{6+\delta}$, $HgBa_2CuO_{4+\delta}$ and $YBa_2Cu_3O_{6+x}$ but in contrast to the doping dependence in La_2CuO_4 derived cuprates which shows the opposite trend [26]. This phenomenology clearly suggests a role for the Fermi surface geometry in determining the CDW wave-vector.

This chapter demonstrates that the charge order in $Bi_2Sr_2CaCu_2O_{8+\delta}$ and Na_x $Ca_{2-x}CuO_2Cl_2$ consists of nanoscale domains of unidirectional d-symmetry form factor CDW. Recent high-magnetic field measurements in $YBa_2Cu_3O_{6+x}$ reveal a magnetic-field induced CDW that is completely unidirectional [43, 46]. This is suggestive that the CuO_2 plane has an intrinsic instability to unidirectional ordering. A cautionary caveat is that $YBa_2Cu_3O_{6+x}$ is structurally orthorhombic, and so posseses no symmetry between Cu-O directions. I propose that measurements of magnetic field

induced CDW in cuprates with a structural symmetry between the Cu-O directions be performed with the aim of directly demonstrating this unidirectional tendency of the CuO_2 plane.

References

1. J.-X. Li, C.-Q. Wu, D.-H. Lee, Checkerboard charge density wave and pseudogap of high-Tc cuprate. Phys. Rev. B **74**(18), 184515 (2006)
2. K. Seo, H.-D. Chen, J. Hu, D-wave checkerboard order in cuprates. Phys. Rev. B **76**(2), 020511 (2007)
3. D.M. Newns, C.C. Tsuei, Fluctuating CuOCu bond model of hightemperature superconductivity. Nat. Phys. **3**(3), 184–191 (2007)
4. C. Honerkamp, H.C. Fu, D.-H. Lee, Phonons and d-wave pairing in the two-dimensional Hubbard model. Phys. Rev. B **75**(1), 014503 (2007)
5. M. Metlitski, S. Sachdev, Instabilities near the onset of spin density wave order in metals. New J. Phys. **12**(10), 105007 (2010)
6. Y. Wang, A. Chubukov, Charge-density-wave order with momentum (2Q, 0) and (0, 2Q) within the spin-fermion model: continuous and discrete symmetry breaking, preemptive composite order, and relation to pseudogap in hole-doped cuprates. Phys. Rev. B **90**(3), 1–52 (2014)
7. T. Holder, W. Metzner, Incommensurate nematic fluctuations in two-dimensional metals. Phys. Rev. B **85**(16), 165130 (2012)
8. K.B. Efetov, H. Meier, C. Pépin, Pseudogap state near a quantum critical point. Nat. Phys. **9**(7), 442–446 (2013)
9. S. Bulut, W.A. Atkinson, A.P. Kampf, Spatially modulated electronic nematicity in the three-band model of cuprate superconductors. Phys. Rev. B **88**(15), 155132 (2013)
10. S. Sachdev, R. La Placa, Bond order in two-dimensional metals with antiferromagnetic exchange interactions. Phys. Rev. Lett. **111**(2), 027202 (2013)
11. J.C.S. Davis, D.-H. Lee, Concepts relating magnetic interactions, intertwined electronic orders, and strongly correlated superconductivity, in *Proceedings of the National Academy of Sciences of the United States of America* (2013), pp. 1–8
12. A. Allais, J. Bauer, S. Sachdev, Density wave instabilities in a correlated two-dimensional metal. Phys. Rev. B **90**(15), 1–5 (2014)
13. M.H. Fischer et al., Nematic and spin-charge orders driven by hole-doping a charge-transfer insulator. New J. Phys. **16** (2014)
14. C. Pépin et al., Pseudogap, charge order, and pairing density wave at the hot spots in cuprate superconductors. Phys. Rev. B **90**(19), 1–16 (2014)
15. D. Chowdhury, S. Sachdev, Density-wave instabilities of fractionalized Fermi liquids. Phys. Rev. B **90**(24), 1–10 (2014)
16. W.A. Atkinson, A.P. Kampf, S. Bulut, Charge order in the pseudogap phase of cuprate superconductors. New J. Phys. **17**(1), 13025 (2015)
17. Y. Yamakawa, H. Kontani, Spin-fluctuation-driven nematic charge-density wave in cuprate superconductors: impact of Aslamazov–Larkin vertex corrections. Phys. Rev. Lett. **114**(25), 1–6 (2015)
18. M.J. Lawler et al., Intra-unit-cell electronic nematicity of the high-Tc copperoxide pseudogap states. Nature **466**(7304), 347–351 (2010)
19. K. Fujita et al., Simultaneous transitions in cuprate momentum-space topology and electronic symmetry breaking. Science **344**(6184), 612–616 (2014)
20. M.H. Hamidian et al., Picometer registration of zinc impurity states in $Bi_2Sr_2CaCu_2O_{8+\delta}$ for phase determination in intra-unit-cell Fourier transform STM. New J. Phys. **14**(5), 053017 (2012)

21. P. Monthoux, $d_{x^2-y^2}$ pairing and spin fluctuations in the cuprate superconductors: a progress **56**(12), 1–8 (2003)
22. T.P. Devereaux et al., Anisotropic electron-phonon interaction in the cuprates. Phys. Rev. Lett. **93**(11), 1–4 (2004)
23. M. Le Tacon et al., Inelastic X-ray scattering in $YBa_2Cu_3O_{6.6}$ reveals giant phonon anomalies and elastic central peak due to charge-density-wave formation. Nat. Phys. **10**(1), 52–58 (2013)
24. V. Mishra, M.R. Norman, Strong coupling critique of spin fluctuation driven charge order in underdoped cuprates. Phys. Rev. B **92**(6), 1–4 (2015)
25. K. Fujita et al., Spectroscopic imaging scanning tunneling microscopy studies of electronic structure in the superconducting and pseudogap phases of cuprate high-Tc superconductors. J. Phys. Soc. Jpn. **81**(1), 011005 (2012)
26. R. Comin, A. Damascelli, Resonant x-ray scattering studies of charge order in cuprates (2015), pp. 1–26
27. M. Vojta, Lattice symmetry breaking in cuprate superconductors: stripes, nematics, and superconductivity. Adv. Phys. **58**(6), 699–820 (2009)
28. Y. Kohsaka et al., How Cooper pairs vanish approaching the Mott insulator in $Bi_2Sr_2CaCu_2O_{8+\delta}$. Nature **454**(7208), 1072–1078 (2008)
29. Y. Kohsaka et al., Visualization of the emergence of the pseudogap state and the evolution to superconductivity in a lightly hole-doped Mott insulator. Nat. Phys. **8**(7), 534–538 (2012)
30. R. Comin et al., Symmetry of charge order in cuprates. Nat. Mater. **14**(8), 796–800 (2015)
31. E.M. Forgan et al., The microscopic structure of charge density waves in underdoped $YBa_2Cu_3O_{6.54}$ revealed by X-ray diffraction. Nat. Commun. **6**, 10064 (2015)
32. A.J. Achkar et al., Orbital symmetry of charge-density-wave order in $La_{1.875}Ba_{0.125}CuO_4$ and $YBa_2Cu_3O_{6.67}$. Nat. Mater. **15**(6), 616–620 (2016)
33. M.A. Metlitski, S. Sachdev, Quantum phase transitions of metals in two spatial dimensions. II. Spin density wave order. Phys. Rev. B **82**(7), 075128 (2010)
34. K. Lee, S.A. Kivelson, E.-A. Kim, Cold-spots and glassy nematicity in underdoped cuprates. 014204 (2016), pp. 1–9
35. E.H. Da Silva Neto et al., Ubiquitous interplay between charge ordering and high-temperature superconductivity in cuprates. Science **393** (2013)
36. S. Blanco-Canosa et al., Momentum-dependent charge correlations in $YBa_2Cu_3O_{6+\delta}$ superconductors probed by resonant x-ray scattering: evidence for three competing phases. Phys. Rev. Lett. **110**(18), 1–5 (2013)
37. R. Comin et al., Charge order driven by Fermi-arc instability in $Bi_2Sr_{2-X}La_xCuO_{6+\delta}$. Science **343**, 390–392 (2014)
38. W. Tabis et al., Charge order and its connection with Fermi-liquid charge transport in a pristine high-Tc cuprate. Nat. Commun. **5**, 5875 (2014)
39. L. Nie, G. Tarjus, S.A. Kivelson, Quenched disorder and vestigial nematicity in the pseudogap regime of the cuprates. Proc. Natl. Acad. Sci. **111**(22), 7980–7985 (2014)
40. A.J. Achkar et al., Impact of quenched oxygen disorder on charge density wave order in $YBa_2Cu_3O_{6+x}$. Phys. Rev. Lett. **113**(10), 1–5 (2014)
41. J. Chang et al., Direct observation of competition between superconductivity and charge density wave order in $YBa_2Cu_3O_{6.67}$. Nat. Phys. **8**(12), 871–876 (2012)
42. G. Ghiringhelli et al., Long-range incommensurate charge fluctuations in $(Y, Nd)Ba_2Cu_3O_{6+x}$. Science **337**(6096), 821–825 (2012)
43. H. Jang et al., Ideal charge density wave order in the high-field state of superconducting YBCO (2016), arXiv:1607.05359
44. R. Comin et al., Broken translational and rotational symmetry via charge stripe order in underdoped $YBa_2Cu_3O_{6+y}$. Science **347**(6228), 1335–1339 (2015)
45. J. Robertson et al., Distinguishing patterns of charge order: stripes or checkerboards. Phys. Rev. B **74**(13), 134507 (2006)
46. J. Chang et al., Magnetic field controlled charge density wave coupling in underdoped $YBa_2Cu_3O_{6+x}$. Nat. Commun. **7**, 11494 (2016)

47. P. Corboz et al., Stripes in the two-dimensional t-J model with infinite projected entangled-pair states. Phys. Rev. B **84**(4), 1–5 (2011)
48. Q.-H. Wang, D.-H. Lee, Quasiparticle scattering interference in hightemperature superconductors. Phys. Rev. B **67**(2), 020511 (2003)
49. B. Burk et al., Charge-density-wave domains in 1T - TaS2 observed by satellite structure in scanning-tunneling-microscopy images. Phys. Rev. Lett. **66**(23), 3040–3043 (1991)
50. A. Mesaros et al., Commensurate 4a0 period charge density modulations throughout the $Bi_2Sr_2CaCu_2O_{8+x}$ pseudogap regime (2016)
51. A. Damascelli, Z. Hussain, Z.-X. Shen, Angle-resolved photoemission studies of the cuprate superconductors. Rev. Mod. Phys. **75**(2), 473–541 (2003)
52. E.H. da Silva Neto et al., Charge ordering in the electron-doped superconductor $Nd_{2-x}Ce_xCuO_4$. Science **347**(6219), 282–285 (2015)

Chapter 5
The Scanned Josephson Tunnelling Microscope

The main results of this chapter are reported in "Direct Detection of a Cooper-pair Density Wave in $Bi_2Sr_2CaCu_2O_{8+\delta}$", *Nature*, **532**, 343 (2016).

This chapter details the development of a scanned Josephson tunnelling microscope. Motivated by the search for a pair density wave in cuprates, we employ a high temperature d-wave superconducting STM tip operating at temperatures $<50\,mK$ [1].

Scanned Josephson tunnelling microscopy (SJTM) is a direct probe of the superconducting order parameter on the nanometer scale [2]. It utilises the tunnelling of Cooper-pairs between a superconducting STM tip and a superconducting sample to measure the Cooper-pair condensate directly. In contrast, traditional STM measures the spectrum of single-particle excitations. Prior to the development of SJTM, superconductivity could be probed on the nanometer scale only indirectly using STM (by measuring the single-particle tunnelling gap) or with atomic site sensitivity using NMR or μSR.

There are many cases where the gap in the single-particle tunnelling spectrum is not sufficient to characterise spatial variations in superconductivity. Firstly, it is known that at magnetic impurities in s-wave superconductors the superconducting order parameter, Ψ, is suppressed whereas the single-particle gap, Δ, is unperturbed [3–6]. Similarly, there is also a gap at the centre of superconducting vortices in cuprate superconductors where $\Psi \to 0$ [7]. Finally, there are pair density wave states which we would not expect to exhibit a modulation in Δ and thus cannot be unambiguously detected by STM.

In the face of these adversities a handful of groups have initiated efforts to develop SJTM as a direct probe of the superconducting order parameter [8–14]. In our group we have focussed on an implementation of SJTM using high temperature d-wave superconducting tips to search for a pair density wave in cuprate superconductors [1].

5.1   Fundamentals of SJTM Operation

The purpose of the scanned Josephson tunnelling microscope is to directly visualise spatial variations in the superconducting order parameter on the nanometer scale. To achieve this we employ a superconducting STM tip, as shown in Fig. 5.1a. In contrast to normal STM, this allows the tunnelling of Cooper pairs between the tip and a superconducting sample, otherwise known as the Josephson effect. As will be detailed in Sect. 5.3, this tunnelling of Cooper pairs leads to a peak in the tunnelling current near zero voltage bias. The magnitude of this peak current can be used as a direct measure of the superconducting order parameter.

The superconducting tip also allows superconductor-insulator-superconductor (SIS) single-particle tunnelling between the tip and sample, as discussed in Sect. 2.1.4. Thus, the same tip-sample junction can be used to measure both the superconducting order parameter and properties of the single-particle excitation spectrum in the sample, such as the superconducting gap energy or the energy of an impurity resonance.

SJTM operates like an enhanced version of the spectroscopic-imaging STM (SI-STM) that was discussed in Chap. 2. As with SI-STM, junctions between the tip and sample will be established with set-point voltage and current, V_s and I_s, on a fine two-dimensional grid of points $\{\vec{r}_i\}$. At each of these points the STM feedback loop will be turned off upon attaining the set-point current and the tip-sample separation, z_i, recorded in the topograph, $T(\vec{r})$, as $T(\vec{r}_i) = z_i$.

The bias voltage, V_B,[1] is then ramped and the current and differential conductance, $I(V_B)$ and $g(V_B) = dI/dV_B$, recorded. For each point on the surface of the sample, $I(V_B)$ and $g(V_B)$ such as those shown in Figs. 5.1b, c are recorded. Combining the measurements from all points in the field of view yields the familiar spectroscopic maps $I(\vec{r}, E = eV_B)$ and $g(\vec{r}, E = eV_B)$.

For $|V_B|, |V_s| > 1\text{mV}$, $T(\vec{r})$, $I(\vec{r}, E = eV_B)$ and $g(\vec{r}, E = eV_B)$ are entirely equivalent to those obtained using normal SI-STM, albeit with a more complicated tip density of states. This is because, in this voltage range, the current is carried almost entirely by single particles. Conversely, for $|V_B| \lesssim 10-100\,\mu\text{V}$ the current is carried predominantly by Cooper pairs. This allows us to extract another spectroscopic map, $I_c(\vec{r})$, which directly measures spatial variations in the superconducting order parameter.

In Sect. 5.3 I will show that the expected signature of Cooper pair tunnelling is a steep quasi-linear increase in current away for $V_B = 0$, reaching a maximum current I_c, before dropping sharply. Figure 5.1d shows an enlarged portion of Fig. 5.1b near $V_B = 0$ that exhibits just this phenomenology. On increasing V_B beyond the point where the current drops sharply, the current once again increases but with a much smaller gradient. Here the current is predominantly carried by single particles.

The Cooper pair tunnelling is confined to a small range of voltages around $V_B = 0$ and exhibits a much larger differential conductance than the single-particle tunnelling channel (steeper gradient near $V_B = 0$ in Fig. 5.1d). This allows us to effectively

---

[1]In this chapter the bias voltage output by the STM electronic control unit will be denoted V_B to distinguish it from the voltage dropped across the tunnelling junction V_{JJ}. See Sect. 5.3 for details.
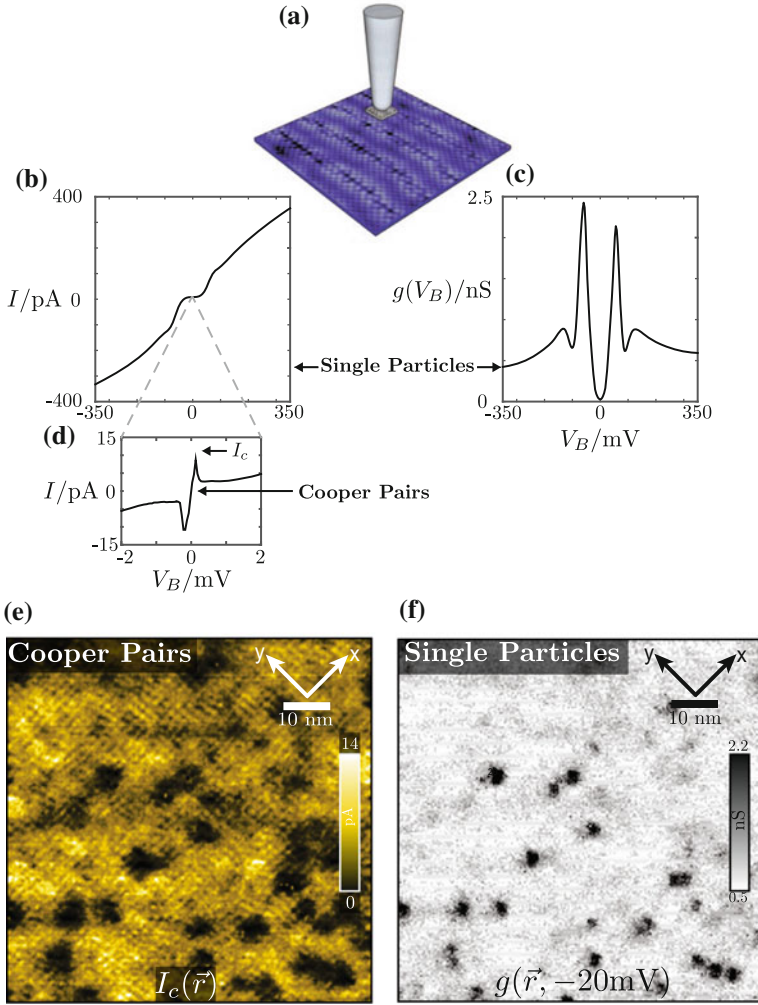
Fig. 5.1 a A high temperature d-wave scanned Josephson tunnelling microscope (SJTM). A nanometer sized piece of $Bi_2Sr_2CaCu_2O_{8+\delta}$ is attached to a tungsten STM tip to form a super-conducting STM tip. **b** A typical $I(V_B)$ characteristic for tunnelling between a $Bi_2Sr_2CaCu_2O_{8+\delta}$ sample and our $Bi_2Sr_2CaCu_2O_{8+\delta}$ nano-flake tip. For $|V_B| > 1\,mV$ the current is carried almost entirely by single-particle tunnelling. **c** $g(V_B) = dI/dV_B$ corresponding to **b**. **d** Enlargement of **b** near $V_B = 0$ showing a region with far greater conductance than the single-particle channel that terminates in a peak current I_c. In this region the current is carried predominantly by Cooper pair tunnelling. **e** $I_c(\vec{r})$ map visualising variations in the superconducting order parameter. It is derived from $I(V_B)$ curves of the type shown in **d**, measured on a fine grid of points in the field of view. **f** $g(\vec{r}, -20\,mV)$ for the same field of view as **e**, simultaneously visualising variations in the single-particle excitation spectrum

separate single-particle and Cooper pair tunnelling contributions and hence simultaneously visualise superconducting order parameter and local density of states variations using the spectroscopic maps $I_c(\vec{r})$ and $g(\vec{r}, E = eV_B)$ respectively. $I_c(\vec{r})$ and $g(\vec{r}, E = eV_B)$ measured in the same field of view are shown in Fig. 5.1e, f. This ability to simultaneously and directly visualise both the ground state condensate and its single-particle excitation spectrum lies at the heart of SJTM's utility.

Having briefly described the utility and operation of SJTM I will now discuss how the Josephson effect may be used as a probe of the superconducting order parameter and how, for our ultra-small junctions, it leads to $I(V_B)$ characteristics of the form shown in Fig. 5.1d.

5.2 The Josephson Effect as a Measure of the Superconducting Order Parameter

In Chap. 1 I described superconductivity as being defined by the phase rigidity of a charged condensate. Perhaps the most striking physical manifestation of this phase rigidity is the Josephson effect [15]. Josephson realised that if two superconductors were coupled, for instance through a tunnel junction, that this phase rigidity should extend to coupling the phases of the two superconductors. This insightful, yet controversial, assertion led to him being awarded the Nobel Prize in 1973 following the experimental confirmation of his theory [16].

To examine the consequences of coupling between superconductors let us follow a simple phenomenological treatment before returning later to a microscopic description which is closer to Josephson's original reasoning. Consider two isolated superconductors with order parameters $\Psi_1 = |\Psi_1|e^{i\theta_1}$ and $\Psi_2 = |\Psi_2|e^{i\theta_2}$. Then introduce a coupling between these superconductors and consider its first symmetry allowed term in the free energy expansion,

$$F_J = \frac{1}{2}\kappa(\Psi_1\Psi_2^* + \Psi_2\Psi_1^*) \tag{5.1}$$

$$= \kappa|\Psi_1||\Psi_2|\cos(\theta_1 - \theta_2) \tag{5.2}$$

$$= \kappa|\Psi_1||\Psi_2|\cos(\phi) , \tag{5.3}$$

where κ is a constant that characterises the strength of the coupling between the condensates.

The coupling between the superconductors depends linearly on the magnitude of each the superconducting order parameters and, crucially, on the difference in phase between them, ϕ. Thus, this coupling term represents a rigidity to changes in the relative phase of the two superconductors.

However, Eq. 5.3 is not gauge invariant. To satisfy local gauge symmetry then under a transformation of the magnetic vector potential, $\vec{A}(\vec{r}, t) \rightarrow \vec{A}(\vec{r}, t) + \nabla \chi(\vec{r}, t)$, the phase of the superconductors and the electric potential, $\Phi(\vec{r}, t)$, must undergo transformations,

$$\theta_1 \rightarrow \theta_1 - \frac{2e}{\hbar} \chi(\vec{r}_1, t) \tag{5.4}$$

$$\theta_2 \rightarrow \theta_2 - \frac{2e}{\hbar} \chi(\vec{r}_2, t) \tag{5.5}$$

$$\Phi(\vec{r}, t) \rightarrow \Phi(\vec{r}, t) - \frac{\partial \chi(\vec{r}, t)}{\partial t} . \tag{5.6}$$

Thus to make our original coupling free energy in Eq. 5.3 invariant under local gauge transformations, we should replace ϕ with a gauge invariant phase difference,

$$\gamma = \phi + \frac{2e}{\hbar} \int_1^2 \vec{A} \cdot d\vec{l} , \tag{5.7}$$

where the integral is along any line joining the two superconductors. This yields a coupling free energy,

$$F_J = \kappa |\Psi_1||\Psi_2| \cos(\gamma) , \tag{5.8}$$

which is invariant under local gauge transformations.

We can also use local gauge invariance to address the relationship between the phase difference and voltage, V_{JJ}, across the junction. In the absence of a magnetic field, the voltage across the junction is given by the difference in the electric potential, $\Delta \Phi = \Phi(\vec{r}_2) - \Phi(\vec{r}_1)$. If there is no voltage across the junction then ϕ should take the value that minimises Eq. 5.3 and there should be no time evolution of the phase. This must be true in any gauge. By reference to Eqs. 5.4–5.6 one can see that the only way of relating ϕ and $\Delta \Phi$ that enforces this is through

$$\frac{d\phi}{dt} = \frac{2e}{\hbar} \Delta \Phi , \tag{5.9}$$

which one can verify is gauge invariant.

To find a gauge invariant relationship between the phase difference and V_{JJ} we should now take the time derivative of the gauge invariant phase,

$$\frac{d\gamma}{dt} = \frac{d\phi}{dt} + \frac{2e}{\hbar} \frac{d}{dt} \int_1^2 \vec{A} \cdot d\vec{l} \tag{5.10}$$

$$= \frac{d\phi}{dt} - \frac{2e}{\hbar} \int_1^2 (\nabla \Phi + \vec{E}) \cdot d\vec{l} \tag{5.11}$$

$$= \frac{d\phi}{dt} - \frac{2e}{\hbar} \Delta \Phi - \frac{2e}{\hbar} \int_1^2 \vec{E} \cdot d\vec{l} . \tag{5.12}$$

Then substituting for $\frac{d\phi}{dt}$ using the gauge-invariant relationship in Eq. 5.9 we obtain

$$\frac{d\gamma}{dt} = \frac{2eV_{JJ}}{\hbar} \ . \tag{5.13}$$

This is one of Josephson's famous equations relating the rate of change of the gauge invariant phase to the voltage across the junction.

   In Chap. 1 I showed that phase rigidity in a superconductor led directly to the possibility of equilibrium supercurrents. Anticipating that phase rigidity in a Josephson junction will do the same we can calculate the reversible work done by an external current source in changing the phase difference across the junction using,

$$dF_J = I_p V_{JJ} dt \tag{5.14}$$

$$= I_p \frac{\hbar}{2e} \frac{\partial\gamma}{\partial t} dt \ , \tag{5.15}$$

and thus

$$I_p = \frac{\hbar}{2e} \frac{dF_J}{d\gamma} \ . \tag{5.16}$$

Substituting for F_J from Eq. 5.8 we then arrive at Josephson's other equation,

$$I_p = I_J \sin(\gamma) \ , \tag{5.17}$$

where

$$I_J = \frac{\hbar}{2e} \kappa |\Psi_1||\Psi_2| \ . \tag{5.18}$$

Remembering that this is an equilibrium current that must flow without dissipation, these equations imply that there is a phase-difference dependent Cooper pair current that can flow between the junctions without any voltage dropped, i.e. a supercurrent. Importantly for the research presented in this thesis, the maximum supercurrent that can flow is proportional directly to $|\Psi_1|$ and $|\Psi_2|$. The significance of all of this to SJTM is that if one can measure the quantity I_J as a function of position on a sample's surface, then it follows directly from Eq. 5.18 that we can map spatial variations in the sample's order parameter.

   Recapping, we have made three assumptions:

1. Superconductors are phases of matter which break a global phase symmetry.
2. Local gauge-invariance is preserved.
3. The order parameters of the superconductors are allowed to weakly couple.

The consequences of these assumptions were the Josephson equations,

$$I_p = I_J \sin(\phi) \tag{5.19}$$

$$\frac{d\phi}{dt} = \frac{2eV_{JJ}}{\hbar} \ , \tag{5.20}$$

which I have chosen to write in a form that assumes $\vec{B} = 0$, as I will not discuss magnetic fields in the remainder of this chapter. Thus, with a minimal number of assumptions we conclude that any SJTM measurement of I_J will map spatial variations in the superconducting order parameter, regardless of the microscopic details of the condensate. The subject of Sects. 5.3 and 5.6 will be how to measure I_J from the current-voltage characteristics of the ultra-small Josephson junctions used in SJTM when they are embedded in realistic experimental circuits.

The most famous objector to Josephson's idea was Bardeen. The essence of his objection was that assumption (3) above was violated. Quoting from Ref. [17] Bardeen writes:

In a recent note, Josephson uses a somewhat similar formulation to discuss the possibility of superfluid flow across the tunnelling region, in which no quasi-particles are created. However, as pointed out by the author, pairing does not extend into the barrier, so that there can be no such superfluid flow.

However, it is possible to microscopically demonstrate that the phase of two superconductors can couple through a tunnelling junction. The approach taken by Josephson was the tunnelling Hamiltonian formalism introduced in Chap. 2 with left and right electrodes described by BCS wave-functions with gaps $\Delta_1 = |\Delta_1|e^{i\theta_1}$ and $\Delta_2 = |\Delta_2|e^{i\theta_2}$ and same the tunnelling Hamiltonian we used to calculate single-particle tunnelling rates,

$$\hat{H}_T = \sum_{\vec{k},\vec{q}} M_{\vec{k},\vec{q}} \left(\hat{c}^{\dagger}_{\vec{k}\sigma} \hat{c}_{\vec{q}\sigma} + \hat{c}^{\dagger}_{-\vec{q}-\sigma} \hat{c}_{-\vec{k}-\sigma} \right) + H.C \ , \tag{5.21}$$

where $\hat{c}^{\dagger}_{\vec{k}\sigma}$ creates an electron in state $\vec{k}$ with spin σ on the left electrode and $\hat{c}^{\dagger}_{\vec{q}\sigma}$ creates an electron in state $\vec{q}$ with spin σ on the right electrode [18].

Following the treatment of Anderson in Ref. [19], the second order perturbative correction to the ground state energy due to $\hat{H}_T$ at $T = 0$ is given by

$$\Delta E = -N_1(0)N_2(0)|M|^2 \frac{|\Delta_1||\Delta_2|}{|\Delta_1| + |\Delta_2|} K \left(\left| \frac{|\Delta_1| - |\Delta_2|}{|\Delta_1| + |\Delta_2|} \right| \right) \cos(\phi) \ , \tag{5.22}$$

where $N_1(0)$ and $N_2(0)$ are the densities of states of the two electrodes, $K(x)$ is a complete elliptical integral of the first kind, $|M_{\vec{k},\vec{q}}| = |M|$ and terms independent of ϕ have been omitted. This microscopically establishes that, in as much as the tunnelling Hamiltonian formalism is a valid description of a tunnelling junction, there is a coupling between the phases of the two superconductors.

Comparing Eqs. 5.3–5.22 and noting that the normal state resistance of the junction, R_N, is given by,

$$\frac{1}{R_N} = \frac{4\pi e^2}{\hbar} |M|^2 N_1(0) N_2(0) \ , \tag{5.23}$$

one arrives at a expression for I_J in terms of microscopic parameters of the superconductors:

$$I_J R_N = \frac{2}{e} \frac{|\Delta_1||\Delta_2|}{|\Delta_1| + |\Delta_2|} K\left(\left|\frac{\Delta_1 - \Delta_2}{\Delta_1 + \Delta_2}\right|\right) \ . \tag{5.24}$$

For non-zero temperature Ambegaokar and Baratoff found a similar analytic expression in the case where $|\Delta_1| = |\Delta_2| = |\Delta(T)|$:

$$I_J R_N = \frac{\pi|\Delta(T)|}{2e} \tanh\left(\frac{|\Delta(T)|}{2k_B T}\right) \ . \tag{5.25}$$

We can make a connection between this expression and the phenomenological one in Eq. 5.18 using the work of Gor'kov, who showed that for $T \approx T_c$, $\Delta \propto \Psi$ [20]. Expanding Eq. 5.25 about $\Delta = 0$ gives $I_J \propto |\Delta|^2 \propto |\Psi|^2$. Equation 5.18 has the same dependence on $|\Psi|$, demonstrating the consistency of both approaches. For $T \to 0$ Eq. 5.25 yields $I_J \propto \Delta$. In this limit one can demonstrate consistency between Eqs. 5.25 and 5.18 by noting that the superfluid density, $\rho_s \propto |\Psi|^2$, is proportional to $N(0)\Delta$ for $T \to 0$.

Later in this chapter I will present SJTM measurements of the cuprate superconductor $Bi_2Sr_2CaCu_2O_{8+\delta}$ which has a predominantly d-wave superconducting order parameter. The internal structure of the pair wave-functions will only enter into our phenomenological calculation of the Josephson current in the coupling constant κ, leaving the form of the Josephson equations unchanged. The value of κ will depend on the pairing symmetry on either side of the junction, as well as details of the junction itself, such as its orientation with respect to the crystallographic axes of the superconductors.

Šmakov et al. calculated I_J using the tunnelling Hamiltonian formalism for c-axis tunnelling between an s-wave superconductor with gap $|\Delta_k| = |\Delta_0|$ and a d-wave superconductor with gap $|\Delta_k| = |\Delta_0|(\cos(k_x) - \cos(k_y))$, finding that $I_J = 0$[2]. Anticipating that I_J will be highly suppressed for Josephson tunnelling between a d-wave superconductor and an s-wave superconducting tip our implementation of cuprate SJTM uses a d-wave tip, whose fabrication is detailed in Sect. 5.5.

For a d-wave to d-wave junction, I_J is sensitive to the relative orientation of the tip and sample order parameters. It is maximal when they are aligned and zero when rotated from each other by an azimuthal angle $\alpha = \frac{\pi}{4}$ [2]. In Sect. 5.5 I present evidence that the crystallographic axes of our $Bi_2Sr_2CaCu_2O_{8+\delta}$ nano-flake tip are aligned with those of the sample in our measurements. Generally though, the relative orientation of the tip and sample only affects the absolute magnitude of I_J and does not impact the ability of SJTM to measure relative spatial variations in I_J.

---

[2]Physical quantities are not identically zero by coincidence, this is a result of an underlying symmetry. Consider two tetragonal superconductors with order parameters Ψ_1 and Ψ_2 separated along their c-axis by a junction that is invariant under 90° rotations about that axis such as vacuum or an amorphous insulator. The coupling free energy, $F_J = \frac{1}{2}\kappa(\Psi_1\Psi_2^* + \Psi_2\Psi_1^*)$, must be invariant under those same 90° rotations. Consequently, if Ψ_1 and Ψ_2 transform as different irreducible representations of the tetragonal point group then κ must be identically zero. Thus κ is identically zero if Ψ_1 and Ψ_2 transform as B_{1g} ($d_{x^2-y^2}$) and A_{1g} (s-wave) representations respectively.

5.3   Josephson Current-Voltage Characteristics in Ultra-small Junctions

In the above I demonstrated that the intrinsic Josephson critical current, I_J, of a tunnelling junction formed between a superconducting sample and a superconducting STM tip can be used as a direct measure of the superconducting order parameter in the sample, regardless of microscopic details of the condensate. In SJTM we hope to measure I_J using the current-voltage characteristic, $I(V_{JJ})$, of the tip-sample Josephson junction. However, the ultra-small tip-sample junctions required to attain nanometer resolution can have radically different current-voltage characteristics to the micron scale junctions most of us are familiar with. At the root of this are the strong phase fluctuations present in ultra-small junctions.

In the following I will discuss the physics of ultra-small Josephson junctions and their expected current-voltage characteristics under conditions applicable to SJTM. To this end, I will begin by reviewing the more familiar current-voltage characteristics of Josephson junctions with strong phase coupling, which are typically larger.

The material contained in this section is necessarily quite technical. While included here for logical flow, one way to use this material would be to refer back to it as necessary from the Sects. 5.4–5.8 which detail the experimental implementation and validation of SJTM.

5.3.1 $I(V_{JJ})$ Characteristics for Josephson Junctions with Strong Phase Coupling

The Josephson equations,

$$I_p = I_J \sin \phi \qquad (5.26a)$$

$$\frac{d\phi}{dt} = \frac{2e}{\hbar} V_{JJ} , \qquad (5.26b)$$

demonstrate that in order to calculate the current-voltage characteristic of a Josephson junction, $I(V_{JJ})$, we must first understand the dynamics of the phase difference, ϕ, across the junction.

We can model the dynamics of ϕ semi-classically using the parallel combination of a Josephson circuit element, a capacitance and a resistance as shown in Fig. 5.2. The Josephson element represents the tunnelling current of Cooper-pairs and obeys Eq. 5.26a. The capacitance, C_J, is that between the electrodes and the resistance, R, represents their single-particle tunnelling channel. This model is known as the Resistively and Capacitively Shunted Junction (RCSJ) model [21, 22].
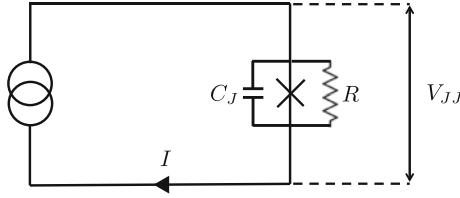
Fig. 5.2 Circuit diagram for the Resistively and Capacitively Shunted Junction (RCSJ) model. A Josephson circuit element carrying a Cooper-pair current is current biased in parallel with a capacitance, C_J, and ohmic resistance, R. For an SJTM experiment, C_J is between the tip and sample and R represents the single-particle tunnelling channel of the junction (which would in reality be non-ohmic). A voltage, V_{JJ}, develops across the junction as a result of the current bias, I

The equation of motion for ϕ,

$$I = I_J \sin \phi + \frac{V_{JJ}}{R} + C_J \frac{dV_{JJ}}{dt} \, , \tag{5.27}$$

is obtained by conservation of current. Substituting for V_{JJ} from Eq. 5.26b we obtain

$$\frac{d^2\phi}{d\tau^2} + \frac{1}{Q}\frac{d\phi}{d\tau} + \sin \phi = \frac{I}{I_J} \, , \tag{5.28}$$

where $\tau = \omega_p t$, $Q = \omega_p R C_J$ and $\omega_p = \sqrt{\frac{2eI_J}{\hbar C}}$. In the limit where $\phi(\text{mod}) \, 2\pi \to 0$ this describes a damped driven harmonic oscillator with quality factor Q and resonant frequency ω_p, known as the Josephson plasma frequency. In analogy to a mechanical system, the capacitance provides the inertia, the shunt resistance the damping and the Josephson element is the "spring".

If we bias the junction with a DC current, the dynamics of ϕ have an intuitive mechanical analogue. When $I(t) = I_{DC}$ Eq. 5.28 describes a massive particle, moving with viscous drag, through a potential,

$$U(\phi) = -E_J \cos \phi - \frac{\hbar I_{DC}}{2e}\phi \, , \tag{5.29}$$

resembling a "tilted washboard". $E_J = \frac{\hbar I_J}{2e}$, the Josephson energy, is the potential barrier between adjacent minima in this Josephson potential. The famous zero voltage state of the DC Josephson effect corresponds to the particle resting in metastable equilibrium in a minimum of the potential. We will use this washboard analogy, depicted in Fig. 5.3, to understand the different dynamic regimes of Josephson tunnelling and their $I(V_{JJ})$ characteristics.

As for a mechanical oscillator, the dynamical regimes of a Josephson junction are determined by its quality factor Q. If $Q^2 \gg 1$ the junction is under-damped and its dynamics are dominated by its capacitance. In the mechanical analogy this means that the work done by gravity in moving the particle to an adjacent minimum
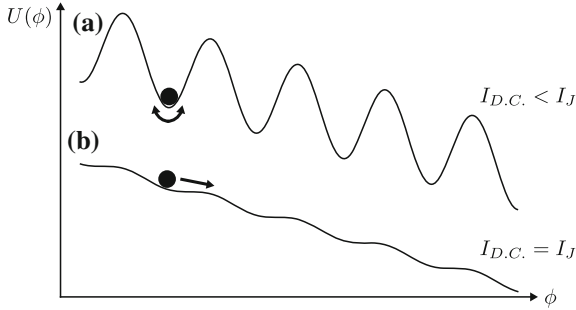
Fig. 5.3 The tilted washboard potential of the RCSJ model presented in Fig. 5.2 for the cases **a** $I_{DC} < I_J$ and **b** $I_{DC} = I_J$. The *red circle* symbolises a fictitious point-particle whose dynamics, under gravity and viscous damping, are analogous to that of the ϕ
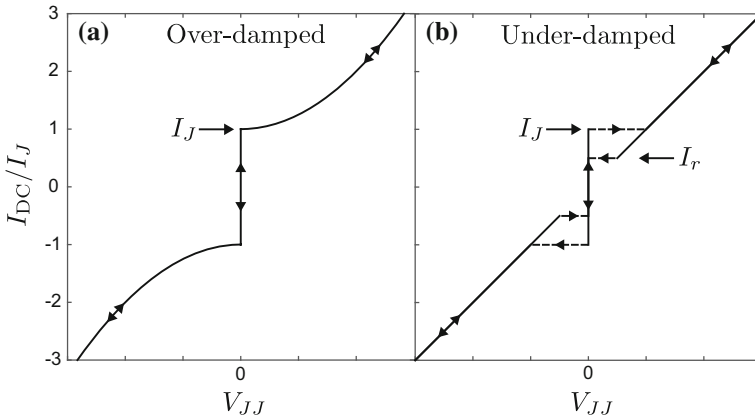
Fig. 5.4 $I(V_{JJ})$ characteristic for Josephson junctions with coherent phase dynamics when they are **a** over-damped and **b** under-damped. In the case of the under-damped junction there is significant hysteresis with a difference between the Josephson critical current, I_J, and the re-trapping current, I_r

of the washboard potential is much greater than the energy dissipated by the viscous damping. Conversely, if $Q^2 \ll 1$ the junction is over-damped and the phase dynamics are viscous, with the velocity of the particle directly proportional to the force on it. Whether the dynamics are over or under-damped will be critical for the form of the $I(V_{JJ})$ characteristic.

As the DC current bias in increased, the slope of the washboard potential increases. For $I_{DC} < I_J$ the phase will remain stationary in a minimum of the potential. Equation 5.26b tells us that this means $V_{JJ} = 0$. As such, all current will flow without resistance through the Josephson junction and none will flow through the shunt resistance. When $I_{DC} = I_J$ there ceases to be a minimum in the potential and the particle will roll down the slope resulting in $V_{JJ} \neq 0$ and current flowing through the shunt resistance as shown in Fig. 5.4. This behaviour is the same regardless of whether the junction is over-damped or under-damped.

The $I(V_{JJ})$ characteristics of the under and over-damped regimes differ when I_{DC} is subsequently decreased. For the over-damped junction, where the phase has negligible inertia, it will become re-trapped as soon as $I_{DC} < I_J$ and a minimum exists in the potential. The re-trapped current, I_r, equals I_J and there is no hysteresis in the $I(V_{JJ})$ curve.

For the under-damped junction, the inertia of the mass is sufficient to carry it over the maxima in the potential that appear for $I_{DC} < I_J$. For a current $I_r < I_J$, the damping will be sufficient to re-trap the phase in a minimum of the potential and the voltage across the junction will return to zero. This results in the significant hysteresis shown in Fig. 5.4b.

For real Josephson junctions fluctuations in ϕ will inevitably result from thermal voltage noise [23, 24]. For a junction biased with current $I_{DC} < I_J$ the phase will oscillate around a minimum in the tilted-washboard potential. A sufficiently strong thermal fluctuation in ϕ will knock the phase into an adjacent minimum. The subsequent dynamics of the junction will depend upon the value of Q^2.

For an under-damped junction with $Q^2 \gg 1$ the phase will continue to roll down the washboard potential, resulting in premature switching to the resistive state of the junction. For the over-damped junction with $Q^2 \ll 1$ the phase will be re-trapped in the adjacent minimum and the junction will return to the zero-resistance state. The phase slip will give rise to a voltage pulse.

If the phase dynamics of a Josephson junction are over-damped and phase fluctuations sufficiently strong that these phase slip events occur frequently, then the time-average of the associated voltage pulses will result in a non-zero DC voltage across the junction. Consequently the resistance for the Cooper pair current through the junction will be small but non-zero.

A general criterion for whether a zero-resistance DC Josephson current will be observable can be obtained by comparing the height of the potential barrier between adjacent minima in the Josephson potential, $2E_J$, to the characteristic energy of thermal fluctuations, kT. A zero-resistance DC Josephson effect will only be observed if

$$\frac{E_J}{kT} \gg 1 . \tag{5.30}$$

For the ultra-small junctions used in SJTM, E_J is typically $\lesssim kT$. Consequently, no zero-resistance DC Josephson effect will be observed. However, its turns out that we are still able to measure a Cooper pair current in these junctions. From their $I(V_{JJ})$ characteristics we can extract the intrinsic critical current, I_J, and hence measure the superconducting order parameter in our sample. I will now move on to discuss the form we expect these $I(V_{JJ})$ characteristics to take and how I_J can be extracted from them.

Fig. 5.5 A modified circuit diagram for a current biased RCSJ model that is shunted by an frequency dependent impedance $Z(\omega)$
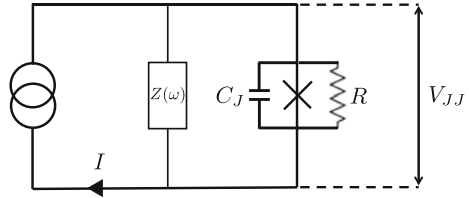
5.3.2 Thermal Phase Fluctuations in Ultra-small Josephson Junctions

The ultra-small size of SJTM junctions means that they have $I_J \sim 1\,\text{nA}$ which corresponds to an E_J/k of $\sim 10\,\text{mK}$. In the experimentally accessible temperature range we will have $E_J \lesssim kT$. Consequently, the DC Josephson effect presented in Fig. 5.4 will typically not be observed in SJTM. In Sect. 5.3.3 I will discuss how this can be true even at $T = 0$ due to quantum phase fluctuations arising from the junction's charging energy.

Another facet of the ultra-small size of SJTM junctions is that they can have a junction capacitance, C_J, as small as $\sim$1fF and a shunt resistance provided by the SIS single-particle tunnelling channel of $\sim 0.1-100\,\text{M}\Omega$ [8–14]. On the face of it the small capacitance would favour over-damping while the large resistance favours under-damping. However, the single-particle tunnelling channel presented by $R(V_{JJ})$ in Fig. 5.2 is not the relevant characteristic resistance in this problem.

The frequency scale of phase slippage and re-trapping events is given by the Josephson plasma frequency, ω_p, which is typically $\sim 10^{11}$ Hz. At these frequencies the damping of ultra-small Josephson junctions used in SJTM experiments will be dominated by the shunt impedance of the bias circuitry and not the DC resistance of the single-particle tunnelling channel [25]. This shunting of the junction by its electromagnetic environment is given a lumped circuit representation in Fig. 5.5 by including a frequency dependent shunt impedance $Z(\omega)$ in parallel with the junction.

At frequencies near DC, $Z(\omega)$ is effectively infinite. However, for frequencies $\sim 10^{11}$ Hz the junction can dissipate energy by radiating microwaves. In this frequency range the shunting impedance of the leads attached to the junction can be modelled as an infinite transmission line [26–29]. This is justified because the impedance to radiating microwaves will be controlled by the first few millimeters ($\sim$one wavelength) of the leads around the junction and any discontinuities in the leads will occur on a length scale much greater than this.

The high-frequency impedance of such a transmission line is given by $Z_1 \sim \frac{Z_0}{2\pi} \sim 100\Omega$, where Z_0 is the impedance of free space [26–29]. This real, dissipative impedance is much less than that provided by the single-particle tunnelling channel and leads to the junction being over-damped at high-frequencies.

This over-damping of SJTM junctions at high frequencies allows the observation of a Cooper-pair current even if $E_J \lesssim kT$. In this case, using the tilted washboard analogy, the rate of hopping to adjacent minima will be large but the over-damping

(a)

(b)
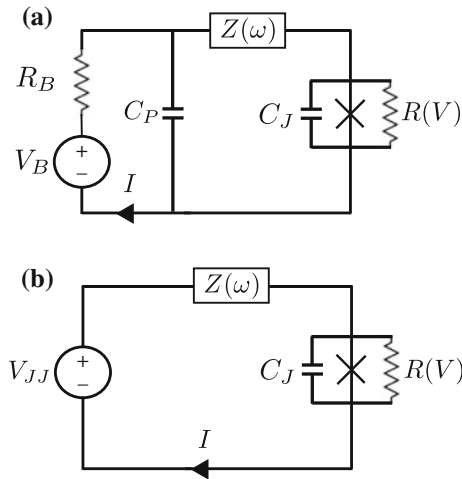
Fig. 5.6 **a** An RCSJ model is biased by a non-ideal current source consisting of a voltage source in series with a large biasing resistance R_B. A parasitic capacitance, C_P, and a frequency dependent impedance, $Z(\omega)$, representing the electromagnetic environment of the junction are included. For an SJTM experiment C_P is typically $\gg C_J$. As a result the voltage across the junction is approximately time-independent and it may be regarded as effectively voltage biased as shown in **b**

will ensure that the phase is re-trapped during each event. This allows the dynamics to be modelled as a biased random-walk with the phase diffusing down the washboard potential. The smaller barrier height for hopping down the washboard will lead to a time-average phase velocity $\langle \dot{\phi} \rangle$ and hence DC voltage $\frac{\hbar}{2e} \langle \dot{\phi} \rangle$.

Before calculating the $I(V_{JJ})$ expected from this phase-diffusion process we must first address whether the junction is under current or voltage bias conditions. While this may at first seem to be obvious from the type of source used in the circuit, there is a subtlety that arises from the parasitic capacitance of the leads attached to the junction.

In Fig. 5.6a I take the ideal current biased circuit in Fig. 5.5, explicitly include a parasitic capacitance between the junction leads, C_P, and replace the ideal current source by a voltage source in series with a large biasing resistor R_B.[3] In SJTM experiments C_J can be as small as $\sim$1fF and C_P is typically $\sim$1nF. As a result, the voltage across C_P can be well approximated as independent of time even though the current flowing through the Josephson junction consists of current spikes corresponding to tunnelling events [28].

---

[3]Note that although in going from Figs. 5.5 and 5.6a the impedance $Z(\omega)$ has been moved from being in parallel with the junction to in series with it, this still represents a high-frequency dissipative shunt because it is in series with the junction capacitance C_J.

Fig. 5.7 $I(V_{JJ})$ characteristics for an over-damped junction in the presence of strong thermal fluctuations. The curves plotted correspond to Eq. 5.31 with $T = 500\,\text{mK}$, $Z = 100\,\Omega$ and $I_J = 100\,\text{pA} - 1\,\text{nA}$ in equal increments. $I_c \propto I_J^2$ denotes the maximum Cooper pair current
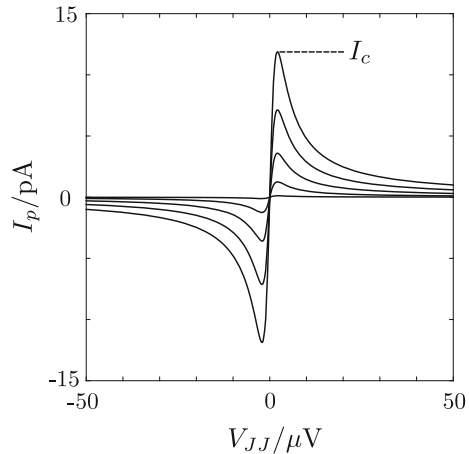
This time-independence of the voltage across C_P renders the junction effectively voltage biased. Thus, in modelling the behaviour of the junction we can replace the circuit in Fig. 5.6a by that in Fig. 5.6b. In this scheme the actual voltage source and biasing resistor are replaced by an effective voltage source with potential difference V_{JJ} across it. V_{JJ} must be determined self-consistently from the DC current flowing through the junction, i.e. $V_{JJ} = V_B - R_B I(V_{JJ})$.

To calculate the $I(V_{JJ})$ characteristic for a junction in the phase-diffusion regime Ivanchenko and Zi'lberman used a circuit as in Fig. 5.6b with $R(V) = \infty$ and real impedance, $Z(\omega) = Z$, in thermal equilibrium at temperature T acting as source of Johnson voltage noise across the junction [24]. In the limit where $E_J \ll kT$ and $C \to 0$, the solution to the resulting stochastic equation is

$$I_p(V_{JJ}) = \frac{I_J^2 Z}{2} \frac{V_{JJ}}{V_{JJ}^2 + V_C^2} \, , \tag{5.31}$$

where $V_C = 2eZkT/\hbar$. These $I_p(V_{JJ})$ curves are plotted in Fig. 5.7. Note that the subscript p has been applied to denote that this current arises entirely from the flow of Cooper pairs.

There are several pertinent features of these $I_p(V_{JJ})$ curves. Firstly, as I_J is decreased the average diffusive phase velocity increases and with it the resistance of the junction near $V_{JJ} = 0$. Comparing Figs. 5.4 and 5.7 we can see that the effect of strong phase fluctuations has been to give a finite slope to the $I_p(V_{JJ})$ curves at $V_{JJ} = 0$. Secondly, they exhibit a peak in the Cooper-pair current at non-zero voltage, V_C, whose magnitude, I_c is proportional to I_J^2. This fact is crucial for the operation of SJTM because measuring spatial variations in I_c allows one to measure spatial variations in I_J and hence the superconducting order parameter.

5.3.3 Including Both Thermal and Quantum Phase Fluctuations

In the previous section I treated the dynamics of the phase classically, despite its quantum origin. The conclusion was that strong thermal fluctuations in ϕ lead to $I_p(V_{JJ})$ curves that have a finite slope at $V_{JJ} = 0$ and a peak Cooper-pair current proportional to I_J^2. In this section I will take into account quantum fluctuations of the phase resulting from the Coulomb charging of the junction and find that these properties of $I_p(V_{JJ})$ persist.

In the limit of strong fluctuations of the phase difference across a Josephson junction there is no DC Josephson effect. However, one can still measure I_J through the current that arises from incoherent tunnelling of Cooper pairs between the electrodes. As the Josephson effect is often described as the tunnelling of Cooper pairs, the distinction between incoherent Cooper pair tunnelling and the coherent tunnelling that occurs in the standard Josephson effect warrants some explanation.

Consider the following model Hamiltonian of a junction between two superconducting electrodes labelled 1 and 2, each with optimum Cooper pair number, N_0, that minimises its electrostatic self-energy,

$$\hat{H} = E_C \hat{N}^2 - E_J \cos(\hat{\phi}) , \qquad (5.32)$$

where $\hat{N} = \hat{N}_1 - \hat{N}_2$ is the Cooper pair number imbalance operator. $E_C = 2e^2/C_J$ is the charging energy of the junction and $E_J = \frac{\hbar I_J}{2e}$ is the Josephson energy. Note that $\hat{N}$ and $\hat{\phi}$ do not commute and obey an uncertainty relationship $\Delta N \Delta \phi \leq \frac{1}{2}$.

Let's work in the basis of number projected BCS wave-functions $|N\rangle_1$ and $|N\rangle_2$ for the electrodes. Writing the Josephson term in the form,

$$E_J \cos(\hat{\phi}) = \frac{E_J}{2} \left(e^{i\hat{\theta}_2} e^{-i\hat{\theta}_1} + e^{-i\hat{\theta}_2} e^{i\hat{\theta}_1} \right) , \qquad (5.33)$$

and noting that $e^{-i\hat{\theta}_i}|N\rangle_i = |N+1\rangle_i$, we see that this term acts to transfer a Cooper pair between the two electrodes. Consequently, it has vanishing expectation if the state of the two electrodes has a definite number of Cooper pairs on each electrode.

In the limit where $E_J \gg E_C$ the ground state will be well approximated by a coherent superposition of product states with total Cooper pair number $2N_0$ but different numbers of Cooper pairs on each electrode,

$$|\Psi\rangle = \sum_j \alpha_j |N_0 - j\rangle_1 |N_0 + j\rangle_2 , \qquad (5.34)$$

so as to give the ground state a definite phase difference [25]. Thus, the ground state energy is phase difference dependent and this phase rigidity will result in a phase dependent equilibrium Cooper pair current, i.e. the Josephson effect. This is what I will term coherent Cooper pair tunnelling because the ground state of the junction

Fig. 5.8 A Cooper-pair (*blue*) tunnels to the condensate on the other side of a potential barrier under voltage bias V_{JJ} by emitting a photon of energy $\hbar\omega = 2eV_{JJ}$
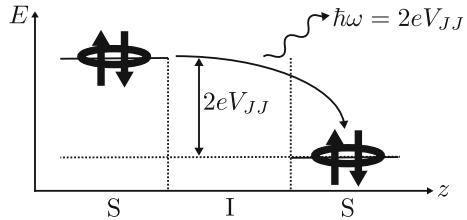
has coherence between states that differ by the transfer of a Cooper pair between the electrodes.

In the opposite limit where $E_C \gg E_J$ the ground state is well approximated by a product state with a definite number of Cooper pairs on each electrode,

$$|\Psi\rangle = |N_0\rangle_1 |N_0\rangle_2 \,, \tag{5.35}$$

so as to minimise the charging energy of the junction. The expectation of the Josephson term is then zero, resulting in the absence of a phase dependence to the ground state energy and consequently no equilibrium Josephson current.

However, we can regard the Josephson term as a Cooper pair tunnelling Hamiltonian and treat it perturbatively using Fermi's golden rule. At $T = 0$ the Cooper pair tunnelling rate from electrode 1–2 is given by,

$$\Gamma_{1\to 2} = \frac{2\pi}{\hbar} |\langle N_0 + 1|_2 \langle N_0 - 1|_1 E_J e^{-i\hat{\phi}} |N_0\rangle_1 |N_0\rangle_2|^2 \delta(\mu_1 - \mu_2) \,, \tag{5.36}$$

where μ_1 and μ_2 are the chemical potentials for Cooper pairs in the two electrodes. This process I will refer to as incoherent Cooper pair tunnelling.

Two important points arise from this. In contrast to single-particle tunnelling there is not a continuum of initial and final states. Thus $\Gamma_{1\to 2}$ is only non-zero when $\mu_1 - \mu_2 = 2eV_{JJ} = 0$, where V_{JJ} is the voltage across the junction. But in this case $\Gamma_{1\to 2} = \Gamma_{2\to 1}$ by symmetry and there is no net Cooper pair tunnelling current. The only way that a net Cooper pair current can occur is if Cooper pairs tunnel inelastically, by exchanging energy $2eV_{JJ}$ with their environment when they tunnel, as depicted in Fig. 5.8. This means that the exact form of $I_p(V_{JJ})$ will depend sensitively on the details of the interaction with the environment.

However, what we can tell from Eq. 5.36 is that the current will scale with $E_J^2 \propto I_J^2$. It is this property of incoherent Cooper pair tunnelling that will allow us to measure I_J in ultra-small SJTM junctions despite the absence of a coherent Josephson effect. Note that this is exactly the same scaling behaviour exhibited by the classical phase diffusion model in the limit of strong thermal phase fluctuations. This is a result of the fact that in both cases, phase fluctuations mean that states with a different number inbalance of Cooper pairs on the electrodes are combined only incoherently and hence the Cooper pair current arises from incoherent tunnelling.

What follows below is a extension of the argument above to include the effects of finite temperature and the electromagnetic environment. I will follow the treatment of Devoret et al. [30] who treated single-particle tunnelling junctions as open quantum systems and coupled them to a Caldera-Leggett model for the electromagnetic environment. This approach was subsequently extended to Josephson junctions in Refs. [31–34]. Full details of the calculation below can be found in Ref. [28].

A Hamiltonian for the Josephson junction embedded in its environment is given by,

$$\hat{H} = \hat{H}_0 - E_J \cos(\hat{\phi}) + \hat{H}_{\text{env}} \,, \tag{5.37}$$

where $\hat{H}_0$ describes the Cooper pair condensates in the electrodes and the environment Hamiltonian,

$$\hat{H}_{\text{env}} = \frac{\hat{Q}^2}{2C_J} + \sum_{n=1}^{\infty} \left[\frac{\hat{q}_n^2}{2C_n} + \left(\frac{\hbar}{e} \right)^2 \frac{1}{2L_n} \left(\hat{\tilde{\phi}} - \hat{\phi}_n \right)^2 \right] \,, \tag{5.38}$$

encodes the the electrostatic charging energy of the junction capacitance and the coupling to a dissipative reservoir [34]. Here $\hat{Q}$ is the charge on the junction capacitance C_J. Note that in using the operator $\hat{\tilde{\phi}} = \hat{\phi} - \frac{2e}{\hbar} V_{JJ} t$ we are subtracting the trivial time dependence of ϕ. The reservoir in this open quantum system is modelled as an infinite number of LC resonators of resonant frequency, $\omega_n = 1/\sqrt{L_n C_n}$, bi-linearly coupled to the phase difference across the junction. Models for the reservoir of this type were first introduced by Caldera and Leggett [35].

If $E_J \ll E_C$ or kT then we may treat the term $-E_J \cos(\phi)$ perturbatively. Applying Fermi's golden rule the forward tunnelling rate is given by,

$$\Gamma_{i \to f} = \frac{2\pi}{\hbar} |\langle f | E_J e^{-i\hat{\phi}} | i \rangle|^2 \delta(E_i - E_f) \,, \tag{5.39}$$

where the initial and final states $|i\rangle$ and $|f\rangle$ are the combined states of the electrodes and the environment, with E_i and E_f their corresponding energies. Tracing out the environmental degrees of freedom as detailed in Ref. [28] the forward tunnelling rate is given by,

$$\vec{\Gamma} = \frac{E_J^2}{4\hbar^2} \int_{-\infty}^{\infty} dt \exp\left(i \frac{2e}{\hbar} V t \right) \langle e^{\hat{\tilde{\phi}}(t)} e^{\hat{\tilde{\phi}}(0)} \rangle \,, \tag{5.40}$$

with the average $\langle ... \rangle$ taken with respect to the partition function $\text{Tr}\{\exp(-\hat{H}_{env}/kT)\}$. This can be rewritten in the more compact form,

$$\vec{\Gamma} = \frac{E_J^2}{4\hbar^2} P(2\,eV) \,, \tag{5.41}$$

where,

$$P(E) = \frac{1}{2\pi\hbar} \int_{-\infty}^{\infty} dt \, \exp\left[J(t) + \frac{i}{\hbar}Et\right], \tag{5.42}$$

with phase correlation function $J(t) = \langle\left[\hat{\tilde{\phi}}(t) - \hat{\tilde{\phi}}(0)\right]\hat{\tilde{\phi}}(0)\rangle$. $P(E)$ can be interpreted as the probability of a Cooper pair exchanging energy E with the environment.

Using the Caldera–Leggett model in Eq. 5.38 for the environment, $J(t)$ can be expressed in terms of a single parameter $Z_t(\omega) = [i\omega C_J + Z^{-1}(\omega)]^{-1}$ to be

$$J(t) = 2\int_{-\infty}^{\infty} \frac{d\omega}{\omega} \frac{\mathrm{Re}Z_t(\omega)}{R_Q} \left(\frac{e^{-i\omega t} - 1}{1 - e^{-\hbar\omega/kT}}\right), \tag{5.43}$$

where $Z_t(\omega)$ is the input impedance of the environment and $R_Q = h/4e^2$ is the quantum of resistance. Assuming a knowledge of the total impedance, $Z_t(\omega)$, then the tunnelling current is given by the difference between the forwards and backwards tunnelling rates of Cooper-pairs:

$$I_p(V_{JJ}) = 2e[\vec{\Gamma}(2eV_{JJ}) - \vec{\Gamma}(-2eV_{JJ})] = \frac{\hbar\pi e I_J^2}{4e}[P(2eV_{JJ}) - P(-2eV_{JJ})]. \tag{5.44}$$

This is a simple and powerful expression for the Cooper pair tunnelling current I_p. Its physical interpretation is the difference in probability for a Cooper pair to emit energy or absorb energy $2eV_{JJ}$ into the environment, multiplied by a pre-factor $\frac{\hbar\pi e I_J^2}{4e}$ which depends only on the superconducting order parameters in the electrodes and the strength of coupling between them.

5.3.4 Expected Pair-Current $I_P(V)$ in Ultra-small Josephson Junctions

The details of $Z_t(\omega)$ for the junctions used in SJTM experiments are in general difficult to know or control. However, as discussed in Sect. 5.3.2, at high frequencies the leads attached to the junction provide an impedance well approximated as ohmic and equal to $Z_1 \approx Z_0/2\pi \approx 100\,\Omega$. In this case, at $T = 0$, $P(E)$ is sharply peaked at $E = 0$ as shown in Fig. 5.9a and equal to zero for $E < 0$ [28].

Non-zero temperatures redistribute weight in $P(E)$ to larger voltages, with the weight at negative energies given by the principle of detailed balance, $P(-E) = e^{-\beta E}P(E)$, as shown schematically in Fig. 5.9b. From Eq. 5.44 the pair current can then be directly calculated as shown in Fig. 5.9c.

(a)

(b)

(c)
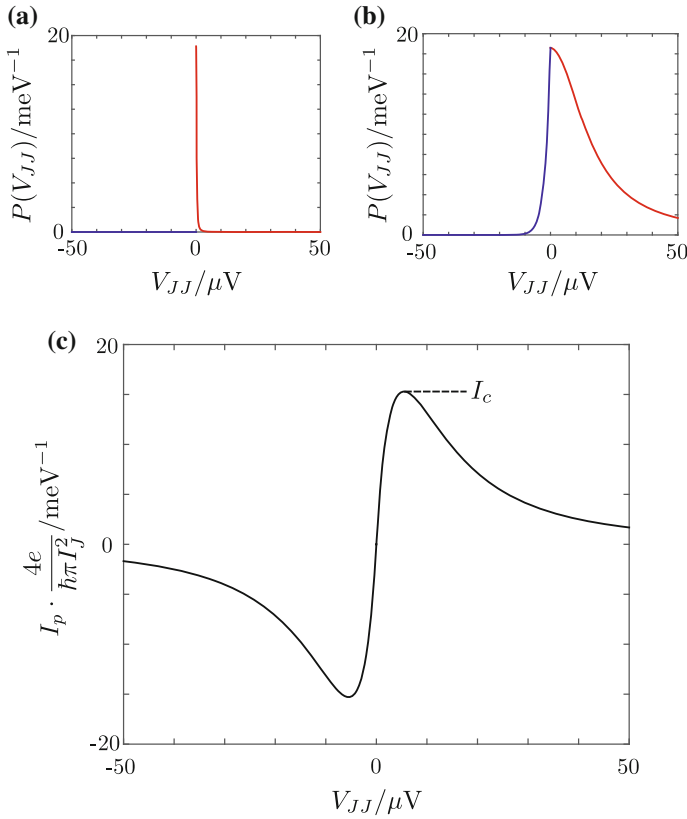
Fig. 5.9 a Schematic $P(E)$ for an SJTM junction at $T = 0$. The probability for a Cooper-pair to tunnel whilst emitting a photon (*red*) is strongly peaked at $V_{JJ} = 0$. The probability for tunnelling with absorption of a photon (*blue*) is zero. **b** Schematic $P(E)$ for an SJTM junction at $T \neq 0$. The effect of $T \neq 0$ is to broaden the distribution and populate the modes of the environment so that a Cooper-pair may absorb a photon whilst tunnelling. **c** $I(V_{JJ})$ calculated directly from the difference of the red and blue curves in **b** (see Eq. 5.42). It exhibits a peak current at $V_{JJ} \neq 0$ whose magnitude is proportional to I_J^2. This peak may be used to spatially map variations in the superconducting order parameter Ψ

Figure 5.9c is extremely similar to the $I(V_{JJ})$ curves in Fig. 5.7 that were calculated in the presence of strong classical phase fluctuations. Both exhibit a resistance at $V_{JJ} = 0$ that increases with decreasing I_J as well as a peak in the pair current whose magnitude is proportional to I_J^2. This reflects the fact that the effects of both quantum and thermal phase fluctuations are roughly the same. They both prohibit coherent Cooper pair tunnelling and thus the pair current must flow through incoherent Cooper pair tunnelling.

In an SJTM experiment we wish to measure spatial variations in I_J because it is directly proportional the superconducting order parameter in the sample. We will impose a constant temperature and $Z_t(\omega)$, being dominated by the measurement

apparatus rather than sample, will also remain constant. Relative spatial variations in I_J, and hence Ψ can thus be mapped by picking any feature of the $I(V_{JJ})$ curve that is easy to identify experimentally and taking the current or derivative at this point. A sensible experimental strategy is to measure the spatial variations in the peak Cooper-pair current, which we will call I_c. Using Eq. 5.44 we see that $I_c \propto I_J^2$. Having established in Sect. 5.2 that $I_J \propto |\Psi|$, this shows us that using SJTM to measure I_c as a function of position will yield a spatial map of relative variations in $|\Psi|^2$.

5.4   Experimental Strategy for Cuprate SJTM

The technical challenge of large field-of-view nanometre-resolution SJTM imaging is to measure, in a reasonable time (days), an array of I_c values with $\sim$1% precision using typically 256×256 pixels. To enact this scheme you require the following:

1. As large a superconducting tip gap, Δ_T, as possible so as to maximise I_J and hence the observed I_c (see Eq. 5.25).
2. A d-wave superconducting STM tip so as to maximise its Josephson coupling to the predominantly d-wave superconducting condensate of the cuprates.
3. An ultra-low-vibration STM that is engineered for sub-picometre stability in taking spectroscopic data while out of feedback. It should operate at the lowest practical temperatures to minimise the surpression of I_c by thermal fluctuations.
4. Environmental radio-frequency (RF) shielding to protect the Josephson junctions formed by the tip and sample from ambient microwave radiation.

Motivated by point (1) above we achieve a large Δ_T by picking up a nanometre-sized flake of $Bi_2Sr_2CaCu_2O_{8+\delta}$ on the end of our tungsten tip. This also satisfies point (2) because the tip has a d-wave superconducting order parameter. Points (3) and (4) are fulfilled by using a dilution refrigerator based STM operating below 50 mK, housed in an RF shielded, vibrationally isolated room of the type described in Sect. 2.5.

Clearly the fabrication of $Bi_2Sr_2CaCu_2O_{8+\delta}$ nano-flake superconducting tips was critical to our experimental scheme. In the following section I will describe the fabrication and characterisation of these tips in greater detail.

5.5   Superconducting STM Tips for Cuprate SJTM

In the following I will discuss the fabrication of the $Bi_2Sr_2CaCu_2O_{8+\delta}$ nano-flake tips used in our cuprate SJTM experiments. I will also characterise the superconductivity and geometry of these tips as well as demonstrating their stability during spectroscopic imaging.

Fig. 5.10 Conversion of
single-particle SIN (*dashed*)
to single-particle SIS (solid)
spectra when
$Bi_2Sr_2CaCu_2O_{8+\delta}$
nano-flake adheres to
tungsten tip. The tip gap
$\Delta_T \approx 25\,meV$ is the
difference between the SIN
and SIS peaks (*red
double-headed arrows*)
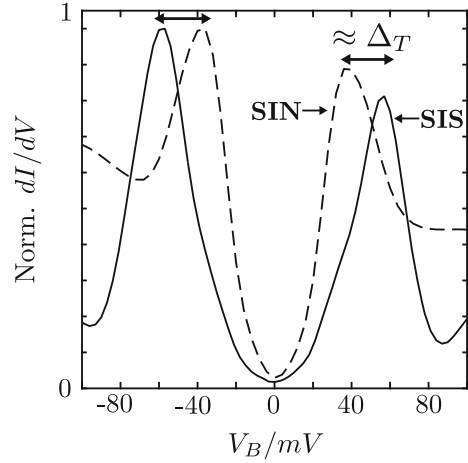
5.5.1 Fabrication of Superconducting Bi₂Sr₂CaCu₂O₈₊δ Nano-flake Tips

For the reasons discussed above, in implementing cuprate SJTM we chose to make
superconducting tips by picking up a piece of our $Bi_2Sr_2CaCu_2O_{8+\delta}$ sample on the
end of normal tungsten STM tips. This was achieved by manually adjusting the z-
piezo voltage to extend the tip into the fragile $Bi_2Sr_2CaCu_2O_{8+\delta}$ surface. However,
this does not always result in a superconducting tip.

The first crucial test of whether the tip is superconducting is to measure the dif-
ferential tunnelling conductance spectrum $g(V_B)$. For a normal tungsten STM tip
on a $Bi_2Sr_2CaCu_2O_{8+\delta}$ surface this is shown as the dashed curve in Fig. 5.10. This
conductance spectrum can be thought of as the superconducting density of states
in the material (see Sect. 2.1.4). If, after picking up a piece of the sample, both tip
and sample have a superconducting density of states, this converts the measured
superconductor-insulator-normal (SIN) tunnelling spectrum to a superconductor-
insulator-superconductor (SIS) spectrum.

As detailed in Sect. 2.1.4, the SIS single-particle tunnelling current, $I(V_B)$, is
given by,

$$I(V_B) = \frac{2\pi e}{\hbar}|M|^2 \int_0^{eV_B} n_S(\epsilon)n_T(E + eV_B)d\epsilon \,, \qquad (5.45)$$

and the differential conductance,

$$g(V_B) = \frac{dI}{dV_B} = \frac{2\pi e^2}{\hbar}|M|^2 \left[n_S(E)n_T(E + eV_B) + \int_0^{eV_B} n_S(\epsilon)\frac{\partial}{\partial(eV_B)}n_T(\epsilon + eV_B)d\epsilon \right] \,,$$
$$(5.46)$$

where $n_S(E)$ and $n_T(E)$ are the sample and tip superconducting density of states
respectively.
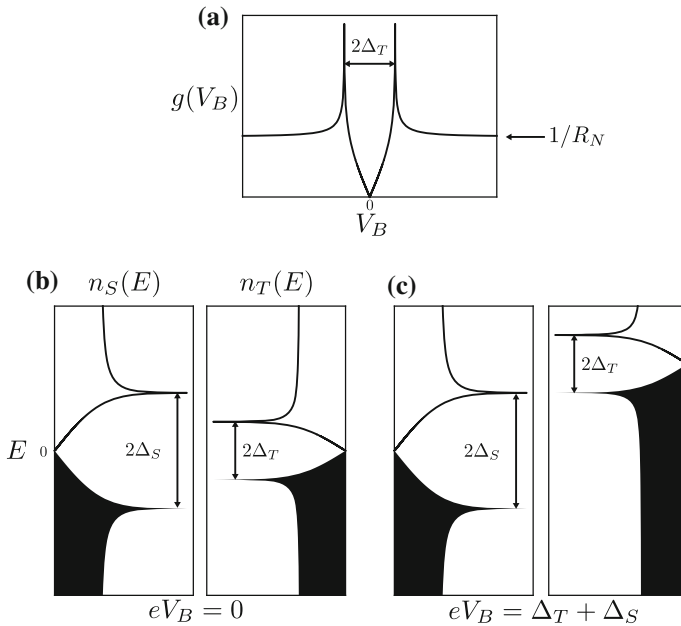
Fig. 5.11   a Schematic dI/dV_B spectrum for a d-wave superconductor with gap Δ_T. **b** Schematic of SIS tunnelling between a superconducting tip with energy gap Δ_T and sample with gap Δ_S. Filled states are *shaded*. No bias has been applied across the junction and there is no net tunnelling current. **c** A bias $(\Delta_S + \Delta_T)/e$ is applied across the junction that aligns the filled coherence peak of the tip and the empty coherence peak of the sample. This gives rise to a peak in dI/dV_B

For tip and sample superconductors with single-particle coherence peaks separated by $2\Delta_T$ and $2\Delta_S$ respectively, this leads to an SIS spectrum with an energy separation $2\Delta_{SIS} \approx 2(\Delta_S + \Delta_T)$ between conductance peaks. This occurs because the differential tunnelling conductance will peak when V_B is such that the unfilled coherence peak of the tip aligns in energy with the filled coherence peak of the sample and visa versa. This is most easily understood graphically as shown in Fig. 5.11.

Figure 5.10 demonstrates this phenomenology for one of our $Bi_2Sr_2CaCu_2O_{8+\delta}$ nano-flake tips. The dashed line is a spatially averaged SIN tunnelling spectrum taken with a normal tungsten STM tip on a $Bi_2Sr_2CaCu_2O_{8+\delta}$ sample with hole concentration $p = 0.17$. The solid line is an average SIS spectrum between a $Bi_2Sr_2CaCu_2O_{8+\delta}$ nano-flake tip and a $Bi_2Sr_2CaCu_2O_{8+\delta}$ sample of the same hole concentration. The difference in energy between the coherence peaks of the two spectra (indicated by red double headed arrows) indicates that the tip has a gap $\Delta_T \approx 25$ meV.

That the tunnelling spectra of our nano-flake tips show strong agreement with our expectations for SIS tunnelling is good evidence that they are indeed superconducting. Of course, the strongest evidence comes from the fact that the nano-flake tips exhibit an $I(V_B)$ for $V_B \lesssim 100\,\mu$V that is characteristic of Cooper-pair tunnelling. This will be discussed in detail in Sect. 5.6.

(a)

(c)

(e)

(b)

(d)

(f)
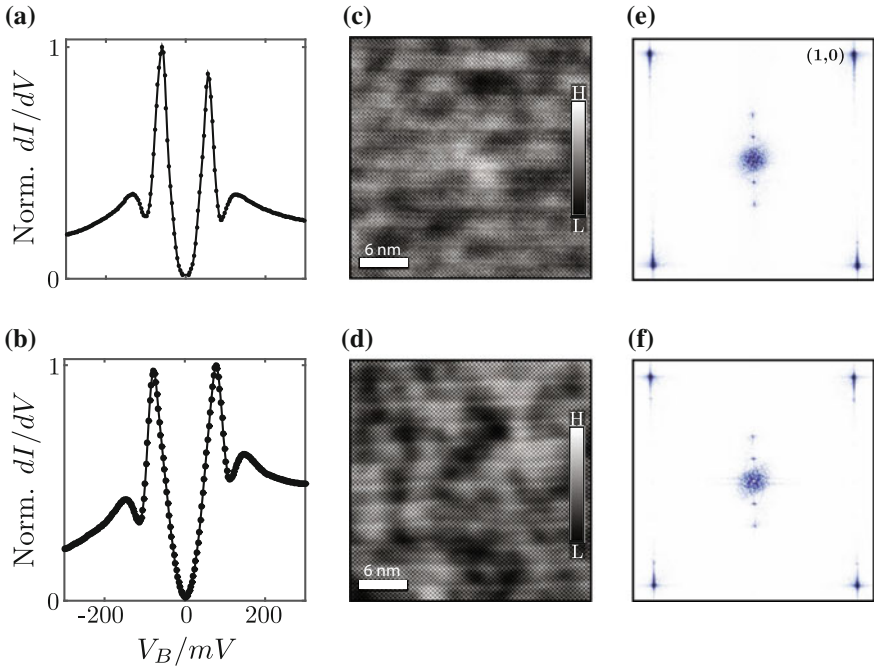
Fig. 5.12 Typical dI/dV_B spectrum, topography and magnitude of its Fourier transform $\tilde{T}(\vec{q})$ measured with two completely distinct $Bi_2Sr_2CaCu_2O_{8+\delta}$ tips on two different $Bi_2Sr_2CaCu_2O_{8+\delta}$ samples: tip 1 (**a**, **c** and **e**) and tip 2 (**b**, **d** and **f**)

5.5.2 Characterisation of Nano-flake Tip Geometry

Having characterised the superconductivity in our nano-flake tips I will now move on to discuss their geometry, i.e. their size, resolution and orientation with respect to the crystallographic axes of the sample crystal.

In Fig. 5.12 I compare the performance of two completely different $Bi_2Sr_2CaCu_2$ $O_{8+\delta}$ nano-flake tips. Figure 5.12a, b show their measured dI/dV_B spectra; they are obviously very similar. Figure 5.12c, d show SIS topographic images for these two tips and Fig. 5.12e, f are their corresponding Fourier transforms.

In both the real-space topographs and their Fourier transforms the $Bi_2Sr_2CaCu_2$ $O_{8+\delta}$ bulk crystal super-modulation (see Sect. 2.6.1) is easily resolved. Further, for both tips, topographic inhomogeneities can be resolved on the scale of ∼1 nm. Together these observations indicate that our nano-flake tips have a spatial resolution of ∼1 nm.

Although Bragg peaks at reciprocal lattice vectors can be seen in both Fourier transforms (Fig. 5.12e, f), this does not indicate that our tips have true atomic resolution. Strong atomic modulations would occur for a tip of infinite extent, as long as its crystallographic axes are aligned with the sample, due to the strong variation

(a)

(c) Tip Model Aligned

Simulated SIS Topograph

(e) Tip Model Misaligned

Simulated SIS Topograph

(b)

(d)

(f)
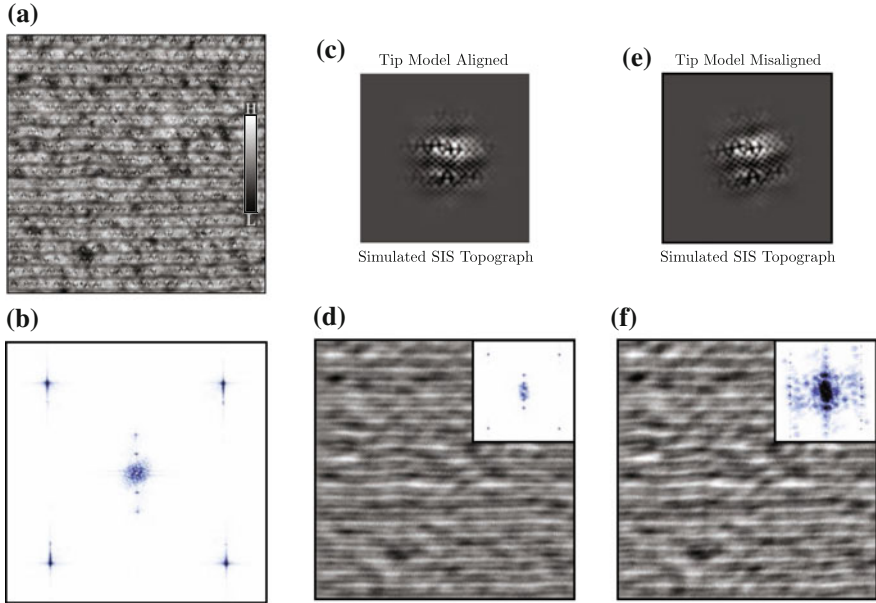
Fig. 5.13 **a** Surface topography $T(\vec{r})$ of $Bi_2Sr_2CaCu_2O_{8+\delta}$ sample, obtained with a conventional metallic tungsten tip. **b** Magnitude of Fourier transform (FT) of **a**. **c** Model for $Bi_2Sr_2CaCu_2O_{8+\delta}$ nanoflake tip that is aligned with the $Bi_2Sr_2CaCu_2O_{8+\delta}$ surface in **a**. **d** Convolution of $Bi_2Sr_2CaCu_2O_{8+\delta}$ surface image in **a** and aligned $Bi_2Sr_2CaCu_2O_{8+\delta}$ nanoflake tip in **c**. *Inset* shows resultant Fourier Transform with Bragg peaks in the corners and supermodulation peaks. **e** Model for BSCCO nanoflake tip that is misaligned with the $Bi_2Sr_2CaCu_2O_{8+\delta}$ surface in **a**. **f** Convolution of $Bi_2Sr_2CaCu_2O_{8+\delta}$ surface image in **a** and misaligned $Bi_2Sr_2CaCu_2O_{8+\delta}$ nanoflake tip in **e**. Inset shows resulting Fourier transform with many additional broad peaks caused by Moiré pattern effects. Comparison to **d** and Fig. 5.12e, f demonstrates that the tip used in the studies reported here was well aligned with the sample

in tunnelling matrix elements as the atoms in the tip and sample move in and out of alignment.

To check the relative orientation of the $Bi_2Sr_2CaCu_2O_{8+\delta}$ nano-flake crystal axes to the axes of the sample, we evaluate simulations to see what might be expected of such a tip. Figure 5.13a, b show a measured SIN topograph $T(\vec{r})$ of $Bi_2Sr_2CaCu_2O_{8+\delta}$ taken with a conventional tungsten tip, and its Fourier transform. To simulate what would be observed if the crystal axes of a $Bi_2Sr_2CaCu_2O_{8+\delta}$ nano-flake were oriented (or not) to those of the sample crystal axes, we extract a typical ∼2-nm-diameter patch from this image and then convolute the patch image with $T(\vec{r})$. This results in a simulated SIS topograph that is expected when using a $Bi_2Sr_2CaCu_2O_{8+\delta}$ nano-flake tip with (or without) axes aligned to the crystal axes.

If the axes of the patch are aligned to the crystal as in Fig. 5.13c, the result is as in Fig. 5.13d. If the axes are misaligned with the crystal as in Fig. 5.13e, the result is as in Fig. 5.13f (see the Fourier transform in the inset). As the vivid Moiré effects in the Fourier transform of the latter are not observed in the actual experiments (Fig. 5.12e, f), we conclude that the axes of the nano-flake are aligned with those of the $Bi_2Sr_2CaCu_2O_{8+\delta}$ bulk crystal. This is perhaps not surprising given that the nano-flake tips were extracted from the very same surface that they are measuring.

5.5.3 Stability of Tips During $I_c(\vec{r})$ Measurement

Given that our nano-flake tips are extended objects extracted from the fragile $Bi_2Sr_2CaCu_2O_{8+\delta}$ surface it is important to establish that our tips are in the vacuum tunnelling limit, as opposed to the point contact regime, and that they exhibit the stability necessary for spectroscopic imaging. The latter requires that the tip is not altered by interaction with the surface during measurement, so that a repeat of that measurement yields an almost identical result.

In Fig. 5.14a, b we show topographic images taken with the same $Bi_2Sr_2CaCu_2O_{8+\delta}$ nano-flake tip before and after a typical $I_c(\vec{r})$ mapping experiment. Comparison of the topographs shows them to be virtually identical and demonstrates that no significant changes occur in the geometry of the tip during the map. The implication is that the nano-flake at the end of the tip never once touches the surface and that all such $I_c(\vec{r})$ studies reported are in the vacuum tunnelling limit.
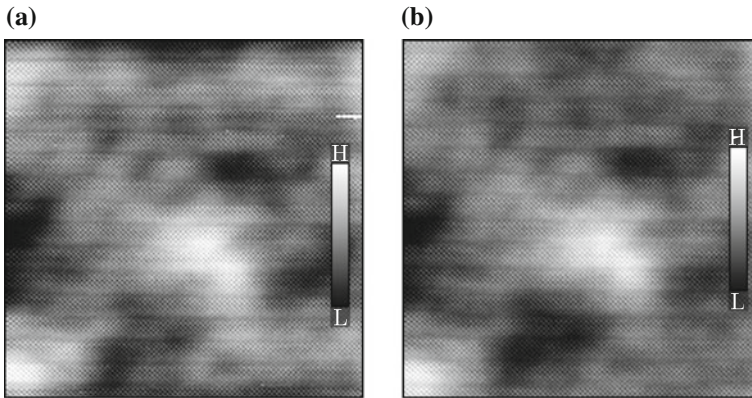
(a)   **(b)**

Fig. 5.14 a Topograph taken with $Bi_2Sr_2CaCu_2O_{8+\delta}$ tip before typical $I_c(\vec{r})$ SJTM map. **b** Topograph taken with same $Bi_2Sr_2CaCu_2O_{8+\delta}$ tip after the same $I_c(\vec{r})$ SJTM map. Comparison of **a** and **b** shows that tip and surface are very well preserved in our SJTM protocol

5.6 Experimental Josephson Current-Voltage Characteristics

In the following I will make predictions for the $I(V_B)$ and $I(V_{JJ})$ we expect to measure for Josephson tunnelling between a $Bi_2Sr_2CaCu_2O_{8+\delta}$ sample and the $Bi_2Sr_2CaCu_2O_{8+\delta}$ nano-flake tips characterised in the previous section. The physics of ultra-small Josephson junctions such as these was discussed in Sect. 5.3.1. The strong non-linearity of the $I(V_{JJ})$ characteristics expected for these Josephson junctions means that the form of $I(V_B)$ measured in experiments is very sensitive to other elements in the measurement circuit. Here I will include details of the measurement circuit used in our SJTM experiments and predict $I(V_B)$ and $I(V_{JJ})$ that can be compared directly with experiment.

Figure 5.15a shows a diagram of the hybrid STM/SJTM measurement circuit used in our experiments. A load resistor $R_B = 10\,M\Omega$ is biased, in series with the Josephson junction formed between the STM tip and the sample, by a voltage V_B. The tip-sample junction is represented by the parallel combination of an ideal Josephson element with intrinsic critical current, I_J, a junction capacitance, C_J, and non-linear resistor, $R(V_{JJ})$, that represents the SIS single-particle tunnelling channel. The voltage dropped across the junction is denoted as V_{JJ}. The ideal ammeter in this diagram is a low-noise current-to-voltage pre-amplifier in actual experiments, as detailed in Fig. 2.9.

To model the $I(V_B)$ characteristics of the circuit I will take the current due to incoherent Cooper-pair tunnelling, $I_P(V_{JJ})$, to be,

$$I_P(V_{JJ}) = aI_J^2 \frac{V_{JJ}}{V_{JJ}^2 + V_C^2} \,, \qquad (5.47)$$

which is the form predicted by Ivanchenko and Zi'lberman for classical phase diffusion in the limit $C_J \to 0$ (see Sect. 5.3.1) [24]. Here I use this function only as an approximate analytic form for the pair current because it exhibits a pair current peak at voltage $V_C \neq 0$ which scales in magnitude with I_J^2. As detailed in Sect. 5.3.4 these are generic features of ultra-small Josephson junctions in a low impedance environment and so this approach is justified. Equation 5.47 is not intended to be used to extract the absolute value of I_J.

Although the Josephson junction could be regarded as current biased due to the use of a large series resistance, it can be effectively treated as voltage biased, as discussed in detail in Sect. 5.3.2 [28, 30]. This is because the parasitic capacitance between the leads on either side of the junction, C_P, is typically much larger than the capacitance of the junction itself. As a result, the voltage across C_P can be well approximated as independent of time even though the current flowing through the Josephson junction consists of current spikes corresponding to tunnelling events. This renders the junction effectively voltage biased.
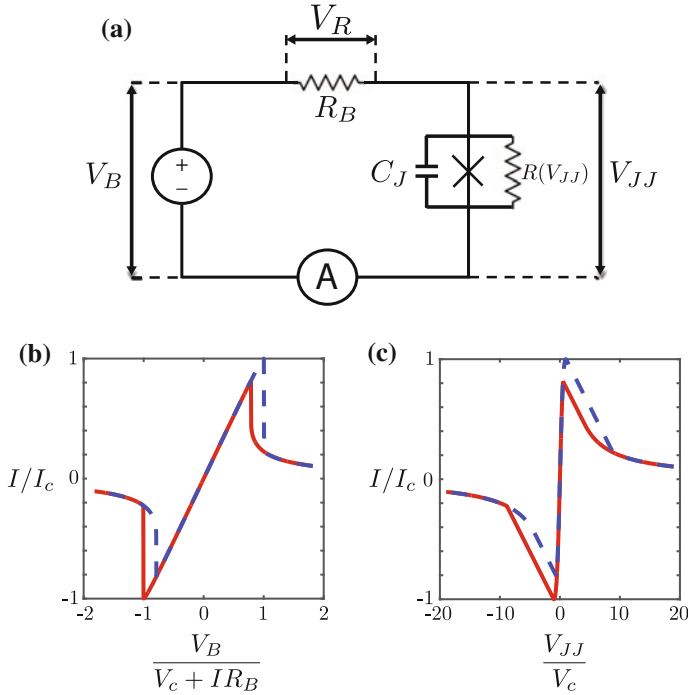
Fig. 5.15 **a** Circuit diagram of the hybrid STM/ SJTM setup used in these experiments. The voltage bias V_B is from the usual STM bias controller; the load resistor $R_B = 10\,\text{M}\Omega$; the single-particle tunnelling resistance of the Josephson junction formed between the tip and sample is $R(V_{JJ})$, and the voltage actually developed across the junction is V_{JJ}. **b** The dynamics of this circuit produces two predominant effects. First there is a discontinuous change in the $I(V_B)$ characteristic when the current reaches a value $I_c \propto I_J^2$ measured with the external ammeter shown. The second predicted effect is strong hysteresis depending on which direction the external voltage is swept; this is shown as the difference between the *solid-red* and *dashed-blue lines*. Both effects are seen very clearly and universally in the measured $I(V_B)$ throughout our studies. **c** The current as in **b** but plotted against the voltage across the Josephson junction V_{JJ}

The DC $I(V_B)$ for the circuit shown in Fig. 5.15a is then given by the simultaneous solution of

$$I = \frac{V_R}{R_B} = aI_J^2 \frac{V_{JJ}}{V_{JJ}^2 + V_C^2} \tag{5.48a}$$

and

$$V_B = V_R + V_{JJ}. \tag{5.48b}$$

We set $R(V_{JJ}) = \infty$ because the shunt provided by the SIS single-particle tunnelling channel has a characteristic resistance that is typically much larger than that of the Josephson junction for small V_{JJ}.

Fig. 5.16 Measured evolution of the SJTM $I(V_{JJ})$ with diminishing tip-sample distance (diminishing R_N) at $T = 45$ mK (junction formation conditions given in *blue* text). The maximum current I_c for a typical $I(V_{JJ})$ used in an $I_c(\vec{r})$ measurement is indicated by a *dashed green arrow*
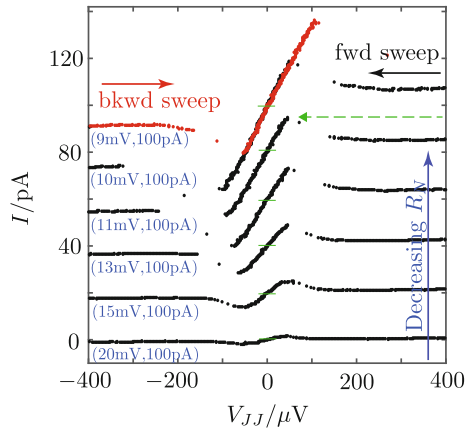
Figure 5.15b shows the numerical solutions to Eq. 5.48. The red and blue lines show the trajectories that the forwards and backwards sweeps take through the $I(V_B)$ plane. The non-linearity of the circuit introduces discontinuities in the measured $I(V_B)$. A discontinuity occurs at the point where the current reaches the maximum pair current that the junction can pass, $I = I_c$, and thus makes this current experimentally identifiable by the sharp $I(V_B)$ feature associated with it. Figure 5.15c shows the same trajectories but as a function of the voltage across the junction V_{JJ}.

This circuit's non-linearity also generates hysteresis in the $I(V_B)$ characteristic even if the dynamics of the Josephson junction itself are non-hysteretic. This hysteresis is indeed observed throughout our SJTM studies of $Bi_2Sr_2CaCu_2O_{8+\delta}$ and systematic errors due to the hysteresis are avoided during our $I = I_c(\vec{r})$ imaging experiments by sweeping the applied voltage always in the same direction once the Josephson junction has been formed at each location $\vec{r}$.

We are now in a position to compare the above predictions with the Josephson tunnelling signatures detected in our experiment. Figure 5.16 shows the $I(V_{JJ})$ characteristic between our $Bi_2Sr_2CaCu_2O_{8+\delta}$ nano-flake tip and a $Bi_2Sr_2CaCu_2O_{8+\delta}$ sample, for $T = 45$ mK and fixed $\vec{r}$, as a function of decreasing junction resistance, $R_J = V_s/I_s$, and thus decreasing tip-sample distance.

First notice that, as predicted in the previous section and with comparison to Fig. 5.15c, these $I(V_{JJ})$ curves have a sharp discontinuity at their maximum current and exhibit pronounced hysteresis. Further, as the Josephson critical current I_J increases with diminishing distance, the magnitude of the pair current peak increases as expected. These features are in accord with our predictions for $I(V_{JJ})$ arising from incoherent Cooper pair tunnelling between a superconducting tip and sample. Taken together they further demonstrate that our $Bi_2Sr_2CaCu_2O_{8+\delta}$ nano-flake tip is indeed superconducting.

As discussed in Sect. 5.3, the maximum Cooper pair current arising from incoherent Josephson tunnelling, I_c, is proportional to I_J^2 and I_J is directly proportional to the amplitude of the sample superconducting order parameter $|\Psi|$. Thus, I_c as
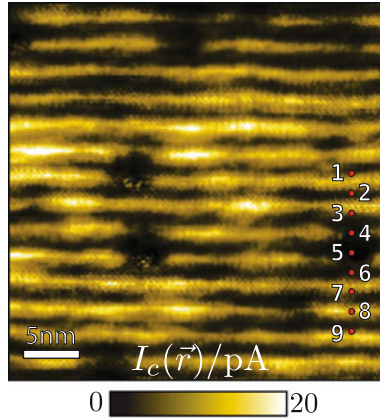
Fig. 5.17 Typical SJTM $I_c(\vec{r})$ measurement of $Bi_2Sr_2CaCu_2O_{8+\delta}$ sample with $p = 17\%$ using a $Bi_2Sr_2CaCu_2O_{8+\delta}$ nanoflake tip. Strong quasi-periodic modulations along the vertical axis are due to the $Bi_2Sr_2CaCu_2O_{8+\delta}$ bulk crystal super-modulation. Red dots numbered 1–9 pass through the location of zinc impurity atom and are the locations for a series of $I(V_B)$ curves shown in Fig. 5.19 that demonstrate the almost complete suppression of I_c at the impurity site

measured from one of our $I(V_{JJ})$ curves is related to the sample's superconducting order parameter through $I_c \propto |\Psi|^2 \propto \rho_s$, where ρ_s is the sample superfluid stiffness. This means that by measuring $I(V_{JJ})$ at a series of points across the surface of a sample it is possible to create a spectroscopic map, $I_c(\vec{r})$, that directly measures spatial variations in the superconducting condensate through $I_c(\vec{r}) \propto |\Psi(\vec{r})|^2 \propto \rho_s(\vec{r})$.

In general, we functionally define the quantity $I_c(\vec{r})$ to be the maximum magnitude of current achieved on sweeping away from $V_B = 0$ with the tip at position $\vec{r}$ on the surface. An example of an $I_c(\vec{r})$ map is shown in Fig. 5.17. The most immediately apparent features are a strong quasi-periodic modulation along the vertical axis and dark regions where I_c is almost completely suppressed. These are due to the $Bi_2Sr_2CaCu_2O_{8+\delta}$ bulk crystal super-modulation and individual Zn impurity atoms respectively. In the following section I will use these features to validate SJTM as a probe of the superconducting order parameter using their known effect on the superconductivity in $Bi_2Sr_2CaCu_2O_{8+\delta}$.

5.7   Validating SJTM as a Probe of the Order Parameter

The experiments reported in this chapter are the first that successfully map spatial variations in the superconducting order parameter with nanometre resolution using SJTM. As such, it is pertinent to validate our SJTM method as a faithful probe of spatial variations in the superfluid density, in a model independent way. In the following we achieve this using known features of the superconductivity in $Bi_2Sr_2CaCu_2O_{8+\delta}$,

namely a modulation of the superconducting gap with the bulk structural super-modulation and the suppression of the superfluid density at individual Zn impurity atoms.

5.7.1   Imaging the Suppression of $\Psi(\vec{r})$ at Individual Zinc Impurities

To test the Cooper-pair condensate visualisation capabilities of this $I_c(\vec{r})$ imaging technique directly, we use two approaches. First we study $I_c(\vec{r})$ in the vicinity of Zn impurity atoms. This is an excellent test of our technique because muon spin rotation studies have shown that the superfluid density is completely suppressed in a radius of a few nanometers around each Zn atom [36].

Figure 5.18a shows a 76 nm × 76 nm image of the SIS single-particle tunnelling conductance $g(\vec{r}, -20\,meV)$. One can locate each Zn impurity atom by its characteristic scattering resonance peak, which is shifted by convolution with the superconducting tip density of states from its resonance energy, $\Omega = 1.5\,meV$, to $|E| = \Omega + \Delta_T \approx 25\,meV$ (vertical red line in the inset to Fig. 5.18a) [37]. Thus, the Zn impurity atoms are at the dark spots in Fig. 5.18a.

In Fig. 5.18b I show $I_c(\vec{r})$ measured at 45 mK in the same field of view as Fig. 5.18a. This reveals how $I_c(\vec{r})$ is suppressed within a radius of approximately 3 nm around each Zn atom site. The evolution of measured $I(V_B)$ curves at a specific sequence of locations along a line passing through a Zn impurity is shown in Fig. 5.19. The almost complete ($\sim$95%) suppression of I_c as this sequence passes through the site of a Zn atom is seen in panel 5 of Fig. 5.19. These typical data demonstrate directly the unprocessed signal-to-noise ratio for measurement of I_c and how the spatial evolution of unprocessed $I(V_B)$ spectra yields the high fidelity seen in the $I_c(\vec{r})$ images.

The almost complete suppression of $I_c(\vec{r})$ at positions which are independently determined to be Zn impurity sites (through their single-particle tunnelling signature) is a model independent verification that $I_c(\vec{r})$ measured in our SJTM experiments is a faithful probe of variations in the superconducting order parameter.

5.7.2   Modulation of Superconductivity by the Bulk Structural Super-Modulation

A second test is possible because of the bulk crystal super-modulation at wave-vector $\vec{Q}_{SM}$ present in $Bi_2Sr_2CaCu_2O_{8+\delta}$ (see Sect. 2.6.1). One way in which this is manifest is the strong quasi-periodic modulations in the topograph $T(\vec{r})$, as shown using an normal tungsten tip in Fig. 5.20a. This super-modulation is known to modulate the single-particle tunnelling gap at the same wave-vector, as demonstrated by SIN

Fig. 5.18 **a** Single-particle SIS conductance map $g(r, E = -20\,\text{meV})$. The *inset* is the conductance spectrum at a Zinc impurity site. The convolution of $\Omega = 1.5\,\text{meV}$ Zn impurity resonance with the superconducting spectrum of the tip shifts the resonance to $|E| \approx |\Omega| + |\Delta_T|$. The measured SIS $g(r, E = -20\,\text{meV})$ image near this energy (*vertical red line*) identifies the site of each Zn. **b** $I_c(\vec{r})$ image measured at $45\,\text{mK}$ in the same field of view as **a**. A deep minimum ($\approx 95\%$ suppression) occurs in $I_c(\vec{r})$ surrounding each Zn site where the Cooper-pair condensate is suppressed. For visual clarity modulations at the wave-vector of the crystal super-modulation have been removed by the Fourier filtration method described in Sect. 2.8

(a)

(b)
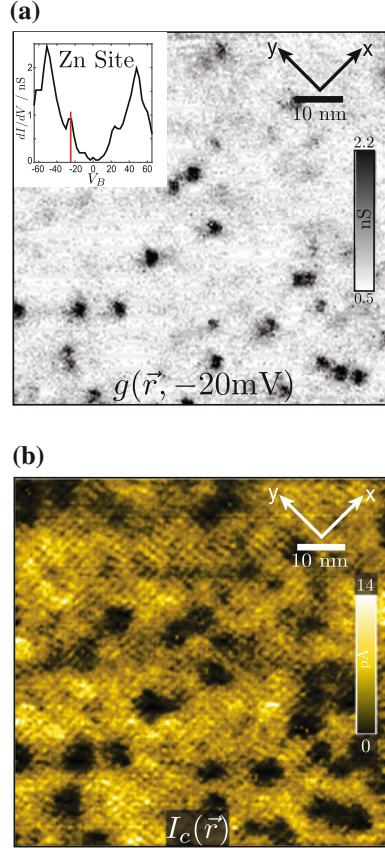
tunnelling measurements shown in Fig. 5.20c–f [38]. We searched for a concomitant modulation in $I_c(\vec{r})$ to further validate our cuprate SJTM method.

Turning back to measurements made with $Bi_2Sr_2CaCu_2O_{8+\delta}$ nano-flake tips, Fig. 5.21a shows clear modulations in I_c at $\vec{Q}_{SM}$. In Fig. 5.21b we plot the Fourier transform of the SIS topograph, $\tilde{T}(\vec{q})$, in grey and $\tilde{I}_c(\vec{q})$ in orange, both measured simultaneously along the (1,1) direction through $\vec{Q}_{SM}$. This directly demonstrates the capability of SJTM to visualise Cooper-pair density modulations induced by the $Bi_2Sr_2CaCu_2O_{8+\delta}$ crystal super-modulation.

Overall, these tests show that $I_c(\vec{r})$ faithfully measures spatial variations in the superconducting order parameter. Thus, we have achieved nanometer resolution Cooper pair condensate visualisation using our $Bi_2Sr_2CaCu_2O_{8+\delta}$ nano-flake tip SJTM approach.
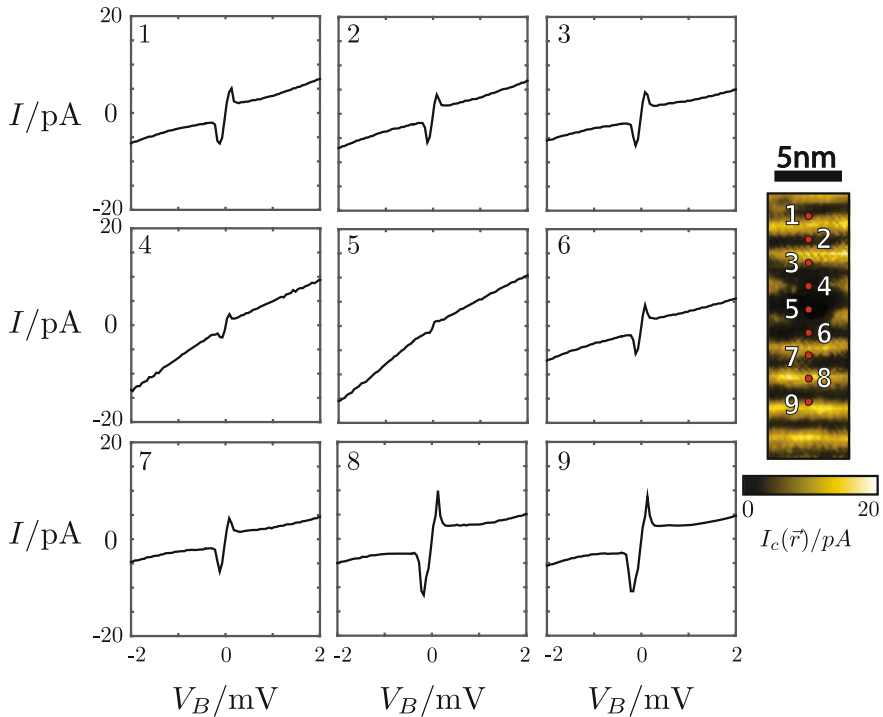
Fig. 5.19 Nine individual $I(V_B)$ spectra measured at the locations passing through a zinc impurity site, indicated by numbers 1–9 in the $I_c(\vec{r})$ image (*right hand side*). The $I_c(\vec{r})$ image is a small section of that shown in Fig. 5.17. As the sequence passes through the site of a Zn atom, the value of I_c diminishes by $\approx 95\%$ from its maximum, as expected from μSR experiments

5.8   Conclusions and Future Directions of SJTM

Using a $Bi_2Sr_2CaCu_2O_{8+\delta}$ nanoflake tip SJTM we have made the first direct, nanometer-resolution visualisation of the condensate in any superconductor. In doing so we have visualised the suppression of the superconducting order parameter at Zn impurities in $Bi_2Sr_2CaCu_2O_{8+\delta}$, confirming a well known result of μSR studies and validating our method.

5.8.1   Future State of the Art in Condensate Imaging

In detecting atomic-scale spatial variations in the superconducting condensate directly, our SJTM has fulfilled much of the promise it showed in its conception [2]. The next advance in the state of the art will be to achieve intra unit cell resolution imaging capabilities on a cuprate superconductor. Such resolution has recently
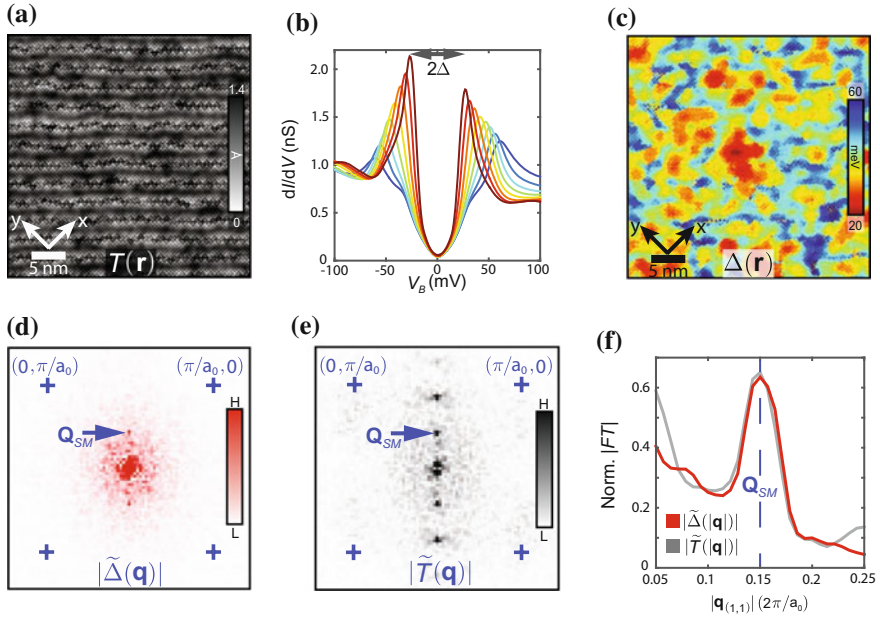
Fig. 5.20 **a** Typical 35 nm × 35 nm topographic image $T(\vec{r})$ of $Bi_2Sr_2CaCu_2O_{8+\delta}$ surface (crystal supermodulation runs vertically). **b** Typical $g(E) = dI/dV_B(E = eV)$ differential conductance spectra of $Bi_2Sr_2CaCu_2O_{8+\delta}$. The maximum energy gap Δ is half the distance between peaks. **c** $\Delta(\vec{r})$ (gapmap) for $p \sim 17\%$ $Bi_2Sr_2CaCu_2O_{8+\delta}$ in same field of view as **a**. **d** Magnitude of Fourier transform of **c**, $|\tilde{\Delta}(\vec{q})|$ (crosses at $q = (\pi/a_0, 0);(0, \pi/a_0)$) showing a single peak due to the super-modulation (*blue arrow*). **e** Fourier transform magnitude of topograph $|\tilde{T}(\vec{q})|$ (crosses at $q = (\pi/a_0, 0);(0, \pi/a_0)$). The super-modulation is a quasi-periodic modulation along the (1,1) direction with wavevector $\vec{Q}_{SM}$ indicated by *blue arrow*. **f** Simultaneously measured $|\tilde{\Delta}(\vec{q})|$ and $|\tilde{T}(\vec{q})|$ from **d**, **e** along the (1,1) direction. Their primary peaks coincide
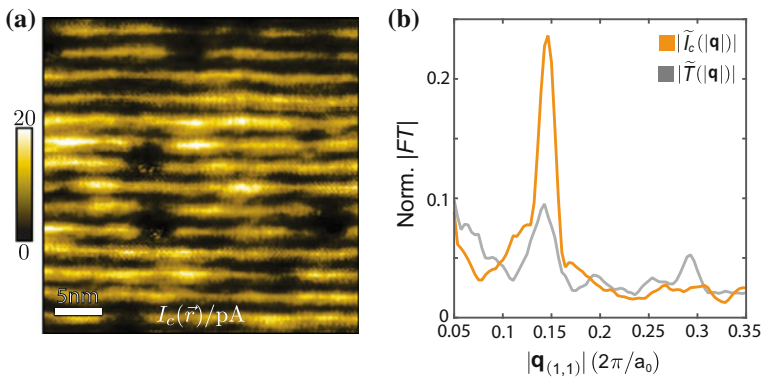
Fig. 5.21 **a** $I_c(\vec{r})$ map showing clear modulations at $\vec{Q}_{SM}$. **b** Simultaneously measured magnitude of $\tilde{I}_c(\vec{q})$ (Fourier transform of **a**) and $\tilde{T}(\vec{q})$ along the CuO_2 (1,1) direction. The primary peaks in $\tilde{I}_c(\vec{q})$ and $\tilde{T}(\vec{q})$ from the super-modulation coincide, demonstrating the ability of SJTM to visualise modulations in $\Psi(\vec{r})$

been achieved on the surface of lead, using a lead coated tungsten tip [14]. For cuprate SJTM however, our nanoflake tip approach is unlikely to ever yield intra unit cell resolution.

An obvious scheme to improve the resolution of cuprate SJTM would be to use a superconducting tip material that can be formed into a sharp point either mechanically or by chemical/physical etching. However, these materials typically have a superconducting gap that is at least an order of magnitude smaller than a $Bi_2Sr_2CaCu_2O_{8+\delta}$ nanoflake tip, greatly reducing I_c for a given junction resistance.

Furthermore, because the practical material choices are s-wave superconductors we expect a strong suppression of I_c (at a given junction resistance) due to the fact that the s-wave component, Δ_s of the cuprate order parameter ranges from $\Delta_s \approx 0 - 0.1\Delta_d$, depending on cuprate material [39, 40]. To achieve a similar magnitude of I_c as those reported here, the junction resistance would have to be greatly reduced.

The micaceous nature of $Bi_2Sr_2CaCu_2O_{8+\delta}$ makes its surface unstable to a sharp metallic tip at low junction resistances. However, $YBa_2Cu_3O_{6+x}$ has $\Delta_s \sim 0.1\Delta_d$ and a stable surface. This material, in combination with a conventional superconducting STM tip, could yield intra unit cell resolution cuprate SJTM.

5.8.2   *Inelastic Cooper-Pair Tunnelling Spectroscopy*

SJTM utilises the inelastic tunnelling of Cooper-pairs to access the superconducting order parameter. As discussed in Sect. 5.3.3, this is the simplest form of inelastic tunnelling because the Cooper-pair condensate does not form a continuum of initial and final states. This allows an easier route to determine the environmental impedance, $Z_t(\omega)$, than inelastic single-particle tunnelling spectroscopy.

While the super-current peak observed in our SJTM $I(V_{JJ})$ is a generic result of the small ohmic impedance provided by the environment, in principle we can detect resonances in $Z_t(\omega)$. Indeed, resonances arising from the antenna modes of the tip have already been observed in the Josephson tunnelling current [11, 12, 14].

If a molecule absorbed onto a superconducting substrate has an absorption line at a frequency ν, it could be detected in the inelastic Cooper-pair tunnelling current as a peak at $2eV_{JJ} = h\nu$. Alternatively the GHz radiation field emitted from a typical SJTM junction could be used in the coherent manipulation of single spins as suggested in Ref. [12], where large GHz photon fluxes have already been demonstrated. The principle advantage of performing atomically resolved spectroscopy or atomic manipulation of this kind with SJTM as opposed to a normal STM tip, is that the source and detector of high frequency signals is the junction itself. As such, normal low-temperature STM cryostats with wiring designed for low frequency signals can be used, greatly simplifying the experimental design.

References

1. M.H. Hamidian et al., Detection of a cooper-pair density wave in Bi2Sr2CaCu2O8+x. Nature **532**(7599), 343–347 (2016)
2. J. Šmakov, I. Martin, A.V. Balatsky, Josephson scanning tunneling microscopy. Phys. Rev. B **64**(21), 212506 (2001)
3. A. Yazdani et al., Probing the local effects of magnetic impurities on superconductivity. Science **275**(5307), 1767–1770 (1997)
4. M.I. Salkola, A.V. Balatsky, J.R. Schrieffer, Spectral properties of quasiparticle excitations induced by magnetic moments in superconductors. Phys. Rev. B **55**(18), 12648 (1997)
5. S.H. Ji et al., High-resolution scanning tunneling spectroscopy of magnetic impurity induced bound states in the superconducting gap of Pb thin films. Phys. Rev. Lett. **100**(22), 16–18 (2008)
6. K.J. Franke, G. Schulze, J.I. Pascual, Competition of superconducting phenomena and kondo screening at the nanoscale. Science **332**(6032), 940–944 (2011)
7. S.H. Pan et al., STM studies of the electronic structure of vortex cores in $Bi_2Sr_2CaCu_2O_8 + \delta$. Phys. Rev. Lett. **85**(7), 1536–1539 (2000)
8. O. Naaman, W. Teizer, R.C. Dynes, Fluctuation dominated Josephson tunneling with a scanning tunneling microscope. Phys. Rev. Lett. **87**(9), 097004 (2001)
9. J.G. Rodrigo, H. Suderow, S. Vieira, On the use of STM superconducting tips at very low temperatures. Eur. Phys. J. B **40**(4), 483–488 (2004)
10. T. Proslier et al., Probing the superconducting condensate on a nanometer scale. Europhys. Lett. **962**, 7 (2006)
11. A. Roychowdhury et al., Microwave photon-assisted incoherent cooper-pair tunneling in a Josephson STM. Phys. Rev. Appl. **4**(3), 1–7 (2015)
12. B. Jäck et al., A nanoscale gigahertz source realized with Josephson scanning tunneling microscopy. Appl. Phys. Lett. **106**(1), 013109 (2015)
13. B. Jäck et al., Critical Josephson current in the dynamical Coulomb blockade regime. Phys. Rev. B **93**(2), 020504 (2016)
14. M.T. Randeria et al., Scanning Josephson spectroscopy on the atomic scale (2016)
15. B. Josephson, Possible new effects in superconductive tunnelling. Phys. Lett. **1**(7), 251–253 (1962)
16. P.W. Anderson, J.M. Rowell, Probable observation of the Josephson superconducting tunneling effect. Phys. Rev. Lett. **10**(6), 230–232 (1963)
17. J. Bardeen, Tunneling into superconductors. Phys. Rev. Lett. **9**(4), 147–149 (1962)
18. M.H. Cohen, L.M. Falicov, J.C. Phillips, Superconductive tunneling. Phys. Rev. Lett. **8**(8), 316–318 (1962)
19. P.W. Anderson, Special Effects in Superconductivity (Academic Press Inc., Cambridge, 1964), pp. 113–135
20. L.P. Gor'kov. Microscopic Derivation of the Ginzburg–Landau Equations in the Theory of Superconductivity (1959)
21. W.C. Stewart, Current-voltage characteristics of Josephson junctions. Appl. Phys. Lett. **12**(8), 277–280 (1968)
22. D.E. McCumber, Effect of ac impedance on dc voltage-current characteristics of superconductor weak-link junctions. J. Appl. Phys. **39**(7), 3113–3118 (1968)
23. V. Ambegaokar, B.I. Halperin, Voltage due to thermal noise in the dc Josephson effect. Phys. Rev. Lett. **22**(25), 1364–1366 (1969)
24. Y.M. Ivanchenko, L.A. Zil'berman, The Josephson effect in small tunnel contacts. Soviet Phys. JETP **28**(6), 1272–1276 (1969)
25. M. Tinkham, *Introduction to Superconductivity* (McGraw-Hill Book Co., New York, 1975)
26. R.L. Kautz, J.M. Martinis, Noise-affected I - V curves in small hysteretic Josephson junctions. Phys. Rev. B **42**(16), 9903–9937 (1990)
27. J.M. Martinis, R.L. Kautz, Classical phase diffusion in small hysteretic Josephson junctions. Phys. Rev. Lett. **63**(14), 1507–1510 (1989)

28. H. Grabert, M.H. Devoret, in *Single Charge Tunneling*, vol. 294, NATO ASI Series, ed. by H. Grabert, M.H. Devoret (Springer, Boston, 1992)
29. A.N. Cleland, J.M. Schmidt, J. Clarke, Charge uctuations in smallcapacitance junctions. Phys. Rev. Lett. **64**(13), 1565–1568 (1990)
30. M. Devoret et al., Effect of the electromagnetic environment on the Coulomb blockade in ultrasmall tunnel junctions. Phys. Rev. **65**(15), 2015–2018 (1990)
31. G. Falci, V. Bubanja, G. Schön, Quantum tunnelling in small-capacitance Josephson junctions in a general electromagnetic environment. EPL (Europhys. Lett.) 109 (1991)
32. G. Falci, V. Bubanja, G. Schon, Quasiparticle and Cooper pair tunneling in small capacitance Josephson junctions. Z. Phys. B-Condens. Matter 85, 451–458 (1991)
33. G.L. Ingold, H. Grabert, Finite-temperature current-voltage characteristics of ultrasmall tunnel junctions. Europhys. Lett. (EPL) **14**(4), 371–376 (1991)
34. G.L. Ingold, H. Grabert, U. Eberhardt, Cooper-pair current through ultrasmall Josephson junctions. Phys. Rev. B **50**(1), 395–402 (1994)
35. A.O. Caldeira, A.J. Leggett, Quantum tunneling in a dissipative system. Ann. Phys. **149**, 374–456 (1983)
36. B. Nachumi et al., Muon spin relaxation studies of Zn-substitution effects in high-Tc cuprate superconductors. Phys. Rev. Lett. **77**, 5421–5424 (1996)
37. S.S. Pan et al., Imaging the effects of individual zinc impurity atoms on superconductivity in $Bi_2Sr_2CaCu_2O_8 + \delta$. Nature **403**(6771), 746–50 (2000)
38. J.A. Slezak et al., Imaging the impact on cuprate superconductivity of varying the interatomic distances within individual crystal unit cells. Proc. Natl. Acad. Sci. U.S.A. **105**(9), 3203–8 (2008)
39. H. Kimura et al., Josephson scanning tunneling microscopy: a local and direct probe of the superconducting order parameter. Phys. Rev. B **80**(14), 1–16 (2009)
40. A.G. Sun et al., Observation of Josephson pair tunneling between a high-Tc cuprate ($YBa_2Cu_3O_7 - \delta$) and a conventional superconductor (Pb). Phys. Rev. Lett. **72**(14), 2267–2270 (1994)

Chapter 6
Pair Density Waves in Cuprates

In this chapter I will define what is meant by a pair density wave (PDW). I will also discuss how the PDW couples to charge density wave, spin density wave and uniform superconducting orders. After reviewing the experimental evidence and theoretical proposals for a PDW in cuprate superconductors, I will discuss how to experimentally distinguish between these proposals.

6.1 The Pair Density Wave

In 1964 Fulde, Ferrel, Larkin and Ovchinnikov (FFLO) predicted a new state of matter: a superconductor where the pairing amplitude modulates periodically in space [1, 2]. The family of states with such a periodically modulating pairing amplitude are known as pair density waves [3]. Phenomenologically we can examine these states by expanding the pairing amplitude in order parameters,

$$
\begin{aligned}
\langle \hat{\psi}_\sigma^\dagger(\vec{r}_1)\hat{\psi}_{-\sigma}^\dagger(\vec{r}_2)\rangle &= F_0(\vec{r}_1 - \vec{r}_2)\Psi_0(\vec{R}) \\
&+ F_1(\vec{r}_1 - \vec{r}_2)\left[\Psi_{\vec{Q}_x}(\vec{R})e^{i\vec{Q}_x\cdot\vec{R}} + \Psi_{-\vec{Q}_x}(\vec{R})e^{-i\vec{Q}_x\cdot\vec{R}} + \Psi_{\vec{Q}_y}(\vec{R})e^{i\vec{Q}_y\cdot\vec{R}} + \Psi_{-\vec{Q}_y}(\vec{R})e^{-i\vec{Q}_y\cdot\vec{R}}\right] + \dots,
\end{aligned}
\tag{6.1}
$$

where $\hat{\psi}_\sigma^\dagger(\vec{r}_1)$ creates a quasi-particle of spin σ at location $\vec{r}_1$ and $\vec{R} = (\vec{r}_1 + \vec{r}_2)/2$. Ψ_0 is a complex scalar field corresponding to a uniform charge 2e superconductor. $\Psi_{\vec{Q}_x}$, $\Psi_{-\vec{Q}_x}$, $\Psi_{\vec{Q}_y}$ and $\Psi_{-\vec{Q}_y}$ are pair density wave (PDW) order parameters [3, 4]. They also are complex scalar fields, but they carry momenta $\vec{Q}_{\pm x}$ and $\vec{Q}_{\pm y}$ running along orthogonal directions $\vec{x}$ and $\vec{y}$.

With the uniform superconducting component Ψ_0 equal to zero, the PDW will itself break a global U(1) phase symmetry making the pair density wave a superconductor, capable of exhibiting flux quantisation and a Meissner effect. It will also breaks lattice translational symmetry and may additionally break lattice rotational

and time-reversal symmetry. In general $\Psi_{\vec{Q}}$ and $\Psi_{-\vec{Q}}$ are independent complex numbers so as to encode both the broken global U(1) phase symmetry that makes it a superconductor and the broken U(1) symmetry that corresponds to the phase of the spatial modulation.

Here I have chosen to consider a tetragonal system with quasi two-dimensional order so that the PDW wave-vectors lie in the square planes of the tetragonal lattice. In the context of the cuprate high-temperature superconductors $\vec{x}$ and $\vec{y}$ will be the two symmetry equivalent Cu-O directions in the CuO_2 planes. The symmetry of the uniform superconducting order parameter Ψ_0 is manifest in how $F_0(\vec{r}_1 - \vec{r}_2)$ transforms under a 90° rotation of the co-ordinate system. An $A_{1g}(s$-wave) order parameter is invariant under such a rotation whereas a B_{1g} ($d_{x^2-y^2}$) order parameter will change sign.

The function $F_1(\vec{r}_1 - \vec{r}_2)$ is the form factor of the PDW. As for the case of the CDW discussed in Chaps. 1 and 4, the fact that the PDW breaks translational symmetry means that its form factor is not sufficient in itself to determine which irreducible representation of the point group the PDW transforms as. However, if $F_1(\vec{r}_1 - \vec{r}_2)$ is even under 90° rotation then the PDW can be termed to have an s-wave symmetry form factor whereas if it is odd it has a d-wave symmetry form factor [5].

The expansion in Eq. 6.1 can be regarded as the wave-function of a Cooper-pair and thus the coordinate $\vec{R}$ as the centre of mass of the Cooper-pair. For the uniform superconducting component, Ψ_0, the conjugate momentum, $\vec{Q}$, of the Cooper-pair is zero, as we would expect from the pairing of quasi-particles at opposite momenta in BCS theory. In the PDW state the order parameters have non-zero momentum $\pm\vec{Q}_{x,y}$ associated with them because they arise from the pairing of quasi-particles at momenta $\vec{k}$ and $-\vec{k}+\vec{Q}$ to form a Cooper-pair with centre of mass momentum $\vec{Q}$. This is shown schematically in Fig. 6.1a.
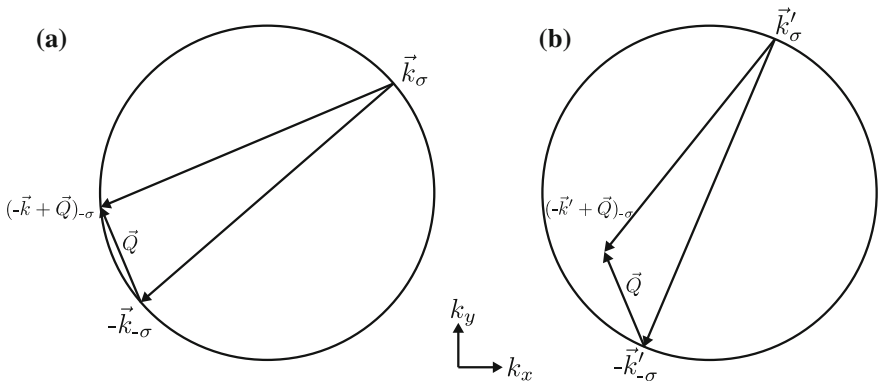
Fig. 6.1 a Schematic of Cooper pairing on a cylindrical Fermi surface, leading to the formation of PDW state. A quasi-particle with momentum $\vec{k}$ and spin σ pairs with another at momentum $-\vec{k}+\vec{Q}$ and spin $-\sigma$. They form a Cooper pair with centre of mass momentum $\vec{Q}$ and hence a PDW with wave-vector $\vec{Q}$. In general, there is no weak-coupling instability to the PDW state because $\vec{k}$ and $-\vec{k}+\vec{Q}$ only lie on the Fermi surface for one choice of $\vec{k}$ as depicted in **b**

In Chap. 1 I discussed how for arbitrarily weak effective interaction $U < 0$, the RPA particle-particle susceptibility

$$\chi_{pp}(\vec{q}, \omega) = \frac{\chi_{pp}^0(\vec{q}, \omega)}{1 + U\chi_{pp}^0(\vec{q}, \omega)} \, , \tag{6.2}$$

always diverges for finite temperature for $\vec{q}, \omega \to 0$. This is because, in the presence of time-reversal symmetry, the bare susceptibility χ_{pp}^0 diverges logarithmically with decreasing temperature, as discussed in Chap. 1. This famous "BCS log" leads to uniform superconducting phases such as that represented by Ψ_0. For finite momentum pairing there is, in general, no divergent susceptibility to particle-particle pairing based on fermiology alone, as was also the case for the particle-hole (CDW) susceptibility in dimension higher than one [6]. This is apparent in Fig. 6.1b from the fact that $\vec{k}' = -\vec{k} + \vec{Q}$ only lies on the Fermi surface for one choice of $\vec{k}$. Therefore we expect a phase transition to a PDW state only in the presence of a special Fermi surface or strong interactions between quasi-particles.

FFLO considered an example of a special Fermi surface, i.e. that of a metal in a large applied magnetic field [1]. Here, Fermi surfaces of opposite spin will be Zeeman split by an energy $g\mu_B B$, where g is the effective g-factor for quasi-particles in the normal metal (Fig. 6.2). If the material were to form a uniform superconductor, where the formation of spin-singlet Cooper pairs does not allow any magnetisation of the itinerant quasi-particles, the paramagnetic energy of the superconductor
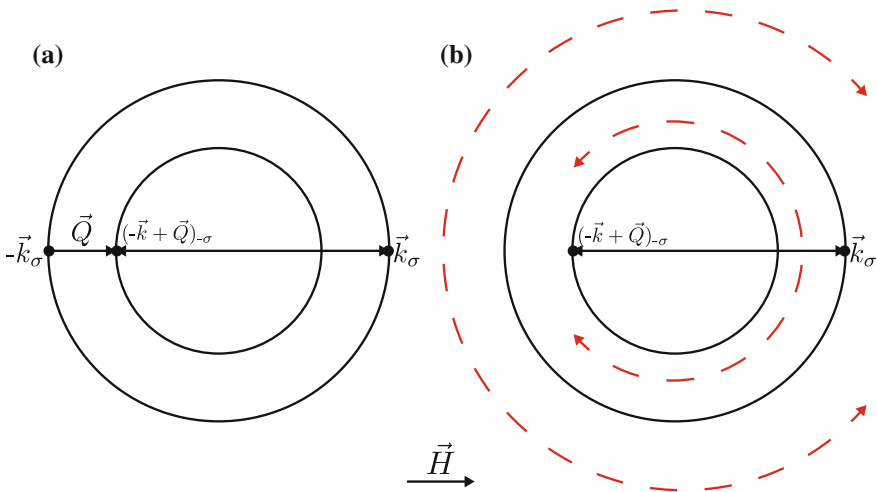
Fig. 6.2 **a** Spin singlet Cooper pairing between Zeeman split Fermi surfaces leads to the formation of an FF state with wave-vector $\vec{Q}_H \approx 2\mu_B \vec{H}/\hbar v_F$. **b** In such an FF state pairing only occurs on sections of the Fermi surface near the *black dots*, leaving large sections of Fermi surface un-paired as indicated by the *dashed red lines*. This allows for a net magnetisation and renders the condensation energy of the FF state less than that of the uniform BCS state

would be higher than that of the normal metal by $E_p = 1/2\chi_n H^2$ where χ_n is the spin-susceptibility of the normal metal and H the magnetic induction. However, the energy of the superconductor will be lowered from that of the normal metal by its condensation energy $E_{con} = 1/2N(0)\Delta_0^2$ [7], where Δ_0 is the BCS gap.

Somewhat rarely, it will be the competition between the energy scales E_p and E_{con} that determines the upper critical field H_{c2} of a type-II superconductor. If this were the only contribution to pair-breaking then at $T = 0$ we would expect a first-order phase transition between the superconducting and normal metal states when $E_p = E_{con}$, leading to a pauli-limited upper critical field $H_{c2}^p = \sqrt{2}\Delta_0/g\mu_B$ [8, 9]. The more usual situation is that H_{c2} is dominated by the orbital contribution; that is the decrease in condensation energy caused by the kinetic energy of the super-currents surrounding the vortex cores. In the case where the upper critical field is determined only by this orbital contribution, the upper critical field $H_{c2}^{orb} = \Phi_0/2\pi\xi^2$ is reached when vortex cores overlap [63]. The relative importance of these two contributions can be measured by the Maki parameter [63]

$$\alpha = \sqrt{2}\frac{H_{c2}^{orb}}{H_{c2}^p} \ . \tag{6.3}$$

Fulde and Ferrel noted that for materials with $\alpha \ll 1$ superconductivity can be extended to magnetic fields larger than H_{c2}^p by forming a pair density wave state,

$$\langle\psi_\sigma^\dagger(\vec{r}_1)\psi_{-\sigma}^\dagger(\vec{r}_2)\rangle = \Psi_{\vec{Q}_H}e^{i\vec{Q}_H\cdot\vec{R}} \ , \tag{6.4}$$

where pairing between sections of the Zeeman split Fermi surfaces results in Cooper-pairs with centre-of-mass momentum $\vec{Q}_H \approx 2\mu_B\vec{H}/\hbar v_F$ [1]. This is shown schematically in Fig. 6.2a. In this Fulde-Ferrel (FF) state the magnitude of the superconducting order parameter is constant, while its phase rotates with period $2\pi/|\vec{Q}_H|$. As shown in Fig. 6.2b, only part of the Fermi surface is paired in this state with the other de-paired sections allowing a net magnetisation. While the condensation energy of the FF state is less than that of the uniform BCS state, this net magnetisation reduces the Zeeman energy and leads the FF state to be favoured over the uniform BCS state at high fields.

The FF state breaks time-reversal symmetry by including a modulation of the pairing amplitude at $\vec{Q}_H$ but not $-\vec{Q}_H$. Larkin and Ovchinnikov considered a state that preserves time-reversal symmetry by taking a linear combination of these two degenerate states to give

$$\langle\hat{\psi}_\sigma^\dagger(\vec{r}_1)\hat{\psi}_{-\sigma}^\dagger(\vec{r}_2)\rangle = \Psi_{\vec{Q}_H}e^{i\vec{Q}_H\cdot\vec{R}} + \Psi_{-\vec{Q}_H}e^{-i\vec{Q}_H\cdot\vec{R}} \tag{6.5}$$

with $\Psi_{-\vec{Q}_H} = \Psi*_{\vec{Q}_H}$ [2]. This state has a lower free-energy than the FF state (Eq. 6.4) [9]. In contrast to the FF state, in the LO state the density of Cooper-pairs is modulated.

Despite decades of searching there is still no unambiguous detection of an FFLO state in a superconductor, though its signatures have been detected ultra-cold ^{6}Li gas [10]. This is likely because the conditions under which it can be formed are rather stringent. The superconductor must be strongly type-II and have a small Maki parameter. Additionally it must be very clean, because the FFLO state is readily destroyed by disorder [9]. The strongest contenders for fulfilling these criteria are heavy fermion superconductors and organic superconductors. The status of the search for such a phase in these materials is reviewed in detail by Matsuda and Shimahara in reference [9]. Although there is a great deal of indirect evidence suggesting the existence of an FFLO phase, there is no consensus that an FFLO phase has been observed.

The states considered by FFLO are just two of a number of possible PDW states. By writing down the Ginzburg-Landau expansion for the free-energy density of the PDW we can examine the range of possible states. For a quasi-two dimensional system with square lattice planes this is

$$
f = \alpha \sum_i |\Psi_{\vec{Q}_i}|^2 + \beta_1 \left(\sum_i |\Psi_{\vec{Q}_i}|^2 \right)^2 + \beta_2 \sum_{i<j} |\Psi_{\vec{Q}_i}|^2 |\Psi_{\vec{Q}_j}|^2 + \beta_3 \left(|\Psi_{\vec{Q}_x}|^2 |\Psi_{-\vec{Q}_x}|^2 + |\Psi_{\vec{Q}_y}|^2 |\Psi_{-\vec{Q}_y}|^2 \right)
$$

$$
+ \beta_4 \left[\Psi_{\vec{Q}_x} \Psi_{-\vec{Q}_x} \left(\Psi_{\vec{Q}_y} \Psi_{-\vec{Q}_y} \right)^* + \left(\Psi_{\vec{Q}_x} \Psi_{-\vec{Q}_x} \right)^* \Psi_{\vec{Q}_y} \Psi_{-\vec{Q}_y} \right]
$$

$$
+ \kappa_1 \sum_i |\vec{D}\Psi_{\vec{Q}_i}|^2 + \kappa_2 \sum_i (-1)^i \left[|D_x \Psi_{\vec{Q}_i}|^2 - |D_y \Psi_{\vec{Q}_i}|^2 \right] + \kappa_3 \sum_i |D_z \Psi_{\vec{Q}_i}|^2 + \frac{1}{2} (\nabla \times \vec{A})^2 , \quad (6.6)
$$

where $(-1)^i$ is -1 for $\vec{Q}_i = \pm \vec{Q}_x$ and 1 for $\vec{Q}_i = \pm \vec{Q}_y$ with $\vec{D} = -i\nabla - 2e\vec{A}$ and $\vec{B} = \nabla \times \vec{A}$.

The possible PDW phases resulting from this free-energy density in Eq. 6.6 are listed in Table 6.1. The FF and LO states discussed above are numbered 1 and 3 respectively. In Sect. 6.4 I will explicitly discuss the coupling of the PDW order parameter to that of a charge density wave (CDW) and spin density wave (SDW), with the result that different PDW states will induce CDW and SDW at different wave-vectors. These results are summarised in Table 6.1 and may be used as a tool to differentiate between different PDW states [3].

Table 6.1 Possible PDW phases (numbered 1–5) allowed by the free energy density in Eq. 6.6. These phases will induce CDW and SDW at the wave-vectors listed in the table due to their symmetry allowed coupling to the PDW in the free energy density as detailed in Sect. 6.4

Phase	$\Psi_{\vec{Q}_x}$	$\Psi_{\vec{Q}_y}$	$\Psi_{-\vec{Q}_x}$	$\Psi_{-\vec{Q}_y}$	CDW Modes	SDW Modes
1	$e^{i\phi_1}$	0	0	0	None	None
2	$e^{i\phi_1}$	$e^{i\phi_2}$	0	0	$\rho_{\vec{Q}_x - \vec{Q}_y}$	$S^Z_{\vec{Q}_x - \vec{Q}_y}$
3	$e^{i\phi_1}$	0	$e^{i\phi_2}$	0	$\rho_{2\vec{Q}_x}$	None
4	$e^{i\phi_1}$	$e^{i\phi_2}$	$e^{i\phi_3}$	$e^{i[\phi_1+\phi_3-\phi_2]}$	$\rho_{2\vec{Q}_x}, \rho_{2\vec{Q}_y}, \rho_{\vec{Q}_x - \vec{Q}_y}$	None
5	$e^{i\phi_1}$	$ie^{i\phi_2}$	$e^{i\phi_3}$	$ie^{i[\phi_1+\phi_3-\phi_2]}$	$\rho_{2\vec{Q}_x}, \rho_{2\vec{Q}_y}$	$S^Z_{\vec{Q}_x - \vec{Q}_y}, S^Z_{\vec{Q}_x + \vec{Q}_y}$

Clearly the case considered by FFLO is a very special situation and in general we do not expect PDW formation in weakly coupled superconductors. However, we might still expect a divergent susceptibility to a PDW state to arise from a strongly correlated many-body state. It has been proposed that a PDW exists in the cuprates for this very reason. In the following sections I will review the experimental evidence and theoretical proposals for the cuprate PDW.

6.2 Experimental Evidence for a Cuprate PDW

Prior to the new results presented in Chap. 7 there was no direct evidence for a spatially modulating pairing amplitude in the cuprates. However, there were many intriguing pieces of indirect experimental evidence that led to proposals of a PDW in cuprates. In this section I will review this evidence before going on to discuss the various theoretical proposals for the cuprate PDW state in the next section.

6.2.1 Decoupling of Superconductivity Between the CuO_2 Planes

The strongest evidence for a PDW state comes from the group of cuprate materials based on the insulator La_2CuO_4. Many of these materials form "stripe" order where co-linear anti-ferromagnetic spin and charge modulations $\vec{Q}_s$ and $\vec{Q}_c$ exist with the relationship $\vec{Q}_c = 2\vec{Q}_s \approx (\frac{1}{4}, 0); (0, \frac{1}{4})$ [11]. The stripe order is strongest in the vicinity of hole-doping $p \approx 1/8$ where there is an anomalous suppression in the bulk superconducting T_c, known as the "1/8th anomaly" [12]. The principal observation pointing to PDW order in these materials is that there are many signatures that the individual CuO_2 planes become superconducting at a temperature much higher than the bulk T_c.

In $La_{2-x}Ba_xCuO_4$ a large anisotropy between the in-plane resistivity, ρ_{ab}, and out-of-plane resistivity, ρ_c, onsets at the same temperature as spin-stripe order $T_{spin} = 42K$ [13]. This anisotropy is most pronounced in the temperature range $10K < T < 16K$. Here ρ_{ab} is, to within error, zero; whilst ρ_c has a value characteristic of a bad metal (1-10mΩcm). For $16K < T < T_{spin}$, ρ_{ab} exhibits a temperature dependence that fits that predicted above a Berezinskii-Kosterlitz-Thouless transition, indicating that superconducting fluctuations are confined to the 2D planes.

Similarly, below T_{spin} a diamagnetic response is seen in the magnetic susceptibility for fields perpendicular to the CuO_2 planes (requiring screening currents in the plane) whereas none is seen for a field within the planes (requiring screening currents along the c-axis) [14]. Together, these observations are highly indicative of the fact that superconductivity onsets within the CuO_2 planes at a temperature significantly higher than the bulk T_c.

On tuning, by chemical doping, to within the stripe-ordered region of the phase diagram there is also strong suppression of the superfluid stiffness along the c-axis [15]. The layered, quasi-2D nature of the cuprate superconductors means that their response to an electric field polarised along the c-axis can be modeled as a stack of intrinsic Josephson junctions where the CuO_2 planes are the superconducting electrodes, separated by weak links formed by the dopant layers [16].

As discussed in Sect. 5.3.1, the dynamics of a Josephson junction are analogous to that of a damped pendulum with resonant Josephson plasma frequency $\hbar\omega_J = \sqrt{2E_J E_C}$, where E_J is the Josephson coupling energy and E_C the capacitive charging energy. In c-axis polarised optical spectroscopy, this leads to an adsorption edge with frequency proportional to $\sqrt{E_J}$ for fixed interlayer capacitance. This is known as the Josephson plasma resonance.

In $La_{1.85-y}Nd_y Sr_{0.15}CuO_4$ the Josephson plasma resonance rapidly shifts to lower frequencies as y is increased towards the stripe-ordered region. Upon exceeding the critical Nd concentration where stripe-order is stabilised, the Josephson plasma resonance all but disappears [15]. Furthermore, when a c-axis magnetic field is applied to $La_{1.9}Sr_{0.1}CuO_4$ there is a pronounced reduction of the Josephson plasma resonance frequency while the in-plane superfluid density shows little change [17]. These results point towards a situation where entry into the stripe-ordered phase strongly suppresses the Josephson coupling between adjacent CuO_2 planes, so that the bulk T_c for 3D superconductivity is much less than that at which the CuO_2 planes themselves become superconducting.

It has been proposed that the frustration of interlayer Josephson coupling needed to explain these anomalous observations would naturally be provided by the existence of a particular PDW state within the stripe-ordered region of the La_2CuO_4 family phase diagram [18, 19]. What is known experimentally is that co-linear CDW and SDW order with wave-vectors along the Cu-O directions exists with periodicity $\approx 4a_0$ and $8a_0$ respectively [11]. This is attributed to the segregation of holes in the CuO_2 plane into regions of un-doped antiferromagnetic insulator separated by domain walls of holes with a periodicity of $4a_0$ [20].

Across the domain walls the (π, π) anti-ferromagnetism undergoes a π phase-shift resulting in an SDW periodicity of $8a_0$. The picture put forward by Berg et al. is that the hole rich regions superconduct but are separated by regions of correlated insulator that result in a negative Josephson coupling between them. This leads to a π phase-shift of the pairing amplitude across the insulating region. The result of this is a spatially modulated superconducting order parameter with periodicity $8a_0$ and a mean of zero.

In the low temperature tetragonal (LTT) phase of $La_{2-x}Ba_x CuO_4$ where stripe-order is found there are two CuO_2 planes per unit cell [21, 22]. It is widely thought that the stripes are orthogonal in adjacent planes and that the stripes are offset from each other by $2a_0$ in adjacent unit cells to minimise coulomb repulsion as shown in Fig. 6.3 [20]. This would lead to an exact cancellation of the Josephson coupling between the first, second and third neighbour planes [19].

(a)

$$\rho_c/\rho_{ab} \sim 2 \times 10^3$$

$T_{\text{co}} = 54\text{K}$

$$\rho_c/\rho_{ab} \sim 5 \times 10^3$$

$T_{\text{spin}} = 42\text{K}$

$$\rho_c/\rho_{ab} \sim 8 \times 10^4$$

$T^{**} = 35\text{K}$

$$\rho_{ab} \sim 10 \times 10^{-3}\text{m}\Omega\text{cm}$$
$$\max\{\rho_c\} \sim 8 \times 10^2\text{m}\Omega\text{cm}$$

$T_{\text{KT}} = 16\text{K}$

$$\rho_{ab} \sim 0 \; \rho_c \sim 10\text{m}\Omega\text{cm}$$

$T_{3D} = 10\text{K}$

$$\rho_{ab} \sim 0 \; \rho_c \sim 0$$

$T_c = 4\text{K}$

Meissner State

0K

(b)

$4a_0$

[001]

[010]

[100]
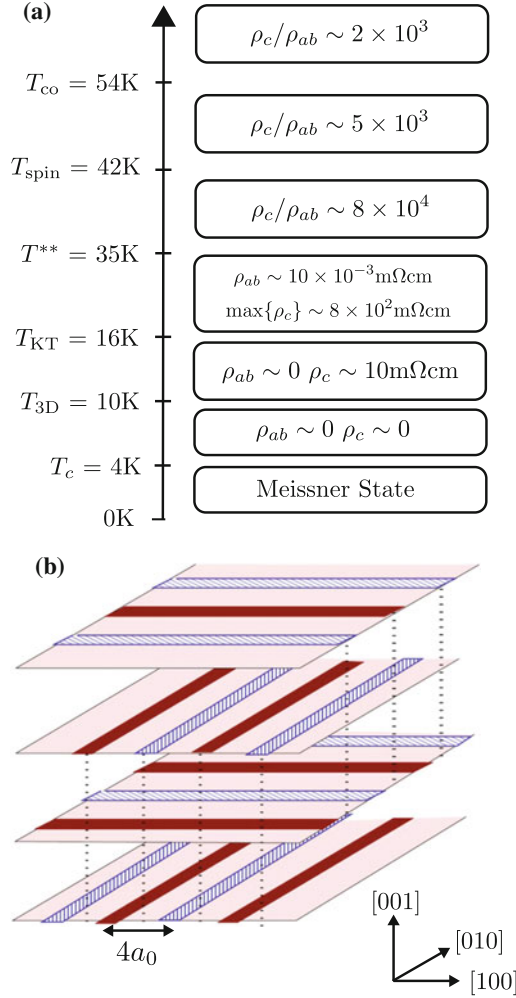
Fig. 6.3 a Hierarchy of temperature scales associated with spin-stripe order at $x = 1/8$ in La$_{2-x}$Ba$_x$CuO$_4$. A large resistivity anisotropy sets in below T_{spin}. For 10K < T < 16K the in plane resistivity, ρ_{ab}, is zero to within error whilst the out-of-plane resistivity, ρ_c, takes the value of a bad metal. This indicates that CuO$_2$ planes themselves are superconducting at temperatures above T_c. A PDW state has been proposed to explain these observations [19]. **b** Schematic of the PDW state proposed to exist in the spin stripe ordered state at $x = 1/8$ in La$_{2-x}$Ba$_x$CuO$_4$. *Pink* areas depict regions of un-doped antiferromagnetic insulator. *Red* and *grey* regions are domain walls between the insulator regions where holes aggregate at intervals of $4a_0$ forming a CDW with $\vec{Q}_C = (\frac{1}{4}, 0); (0, \frac{1}{4})\frac{2\pi}{a_0}$. These hole-rich regions are superconducting. *Red* and *grey* depict a superconducting order parameter of opposite sign. The state is hence a PDW (of the LO type) with wave-vector $\vec{Q}_P = (\frac{1}{8}, 0); (0, \frac{1}{8})\frac{2\pi}{a_0}$. The stripes are thought to be orthogonal in nearest neighbour layers due to the LTT crystal structure [11, 21, 22] and stripes in 2nd nearest neighbour layers are offset by 2a$_0$ [20]. The *dashed lines* demonstrate that this configuration leads to a cancellation of the c-axis Josephson coupling between first, second and third nearest neighbours. Figure adapted with permission from reference [19]

Within the planes however, a sufficiently long range ordered PDW state would exhibit many of the same properties as a uniform superconductor such as zero resistance, a Meissner effect and flux quantisation [4], due to its broken gauge symmetry. As such, this specific PDW proposal for the stripe ordered cuprates would offer an explanation for the observed resistivity anisotropy and suppression of the Josephson plasma resonance.

Is is natural to ask whether cuprate materials beyond the La_2CuO_4 family exhibit the same phenomenology, thus suggesting that a PDW is ubiquitous in cuprates. The answer is that there are similar signatures but they are much less clear. In $YBa_2Cu_3O_{6+\delta}$ there is evidence for a Josephson plasma resonance at temperatures far above the bulk T_c [23]. There are also magnetisation studies in high magnetic fields that are interpreted as pointing towards PDW correlations [24]. However, beyond the La_2CuO_4 family of cuprates, the most persuasive arguments for the existence of a PDW come from the interpretation of photoemission spectra, which I will now discuss.

6.2.2 Photoemission Spectra

P. A. Lee has put forward a detailed argument that the anti-nodal gap present for $T < T^*$, as observed by ARPES on $Bi_2Sr_2CuO_{6+\delta}$, is compatible with a PDW and incompatible with a CDW or uniform d-wave pairing [25].

At temperatures above T^* a full Fermi surface is observed [26]. For a series of cuts parallel to $\vec{k}_x$ in momentum space (Fig. 6.4a) the dispersion of this band is shown as red points in Fig. 6.4b–e. Clear Fermi momenta k_{F1} and k_{F2} can be determined from where this band crosses the Fermi energy.

For $T_c < T < T^*$ a pseudo-gap opens in the (1,0) directions leaving only arcs of spectral weight along the sections of Fermi surface proximal to the (1,1) directions [27]. The tips of these Fermi arcs are formed when a band moves up to touch the Fermi level from below. At the tip of the arc, the gap to excitations is above the chemical potential. This is incompatible with a mean-field CDW order parameter which would produce a gap below the Fermi energy at these locations [25, 28].

For $T < T_c$ the whole Fermi surface is gapped except at the nodes along the (1,1) directions. Near these nodes a particle-hole symmetric gap is observed that is consistent with a $d_{x^2-y^2}$ superconducting gap [26, 29–32]. The spectrum of excitations below the Fermi energy exhibits maxima at momenta k_{G1} and k_{G2} that are approximately equal to k_{F1} and k_{F2} [26]. Such "back-bending" is familiar from the Bogoliubov spectrum of the BCS Hamiltonian, discussed in Sect. 1.1.2. However, in the anti-nodal region k_{G1} and k_{G2} diverge from k_{F1} and k_{F2} with increasing proximity to the anti-node [26]. This suggests that the anti-nodal gap does not have its origins in $\vec{Q} = 0$ (uniform) superconductivity.

Taken together, these features indicate that the anti-nodal gap does not originate from a CDW or $\vec{Q} = 0$ pairing. Lee explicitly calculates that for an $\approx 8a_0$ unit cell
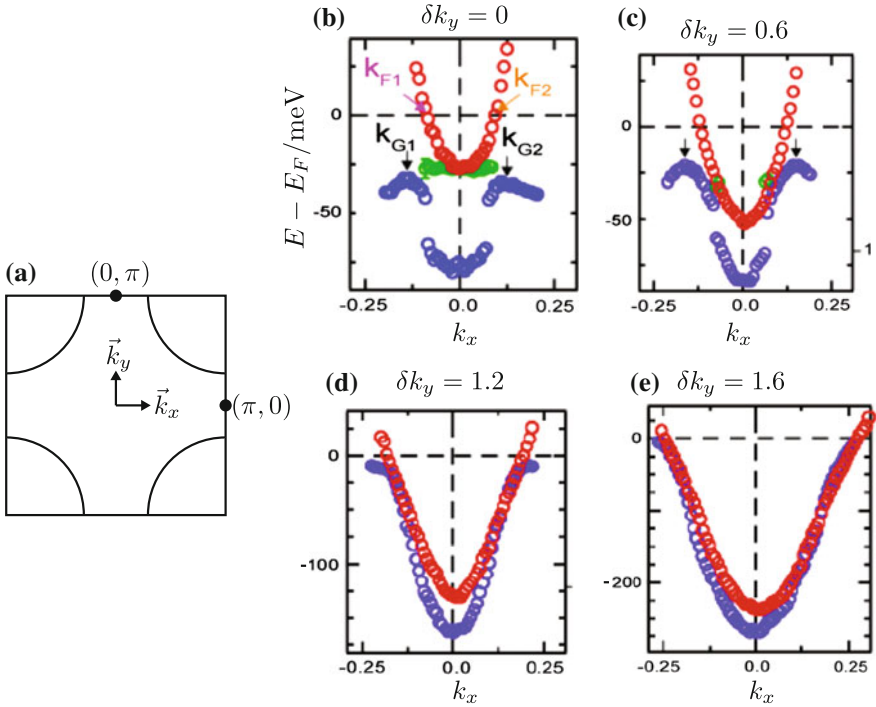
Fig. 6.4 a Schematic Brillouin zone for the single layer cuprate $Bi_2Sr_2CuO_{6+\delta}$ showing a full, hole-like, Fermi surface. **b–e** ARPES data on $Bi_2Sr_2CuO_{6+\delta}$ from R. He et al. [26] reproduced with permission from reference [25]. The four panels show data extracted dispersions for cuts in momentum space parallel to $\vec{k}_x$ at $\delta\vec{k}_y = \pi - \vec{k}_y$. Red circles show the dispersion of the full Fermi surface observed for $T > T^*$. Fermi momenta k_{F1} and k_{F2} are extracted from the points where this band crosses the Fermi energy (E_F). Blue circles show the dispersion of the band below the Fermi energy that is observed for $T < T_c$. It exhibits maxima at momenta k_{G1} and k_{G2} that diverge from k_{F1} and k_{F2} with increasing proximity to the anti-node. This indicates that the anti-nodal gap is not a result of uniform d-wave pairing (see text)

LO type PDW, driven by a mechanism he calls Amperean pairing (see Sect. 6.5.3), all qualitative features of the photoemission spectra can be reproduced [25].

Having reviewed the experimental evidence for a PDW in cuprates, I will now discuss theoretical proposals for how it may arise.

6.3   Coupled Order Parameters

The cuprates habour many putative broken symmetries. The list includes superconducting phase, lattice translational, point group and time-reversal symmetries as well as combinations thereof [33]. Ideally we would like to formulate a description of (at

least parts of) the cuprate phase diagram in terms of a minimal set of order parameters whose couplings to each other produce the full complexity of the system. In this section I will discuss how PDW order couples to other order parameters and hence how it may fit into such a framework.

A common situation in modern condensed matter physics is to be faced with a material where multiple degrees of freedom break a symmetry and to ask the question "which degrees of freedom are in the driving seat and which go along for the ride?" [6, 34]. It is sometimes useful to cast this question in terms of primary and secondary order parameters. To understand what that means one can consider the following free energy expansion,

$$F[\Psi_1, \Psi_2] = \frac{1}{2}\chi_1^{-1}\Psi_1^2 + \frac{1}{4}b\Psi_1^4 + \frac{1}{2}\chi_2^{-1}\Psi_2^2 + \lambda_{12}\Psi_1\Psi_2 + \dots, \qquad (6.7)$$

where Ψ_1 and Ψ_2 are real order parameters. χ_1^{-1} goes to zero at $T = T_c$ and is negative for $T < T_c$. In contrast, χ_2^{-1} and b are positive for all T. For $T < T_c$ the free energy will be minimised by Ψ_1 taking on a non-zero value and spontaneously breaking a $\mathbb{Z}_2$ symmetry. $\mathbb{Z}_n$ refers to an invariance of the free energy under rotations by $2\pi/n$, which for $n = 2$ is the symmetry of the Ising model.

Considering the third term in Eq. 6.7 in isolation, it always raises the free energy to make $\Psi_2 \neq 0$. However, if you consider the coupling term $\lambda_{12}\Psi_1\Psi_2$ then as long as $\Psi_1 \neq 0$ there is always some small non-zero Ψ_2,

$$\Psi_2 = -\chi_2\lambda_{12}\Psi_1 \,, \qquad (6.8)$$

that lowers the free energy regardless of the sign of λ_{12}. This is because Ψ_2 enters the Landau expansion at linear order. Thus in this example, Ψ_2 orders concurrently with Ψ_1 even though it would never have ordered in and of itself. Here we would term Ψ_1 a primary order parameter that induces secondary order in Ψ_2.

The question of which order parameter is in the driving seat is only meaningful if the coupling λ_{12} is relatively small. Otherwise the reduction in free energy from the coupling term can be comparable to that of the quadratic term of the "primary" order parameter. In this case neither order parameter is "in the driving seat", rather they are "intertwined" in a single microscopic instability towards both orders [6].

Nevertheless it can still be useful to describe the thermodynamics of a system in terms of a set of primary order parameters whose products form accompanying secondary orders. For example, as I will shown in Sect. 6.4, a CDW with wave-vector $2\vec{Q}$ can be expressed as a product of PDW order parameters $\Psi_{-\vec{Q}}^*\Psi_{\vec{Q}}$. While this is largely a matter of convenience and economy, if a PDW exists anywhere in the phase diagram (in a region where $\Psi_0 = 0$) then it should be regarded as primary. A pure PDW phase can only be expressed as a composite of uniform superconductivity and CDW by fractionalisation [6].

This prescription also allows for the fact that these secondary order parameters, which are expressed as products of the primary order parameters, may have non-

zero expectation even if the expectation of the primary order parameters themselves vanish. This can occur because for a general observable O, $\langle O^2 \rangle \not\equiv \langle O \rangle^2$.

For instance, a stripe-CDW ($\langle \Psi_{\vec{Q}_x} \rangle \neq 0$, $\langle \Psi_{\vec{Q}_y} \rangle = 0$) breaks rotational and translational symmetry. This stripe-CDW phase can "melt" via two transitions [35]. At the first transition, translation symmetry is restored ($\langle \rho_{\vec{Q}_x} \rangle = 0$) but rotational symmetry is still broken in what is called a nematic phase. In the nematic phase the rotational symmetry breaking is encoded in the nematic order parameter $\mathcal{N} = \langle |\rho_x|^2 \rangle - \langle |\rho_y|^2 \rangle$ which is non-zero even though $\langle \rho_x \rangle = \langle \rho_y \rangle = 0$ [35]. At higher temperatures still a second transition will restore the rotational symmetry.

Having considered conceptually how order parameters couple, I will now go on to discuss the coupling of the PDW to other order parameters.

6.4 Coupling of PDW to Other Order Parameters

In discussing the coupling of a PDW to other order parameters I will, for brevity, consider only uniform superconductivity, CDW and SDW. These are ordering tendencies that are unambiguously experimentally confirmed to exist at zero magnetic field in at least some, if not all, cuprate materials [36, 37].

6.4.1 Coupling to CDW

CDW and PDW order parameters $\rho_{\vec{Q}}$ and $\Psi_{-\vec{Q}}$ may not couple bi-linearly. Although they carry opposite momenta, making the product $\rho_{\vec{Q}} \Psi_{-\vec{Q}}$ translationally invariant, this term is not invariant under phase symmetry transformations. The lowest order coupling that can be admitted is a product of two PDW and one CDW order parameters [3]. The CDW therefore provides an additional contribution to the free energy

$$F_{\text{CDW}} = \sum_{i,j} \left\{ \frac{1}{2} \rho_{i,j} \chi_{C,\vec{Q}_i}^{-1} \rho_{\vec{Q}_i} \rho_{-\vec{Q}_j} + \lambda_{i,j}^C \rho_{\vec{Q}_j - \vec{Q}_i} \left[\Psi_{\vec{Q}_i} \Psi_{\vec{Q}_j}^* + \Psi_{-\vec{Q}_j} \Psi_{-\vec{Q}_i}^* \right] \right\} + \dots$$

(6.9)

which allows for a PDW to induce a CDW of the form

$$\rho_{\vec{Q}_i - \vec{Q}_i} = -\chi_{C,\vec{Q}_i - \vec{Q}_j} \lambda_{i,j}^C \left[\Psi_{\vec{Q}_i} \Psi_{\vec{Q}_j}^* + \Psi_{-\vec{Q}_j} \Psi_{-\vec{Q}_i}^* \right].$$

(6.10)

This implies that, for example, a uni-directional PDW $\{\Psi_{\vec{Q}_x}, \Psi_{\vec{Q}_y}, \Psi_{-\vec{Q}_x}, \Psi_{-\vec{Q}_y}\} = \{e^{i\phi_1}, 0, e^{i\phi_2}, 0\}$ will induce a uni-directional CDW with wave-vector $2\vec{Q}$. The converse is not necessarily true because the PDW appears at quadratic order in this term.

6.4.2 Coupling to SDW

A PDW may only induce SDW order if it itself breaks time-reversal symmetry. Furthermore the types of PDW order described by Eq. 6.6 may only couple to the z-component of spin if the coupling is to be invariant under time-reversal [3]. The additional contribution to the free energy takes the form

$$F_{\text{SDW}} = \sum_{i,j} \left\{ \frac{1}{2} \delta_{i,j} \chi_{S,\vec{Q}_i}^{-1} S_{\vec{Q}_i}^z S_{-\vec{Q}_j}^z + \lambda_{i,j}^S S_{\vec{Q}_j - \vec{Q}_i}^z i \left[\Psi_{\vec{Q}_i} \Psi_{\vec{Q}_j}^* - \Psi_{-\vec{Q}_j} \Psi_{-\vec{Q}_i}^* \right] \right\}.$$

$$(6.11)$$

which allows for a PDW to induce an SDW of the form

$$S_{\vec{Q}_i - \vec{Q}_i}^z = -\chi_{S,\vec{Q}_i - \vec{Q}_j} \lambda_{i,j}^S \left[\Psi_{\vec{Q}_i} \Psi_{\vec{Q}_j}^* - \Psi_{-\vec{Q}_j} \Psi_{-\vec{Q}_i}^* \right]. \qquad (6.12)$$

In contrast to the coupling to CDW, the uni-directional PDW with $\{\Psi_{\vec{Q}_x}, \Psi_{\vec{Q}_y}, \Psi_{-\vec{Q}_x}, \Psi_{-\vec{Q}_y}\} = \{e^{i\phi_1}, 0, e^{i\phi_2}, 0\}$ does not induce any SDW order because it does not itself break time-reversal symmetry. However, a bi-directional PDW $\{\Psi_{\vec{Q}_x}, \Psi_{\vec{Q}_y}, \Psi_{-\vec{Q}_x}, \Psi_{-\vec{Q}_y}\} = \{e^{i\phi_1}, e^{i\phi_2}, 0, 0\}$ would induce SDW with wave-vector $\vec{Q}_x - \vec{Q}_y$. The induced CDW and SDW for the stable PDW phases of the free energy in Eq. 6.6 are summarised in Table 6.1.

6.4.3 Coupling to Uniform Superconductivity

Finally I will now consider the coupling of a PDW to a uniform charge-2e d-wave superconducting order parameter Ψ_0. The lowest order direct coupling between the two is bi-quadratic because it is not possible to construct a bi-linear product of these order parameters that is simultaneously invariant under phase and translational symmetry transformations. However, if CDW and PDW with the same wave-vector, $\vec{Q}$, are present in the system then there is an allowed term that couples all three [4]:

$$F_\Psi = \sum_{i,j} \delta_{i,j} \lambda_{i,j}^\Psi \left[\Psi_0^* \rho_{\vec{Q}_i} \Psi_{-\vec{Q}_j} + \Psi_0 \rho_{\vec{Q}_i}^* \Psi_{-\vec{Q}_j}^* \right]. \qquad (6.13)$$

A corollary of Eq. 6.13 is that if any two of the order parameters Ψ_0, $\Psi_{-\vec{Q}}$ and $\rho_{\vec{Q}}$ are non-zero, they will induce ordering in the third. For example, if a material has an instability towards co-existing superconducting and CDW orders then there must be some PDW induced that reflects the influence of the new periodicity introduced by the CDW on superconductivity. This result will be very important for the conclusions drawn at the end of this chapter.

This section has shown that many secondary order parameters can be induced as products of primary PDW order parameters. In the next section I will discuss various

theoretical proposals for PDW order in cuprates and its proposed relationship to other broken symmetries in the phase diagram.

6.5   Theoretical Proposals for a Cuprate PDW

Physical reasoning for the existence of translational symmetry breaking in cuprates typically falls into one of three categories and the same is true of the PDW. In the first, hole doping leads to frustration of a Mott insulator and mesoscopic phase separation results [38]. In the second these phases condense from a spin-liquid formed from doping the Mott insulator [39]. In a third picture, the problem is approached from the opposite end of the doping axis. In these approaches the multitude of phases in the under-doped region are seen as instabilities of the itinerant metal with a full Fermi surface that exists in the over-doped region of the phase diagram [40, 41].

Theories for PDW falling into these categories will be discussed below. First however, I will examine the evidence from numerics for the existence of a PDW.

6.5.1   Variational Numerical Calculations

The lowest energy variational solution to date for the t-J model on the square lattice at intermediate coupling is that of Corboz et al. [42]. For J/t between 0.2 and 0.8 and hole doping $p < 0.16$ they found two modulated superconducting states that, within the accuracy of the method used, could feasibly be the ground state. Two of these states are shown in Fig. 6.5.

The first of these (Fig. 6.5a) consists of a uniform d-wave superconducting component $\langle \Psi_0 \rangle \neq 0$ coexisting with CDW $\langle \rho_{2\vec{Q}} \rangle \neq 0$. This state necessarily also has a PDW component $\langle \Psi_{2\vec{Q}} \rangle \neq 0$ (see Eq. 6.13) that, in this case, is in-phase with the CDW. The other state (Fig. 6.5b) is a pure-PDW where $\langle \Psi_0 \rangle = 0$ and $\langle \Psi_{\vec{Q}} \rangle \neq 0$. Through Eq. 6.9 this necessarily has a CDW component $\langle \rho_{2\vec{Q}} \neq 0 \rangle$. Which, again is in-phase with the CDW. Both of these have co-existing SDW modulation of the anti-ferromagnetic spin texture. In both cases the nodes of the SDW lie at the maxima of the pairing amplitude.

In as much as the t-J model at intermediate coupling accurately reflects the physics of the cuprates, this makes the existence of a spatially modulated pairing amplitude (with or without a uniform superconducting component) highly plausible.

6.5.2   PDW Within Mean-Field Models

Several works have now found evidence for a PDW type ground state within mean-field type treatments of the superconducting state of strongly correlated electron
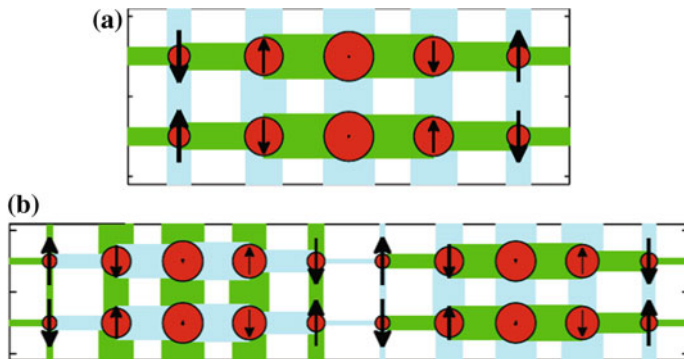
Fig. 6.5 Striped variational solutions to the *t-J* model at intermediate coupling calculated using the iPEPS method by Corboz et al. [42]. The size of the red circles indicates the density of holes on that site. The thickness of the rectangles on the bonds indicate the magnitude of the pairing amplitude with green and blue indicating different signs of the amplitude. The length and orientation of the black arrows denotes the magnetic moment on each site. In **(a)**, a state with $\langle \Psi_0 \rangle \neq 0$ coexisting with CDW and $\langle \Psi_{2\vec{Q}} \rangle$ and $\langle \rho_{2\vec{Q}} \rangle \neq 0$ is depicted. In this case $2\pi/|2\vec{Q}| = 5a_0$. In **(b)** a pure PDW phase with $\langle \Psi_0 \rangle = 0$, $\langle \Psi_{\vec{Q}} \rangle \neq 0$ and $\langle \rho_{2\vec{Q}} \rangle \neq 0$ is shown. The periodicity of the PDW is twice that in (a) as can be seen from the change in sign of the pairing amplitude every $5a_0$. Reproduced from reference [42] with permission

systems [18, 43–47, 64]. Striped phases where superconducting hole-rich regions are separated by regions of anti-ferromagnetism are found. These phases either have the pairing-amplitude changing sign between adjacent regions ($\langle \Psi_0 \rangle = 0$, $\langle \Psi_{\vec{Q}} \rangle \neq 0$, $\langle \rho_{2\vec{Q}} \rangle \neq 0$) or maintaining the same sign ($\langle \Psi_0 \rangle \neq 0$, $\langle \Psi_{\vec{Q}} \rangle = 0$, $\langle \rho_{2\vec{Q}} \rangle \neq 0$, $\langle \rho_{2\vec{Q}} \rangle \neq 0$).

6.5.3 Amperean Pairing

In the preceding section I have discussed attempts to establish a PDW as the ground state of a realistic model of the cuprates. Some authors have instead explored the consequences of a physically motivated ansatz for the form of PDW order that may occur. One such model would be the "Amperean Pairing" proposal of Patrick Lee which is based on a resonating valence bond (RVB) description of the cuprate pseudo-gap [25, 39, 48].

In some RVB type theories the electron is decomposed into a spinless charged boson (the holon) and a neutral spin-1/2 fermion (the spinon) which are coupled by a fluctuating gauge field [39]. It has been shown that a uniform *d*-wave superconducting state can arise from this kind of liquid [49]. In this picture the holons Bose condense and the spinons form a Fermi surface. The spinons may then form *d*-wave pairs via an attractive interaction mediated by the gauge bosons.

The spinons are not charged, meaning that this is not a true superconductor. However the Bose condensation of the charged holons converts the spinons to electrons with a reduced spectral weight and turns this state into a true superconductor [39].

The coupling of the spinons to the transverse gauge field is strong and unscreened. In electromagnetism a current of charged particles creates a transverse magnetic (gauge) field. If there is a second particle with parallel momentum, the particles will experience an attractive force, described by Ampere's law. Similarly, spinons of parallel momentum experience an attractive interaction through the transverse gauge fields they create [50]. P. Lee has argued that pairing of spinons with nearly parallel momenta, mediated by this interaction, can lead to the formation of a PDW state through a process called "Amperean pairing" [25]. As shown in Fig. 6.6a, pairing between spinons in the anti-nodal region of the Brillouin zone in cuprates can lead to Cooper-pairs with non-zero centre of mass momentum: a PDW.

In this picture, the wave-vector of the PDW would be determined by the separation between pieces of the Fermi surface in the anti-nodal region. It would hence consist of a state with PDW order parameter $\langle \Psi_{\vec{Q}} \rangle \neq 0$ where $\vec{Q}$ decreases with increasing hole-doping and is approximately equal to $(\frac{2\pi}{8a_0}, 0); (0, \frac{2\pi}{8a_0})$. Through Eq. 6.9 this would necessarily imply an accompanying CDW $\rho_{2\vec{Q}}$ which would be in agreement with experiment in $YBa_2Cu_3O_{6+x}$, $Bi_2Sr_2CaCu_2O_8$, $Bi_2Sr_2CuO_{6+\delta}$, $Na_xCa_{2-x}CuO_2Cl_2$ and $HgBa_2CuO_{4+\delta}$ [37].

Within this picture charge order is an entirely subsidiary effect to PDW formation. A schematic phase diagram resulting from the Amperean pairing scenario is shown in Fig. 6.6b. The PDW, rendered short-range by disorder, onsets at T_{PDW-MF}, resulting in a pseudo-gap (blue region). At a lower temperature, T_{CDW}, a secondary short-range CDW, $\rho_{2\vec{Q}}$, onsets. On entering the uniform superconducting phase (d-SC) the PDW and secondary CDW persist but with amplitude that decreases with temperature as a result of Fermi surface competition between PDW and d-SC. This is consistent with the gradual decreases in scattering intensity at $2\vec{Q}$ observed by x-ray scattering in $YBa_2Cu_3O_{6+x}$ [51]. As outlined in Sect. 6.2.2, Lee argues argued that this Amperean PDW state would explain many of the peculiar features of the APRES data in $Bi_2Sr_2CuO_{6+\delta}$, including a Fermi arc [25, 26].

Having considered this instability of an exotic spinon Fermi surface, I next discuss an instability to PDW order arising from a more conventional one.

6.5.4 Spin-Fermion "Hot-Spot" Models

Spin-Fermion models of the cuprates take a complete hole-like Fermi surface and couple the fermions via (π, π) spin-fluctuations in the vicinity of an anti-ferromagnetic quantum critical point. These (π, π) fluctuations strongly couple eight points on the Fermi surface where it intersects the anti-ferromagnetic zone boundary [52].
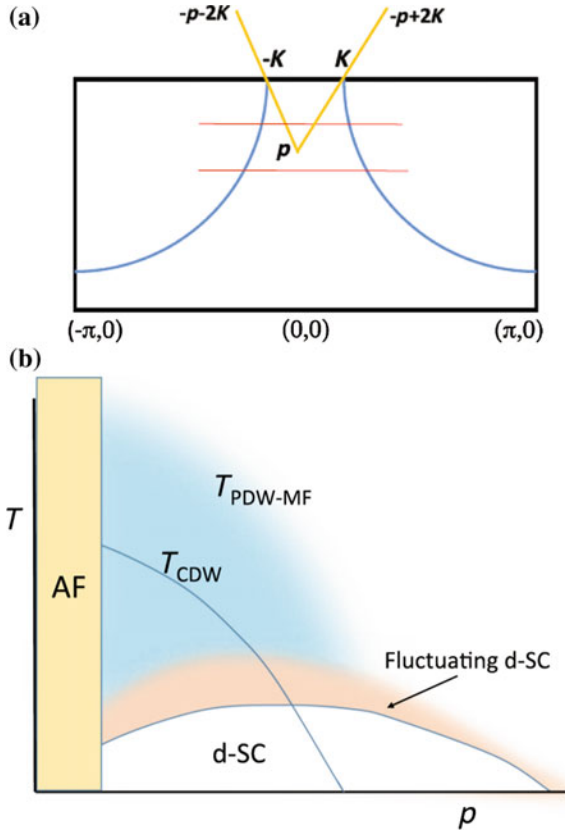
Fig. 6.6 **a** Cartoon diagram of Amperean pairing reproduced from reference [25] with permission. Momenta are measured with respect to the $(0, \pi)$ point. Fermions near the point $\vec{K}$ with momenta $\vec{p}$ and $-\vec{p}+2\vec{K}$ form a Cooper pair with centre of mass momentum $\vec{Q} = 2\vec{K}$. Similarly those near $-\vec{K}$ with momenta $\vec{p}$ and $-\vec{p}-2\vec{K}$ form a Cooper pair with centre of mass momentum $\vec{Q} = -2\vec{K}$. The non-zero centre-of-mass momenta of the Cooper-pairs leads to a PDW. **b** Schematic phase diagram in Amperean pairing scenario reproduced from [25]. PDW, rendered short-range by disorder, onsets at $T_{\text{PDW-MF}}$ resulting in a pseudo-gap (blue region). At a lower temperature, T_{CDW}, a secondary short-range CDW, $\rho_{2\vec{Q}}$, onsets. On entering the uniform d-wave superconducting phase (d-SC) the PDW and secondary CDW persist but with amplitude that decreases with temperature as a result of Fermi surface competition between PDW and d-SC

These interactions can give rise to d-wave superconducting, CDW and PDW orders. However, it is well known that these models do not have a leading instability at the mean-field level to CDW or PDW at the experimentally observed wave-vector, $(2Q, 0); (0, 2Q)$, instead favouring those at $(2Q, 2Q)$[41, 52, 53]. Nevertheless, by studying sub-dominant instabilities towards order at $(2Q, 0); (0, 2Q)$ it is hoped that insight into the nature of the superconducting and density wave states formed can be obtained [5, 54–56].
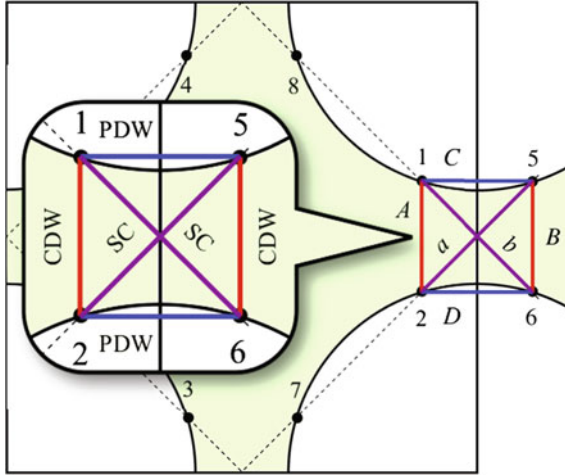
Fig. 6.7 Cartoon of an orthogonal CDW/PDW state in a spin-fermion model reproduced from [56]. (π, π) spin-fluctuations strongly couple eight "hot-spots" on the Fermi surface where it intersects the anti-ferromagnetic zone boundary. These interactions can give rise to d-wave superconducting, CDW and PDW orders. Here a PDW component with wave-vector $(2Q, 0)$ is created by the pairing of hot fermions separated long the x-direction (*blue lines*). A CDW component with wave-vector $(0, 2Q)$ is created by hot-spots separated along the y-direction (*red lines*). The CDW and PDW have the same wave-vector because a PDW field carries the total momentum of the paired fermions whereas a CDW field carries the momentum transfer. Within this type of model uniform d-wave superconductivity arises by pairing of hot fermions diagonally opposite from each other

It was noticed that if the non-linearity of the dispersion and Fermi surface curvature are neglected, spin-fermion models have an emergent SU(2) symmetry linking uniform d-wave superconductivity and d-symmetry form factor CDW with wave-vector $(2Q, 2Q)$ [41, 52, 53]. This means that these orders are exactly degenerate. In a similar vein, a symmetry between CDW and PDW at $(2Q, 0)$; $(0, 2Q)$ has been established [54, 56]. It has also been shown that for large values of the spin-fermion coupling, uni-directional (stripe) CDW/PDW order is preferred over bi-directional (chequerboard) order [54].

Wang et al. considered the scenario depicted in Fig. 6.7. In their model, a mixed CDW/PDW order develops where the CDW and PDW (of the LO type) are orthogonal to each other. With reference to Fig. 6.7a, hot fermions separated along the x-direction, say, will develop PDW order at $(2Q, 0)$ whereas those along y would develop CDW order at $(0, 2Q)$. In doing so they spontaneously break the C_4 lattice rotation symmetry. Time-reversal symmetry is also broken due to spontaneous currents associated with the CDW [54].

The attraction of this model is that CDW and PDW appear at the same wave-vector (modulo 90° rotation), which decreases with increasing hole doping. This is consistent with the wave-vectors observed by STM and scattering techniques in $YBa_2Cu_3O_{6+x}$, $Bi_2Sr_2CaCu_2O_8$, $Bi_2Sr_2CuO_{6+\delta}$, $Na_xCa_{2-x}CuO_2Cl_2$ and $HgBa_2$

$CuO_{4+\delta}$ [37]. Wang et al. also show that this orthogonal PDW/CDW state is consistent with the anti-nodal dispersion observed in the ARPES data of He et al. that motivated the Amperean pairing proposal (see Sect. 6.2.2). Finally, because this model breaks C_4 rotational and time-reversal symmetry it is consistent with reports of such symmetry breaking in cuprates [57–62].

6.6   Experimentally Distinguishing PDW Scenaria

In the previous section I discussed models which are, to varying degrees of approximation, representative of cuprate physics and show evidence for the existence of a PDW state. Where they differ is in the relationship of CDW to the PDW and whether the PDW exists with or without a uniform superconducting component.

Without reference to microscopics we can categorise these models into three groups as summarised in Table 6.2. In all three scenaria uniform d-wave superconductivity is taken to be a primary order parameter. The three scenaria also include CDW order at the experimentally observed wave-vector $\vec{Q}_C = 2\vec{Q} \approx (0.25, 0)\frac{2\pi}{a_0}$ and $(0, 0.25)\frac{2\pi}{a_0}$, either as a primary order parameter or as secondary order expressed in terms of a primary PDW. Table 6.2 shows the relationship between the CDW and any PDW wave-vector present both above and below the uniform T_c.

As can be seen from Table 6.2, by determining the relationship between the PDW wave-vector and any CDW wave-vector(s) both above and below the uniform T_c one can readily distinguish these scenaria. For instance, in scenario 1, a new secondary CDW at wave-vector $\vec{Q}_C/2$ is allowed upon cooling below T_C which would positively identify this scenario.

Table 6.2 Table characterising the possible PDW scenarios in cuprates by which order parameters are primary. Here $2\vec{Q} = \vec{Q}_C$, the experimentally observed CDW wave-vector. PDW with wave-vector $\vec{Q}$ refers to $\Psi_{\vec{Q}} + \Psi_{-\vec{Q}}$ which is a uni-directional LO state (phase 3 in Table 6.1). This is preferred in the models presented in Sect. 6.5. PDWs of type 4 and 2 in Table 6.1 would differ would differ from the type considered here by an additional CDW at $\vec{Q}_x - \vec{Q}_y$ which has never been experimentally detected. PDWs of type 5 and 2 in Table 6.1 would differ from the type considered here by an additional SDW modulation at $\vec{Q}_x - \vec{Q}_y$ and also $\vec{Q}_x + \vec{Q}_y$ in the case of phase 2. An FF type PDW (phase 1 in Table 6.1) has no allowed CDW or SDW modes

Scenario	Temperature	Primary PDW	Primary CDW	Secondary PDW	Secondary CDW
1	$T > T_c$	$\vec{Q}$	None	None	$2\vec{Q}$
-	$T < T_c$	$\vec{Q}$	None	None	$2\vec{Q}, \vec{Q}$
2	$T > T_c$	$2\vec{Q}$	$2\vec{Q}$	None	None
-	$T < T_c$	$2\vec{Q}$	$2\vec{Q}$	None	None
3	$T > T_c$	None	$2\vec{Q}$	None	None
-	$T < T_c$	None	$2\vec{Q}$	$2\vec{Q}$	None

Here I have outlined how to experimentally distinguish different PDW scenarios using the relationship between PDW and CDW wave-vectors above and below T_c. In the following chapter I will report on the use of scanned Josephson tunnelling microscopy (SJTM) a direct probe of the superconducting condensate in cuprates. Periodic modulations of the condensate are detected. Comparing their wavelength to those of the CDW reported on in Chap. 4 I will draw conclusions about the possible PDW scenarios in $Bi_2Sr_2CaCu_2O_{8+x}$.

References

1. P. Fulde, R.A. Ferrell, Superconductivity in a strong spin-exchange field. Phys. Rev. **135**(3A), A550–A563 (1964)
2. A.I. Larkin, Y.N. Ovchinnikov, Inhomogeneous state of superconductors. Sov. Phys. JETP **20**, 762–769 (1964)
3. D.F. Agterberg, H. Tsunetsugu, Dislocations and vortices in pair density wave superconductors. Nat. Phys. **4**(8), 6 (2009)
4. E. Berg, E. Fradkin, S.A. Kivelson, Theory of the striped superconductor. Phys. Rev. B **79**(6), 1–15 (2009)
5. S. Sachdev, R. La Placa, Bond order in two-dimensional metals with antiferromagnetic exchange interactions. Phys. Rev. Lett. **111**(2), 027202 (2013)
6. E. Fradkin, S.A. Kivelson, J.M. Tranquada, Colloquium: Theory of intertwined orders in high temperature superconductors. Rev. Mod. Phys. **87**(2), 457–482 (2015)
7. J. Bardeen, L.N. Cooper, J.R. Schrieffer, Theory of superconductivity. Phys. Rev. **108**(5), 1175–1204 (1957)
8. A.M. Clogston, Upper limit for the critical field in hard superconductors. Phys. Rev. Lett. **9**(6), 266–267 (1962)
9. Y. Matsuda, H. Shimahara, Fulde-Ferrell-Larkin-Ovchinnikov state in heavy fermion super-conductors. J. Phys. Soc. Jpn. **76**(5), 1–16 (2007)
10. Y.-A. Liao et al., Spin-imbalance in a one-dimensional fermi gas. Nature **467**(7315), 567–9 (2010)
11. J.M. Tranquada et al., Evidence for stripe correlations of spins and holes in copper oxide superconductors. Nature **375**(6532), 561–563 (1995)
12. A.R. Moodenbaugh et al., Superconducting properties of La2.xBaxCuO4. Phys. Rev. B **38**(7), 4596–4600 (1988)
13. Q. Li et al., Two-dimensional superconducting uctuations in stripe-ordered La1.875Ba0.125CuO4. Phys. Rev. Lett. **99**(6), 4–7 (2007)
14. M. Hücker et al., Stripe order in superconducting $La_{2-x}2Ba_xCuO_4$ (0.095≤ x ≤ 0.155). Phys. Rev. B **83**(10), 104506 (2011)
15. S. Tajima et al., c-Axis optical response in the static stripe ordered phase of the cuprates. Phys. Rev. Lett. **86**(3), 500–503 (2001)
16. J. Orenstein, Josephson plasmons: The new wave. Nat. Phys. **2**(8), 503–504 (2006)
17. A.A. Schafgans et al., Towards a two-dimensional superconducting state of $La_{2-x}Sr_xCuO_4$ in a moderate external magnetic field. Phys. Rev. Lett. **104**(15), 1–4 (2010)
18. A. Himeda, T. Kato, M. Ogata, Stripe states with spatially oscillating d-wave superconductivity in the two-dimensional $t - t' - j$ model. Phys. Rev. Lett. **88**(11), 117001 (2002)
19. E. Berg et al., Dynamical layer decoupling in a stripe-ordered high-Tc superconductor. Phys. Rev. Lett. **99**(12), 1–4 (2007)
20. P. Abbamonte et al., Spatially modulated 'Mottness' in $La_{2-x}Ba_xCuO_4$. Nat. Phys. **1**(3), 155–158 (2005)

21. M.K. Crawford et al., Lattice instabilities and the effect of copper-oxygen-sheet distortions on superconductivity in doped La_2CuO_4. Phys. Rev. B **44**(14), 7749–7752 (1991)
22. J.D. Axe et al., Structural phase transformations and superconductivity in $La_2 - xBa_xCuO_4$. Phys. Rev. Lett. **62**(23), 2751–2754 (1989)
23. A. Dubroka et al., Evidence of a precursor superconducting phase at temperatures as high as 180 K in $RBa_2Cu_3O_7 - \delta$ (R=Y, Gd, Eu) superconducting crystals from infrared spectroscopy. Phys. Rev. Lett. **106**(4), 1–4 (2011)
24. F. Yu et al., Diamagnetic Response in Under-Doped YBa2Cu3O6:6 in High Magnetic Fields (2014), arXiv: 1402.7371
25. P.A. Lee, Amperean pairing and the pseudogap phase of cuprate superconductors. Phys. Rev. X **4**(3), 1–13 (2014)
26. R.-H. He et al., From a single-band metal to a high-temperature superconductor via two thermal phase transitions. Science **331**(6024), 1579–1583 (2011)
27. A. Damascelli, Z. Hussain, Z.-X. Shen, Angle-resolved photoemission studies of the cuprate superconductors. Rev. Mod. Phys. **75**(2), 473–541 (2003)
28. H.-B. Yang et al., Reconstructed fermi surface of underdoped $Bi_2Sr_2CaCu_2O_8 + \delta$. Phys. Rev. Lett. **107**(4), 047003 (2011)
29. T. Kondo et al., Disentangling cooper-pair formation above the transition temperature from the pseudogap state in the cuprates. Nat. Phys. **7**(1), 21–25 (2010)
30. J.H. Ma et al., Coexistence of competing orders with two energy gaps in real and momentum space in the high temperature superconductor $Bi_2Sr_2 - xLa_xCuO_6 + \delta$. Phys. Rev. Lett. **101**(20), 1–4 (2008)
31. J. Meng et al., Monotonic d-wave superconducting gap of the optimally doped Bi2Sr1:6La0:4CuO6 superconductor by laser-based angle-resolved photoemission spectroscopy. Phys. Rev. B **79**(2), 2–5 (2009)
32. K. Nakayama et al., Evolution of a pairing-induced pseudogap from the superconducting gap of (Bi, Pb)2Sr2CuO6. Phys. Rev. Lett. **102**(22), 13–16 (2009)
33. B. Keimer et al., From quantum matter to high-temperature superconductivity in copper oxides. Nature **518**(7538), 179–86 (2015)
34. R.M. Fernandes, A.V. Chubukov, J. Schmalian, What drives nematic order in iron-based superconductors? Nat. Phys. **10**(2), 97–104 (2014)
35. L. Nie, G. Tarjus, S.A. Kivelson, Quenched disorder and vestigial nematicity in the pseudogap regime of the cuprates. Proc. Natl. Acad. Sci. **111**(22), 7980–7985 (2014)
36. M. Vojta, Lattice symmetry breaking in cuprate superconductors: stripes, nematics, and superconductivity. Adv. Phys. **58**(6), 699–820 (2009)
37. R. Comin, A. Damascelli. Resonant x-ray Scattering Studies of Charge Order in Cuprates. arXiv (2015), pp. 1–26
38. S.A. Kivelson, E. Fradkin, V.J. Emery, Electronic liquid-crystal phases of a doped mott insulator. Nature **393**(6685), 550–553 (1998)
39. P.A. Lee, N. Nagaosa, X.G. Wen, Doping a mott insulator: Physics of high-temperature superconductivity. Rev. Mod. Phys. **78**(1), (2006)
40. Y. Wang, D.F. Agterberg, A. Chubukov, Coexistence of charge-density- wave and pair-density-wave orders in underdoped cuprates. Phys. Rev. Lett. **114**(19), 1–6 (2015)
41. C. Pépin et al., Pseudogap, charge order, and pairing density wave at the hot spots in cuprate superconductors. Phys. Rev. B **90**(19), 1–16 (2014)
42. P. Corboz, T.M. Rice, M. Troyer, Competing states in the t - J model: Uniform d -wave state versus stripe state. Phys. Rev. Lett. **113**(4), 1–5 (2014)
43. F. Loder et al., Mean-field pairing theory for the charge-stripe phase of hightemperature cuprate superconductors. Phys. Rev. Lett. **107**(18), 1–4 (2011)
44. F. Loder, A.P. Kampf, T. Kopp, Superconducting state with a finitemomentum pairing mechanism in zero external magnetic field. Phys. Rev. B **81**(2), 1–4 (2010)
45. M. Raczkowski et al., Unidirectional d -wave superconducting domains in the two-dimensional t-J model. Phys. Rev. B **76**(14), 3–6 (2007)

46. M. Zelli, C. Kallin, A.J. Berlinsky, Quantum oscillations in a π-striped superconductor. Phys. Rev. B **86**(10), 1–16 (2012)
47. K.Y. Yang et al., Nature of stripes in the generalized t-J model applied to the cuprate superconductors. New J. Phys. **11**, (2009)
48. P.W. Anderson, Resonating valence bonds: A new kind of insulator? Mater. Res. Bull. **8**(2), 153–160 (1973)
49. G. Kotliar, J. Liu, Superexchange mechanism and d -wave superconductivity. Phys. Rev. B **38**(7), 5142–5145 (1988)
50. S.S. Lee, P.A. Lee, T. Senthil, Amperean pairing instability in the U(1) spin liquid state with fermi surface and application to κ-(BEDT-TTF)$_2$Cu$_2$(CN)$_3$. Phys. Rev. Lett. **98**(6), 1–4 (2007)
51. J. Chang et al., Direct observation of competition between superconductivity and charge density wave order in YBa2Cu3O6:67. Nat. Phys. **8**(12), 871–876 (2012)
52. M.A. Metlitski, S. Sachdev, Quantum phase transitions of metals in two spatial dimensions. II. Spin density wave order. Phys. Rev. B **82**(7), 075128 (2010)
53. K.B. Efetov, H. Meier, C. Pépin, Pseudogap state near a quantum critical point. Nat. Phys. **9**(7), 442–446 (2013)
54. Y. Wang, A. Chubukov, Charge-density-wave order with momentum (2Q,0) and (0,2Q) within the spin-fermion model: Continuous and discrete symmetry breaking, preemptive composite order, and relation to pseudogap in hole-doped cuprates. Phys. Rev. B **90**(3), 1–52 (2014)
55. D. Chowdhury, S. Sachdev, Feedback of superconducting uctuations on charge order in the underdoped cuprates. Phys. Rev. B **90**(13), (2014)
56. Y. Wang, D.F. Agterberg, A. Chubukov, Interplay between pair- and charge-density-wave orders in underdoped cuprates. Phys. Rev. B **91**(11), 115103 (2015)
57. M.J. Lawler et al., Intra-unit-cell electronic nematicity of the high-Tc copperoxide pseudogap states. Nature **466**(7304), 347–51 (2010)
58. Y. Li et al., Hidden magnetic excitation in the pseudogap phase of a high-Tc superconductor. Nature **468**(7321), 283–285 (2010)
59. P. Hosur et al., Kerr effect as evidence of gyrotropic order in the cuprates. Phys. Rev. B **87**(11), 1–8 (2013)
60. J. Xia et al., Polar kerr-effect measurements of the high-temperature YBa2Cu3O6+x superconductor: Evidence for broken symmetry near the pseudogap temperature. Phys. Rev. Lett. **100**(12), 3–6 (2008)
61. H. Karapetyan et al., Magneto-optical measurements of a cascade of transitions in superconducting La$_1$.875Ba$_0$.125CuO$_4$ Single Crystals. Phys. Rev. Lett. **109**(14), 1–5 (2012)
62. P. Hosur et al., Erratum: Kerr effect as evidence of gyrotropic order in the cuprates [Phys. Rev. B 87, 115116 (2013)]. Phys. Rev. B **91**(3), 039908 (2015)
63. D. Saint-James, *Type II Superconducivity* (Pergamon Press, New York, 1969)
64. R. Soto-Garrido, E. Fradkin, Pair-density-wave superconducting states and electronic liquid-crystal phases. Phys. Rev. B **89**(16), 1–19 (2014)

Chapter 7
Detection of a Cooper-Pair Density Wave in $Bi_2Sr_2CaCu_2O_{8+\delta}$

The main results of this chapter are reported in "Direct Detection of a Cooper-pair Density Wave in $Bi_2Sr_2CaCu_2O_{8+\delta}$", *Nature*, **532**, 343 (2016).

The quantum condensate of Cooper pairs forming a superconductor was originally conceived as being translationally invariant [1]. In theory, however, pairs can exist with non-zero momentum $\vec{Q}$, thus generating a state with a spatially modulated Cooper-pair density [2, 3]. Such a state has been created in ultracold ^{6}Li gas but never observed directly in any superconductor [4]. It is now widely hypothesised that the pseudogap phase of the cuprate superconductors contains such a "pair density wave" state [5–21]. This chapter details the use of nanometre-resolution scanned Josephson tunnelling microscopy to image Cooper pair tunnelling from a d-wave superconducting STM tip to the condensate of the superconductor $Bi_2Sr_2CaCu_2O_{8+x}$. By using Fourier analysis of scanned Josephson tunnelling images, we discover the direct signature of a Cooper-pair density modulation.

7.1 Four Unit-Cell Periodic Modulations in the Cooper-Pair Current

In this chapter I will report on the use of cuprate scanned Josephson tunnelling microscopy (SJTM), whose development is detailed in Chap. 5, to study Bi_2Sr_2 $CaCu_2O_{8+x}$ samples. This technique directly probes the superconducting condensate, through the tunnelling of Cooper-pairs, by forming a nanometer-resolution scannable Josephson junction between a superconducting STM tip and the sample. In our approach to cuprate SJTM this superconducting STM tip is formed by picking up a nanoflake of our $Bi_2Sr_2CaCu_2O_{8+x}$ sample with a normal tungsten STM tip. In operation, a maximum Cooper-pair current $I_c(\vec{r})$ between the tip and sample is measured at a fine grid of points. This allows one to map spatial variations of the superconducting condensate at the nanometer scale.

Fig. 7.1 A 76 nm × 76 nm
$I_c(\vec{r})$ image measured at
45 mK. For visual clarity
modulations at the
wave-vector of the crystal
super-modulation have been
removed by the Fourier
filtration method described
in Sect. 2.8
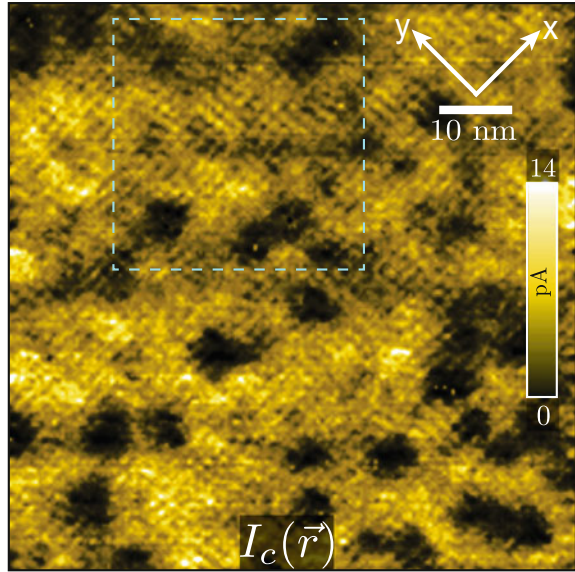
I will present results for $Bi_2Sr_2CaCu_2O_{8+x}$ samples with $T_c = 88$K and hole density $p = 17\%$ at $T = 45$ mK. The two states already reported to coexist at this p value are the high-temperature d-wave superconductor and a CDW with $\vec{Q} = (0.22 \pm 0.02, 0)\frac{2\pi}{a_0}$ and $(0, 0.22 \pm 0.02)\frac{2\pi}{a_0}$ (see Chap. 4). Figure 7.1 shows the measured $I_c(\vec{r})$ in a 76 nm × 76 nm field of view. A 35 × 35 nm portion of this image (dashed box) is shown enlarged in Fig. 7.2a. Clear $I_c(\vec{r})$ modulations are immediately visible in both.

The magnitude of the Fourier transform of $I_c(\vec{r})$, $|\tilde{I}_c(\vec{q})|$, is shown in Fig. 7.2b revealing that modulations in $I_c(\vec{r})$ occur at the wave-vectors $\vec{Q}_P = (0.25 \pm 0.02, 0)\frac{2\pi}{a_0}$ and $(0, 0.25 \pm 0.02)\frac{2\pi}{a_0}$ (dashed red circles in Fig. 7.2b). No peak at $\vec{q} \approx (0.125, 0)\frac{2\pi}{a_0}$ or $(0, 0.125)\frac{2\pi}{a_0}$ is observed above the background.

In Fig. 7.2c I show (as blue dots) the measured value of $I_c(\vec{r})$ along the blue line in Fig. 7.2a. The average amplitude and wavelength of the $I_c(\vec{r})$ modulations (determined from the magnitude and central $\vec{q}$ value of the peaks in Fig. 7.2c) are shown as the red line. From these data, and in general from the magnitude of the peaks at $\vec{Q}_x$ and $\vec{Q}_x$ in Fig. 7.2b, we conclude that the modulation amplitude in $I_c(\vec{r})$ is ~5% of its average value. Therefore, at this doping ($p = 17\%$), the modulation represents a small modulation on top of the uniform component, at least deep within the superconducting state ($T \ll T_c$) where these measurements were taken.

Now I turn to the relationship of the $I_c(\vec{r})$ modulations the known d-symmetry form factor CDW modulations in this material (see Chap. 4). Figure 7.2d shows $\tilde{D}(\vec{q}) = \tilde{O}_x(\vec{q}) - \tilde{O}_y(\vec{q})$, for a $Bi_2Sr_2CaCu_2O_{8+x}$ sample with the same hole doping density and $T = 2$K. This can be regarded as a Fourier transform that measures the
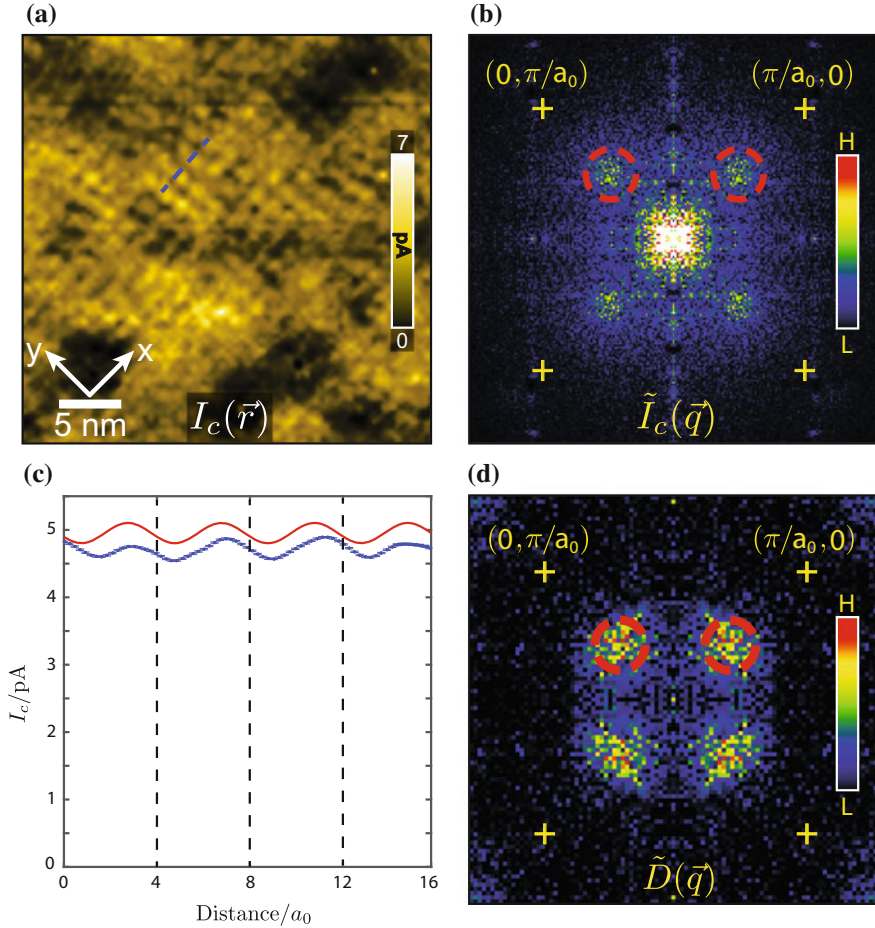
Fig. 7.2 **a** A $35\,nm \times 35\,nm$ field of view $I_c(\vec{r})$ image (*dashed blue box* in Fig. 7.1) showing $I_c(\vec{r})$ modulations parallel to the CuO_2 x and y axes (supermodulation-induced $I_c(\vec{r})$ modulations are removed). **b** $|\tilde{I}_c(\vec{q})|$, the Fourier transform of $I_c(\vec{r})$ in **a** (*yellow crosses* at $\vec{q} = (\pi/a_0, 0)$ and $(0, \pi/a_0)$). Maxima from $I_c(\vec{r})$ modulations (*dashed red circles*) occur at $\vec{Q}_P = (0.25 \pm 0.02, 0)\frac{2\pi}{a_0}$ and $(0, 0.25 \pm 0.02)\frac{2\pi}{a_0}$. No significant modulations occur in $R_N(\vec{q})$ at $\vec{Q}_P$ (see Appendix H). **c** Measured $I_c(\vec{r})$ along the *dashed blue line* in **a** (*blue dotted line*); statistical error bars are the variance of $I_c(\vec{r})$ transverse to the dashed line. The *red line* shows the global amplitude and $\vec{Q}_P$ of the $I_c(\vec{r})$ modulations (from the circled maxima in **b**. **d** Magnitude of $\tilde{D}(\vec{q}) = \tilde{O}_x(\vec{q}) - \tilde{O}_y(\vec{q})$ (*yellow crosses* at $\vec{q} = (\pi/a_0, 0)$ and $(0, \pi/a_0)$) revealing the *d*-symmetry form factor density wave modulations (*dashed red circles*) at $\vec{Q}_C = (0.22, 0)\frac{2\pi}{a_0}$; $(0, 0.22)\frac{2\pi}{a_0}$ for a sample with the same hole doping as in **b**. This Fourier transform is symmetrised about the vertical axis

d-symmetry from factor component of modulations. The locations of *d*-symmetry form factor CDW peaks in $\tilde{D}(\vec{q})$ (dashed red circles) occur at $\vec{Q}_C = (0.22, 0)\frac{2\pi}{a_0}$; $(0, 0.22)\frac{2\pi}{a_0}$.

In the unprocessed data the modulations in electronic structure and topography occur based upon the sum of both oxygen sub-lattices ($\tilde{O}_x(\vec{q}) + \tilde{O}_y(\vec{q})$) and at wave-vector $\vec{Q} = \vec{Q}_{Bragg} \pm \vec{Q}_C$. No response of the tip to these modulations could produce a spurious $I_c(\vec{r})$ modulation at the wave-vector $\vec{Q}_P = (0.25 \pm 0.02, 0)\frac{2\pi}{a_0}$ and $(0, 0.25 \pm 0.02)\frac{2\pi}{a_0}$. Further, no significant modulations occur in the normal state resistance, $R_N(\vec{q})$, at $\vec{Q}_P$ indicating that these modulations are not the result of a variations in the tip-sample distance (see Appendix H).

Obviously, Fig. 7.2b, d are not identical, with $|\tilde{I}_c(\vec{q})|$ exhibiting much narrower peaks, implying a longer spatial coherence length for $I_c(\vec{r})$ modulations. Nevertheless, the $I_c(\vec{r})$ modulation wave-vector, $\vec{Q}_P$, is consistent (within joint error bars) with the wave-vector of the CDW at the same hole doping.

The $I_c(\vec{r})$ modulations also exhibit a primarily s/s'-symmetry form factor. One deduces this because Fig. 7.2b is a conventional Fourier transform based on the sum of all sub-lattices. This is in contrast to the CDW modulations, which exhibits a primarily d-symmetry form factor. Again, no peaks in $|\tilde{I}_c(\vec{q})|$ at $\vec{Q} \approx \vec{Q}_C/2$ are observed above the background. However, if modulations at $\vec{Q} \approx \vec{Q}_C/2$ existed with a d-symmetry form factor, our SJTM would likely not resolve them due to lack of intra-unit-cell resolution.

Having demonstrated in Chap. 5 that our SJTM faithfully probes variations in the superfluid density, the results presented above provide strong, direct evidence for an approximately four unit-cell periodic modulation of the superconducting condensate in $Bi_2Sr_2CaCu_2O_{8+x}$. Furthermore, we have demonstrated that this modulation has approximately the same wave-vector as the known predominantly d-symmetry form factor CDW in this material at the same doping. In the following section I will discuss these $I_c(\vec{r})$ modulations in the context of a PDW component to the superconducting condensate.

7.2 Discussion of $I_c(\vec{r})$ Modulations as a Pair Density Wave

In Chap. 5 I demonstrated that the maximum Cooper-pair current, $I_c(\vec{r})$, faithfully measures spatial variations in the superfluid density. In light of this, we ascribe the periodic $I_c(\vec{r})$ modulations described above as being due to a pair density wave (PDW) component in the superconducting condensate.

As discussed in Chap. 5, the intrinsic Josephson critical current, I_J, is proportional to $|\Psi_0|$. Ψ_0 is the Ginzburg–Landau order parameter for a uniform superconductor, related to the superfluid density, ρ_s, through $\rho_s = \frac{\hbar^2}{2m}|\Psi_0|^2$. As detailed in Chap. 5, the ultra-small junction in our SJTM supports a maximum Cooper pair current $I_c \propto I_J^2$, which is reduced in magnitude as compared to I_J by phase fluctuations across the junction. Thus, measurements of I_c are proportional to $|\Psi_0|^2$.

To explore the consequences of a PDW for our SJTM experiment we model our tip as point-like, with a uniform superconducting order parameter that couples to a modulating order parameter in the sample

$$\Psi(\vec{r}) = \Psi_0 + \Psi_{\vec{Q}_P} e^{i\vec{Q}_P \cdot \vec{r}} + \Psi_{-\vec{Q}_P} e^{-i\vec{Q}_P \cdot \vec{r}} + \ldots . \tag{7.1}$$

The modulation is superposed on top of a uniform superconducting component because our measurements are made deep within the superconducting phase ($T = 45\,\text{mK}$, $T_c = 88\,K$). This will give a corresponding modulation in the intrinsic Josephson critical current $I_J = I_J^0 + I_P \cos(\vec{Q} \cdot \vec{r})$. The maximum Cooper-pair current, $I_c \propto I_J^2$, will then modulate as

$$I_c \propto (I_J^0)^2 + 2I_J^0 I_J^P \cos(\vec{Q}_P \cdot \vec{r}) + (I_J^P)^2 \cos^2(\vec{Q} \cdot \vec{r}) + \ldots . \tag{7.2}$$

The PDW $\Psi_{\vec{Q}_P}$ will manifest itself as a modulation at wave-vector $\vec{Q}_P$ on top of a background corresponding to the uniform d-wave superconductor.

One could also take the opposite point of view and treat the tip as though it were a piece of $Bi_2Sr_2CaCu_2O_{8+x}$, with large extent in the x and y directions, having both a uniform and PDW superconducting component. This is potentially a valid model because the spatial extent of the tip is of the same order of magnitude as the $I_c(\vec{r})$ modulation wave-length. The Josephson coupling between tip and sample is then roughly equivalent to the inter-layer Josephson coupling intrinsic to the material, with a spatial phase shift between the PDW in the two layers that accounts for the position of the tip over the surface.

In this case, one would also expect a PDW with wave-vector $\vec{Q}_P$ to modulate the intrinsic Josephson critical current as $I_J = I_J^0 + I_P \cos(\vec{Q} \cdot \vec{r})$. This would lead to the same form of $I_c(\vec{r})$ given in Eq. 7.2. Again, the PDW $\Psi_{\vec{Q}_P}$ would manifest itself in $I_c(\vec{r})$ as a modulation at wave-vector $\vec{Q}_P$ on top of a background corresponding to the uniform d-wave superconductor.

The data presented in the previous section are clear experimental evidence for modulations of the superconducting condensate in $Bi_2Sr_2CaCu_2O_{8+x}$ with wave-vector $\vec{Q}_P = (0.25 \pm 0.02, 0)\frac{2\pi}{a_0}$. The simple models of the tip-sample Josephson coupling given in this section demonstrate that this can be viewed as a PDW component coexisting with a robust uniform condensate.

7.3   Conclusions

The visualisation of a PDW, a long-term challenge in physics has now been achieved using SJTM. This represents the first direct detection of a periodically modulating superconducting pair-amplitude, akin to the FFLO phase first predicted in 1964. The PDW is observed in $Bi_2Sr_2CaCu_2O_{8+x}$ at 17% hole doping, coexisting with the d-wave high-temperature superconductor. The PDW gives rise to modulations in $I_c(\vec{r})$ whose amplitude is ~5% that due to the d-wave superconductor. The PDW has approximately the same wave-vector as the d-symmetry form factor CDW ($\vec{Q}_P \approx \vec{Q}_C$) that exists at the same doping in this material albeit with an s/s'-symmetry form factor.

That a PDW is detected at $\vec{Q}_P \approx \vec{Q}_C$ with a relatively small amplitude compared to the d-wave superconducting component is consistent with a PDW arising from the coupling of the CDW to the d-wave superconductor (scenario 3 in Table 6.2). This follows naturally from the Ginzburg–Landau analysis in Sect. 6.4 (specifically Eq. 6.13). Furthermore, that no PDW modulations are detected at $\vec{Q} \approx \vec{Q}_C/2$ is seemingly inconsistent with the idea that the CDW should be regarded as a secondary order parameter generated through the product of primary PDW order parameters (scenario 1 in Table 6.2). However, given that our SJTM may not be sensitive to modulations at $\vec{Q} \approx \vec{Q}_C/2$ if they have a d-symmetry form factor, we should not draw that conclusion based on SJTM alone.

If a PDW with wave-vector $\vec{Q}_P \approx \vec{Q}_C/2$ co-exists with the d-symmetry super-conductor it should, in addition the the CDW at $\vec{Q}_C$ present above T_c, induce a CDW at $\vec{Q} = \vec{Q}_C/2$ for $T < T_c$. No CDW at this wave-vector has been reported in $Bi_2Sr_2CaCu_2O_{8+x}$ either by STM or scattering probes. This in turn suggests that if a PDW with $\vec{Q}_C/2$ exists in $Bi_2Sr_2CaCu_2O_{8+x}$ it must be dynamical.

As well as being consistent with a scenario in which primary CDW and d-wave superconducting order parameters couple to form a PDW for $T < T_c$, our results would also be consistent with models where CDW and PDW (both primary) co-exist at the same $|\vec{Q}|$ (scenario 3 in Table 6.2). Through Eq. 6.9 this should produce a CDW at wave-vector $2\vec{Q}_C$, but it is highly plausible that this modulation is too small to detect with present experimental capabilities.

This work is only the first foray into direct, nano-resolved, measurements of the pairing amplitude in cuprate superconductors. One would like to search for the existence of a PDW above the bulk T_c, where $\Psi_0 = 0$, $\Psi_{\vec{Q}} \neq 0$. This would constitute the detection of a truly new state of matter [5, 11]. To search for this with SJTM the best candidate material would be $La_{2-x}Ba_xCuO_4$ at 1/8th doping. Here, the bulk T_c is small enough that SJTM could feasibly operate above it. Additionally, there is a good deal of indirect evidence suggesting that such a state does indeed exist here (see Sect. 6.2). Finally, our SJTM approach to nanometre-resolution Cooper-pair condensate imaging also reveals a direct route to visualisation of FFLO or PDW states in other cuprates, iron-pnictides and unconventional superconductors.

References

1. J. Bardeen, L.N. Cooper, J.R. Schrieffer, Theory of superconductivity. Phys. Rev. **108**(5), 1175–1204 (1957)
2. P. Fulde, R.A. Ferrell, Superconductivity in a strong spin-exchange field. Phys. Rev. **135**(3A), A550–A563 (1964)
3. A.I. Larkin, Y.N. Ovchinnikov, Inhomogeneous state of superconductors. Sov. Phys. JETP **20**, 762–769 (1964)
4. Y.-A. Liao et al., Spin-imbalance in a one-dimensional Fermi gas. Nature **467**(7315), 567–9 (2010)
5. E. Fradkin, S.A. Kivelson, J.M. Tranquada, Colloquium: Theory of intertwined orders in high temperature superconductors. Rev. Mod. Phys. **87**(2), 457–482 (2015)

6. A. Himeda, T. Kato, M. Ogata, Stripe states with spatially oscillating d-wave superconductivity in the two-dimensional $t - t' - J$ model. Phys. Rev. Lett. **88**(11), 117001 (2002)
7. M. Raczkowski et al., Unidirectional d-wave superconducting domains in the two-dimensional t-J model. Phys. Rev. B **76**(14), 3–6 (2007)
8. K.Y. Yang et al. Nature of stripes in the generalized t-J model applied to the cuprate superconductors. New J. Phys. 11 (2009)
9. F. Loder et al., Mean-field pairing theory for the charge-stripe phase of hightemperature cuprate superconductors. Phys. Rev. Lett. **107**(18), 1–4 (2011)
10. P. Corboz, T.M. Rice, M. Troyer, Competing states in the t - J model: Uniform d-wave state versus stripe state. Phys. Rev. Lett. **113**(4), 1–5 (2014)
11. E. Berg et al., Dynamical layer decoupling in a stripe-ordered high-Tc superconductor. Phys. Rev. Lett. **99**(12), 1–4 (2007)
12. K. Seo, H.-D. Chen, J. Hu, Complementary pair-density-wave and d-wavecheckerboard orderings in high-temperature superconductors. Phys. Rev. B **78**(9), 094510 (2008)
13. E. Berg, E. Fradkin, S.A. Kivelson, Charge-4e superconductivity from pair density wave order in certain high temperature superconductors. Nat. Phys. **5**(11), 5 (2009)
14. D.F. Agterberg, H. Tsunetsugu, Dislocations and vortices in pair density wave superconductors. Nat. Phys. **4**(8), 6 (2009)
15. M. Zelli, C. Kallin, A.J. Berlinsky, Quantum oscillations in a π-striped superconductor. Phys. Rev. B **86**(10), 1–16 (2012)
16. P.A. Lee, Amperean pairing and the pseudogap phase of cuprate superconductors. Phys. Rev. X **4**(3), 1–13 (2014)
17. H.-D. Chen et al., Pair density wave in the pseudogap state of high temperature superconductors. Phys. Rev. Lett. **93**(18), 187002 (2004)
18. C. Pépin et al., Pseudogap, charge order, and pairing density wave at the hot spots in cuprate superconductors. Phys. Rev. B **90**(19), 1–16 (2014)
19. H. Freire, V.S. de Carvalho, C. Pépin, Renormalization group analysis of the pair-density-wave and charge order within the fermionic hot-spot model for cuprate superconductors. Phys. Rev. B **92**(4), 045132 (2015)
20. Y. Wang, D.F. Agterberg, A. Chubukov, Interplay between pair- and charge-density-wave orders in underdoped cuprates. Phys. Rev. B **91**(11), 115103 (2015)
21. Y. Wang, D.F. Agterberg, A. Chubukov, Coexistence of charge-density- wave and pair-density-wave orders in underdoped cuprates. Phys. Rev. Lett. **114**(19), 1–6 (2015)

Chapter 8
Summary and Future Directions

In this thesis I have presented research that, through the introduction of two novel techniques, examines the nature of density wave order in cuprates and its relationship to superconductivity.

In Chap. 3 I built upon recent advances in STM visualisation of intra unit cell electronic structure to introduce sub-lattice segregated spectroscopic-imaging STM (SI-STM) in cuprates, whereby the atomic sub-lattices of the CuO_2 plane can be individually addressed. In Chap. 4 I went on to use this technique to reveal that the short-ranged charge density wave (CDW) in $Bi_2Sr_2CaCu_2O_{8+\delta}$ and $Na_xCa_{2-x}CuO_2Cl_2$ has a predominantly d-symmetry form factor. In such a CDW, a breaking of rotational symmetry within the unit is modulated periodically in space, giving the CDW a local d-wave character. Although its existence has been predicted for many years, this is the first observation of a d-symmetry form factor CDW in nature [1–17].

It is natural to ask whether there is any profound connection between the d-wave nature of the CDW form factor and the well known d-wave superconductivity in cuprates. Within itinerant spin-fermion "hot-spot" models of the CDW and superconductivity in cuprates the connection is indeed a deep one [5–8, 12, 14, 15]. Here it arises because both d-symmetry form factor CDW and d-wave superconductivity emerge from the same effective interaction between fermions at specific points in momentum space. If these models are indeed a correct description of the superconductivity and CDW in cuprates, the existence of a predominantly d-symmetry form factor CDW cannot be disentangled from that of the high-temperature d-wave superconductivity.

However, our measurements do not clearly distinguish between different models of CDW formation in cuprates that exhibit a predominantly d-symmetry form factor. For instance, it has also been proposed that the d-symmetry form factor results from the Coulomb repulsion between holes on the two oxygen sites in the CuO_2 plaquette [9, 13, 16, 17]. This favours unequal occupation of these sites, naturally resulting in a local d-wave character to the CDW.

The observation of a short ranged CDW in the electron doped cuprate $Nd_{2-x}Ce_x CuO_4$, where carriers are first doped into bands derived from the Cu $3d_{x^2-y^2}$ orbitals, provides a way to falsify this hypothesis [18]. If measurements sensitive to the CDW

form factor reveal that it is predominantly d-wave in electron doped cuprates, the hypothesis cannot be true.

Independent of a specific model of CDW formation in cuprates, a d-symmetry form factor CDW is a natural partner to d-wave superconductivity in the sense that it acts to protect the coherence of nodal quasi-particles against scattering from the disordered CDW in so called "cold-spots" [19]. That the CDW in $La_{2-x}Ba_xCuO_{4+\delta}$ has a predominantly s'-symmetry form factor, in contrast to other cuprates materials, raises the question of whether its anomalously large suppression of T_c at 1/8th doping can be attributed to the form factor of its CDW [20].

I have also demonstrated that the charge order in $Bi_2Sr_2CaCu_2O_{8+\delta}$ and $Na_xCa_{2-x}CuO_2Cl_2$ consists of nanoscale domains of unidirectional d-symmetry form factor CDW. Recent high-magnetic field measurements in $YBa_2Cu_3O_{6+x}$ reveal a magnetic-field induced CDW that is completely unidirectional [21, 22]. This is suggestive that the CuO_2 plane has an intrinsic instability to unidirectional ordering. A cautionary caveat is that $YBa_2Cu_3O_{6+x}$ is structurally orthorhombic, and so possesses no symmetry between Cu-O directions. I propose that measurements of magnetic field induced CDW in cuprates with a structural symmetry between the Cu-O directions be performed with the aim of directly demonstrating this unidirectional tendency of the CuO_2 plane.

In Chap. 5 I detailed the development of nanometer resolution scanned Josephson tunnelling microscopy (SJTM). By measuring the Cooper pair (Josephson) tunnelling current between a superconducting STM tip and a superconducting sample it was possible to directly visualise the superconducting condensate with nanometer resolution for the first time.

Utilising SJTM, the visualisation of a pair density wave (PDW), a long-term challenge in physics, has now been achieved. This represents the first direct detection of a periodically modulating superconducting condensate, akin to the FFLO phase first predicted in 1964. The PDW is observed in $Bi_2Sr_2CaCu_2O_{8+x}$ at 17% hole concentration, coexisting with the uniform d-wave high-temperature superconductivity. The PDW gives rise to modulations in the Cooper pair tunnelling current whose amplitude is $\sim$5% of that due to the uniform d-wave superconducting component. It has approximately the same wave-vector as the d-symmetry form factor CDW that exists at the same doping in this material, albeit with an s/s'-symmetry form factor.

By comparing the observed PDW wave-vector to that of the CDW above and below T_c, I conclude that the PDW observed in SJTM is either the result of coupling between the CDW and uniform superconductivity, or an instability of the CuO_2 plane to both PDW and CDW order at the same wave-vector. This is in contrast with the possibility that a PDW induces a CDW at twice its fundamental wave-vector. A route toward distinguishing between the two remaining scenaria would be to extend our SJTM measurements to cover a wider range of dopings. Additionally, if we could attain intra unit cell resolution cuprate SJTM we could directly examine the spatial relationship between CDW and PDW, thus determining whether they are independent or not.

Beyond the cuprates, SJTM shows great promise as a direct nano-resolved probe of superconducting condensates. As discussed in Chap. 5, the local single-particle

tunnelling gap of a superconductor is not easily related to the local superfluid stiffness or superconducting order parameter magnitude in all but a few cases. In contrast, SJTM measures the local superfluid stiffness in a way that is independent of any microscopic model of superconductivity.

SJTM has the potential to be a formidable tool in the study of any system where the nanoscale heterogeneity of the superconducting condensate is of interest. This includes superconducting devices and heterostructures, materials where superconductivity is intertwined with orders which break translational symmetry and the study of the effect of impurities on superconductivity.

SJTM could be of considerable use in the study of how to increase the critical current of superconductors through vortex pinning, currently of great technological interest. Because it can be operated in either single-particle or Cooper pair tunnelling modes, SJTM offers the ability to image the nature of defects, both natural and artificial, whilst simultaneously visualising the local superfluid stiffness. This could provide significant advances in our understanding of the vortex pinning processes in technologically relevant materials.

Finally, as detailed in Chap. 5, SJTM utilises the inelastic tunnelling of Cooper-pairs to access the superconducting condensate. This is the simplest form of inelastic tunnelling because the Cooper-pair condensate does not form a continuum of initial and final states. The emission and absorption of electromagnetic radiation in these processes allows for the possibility of nano-resolved spectroscopy or manipulation of adatoms on a superconducting surface.

References

1. J.-X. Li, C.-Q. Wu, D.-H. Lee, Checkerboard charge density wave and pseudogap of high-Tc cuprate. Phys. Rev. B **74**(18), 184515 (2006)
2. K. Seo, H.-D. Chen, J. Hu, D-wave checkerboard order in cuprates. Phys. Rev. B **76**(2), 020511 (2007)
3. D.M. Newns, C.C. Tsuei, Fluctuating CuOCu bond model of hightemperature superconductivity. Nat. Phys. **3**(3), 184–191 (2007)
4. C. Honerkamp, H.C. Fu, D.-H. Lee, Phonons and d-wave pairing in the two-dimensional Hubbard model. Phys. Rev. B **75**(1), 014503 (2007)
5. M. Metlitski, S. Sachdev, Instabilities near the onset of spin density wave order in metals. New J. Phys. **12**(10), 105007 (2010)
6. Y. Wang, A. Chubukov, Charge-density-wave order with momentum (2Q,0) and (0,2Q) within the spin-fermion model: Continuous and discrete symmetry breaking, preemptive composite order, and relation to pseudogap in hole-doped cuprates. Phys. Rev. B **90**(3), 1–52 (2014)
7. T. Holder, W. Metzner, Incommensurate nematic uctuations in twodimensional metals. Phys. Rev. B **85**(16), 165130 (2012)
8. K.B. Efetov, H. Meier, C. Pépin, Pseudogap state near a quantum critical point. Nat. Phys. **9**(7), 442–446 (2013)
9. S. Bulut, W.A. Atkinson, A.P. Kampf, Spatially modulated electronic nematicity in the three-band model of cuprate superconductors. Phys. Rev. B **88**(15), 155132 (2013)
10. S. Sachdev, R. La Placa, Bond order in two-dimensional metals with antiferromagnetic exchange interactions. Phys. Rev. Lett. **111**(2), 027202 (2013)

11. J.C.S. Davis, D.-H. Lee, Concepts relating magnetic interactions, intertwined electronic orders, and strongly correlated superconductivity, in *Proceedings of the National Academy of Sciences of the United States of America* (2013), pp. 1–8

12. A. Allais, J. Bauer, S. Sachdev, Density wave instabilities in a correlated two-dimensional metal. Phys. Rev. B **90**(15), 1–5 (2014)

13. M.H. Fischer et al., Nematic and spin-charge orders driven by hole-doping a charge-transfer insulator. New J. Phys. 16 (2014)

14. C. Pépin et al., Pseudogap, charge order, and pairing density wave at the hot spots in cuprate superconductors. Phys. Rev. B **90**(19), 1–16 (2014)

15. D. Chowdhury, S. Sachdev, Density-wave instabilities of fractionalized Fermi liquids. Phys. Rev. B **90**(24), 1–10 (2014)

16. W.A. Atkinson, A.P. Kampf, S. Bulut, Charge order in the pseudogap phase of cuprate superconductors. New J. Phys. **17**(1), 13025 (2015)

17. Y. Yamakawa, H. Kontani, Spin- uctuation-driven nematic charge-density wave in cuprate superconductors: impact of aslamazov-larkin vertex corrections. Phys. Rev. Lett. **114**(25), 1–6 (2015)

18. E.H. da Silva Neto et al., Charge ordering in the electron-doped superconductor $Nd_2 - xCe_xCuO_4$. Science **347**(6219), 282–285 (2015)

19. K. Lee, S.A. Kivelson, E.-A. Kim, Cold-spots and glassy nematicity in underdoped cuprates. 014204, 1–9 (2016)

20. A.J. Achkar et al., Orbital symmetry of charge-density-wave order in $La_1.875Ba_1.125CuO_4$ and $YBa_2Cu_3O_6$.67. Nat. Mater. **15**(6), 616–620 (2016)

21. J. Chang et al., Magnetic field controlled charge density wave coupling in underdoped $YBa_2Cu_3O_6 + x$. Nat. Commun. 7, 11494 (2016)

22. H. Jang et al., Ideal charge density wave order in the high-field state of superconducting YBCO (2016), arXiv:1607.05359

Appendix A
Publications Arising from Doctoral Studies

Below I list publications arising from my doctoral studies, grouped by subject matter.

A.1 Piezoelectric Strain Tuning

C. W. Hicks, D. O. Brodsky, E. A. Yelland, A. S. Gibbs, J. A. N. Bruin, M. B. Barber, S. D. Edkins, K. Nishimura, S. Yonezawa, Y. Maeno, A. P. Mackenzie. "Strong Increase of T_c of Sr_2RuO_4 Under Both Tensile and Compressive Strain. *Science* **344** 283–285 (2014).

C. W. Hicks, M. E. Barber, S. D. Edkins, D. O. Brodsky, A. P. Mackenzie. "Piezoelectric-based apparatus for strain tuning". *Review of Scientific Instruments* **85**(6) 065003 (2014).

A.2 Spectroscopic Imaging STM of the Cuprate CDW

K. Fujita, M. H. Hamidian, S. D. Edkins, Chung Koo Kim, Y. Kohsaka, M. Azuma, M. Takano, H. Takagi, H. Eisaki, S. Uchida, A. Allais, M. J. Lawler, E. -A. Kim, S. Sachdev, J. C. Davis. "Direct phase-sensitive identification of a d-form factor density wave in underdoped cuprates". *Proceedings of the National Academy of Sciences* **111**(30) E3026–E3032 (2014).

M. H. Hamidian*, S. D. Edkins*, Chung Koo Kim, JC Davis, AP Mackenzie, H Eisaki, S Uchida, MJ Lawler, E-A Kim, Subir Sachdev, K Fujita. "Atomic-scale electronic structure of the cuprate d-symmetry form factor density wave state". *Nature Physics* **12** 150 (2016).

A. Mesaros, K. Fujita, S. D. Edkins, M. H. Hamidian, H. Eisaki, S. Uchida, J. C. Samus Davis, M. J. Lawler, Eun-Ah Kim. "Commensurate $4a_0$ period Charge Density Modulations throughout the $Bi_2Sr_2CaCu_2O_{8+x}$ Pseudogap Regime" *PNAS* **113**(45) 12661–12666 (2016) doi:10.1073/pnas.1614247113.

A.3 Scanned Josephson Tunnelling Microscopy

M. H. Hamidian*, S. D. Edkins*, Sang Hyun Joo*, A. Kostin, H. Eisaki, S. Uchida, M. J. Lawler, E. -A. Kim, A. P. Mackenzie, K. Fujita, Jinho Lee, J. C. Samus Davis. "Detection of a Cooper-pair density wave in $Bi_2Sr_2CaCu_2O_{8+x}$". *Nature* **532** 343 (2016).

   * These authors contributed equally to this publication.

Appendix B
A Form Factor Description of Local Rotational Symmetry in Density Waves

In classifying the local rotational symmetry of density waves there is an ambiguity that arises because the wave-vector already breaks a global rotation symmetry itself. This leads to multiple form factor descriptions of the same state. Here I will adopt the convention introduced by Sachdev and La Placa [1]. Working in a one-site representation of the CuO_2 plane with copper sites at positions $\vec{r}_i$ and $\vec{r}_j$ one can parameterise a CDW order via,

$$\langle \hat{c}_{i\sigma}^{\dagger} \hat{c}_{j\sigma} \rangle = \sum_{\vec{Q}} \left[\sum_{\vec{k}} P(\vec{k}, \vec{Q}) e^{i\vec{k} \cdot (\vec{r}_i - \vec{r}_j)} \right] e^{i\vec{Q} \cdot (\vec{r}_i + \vec{r}_j)/2} , \qquad (B.1)$$

where $\hat{c}_{j\sigma}$ annihilates a fermion with spin σ on a site at position $\vec{r}_i$. Here the wave vector $\vec{Q}$ is associated with a modulation in the average coordinate $(\vec{r}_i + \vec{r}_j)/2$. The form factor describes the dependence on the relative co-ordinate $\vec{r}_i - \vec{r}_i$. An advantage of the formulation in Eq. B.1 is that it provides an efficient characterisation of symmetries. The operator identity $\langle \hat{A}^{\dagger} \rangle \equiv \langle \hat{A} \rangle^*$ requires that

$$P^*(\vec{k}, \vec{Q}) = P(\vec{k}, -\vec{Q}) , \qquad (B.2)$$

and

$$P(\vec{k}, \vec{Q}) = P(-\vec{k}, \vec{Q}) \qquad (B.3)$$

if time-reversal symmetry is preserved.

Here I will consider a $P(\vec{k}, \vec{Q})$ that is non-zero only for $\vec{Q} = \vec{Q}_x = (Q, 0)$ and $\vec{Q} = \vec{Q}_y = (0, Q)$, the experimentally detected wave-vector in cuprates [2–4]. Assuming that time-reversal symmetry is preserved the form factor has the general form

$$P(\vec{k}, \vec{Q}) = P_S + P_{S'} \left(\cos(k_x) + \cos(k_y) \right) + P_D \left(\cos(k_x) - \cos(k_y) \right) + \cdots . \qquad (B.4)$$

For general incommensurate $\vec{Q}$, any even function of $\vec{k}$ is allowed on the right-hand side. The case of a predominantly d-symmetry form factor CDW considered in Chap. 4 is parameterised by $|P_D| \gg |P_{S'}|$ and $|P_D| \gg |P_S|$

We can now make a connection between this abstract parameterisation of the intra-unit-cell rotational symmetry of the CDW and the local observables measured using STM. Making a transformation from the three-site to the single-site model of the CuO_2 layer, we can deduce the relationship

$$\langle \hat{c}_{i\sigma}^\dagger \hat{c}_{j\sigma} + \hat{c}_{j\sigma}^\dagger \hat{c}_{i\sigma} \rangle \begin{cases} \frac{1}{K}\rho(\vec{r}_{Cu}) & \text{for } i = j \\ \frac{1}{K'}\rho(\vec{r}_{O_x}) & \text{for } i, j \text{ n.n along x direction} \\ \frac{1}{K'}\rho(\vec{r}_{O_y}) & \text{for } i, j \text{ n.n along y direction.} \end{cases} \qquad (B.5)$$

Here $\rho(\vec{r})$ is any density-like observable (i.e., invariant under time-reversal and spin rotations) such as charge or local density of states and K and K' are constants. Combining Eqs. B.1, B.4 and B.5 we can now write

$$\rho(\vec{r}_{Cu}) = 2KRe\left\{ \left[\sum_{\vec{k}} P(\vec{k}, \vec{Q}) \right] e^{i\vec{Q}\cdot\vec{r}_{Cu}} \right\} \qquad (B.6a)$$
$$= A_s \cos(\vec{Q} \cdot \vec{r}_{Cu} + \phi_s)$$

$$\rho(\vec{r}_{O_x}) = 2K'Re\left\{ \left[\sum_{\vec{k}} \cos(k_x) P(\vec{k}, \vec{Q}) \right] e^{i\vec{Q}\cdot\vec{r}_{O_x}} \right\} \qquad (B.6b)$$
$$= A_{s'} \cos(\vec{Q} \cdot \vec{r}_{O_x} + \phi_{s'}) + A_D \cos(\vec{Q} \cdot \vec{r}_{O_x} + \phi_D)$$

$$\rho(\vec{r}_{O_y}) = 2K'Re\left\{ \left[\sum_{\vec{k}} \cos(k_y) P(\vec{k}, \vec{Q}) \right] e^{i\vec{Q}\cdot\vec{r}_{O_y}} \right\} \qquad (B.6c)$$
$$= A_{s'} \cos(\vec{Q} \cdot \vec{r}_{O_y} + \phi_{s'}) - A_D \cos(\vec{Q} \cdot \vec{r}_{O_y} + \phi_D)$$

with $A_S = 2K|P_S|$, $A_{S',D} = 2K'|P_{S',D}|$ and $\phi_{S,S',D} = \arg(P_{S,S',D})$.

With the simplification $\phi_S = \phi_{S'} = \phi_D = \phi(\vec{r})$ and allowing for spatial disorder of the phase of the CDW we arrive at

$$\rho(\vec{r}) = \left[S(\vec{r}) + S'(\vec{r}) + D(\vec{r}) \right] \cos(\vec{Q} \cdot \vec{r} + \phi(\vec{r})), \qquad (B.7)$$

with $S(\vec{r}) = A_S$ if $\vec{r} \in \vec{r}_{Cu}$ and otherwise zero; $S'(\vec{r}) = A_{S'}$ if $\vec{r} \in \vec{r}_{O_x}$ or $\vec{r}_{O_y}$ and otherwise zero; $D(\vec{r}) = A_D$ if $\vec{r} \in \vec{r}_{O_x}$, $-A_D$ if $\vec{r} \in \vec{r}_{O_y}$ and otherwise zero. This is Eq. 4.7 in Chap. 4.

The case of a predominantly d-symmetry form factor CDW discussed in this chapter is parameterised by $A_D \gg A_S$ and $A_D \gg A_{S'}$. By inspection of Eq. B.6 one can see that a purely d-symmetry form factor CDW exhibits density modulations only on the O_x and O_y sites, but with a π phase shift between them, as presented in Chap. 4.

Appendix C
Calculating Sub-lattice Fourier Transforms

As discussed in Chap. 4, the projection of a CDW into s-, s'-, and d-symmetry form factor components is conceptually appealing. However, for the purposes of this appendix I will work in terms of the segregated oxygen sublattice images $O_x(\vec{r})$.

In terms of the segregated sub-lattices, a d-symmetry form factor CDW is one for which the CDW on the O_x sites is in anti-phase with that on the O_y sites. For $\vec{q} \neq 0$ ordering the form factor does not uniquely determine the point group symmetry of the CDW and hence in general s-, s'-, and d-symmetry form factors are free to mix. This appendix predicts the consequences of a primarily d-symmetry form factor CDW for $\tilde{O}_{x,y}(\vec{q})$ and shows its consistency with the data presented in Chap. 4.

To deduce the logical consequences of a d-symmetry form factor CDW for the Fourier transforms of the segregated oxygen site images one can start by constructing the dual real and momentum-space representation of the sub-lattices:

$$L_{Cu}(\vec{r}) = \sum_{i,j} \delta(\vec{r} - \vec{R}_{i,j}) \Leftrightarrow \tilde{L}_{Cu}(\vec{q}) = \sum_{h,k} \delta(\vec{q} - G^{h,k}) \tag{C.1}$$

$$L_{O_x}(\vec{r}) = L_{Cu}\left(\vec{r} - \frac{a_0\hat{x}}{2}\right) \Leftrightarrow \tilde{L}_{O_x}(\vec{q}) = e^{i\frac{a_0\hat{x}}{2}}\tilde{L}_{Cu}(\vec{q}) \tag{C.2}$$

$$L_{O_y}(\vec{r}) = L_{Cu}\left(\vec{r} - \frac{a_0\hat{y}}{2}\right) \Leftrightarrow \tilde{L}_{O_y}(\vec{q}) = e^{i\frac{a_0\hat{y}}{2}}\tilde{L}_{Cu}(\vec{q}) \,. \tag{C.3}$$

The $\{R_{i,j}\}$ are the set of direct lattice vectors of the square lattice with lattice constant a_0 and the $G^{h,k}$ are the reciprocal lattice vectors. The displacement of the oxygen sub-lattices from the copper sub-lattice has the effect of modulating the phase of their Bragg peaks along the direction of displacement with periodicity $4\pi/a_0$ in reciprocal space. This is depicted in Fig. C.1a.

Using the convolution theorem, a d-symmetry form factor modulation of the oxygen site density takes on the dual description
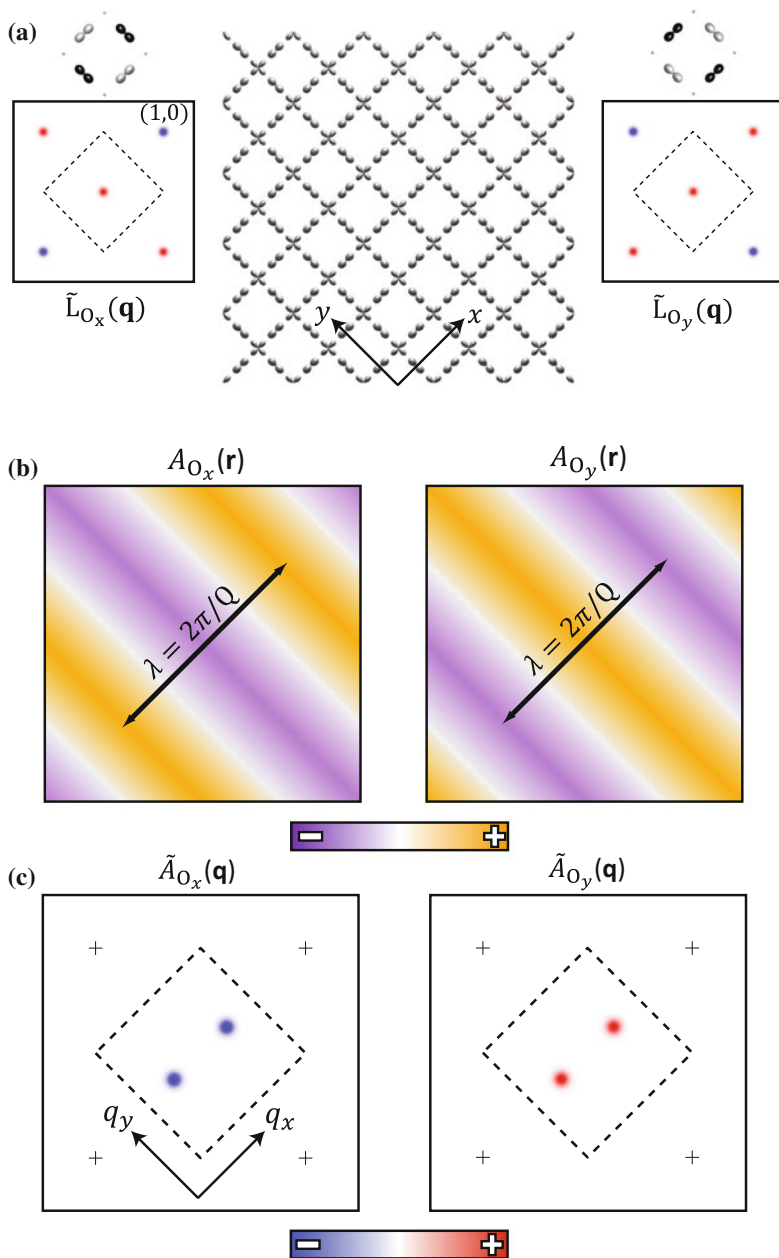
Fig. C.1 **a** Fourier transforms of the x-directed and y-directed oxygen sub-lattices without a CDW modulation. *Gray* orbitals signify those in the sub-lattice under consideration and *black* those in the other sub-lattice. **b** Schematic of continuous functions $A_{O_{x,y}}(\vec{r})$ that when multiplied by the sub-lattice functions $L_{O_{x,y}}(\vec{r})$ yield density waves in anti-phase on the two sub-lattices with a modulation along the x direction. **c** Fourier transforms of the functions $A_{O_{x,y}}(\vec{r})$ exhibiting a relative phase of π as required for a *d*-symmetry form factor density wave

$$O_x(\vec{r}) = L_{O_x}(\vec{r}) \cdot A_{O_x}(\vec{r}) \Leftrightarrow \tilde{O}_x(\vec{q}) \star \tilde{A}_{O_x}(\vec{q}) \tag{C.4}$$

$$O_y(\vec{r}) = L_{O_y}(\vec{r}) \cdot A_{O_y}(\vec{r}) \Leftrightarrow \tilde{O}_y(\vec{q}) \star \tilde{A}_{O_y}(\vec{q}) \tag{C.5}$$

$$A_{O_x}(\vec{r}) = -A_{O_y}(\vec{r}) = A(\vec{r}) \Leftrightarrow \tilde{A}_{O_x}(\vec{q}) = -\tilde{A}_{O_y}(\vec{q}) = \tilde{A}(\vec{q}) . \tag{C.6}$$

The functions $O_{x,y}(\vec{r})$ are the segregated oxygen sub-lattice images. The $A_{O_{x,y}}(\vec{r})$ are continuous functions that when multiplied by the sub-lattice functions yield density waves in anti-phase on the separate oxygen sub-lattices (Fig. C.1b). Figure C.1c shows their Fourier transforms $\tilde{A}_{O_{x,y}}(\vec{q})$. Note that $A(\vec{r})$ may contain arbitrary amplitude and overall phase disorder but maintain the d-symmetry form factor as long as the relative phase relation in Eq. C.6 is maintained.

As shown in Fig. C.2a, the convolutions in Eqs. C.4 and C.5 create an image of $\tilde{A}_{O_{x,y}}(\vec{q})$ at each reciprocal lattice vector that sums to form the total convolution. Labeling the convolution image due to the reciprocal lattice vector (h, k) in the x sub-lattice $\tilde{O}_x^{h,k}(\vec{q})$,

$$\tilde{O}_x(\vec{q}) = \sum_{h,k} \tilde{O}_x^{h,k}(\vec{q}) = \sum_{h,k} e^{i(\vec{G}^{h,k} - \frac{a_0 \hat{x}}{2})} \tilde{A}_{O_x}(\vec{q} - \vec{G}^{h,k}) . \tag{C.7}$$

In creating the (h, k) convolution image, the phase of the sub-lattice Bragg peak at $\vec{G}^{h,k}$ and that of $\tilde{A}_{O_x}(\vec{q})$ must be added:

$$\arg\left\{\tilde{O}_x^{h,k}(\vec{q})\right\} = \arg\left\{\tilde{A}_{O_x}(\vec{q} - \vec{G}^{h,k})\right\} + \arg\left\{e^{i(\vec{G}^{h,k} - \frac{a_0 \hat{x}}{2})}\right\} . \tag{C.8}$$

Thus, is follows immediately that

$$\tilde{O}_x^{0,0} = \tilde{A}(\vec{q}), \ \tilde{O}_y^{0,0} = -\tilde{A}(\vec{q}) \tag{C.9}$$

$$\tilde{O}_x^{1,0} = -\tilde{A}(\vec{q}), \ \tilde{O}_y^{1,0} = -\tilde{A}(\vec{q}) \tag{C.10}$$

$$\tilde{O}_x^{0,1} = \tilde{A}(\vec{q}), \ \tilde{O}_y^{0,1} = \tilde{A}(\vec{q}) \tag{C.11}$$

and hence

$$\tilde{O}_x^{0,0} + \tilde{O}_y^{0,0} = 0, \ \tilde{O}_x^{0,0} - \tilde{O}_y^{0,0} = 2\tilde{A}(\vec{q}) \tag{C.12}$$

$$\tilde{O}_x^{1,0} + \tilde{O}_y^{1,0} = -2\tilde{A}(\vec{q}), \ \tilde{O}_x^{1,0} - \tilde{O}_y^{1,0} = 0 \tag{C.13}$$

$$\tilde{O}_x^{0,1} + \tilde{O}_y^{0,1} = 2\tilde{A}(\vec{q}), \ \tilde{O}_x^{0,1} + \tilde{O}_y^{0,1} = 0 \tag{C.14}$$

A direct consequence of a d-symmetry form factor is that in $\tilde{O}_x(\vec{q}) + \tilde{O}_y(\vec{q})$ the amplitude of the convolution image at $(0, 0)$ is canceled exactly whereas those at the $(\pm 1, 0)$ and $(0, \pm 1)$ points are enhanced as illustrated in Fig. C.2b and c. The converse is true for $\tilde{O}_x(\vec{q}) + \tilde{O}_y(\vec{q})$. This holds for any d-symmetry form factor modulation in the presence of arbitrary amplitude and overall phase disorder.
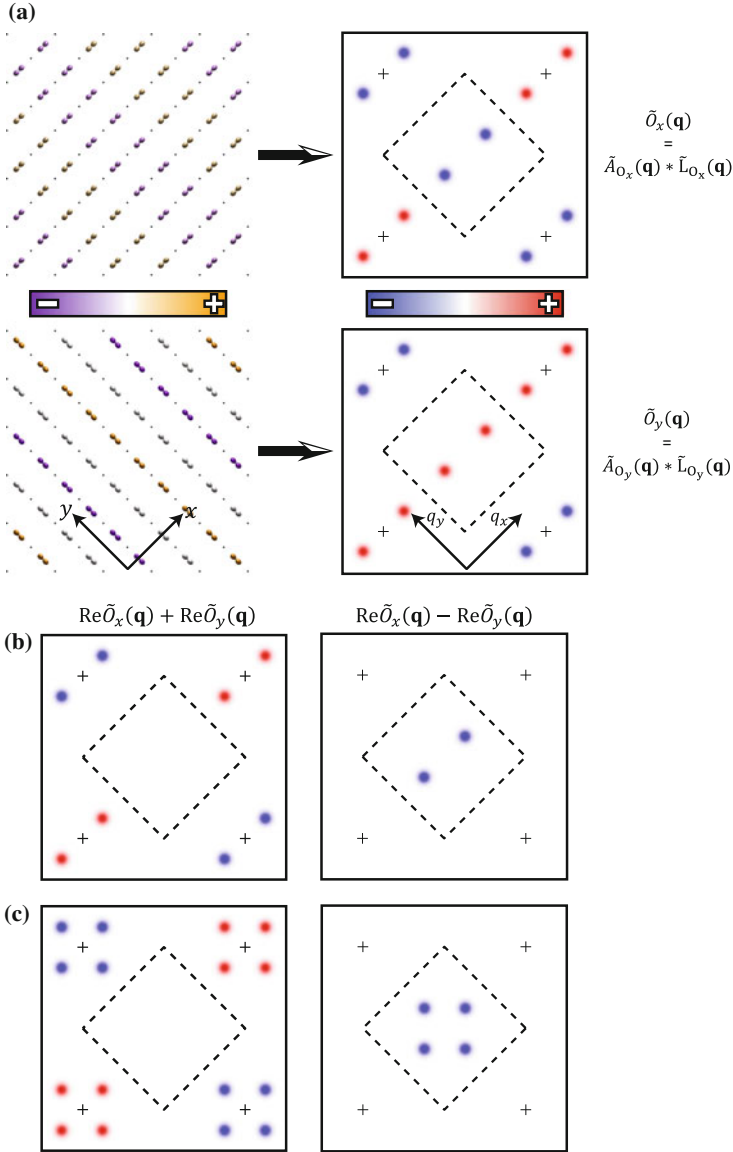
Fig. C.2 **a** Schematic of the segregated sub-lattice images $O_{x,y}(\vec{r})$ and their Fourier transforms $\tilde{O}_{x,y}(\vec{q})$ that can be obtained from Fig. C.1 by application of the convolution theorem. **b** Sum and difference of $Re\tilde{O}_x$ and $Re\tilde{O}_y$ for a d-symmetry form factor CDW with modulation along the x direction at $\vec{Q}_x = (Q, 0)$. Note that the origin of coordinates in real space has been chosen such that the Fourier transforms are purely real. **c** Sum and difference of $Re\tilde{O}_x$ and $Re\tilde{O}_y$ for a d-symmetry form factor CDW with modulations along the x and y directions at $\vec{Q} = (Q, 0), (0, Q)$. The key signature of the d-symmetry form factor is the absence of the peaks at $(Q, 0), (0, Q)$ in $Re\tilde{O}_x(\vec{q}) + Re\tilde{O}_y(\vec{q})$ and their presence in $Re\tilde{O}_x(\vec{q}) - Re\tilde{O}_y(\vec{q})$; the converse is true for the CDW peaks surrounding $(\pm1, 0)$ and $(0, \pm1)$

Empirically (as detailed in Chap. 3), our data contain modulations at two wave vectors $\vec{Q}_x = (Q, 0)$ and $\vec{Q}_y = (0, Q)$ with $Q \approx 1/4$ but with a great deal of fluctuation in the spatial phase of the CDW [5]. Any d-symmetry form factor CDW containing two wave vectors $\vec{Q}_x$ and $\vec{Q}_y$ can be described by

$$A(\vec{r}) = Re\left[e^{i\vec{Q}_x \cdot \vec{r}} \cdot H_x(\vec{r})\right] + Re\left[e^{i\vec{Q}_y \cdot \vec{r}} \cdot H_y(\vec{r})\right] \tag{C.15}$$

$$\tilde{A}(\vec{q}) = \frac{1}{2}\left[\tilde{H}_x(\vec{q} - \vec{Q}_x) + \tilde{H}_x^*(\vec{q} + \vec{Q}_x) + \tilde{H}_y(\vec{q} - \vec{Q}_y) + \tilde{H}_y^*(\vec{q} + \vec{Q}_y)\right]$$
$$\tag{C.16}$$

The complex valued functions $H_{x,y}(\vec{r})$ locally modulate the amplitude and phase of the density wave and hence encode its disorder. The problem now reduces to performing the convolutions contained in Eqs. C.4 and C.5.

For the specific example of $\vec{Q}_x \approx (1/4,)$ and $\vec{Q}_y \approx (0, 1/4)$ considered in our study, the predominantly d-symmetry form factor requires that the peaks at $\pm\vec{Q}_x$ and $\pm\vec{Q}_y$ present in both $\tilde{O}_x(\vec{q})$ and $\tilde{O}_y(\vec{q})$ must cancel exactly in $\tilde{O}_x(\vec{q}) + \tilde{O}_y(\vec{q})$ and be enhanced in $\tilde{O}_x(\vec{q}) - \tilde{O}_y(\vec{q})$. Conversely the peaks at $\vec{Q}' = (1, 0) \pm \vec{Q}_{x,y}$ and $\vec{Q}'' = (0, 1) \pm \vec{Q}_{x,y}$ will be enhanced in $\tilde{O}_x(\vec{q}) + \tilde{O}_y(\vec{q})$ but will cancel exactly in $\tilde{O}_x(\vec{q}) - \tilde{O}_y(\vec{q})$. These are necessary consequences of a CDW with a d-symmetry form factor. This is discussed in the Chap. 4 and in accord with the observations in Fig. 4.7.

Appendix D
Sub-lattice Phase-Resolved Fourier Transforms
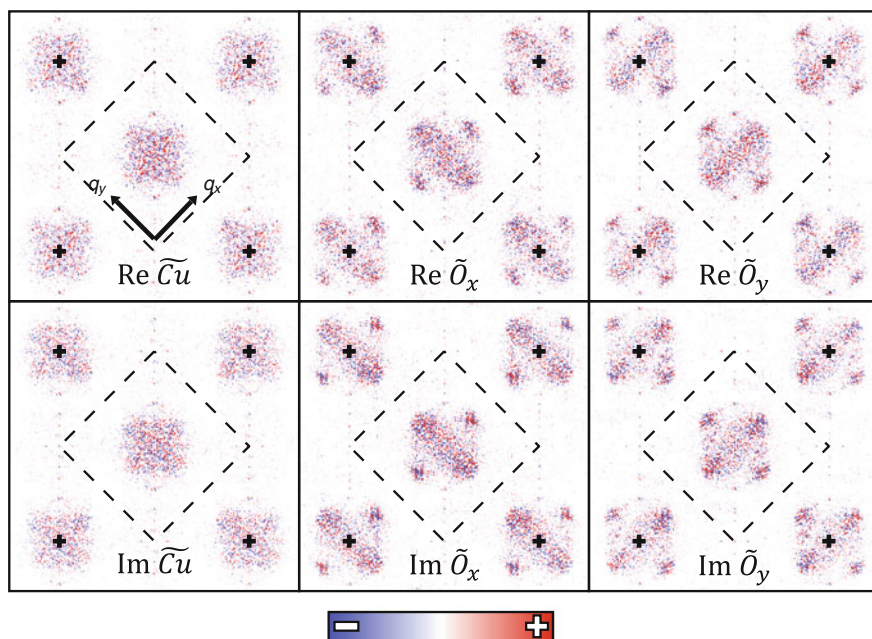
(See Figs. D.1 and D.2).

Fig. D.1 Real and imaginary parts of the sub-lattice segregated Fourier transforms $\tilde{Cu}(\vec{q})$, $\tilde{O}_x(\vec{q})$ and $\tilde{O}_y(\vec{q})$ derived from $R(\vec{r}, |E| = 150\,\text{meV})$ (Fig. 4.6) for a $\text{Bi}_2\text{Sr}_2\text{CaCu}_2\text{O}_{8+\delta}$ sample with hole concentration $p = 8 \pm 1\%$
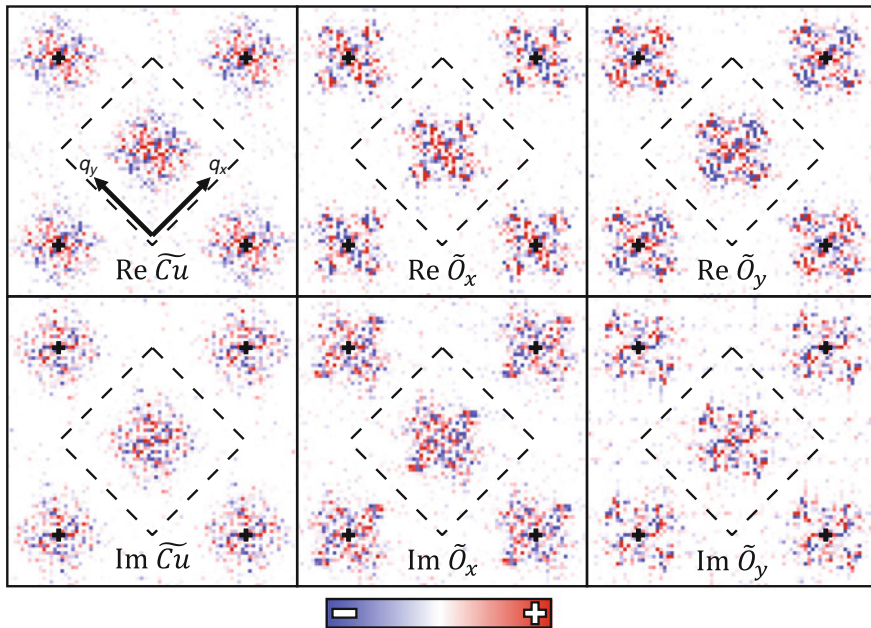
Fig. D.2 Real and imaginary parts of the sub-lattice segregated Fourier transforms $\tilde{Cu}(\vec{q})$, $\tilde{O}_x(\vec{q})$ and $\tilde{O}_y(\vec{q})$ derived from $Z(\vec{r}, |E| = 150\,\text{meV})$ (Fig. 3.1) for a $\text{Na}_x\text{Ca}_{2-x}\text{CuO}_2\text{Cl}_2$ sample with hole concentration $p = 12 \pm 1\%$

Appendix E
Topographic Imaging of the Cuprate d-Symmetry Form Factor Charge Density Wave

In Chap. 4 we studied the d-symmetry form factor charge density wave (CDW) in under-doped cuprates using spectroscopic-imaging STM (SI-STM) by analysing the spectroscopic maps $g(\vec{r}, E)$, $I(\vec{r}, E)$ defined in Chap. 2, and their derivatives $Z(\vec{r}, |E|) = g(\vec{r}, +|E|)/g(\vec{r}, -|E|)$ and $R(\vec{r}, |E|) = I(\vec{r}, +|E|)/I(\vec{r}, -|E|)$. From these we then determined that the CDW in under-doped $Bi_2Sr_2CaCu_2O_{8+\delta}$ and $Na_xCa_{2-x}CuO_2Cl_2$ has a predominantly d-symmetry form factor by examining the sub-lattice segregated Fourier transform $\tilde{D}(\vec{q}) = \tilde{O}_x(\vec{q}) - \tilde{O}_y(\vec{q})$ as detailed in Chaps. 3 and 4.

At dopings near optimal, it is known from several experimental techniques that the intensity of the d-symmetry form factor density wave diminishes rapidly in $Bi_2Sr_2CaCu_2O_{8+\delta}$ [6]. Therefore, to improve the visualisation of the d-symmetry form factor density wave signature at such high-dopings as used here, we use topographic information instead. In constant-current topographic imaging, the STM feedback system adjusts the tip-sample separation, z, as it scans over the sample surface to maintain a set-point current, I_s, at a constant applied tip-sample bias V_s. The topographic image $T(\vec{r})$ is related to the superconductor-insulator-normal metal (SIN) tunnelling current

$$I(\vec{r}, z, E = eV) = f(\vec{r}, z) \int_0^{eV_s} n_s(\vec{r}, \epsilon)d\epsilon \, , \qquad (E.1)$$

where $n_s(\vec{r}, \epsilon)$ is the sample density of states. Here $f(\vec{r}, z)$ encodes all matrix-element variations, which includes those due to surface corrugation, work-function variation and the form of sample and tip wave-functions.

Motivated by standard results from the WKB approximation in the strongly attenuating barrier limit and the work of Tersoff and Hamman described in Chap. 2 we assume that $f(\vec{r}, z)$ takes the form

$$f(\vec{r}, \vec{z}) = \exp(-\kappa z)A(\vec{r}) \, , \qquad (E.2)$$

where κ is a tunnelling decay factor that depends on the work functions of the sample and tip. In constant-current topographic mode the value of z recorded in the topographic image $T(\vec{r})$ is then

$$T(\vec{r}) = \frac{1}{\kappa} \ln \left[\int_0^{eV_s} n_s(\vec{r}, \epsilon) d\epsilon \right] + \frac{1}{\kappa} \ln \left[\frac{I_s}{A(\vec{r})} \right] . \tag{E.3}$$

Thus high signal-to-noise topographic images obtained by constant-current STM imaging reveal contributions from both the surface structure and variations in $n_s(\vec{r}, E)$.

While a single cuprate topographic image will contain the signature of the d-symmetry form factor CDW, subtracting one topographic image from another taken at opposite bias polarity can further enhance the cuprate CDW signal. This is because, as demonstrated in Chap. 4, the d-symmetry form factor CDW modulations at the pseudo-gap energy scale, $|E| \sim \Delta_1$ in $Bi_2Sr_2CaCu_2O_{8+\delta}$ and $Na_xCa_{2-x}CuO_2Cl_2$ modulates in anti-phase between empty and filled states. Hence, a subtraction of topographic images $T^+(\vec{r})$ and $T^-(\vec{r})$, formed with biases $+V_s$ and $-V_s$ and with $eV_s \gtrsim \Delta_1$ should amplify the CDW contrast. Indeed using Eq. E.3 one can see that this should be related to the spectroscopic map $R(\vec{r}, |E|)$ via

$$T^+(\vec{r}) - T^-(\vec{r}) = \frac{1}{\kappa} \ln \left[\frac{\int_0^{eV_s} n_s(\vec{r}, \epsilon) d\epsilon}{\int_0^{-eV_s} n_s(\vec{r}, \epsilon) d\epsilon} \right] = \frac{1}{\kappa} \ln \left[R(\vec{r}, |eV_s|) \right] , \tag{E.4}$$

under the assumption that the factor $A(\vec{r})$ is the same for positive and negative biases.

In Fig. E.1a and b I demonstrate this procedure using two high-resolution, high-signal-to-noise ratio topographs $T(\vec{r})$ taken at opposite bias polarities (80 and –80 mV) with the same conventional tungsten tip for a $Bi_2Sr_2CaCu_2O_{8+\delta}$ sample with $p = 0.17$. They are spatially registered to each other with picometre precision using the algorithm given in Sect. 3.5. Figure E.1c is the difference of these topographs, from which the two oxygen sub-lattice segregated images $O_x(\vec{r}); O_y(\vec{r})$ are then extracted and $\tilde{D}(\vec{q}) = \tilde{O}_x(\vec{q}) - \tilde{O}_y(\vec{q})$ calculated. $\tilde{D}(\vec{q})$, shown here in Figs. E.1d and 7.2d in Chap. 7, reveals a predominantly d-symmetry form factor CDW because of the existence of four maxima at the CDW wave-vector $Q_C = (\pm 0.22, 0)2\pi/a_0$ and $(0, \pm 0.22)2\pi/a_0$.
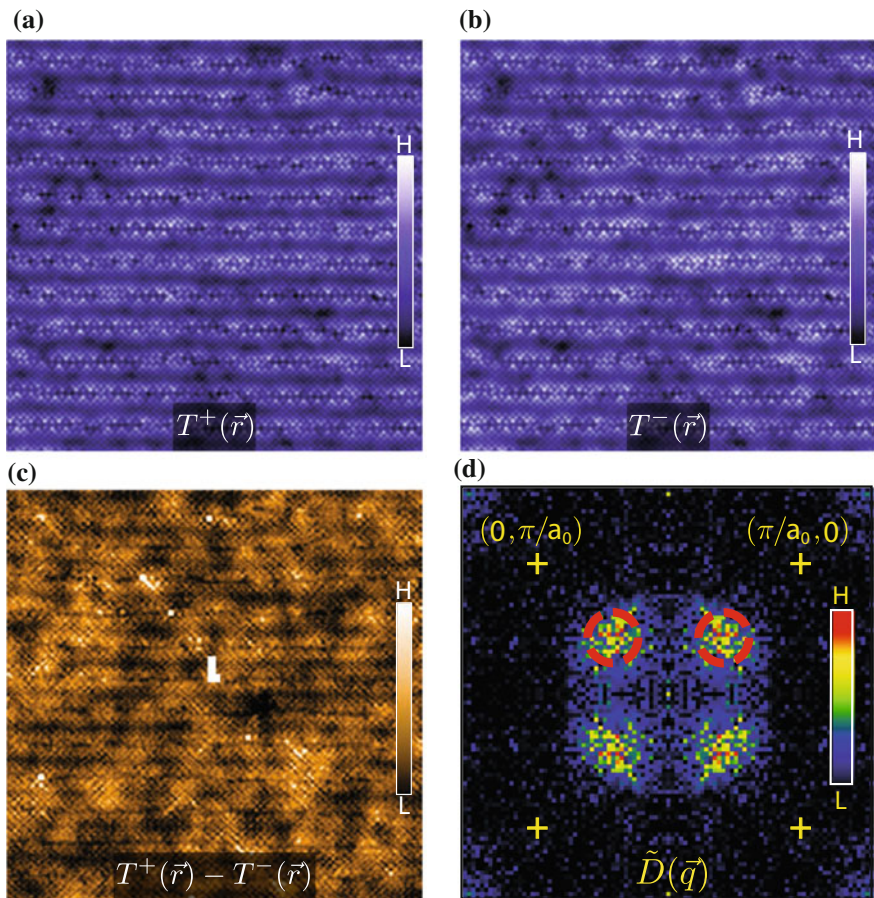
Fig. E.1 **a** Intra unit-cell resolution topograph of $Bi_2Sr_2CaCu_2O_{8+\delta}$ sample with $p = 0.17$, taken with $V_s = +80$ mV and $I_s = 30$ pA. **b** Topograph in identical field of view as **a** and registered to **a** with picometer precision. An setup bias polarity opposite to that in **a** was used with $V_s = -80$ mV and $I_s = 30$ pA. **c** Difference between **a** and **b** showing clear d-symmetry form factor CDW modulations. Their contrast is increased in this subtraction due to a π phase shift between the modulations present in **a** and **b**. **d** Fourier transform $\tilde{D}(\vec{q}) = \tilde{O}_x(\vec{q}) - \tilde{O}_y(\vec{q})$ calculated from **c** revealing d-symmetry form factor CDW modulations at wave-vector $Q_C = (\pm 0.22, 0)2\pi/a_0$ and $(0, \pm 0.22)2\pi/a_0$. This Fourier transform is symmetrised about the vertical axis

Appendix F
Absence of Setup Effect in Relative Spatial Phase Measurements

In Sect. 4.6 I reported a spatial π phase shift between CDW modulations at wave-vectors $\vec{Q} \approx (0, 0.25)(0.25, 0)2\pi/a_0$ in $g(\vec{r}, E = +\Delta_1)$ and $g(\vec{r}, E = -\Delta_1)$ for a $Bi_2Sr_2CaCu_2O_{8+\delta}$ sample with $p \approx 6\%$. In this appendix I demonstrate that this is not due to the setup effect artifact discussed in Sect. 2.4.1.

As detailed in Chap. 2 the differential tunnelling conductance is given by

$$g(\vec{r}, E = eV) = I_S \frac{n(\vec{r}, eV)}{\int_0^{eV_s} n(\vec{r}, \epsilon)d\epsilon} , \tag{F.1}$$

where I_S and V_S are the set-point current and voltage respectively. The term in the denominator is responsible for the setup effect since it imprints the integral of the local density of states (LDOS) over the range of energies 0 to eV_s onto every energy in $g(\vec{r}, E = eV)$.

For example, if $\int_0^{eV_s} n(\vec{r}, \epsilon)d\epsilon$ contains modulations at wave-vector $\vec{Q}$, and $n(\vec{r}, E = E_1)$ does not contain any modulations at this wave-vector, $g(\vec{r}, E_1)$ will exhibit modulations at wave-vector $\vec{Q}$ but in spatial anti-phase with $\int_0^{eV_s} n(\vec{r}, \epsilon)d\epsilon$. Clearly this modulation in $g(\vec{r}, E_1)$ does not reflect any physical modulation in the local density of states at energy E_1.

To guard against this effect in the collection of the data presented in Sect. 4.6, we found set-point parameters V_S and I_S for which $\int_0^{eV_s} n(\vec{r}, \epsilon)d\epsilon$ does not exhibit any d-symmetry form factor modulations at $\vec{Q} \approx (0, 0.25)(0.25, 0)2\pi/a_0$ for a specific hole concentration of $p = 6\%$. To establish that we had indeed found V_S and I_S satisfying these conditions we used the simultaneous topograph to the spectroscopic data presented in Fig. 4.16 ($p = 6\%$).

As detailed in Appendix E, the topographic image $T(\vec{r})$ can be expressed as

$$T(\vec{r}) = \frac{1}{\kappa} \ln \left[\int_0^{eV_s} n_s(\vec{r}, \epsilon)d\epsilon \right] + \frac{1}{\kappa} \ln \left[\frac{I_s}{A(\vec{r})} \right] , \tag{F.2}$$
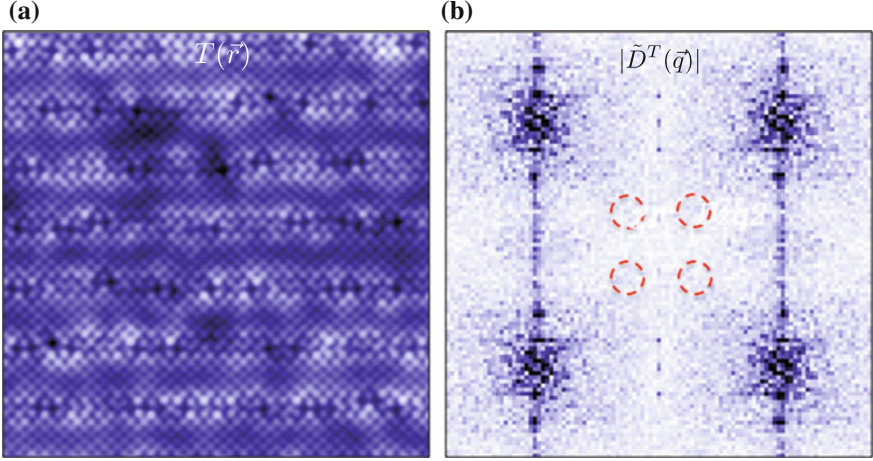
(a)   **(b)**

Fig. F.1 **a** Simultaneous topograph, $T(\vec{r})$ to spectroscopic data shown in Fig. 4.16 for a $Bi_2Sr_2CaCu_2O_{8+x}$ sample with $p \sim 6\%$. A set-point voltage $V_S = 250\,mV$ was used to acquire the topograph. **b** Fourier transform $|\tilde{D}^T(\vec{q})|$ derived from the topograph in **a**. There are no peaks at the wave-vectors $\vec{Q} \approx (0, 0.25)(0.25, 0)2\pi/a_0$ (*red circles*)

where κ is a tunnelling decay factor that depends on the work functions of the sample and tip. $A(\vec{r})$ encodes all other spatial dependencies of the tunnelling matrix elements. The first term in Eq. F.2 measures exactly the denominator of Eq. F.1 that gives rise to the setup effect, i.e. the integrated density of states. Thus, any modulations in $\int_0^{eV_s} n_s(\vec{r}, \epsilon)d\epsilon$ should be apparent in $T(\vec{r})$.

In Fig. F.1a I show the topographic image, $T(\vec{r})$, simultaneous to the spectroscopic data shown in Fig. 4.16. In Fig. F.1b I show the Fourier transform $|\tilde{D}^T(\vec{q})|$ derived from the topograph in (a). No modulations are detected at wave-vectors $\vec{Q} \approx (0, 0.25)(0.25, 0)2\pi/a_0$, signifying that there are no d-symmetry form factor modulations in $\int_0^{eV_S} n(\vec{r}, \epsilon)d\epsilon$ at these wave-vectors. Thus, the spatial π phase shift between d-symmetry form factor CDW modulations in $g(\vec{r}, E = +\Delta_1)$ and $g(\vec{r}, E = -\Delta_1)$ reported in Sect. 4.6 is not due to the setup effect.

Appendix G
Antiphase Modulation of Filled and Empty States at $|E| = \Delta_1$

(See Fig. G.1).

Fig. G.1 Field of view average of difference in spatial phase of d-symmetry form factor CDW modulations in $g(\vec{r}, E)$ *above* and *below* the chemical potential. Data is shown for $Bi_2Sr_2CaCu_2O_{8+\delta}$ samples with $p = 0.11$ and $p = 0.17$. As in Fig. 4.16, CDW modulations at $|E| \sim \Delta_1$ acquire a π phase shift between empty and filled states. In conjunction with the results presented in Fig. 4.16 this demonstrates that this phenomenology is consistent across a range of doings $0.06 \le p \le 0.17$, spanning the pseudogap regime
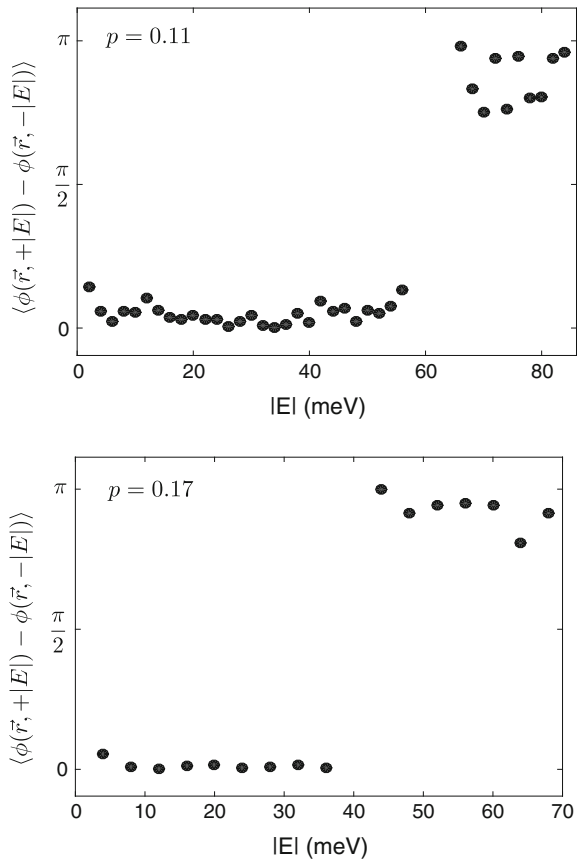
Appendix H
Measuring R_N for Cuprate SJTM

In principle, SJTM allows direct measurement of modulations in the superconducting order parameter amplitude through the product $I_J R_N$. Here I_J is the intrinsic Josephson critical current of the junction and R_N is a characteristic resistance of the single-particle tunnelling channel. In taking this product, variations that affect the matrix elements for tunnelling of Cooper pairs and the single-particle tunnelling conductance $(1/R_N)$ in the same way cancel out.

We use the differential conductance dI/dV_B at a bias voltage V_B far higher than the SIS gap edge as an estimate of the ungapped, "normal state", junction conductance G_N. Simultaneous measurement of this value and $I_c(\vec{r})$ were not possible because the former requires V_B in the hundreds of millivolts while the latter requires V_B of a few tens of microvolts. Moreover, in the picometer range tip-sample separations used in measuring $I_c(\vec{r})$, the single-particle tunnelling current can become destructively large to our $Bi_2Sr_2CaCu_2O_{8+\delta}$ nanoflake tip. Thus the following procedure was adopted:

1. Measure $I_c(\vec{r})$ with set-point current $I_s = I_{s1}$ and bias voltage $V_s = V_{s1}$, as shown in Fig. H.1a.
2. In the same field of view measure $g_1(\vec{r}, E)$, defined as dI/dV for bias voltages V_{s1} to $-V_{s1}$ with set-point condition $I_s = I_{s1}$, $V_s = V_{s1}$.
3. In the same field of view measure $g_2(\vec{r}, E)$ defined as dI/dV with set-point condition $I_s = I_{s2}$, $V_s = V_{s2}$ for bias voltages V_{s2} to $-V_{s2}$, where $V_{s2} \gg V_{s1}$ and $V_{s2} > \Delta_{SIS}$.
4. Over the range $V = [-V_{s1}, V_{s1}]$ determine the coefficients $\alpha(\vec{r})$ and $\beta(\vec{r})$ which scale $g_2(\vec{r}, E)$ onto $g_1(\vec{r}, E)$ via $g_1(\vec{r}, E) = \alpha(\vec{r}) g_2(\vec{r}, E) + \beta(\vec{r})$. In doing the scaling a small region of voltages near $V = 0$ where the Cooper-pair tunnelling (Josephson) signal exhibits is excluded.
5. $R_N(\vec{r})$ for junctions used to measure $I_c(\vec{r})$ is then given by $1/R_N(\vec{r}) = G_N(\vec{r}) = \frac{\alpha(\vec{r})}{2} \left[g_2(\vec{r}, +V_{s2}) + g_2(\vec{r}, -V_{s2}) \right] + \beta(\vec{r})$ as shown in Fig. H.1b.

Now we consider the case of the cuprate supermodulation PDW. The bulk quasi-periodic distortion of the $Bi_2Sr_2CaCu_2O_{8+\delta}$ crystal at wave-vector $\vec{Q}_{SM}$ leads to modulations of the measured $I_c(\vec{r})$ at the same wave-vector superposed on the larger background,
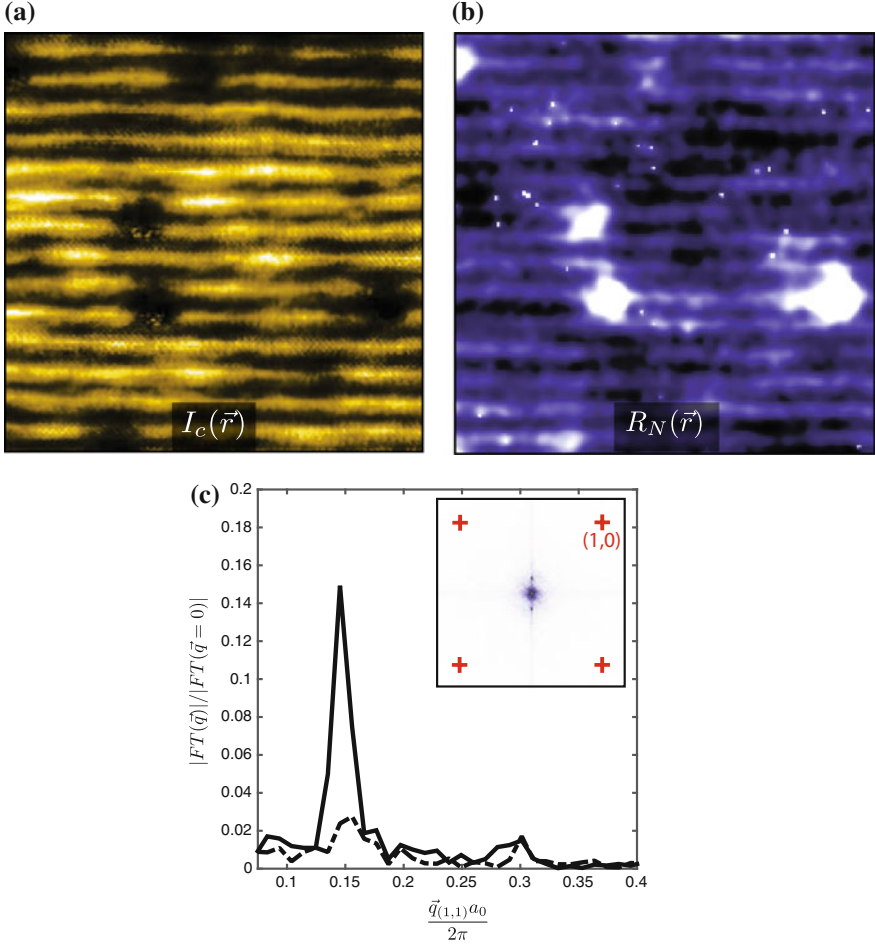
(a)

$I_c(\vec{r})$

(b)

$R_N(\vec{r})$

(c)

Fig. H.1 **a** A typical measured $I_c(\vec{r})$ image of $Bi_2Sr_2CaCu_2O_{8+\delta}$ with the crystal super-modulation effect retained and apparent as strong spatial modulations in I_c along the vertical axis. **b** Measured $R_N(\vec{r})$ image in the same field of view as **a**, with the crystal super-modulation effect retained. The spatial modulations in $R_N(\vec{r})$ along the vertical axis are greatly diminished in relative amplitude compared to $I_c(\vec{r})$ modulations in **a**. **c** The *inset* shows $|\tilde{R}_N(\vec{q})|$, the magnitude of the Fourier transform of $R_N(\vec{r})$ from **b**. It shows that variations in $R_N(\vec{r})$ near $\vec{q} \approx (\pm0.25, 0); (0, \pm0.25)2\pi/a_0$ are negligible. Plotting the simultaneously measured Fourier amplitudes of $\tilde{I}_c(\vec{q})$ (*solid line*) and $\tilde{R}_N(\vec{q})$ (*dashed line*) along the (1,1) direction passing through the wave-vector of the super-modulation $\vec{Q}_{SM}$ shows that $\frac{R_N^P}{R_N^0}/\frac{I_J^P}{I_J^0} \approx 0.25 < 1$. This, together with the *inset*, indicates that modulations in $I_c(\vec{r})$ at $\vec{Q}_{SM}$ and near $\vec{q} \approx (\pm0.25, 0); (0, \pm0.25)2\pi/a_0$ are primarily arising from the variations of the superconducting condensate

$$|\Psi(\vec{r})| \propto I_J(\vec{r}) R_N(\vec{r}) = \left(I_J^0 + I_J^P \cos(\vec{Q}_{SM} \cdot \vec{r}) \right) \left(R_N^0 + R_N^P \cos(\vec{Q}_{SM} \cdot \vec{r} + \phi) \right) \quad \text{(H.1)}$$

$$= I_J^0 R_N^0 + R_N^0 I_J^P \cos(\vec{Q}_{SM} \cdot \vec{r}) + I_J^0 R_N^P \cos(\vec{Q}_{SM} \cdot \vec{r} + \phi) + \cdots ,$$
$$\text{(H.2)}$$

where I allow for an arbitrary phase difference ϕ between modulations in I_J and R_N at $\vec{Q}_{SM}$. For any value of ϕ, one may conclude that the modulation in I_J at $\vec{Q}_{SM}$ is, at least in part, due to a modulation in $\Psi(\vec{r})$ if

$$\frac{R_N^P}{R_N^0} \bigg/ \frac{I_J^P}{I_J^0} < 1 . \quad \text{(H.3)}$$

In the experiments presented in Chaps. 5 and 7 we measure the quantity

$$I_c(\vec{r}) \propto (I_J^0)^2 + 2 I_J^0 I_J^P \cos(\vec{Q}_{SM} \cdot \vec{r}) + \cdots \quad \text{(H.4)}$$

as shown in Fig. H.1a. In Fig. H.1b I show $R_N(\vec{r})$ derived as above. By comparing the amplitude of $\tilde{I}_c(\vec{q})$ and $\tilde{R}_N(\vec{q})$ at $\vec{q} = \vec{Q}_{SM}$, normalised to their $\vec{q} = 0$ value, one may determine $\frac{R_N^P}{R_N^0} \big/ \frac{I_J^P}{I_J^0}$ as in Fig. H.1c. We find that this ratio has a value of ≈ 0.25 and thus modulations in $I_c(\vec{r})$ at $\vec{Q}_{SM}$ can be regarded as being due to those in $\Psi(\vec{r})$.

The inset to Fig. H.1c is $|\tilde{R}_N(\vec{q})|$, showing directly that variations in $R_N(\vec{r})$ near $\vec{q} \approx (\pm 0.25, 0); (0, \pm 0.25) 2\pi/a_0$ are negligible, so that modulations in $I_c(\vec{r})$ at those wave-vectors are those of the condensate itself.

References

1. S. Sachdev, R. La Placa, Bond order in two-dimensional metals with antiferromagnetic exchange interactions. Phys. Rev. Lett. **111**(2), 027202 (2013)
2. R. Comin, A. Damascelli, Resonant x-ray scattering studies of charge order in cuprates. arXiv (2015), pp. 1–26
3. K. Fujita et al., Spectroscopic imaging scanning tunneling microscopy studies of electronic structure in the superconducting and pseudogap phases of cuprate high-tc superconductors. J. Phys. Soc. Jpn. **81**(1), 011005 (2012)
4. M. Vojta, Lattice symmetry breaking in cuprate superconductors: stripes, nematics, and superconductivity. Adv. Phys. **58**(6), 699–820 (2009)
5. M.H. Hamidian et al., Picometer registration of zinc impurity states in $Bi_2Sr2\,CaCu_2O_{8+\delta}$ for phase determination in intra-unit-cell Fourier transform STM. New J. Phys. **14**(5), 053017 (2012)
6. K. Fujita et al., Simultaneous transitions in cuprate momentum-space topology and electronic symmetry breaking. Science **344**(6184), 612–616 (2014)